A NOVEL TRANSIENT TESTING METHOD FOR HEAT/ENERGY WHEEL COMPONENTS

A Thesis Submitted to the College of

Graduate Studies and Research

in Partial Fulfillment of the Requirements for

the Degree of Doctor of Philosophy

in the Department of Mechanical Engineering

University of Saskatchewan

Saskatoon

By

Farhad Fathieh

July 2016

PERMISSION TO USE

In presenting this thesis in partial fulfillment of the requirements for a postgraduate degree from the University of Saskatchewan, I agree that the Libraries of this University may make it freely available for inspection. I further agree that permission for copying of this thesis in any manner, in whole or in part, for scholarly purposes may be granted by the professors who supervised this thesis work or, in their absence, by the Head of the Department or the Dean of the College in which my thesis work was done. It is understood that any copying, publication, or use of this thesis or parts thereof for financial gain shall not be allowed without my written permission. It is also understood that due recognition shall be given to me and to the University of Saskatchewan in any scholarly use which may be made of any material in this thesis. Requests for permission to copy or to make other use of material in this thesis in whole or in part should be addressed to:

Head of the Department of Mechanical Engineering

University of Saskatchewan

57 Campus Drive, Saskatoon, Saskatchewan, S7N 5A9

ABSTRACT

Heat wheels and energy wheels are widely used in ventilation systems to recovery sensible and latent energy, and consequently, reduce the energy required to condition outdoor ventilation air for buildings. This Ph.D. thesis proposes a novel transient testing facility and method to predict the effectiveness of heat/energy wheels by testing a small component of the wheels. The component required for this test is a few coated sheets (for energy wheels) or non-coated sheets (for heat wheels). The effectiveness values predicted for small-scale testing and determined from correlations in the literature agreed within ±3% and within the experimental uncertainty bounds (at wheel angular speed, ω, of 20 rpm when $NTU < 13.1$ and $2 < NTU_m < 10$).

The transient component testing was also used to investigate the effects of physical and sorption properties of mesoporous silica gel on moisture transfer. It was found that the smaller the pore width and the larger the specific surface area, the higher the sorption capacity of the desiccant. However, the smaller pore width increases the vapour diffusion resistance and reduces the sorption rate. It was observed that the energy exchanger coated with silica gel that has an average pore width of 63 Å and an average particle size of 150 μm (63 Å-150 μm) performed better than the two other silica gel coated exchangers (77 Å-55 μm and 115 Å-160 μm), especially when $\omega < 5$ rpm. The latent effectiveness of all the exchangers were nearly the same at higher angular speeds, $\omega > 10$ rpm. Finally, the performance of an exchanger coated with biopolymer starch particles was compared with the silica gel coated exchangers through transient testing. It was found that the starch particles increased the latent effectiveness by 13% at $\omega = 0.5$ rpm compared to the silica gel particles while the latent effectiveness values were nearly equal at $\omega = 20$ rpm. Considering that starch typically costs less than silica gel, bio-desiccants such as starch have great potential to be used in desiccant coated exchangers.

ACKNOWLEDGEMENTS

This thesis would not have been possible without the help of many individuals. First and foremost, I would like to acknowledge my distinguished supervisors, Dr. Carey Simonson, Dr. Richard Evitts, and Professor Robert Besant not only for their encouragement and invaluable feedback throughout my Ph.D. studies, but also for their professional training along the road. Thank you for your kind support and "teachable moments" during the past four years which will be some I cherish forever.

I am immensely grateful to my committee members, Dr. James Bugg, Dr. Lee Wilson, and Dr. David Torvi for the compassion and coaching they have given me throughout my doctorate program.

To my fellow graduate students/post-doctoral fellows, Dr. Ge Gaoming, Dr. A. H. Abdel-Salam, M. Rafati Nasr, M. R. Abdel-Salam, M. R. Naghash, S. Niroumand, Dr. D. Ghadiri Moghadam, M.J. Afshin, A. Oghabi, and H. Kamali: thank you for the countless hours of assistance. I was extremely fortunate to be part of a supportive and active group. I would be remiss if I did not acknowledge R. Retzlaff, D. Duetscher, and Dr. M. Fauchoux for their support and valuable training in developing the test facility and conducting experiments. I also wish to thank my colleagues Dr. S. Ravazi, L. Dehabadi, M. Shakouri, and A. Arzani for their feedback and contributions. My special thanks also go to my family and friends who supported me with endless love and words of encouragement.

I would like to acknowledge the Natural Sciences and Engineering Research Council of Canada (NSERC), the Department of Mechanical Engineering at the University of Saskatchewan, the Government of Saskatchewan's Innovative & Opportunity Scholarship, Russell (Russ) William Haid Award, Frederick Wheeler & W.H.T. Spary Graduate Scholarship for financial support.

DEDICATION

I dedicate this thesis to my wife, my parents, and my brother.

Thank you very much for your support throughout my Ph.D. studies.

TABLE OF CONTENTS

LIST OF FIGURES

LIST OF TABLES

NOMENCLATURE

ACRONYM

DEM	Double Exponential Model
EX	Exchanger
HAS	High Amylose Starch
HVAC	Heating, Ventilating and Air Conditioning
PSA	Particle Size Analyzer
SEM	Single Exponential Model
SG	Silica gel

SYMBOLS

A_{duct}	cross-sectional area of the each duct [m^2]
A_{ht}	total heat surface area of the exchanger [m^2]
b_{ch}	width of exchanger channels [m]
C_p	specific heat capacity [$J(kg^{-1}.K^{-1})$]
C_r^*	heat capacity rate ratio
d_h	hydrodynamic diameter of channels [m]
d_p	desiccant particle size [μm]
F	input forcing function
H^*	operating condition factor
H	convective heat transfer coefficient [$W(m^2.K^{-1})$]
h_m	convective mass transfer coefficient [$m.s^{-1}$]
h_{ch}	height of exchanger channels [m]

L_{ch}	length of exchanger channels [m]
M	mass of matrix [kg]
$\dot{m}_a$	air mass flow rate [$kg \cdot K^{-1}$]
NTU	number of transfer unit on the supply or exhaust side
NTU_m	number of mass transfer unit on the supply or exhaust side
P_v	desiccant specific pore volume [$m^3 \cdot g^{-1}$]
P_w	desiccant pore width [Å]
Q_a	volumetric air flow rate [$L \cdot s^{-1}$]
Re	Reynolds number
RH	relative humidity [%]
S_A	desiccant specific surface area [$m^2 \cdot g^{-1}$]
t	time [s]
t_s	student t-factor
U_B	bias (systematic) uncertainty
U_P	precision uncertainty
U_T	total uncertainty
V_f	airflow face velocity [$m \cdot s^{-1}$]
W	normalized air humidity ratio
W_m	maximum moisture content in desiccant [g/g]
W	air humidity ratio [kg/kg]
$x_{h,FD}$	hydrodynamic entry length [m]
$x_{th,FD}$	thermal entry length [m]

GREEK SYMBOLS

γ	response weighting factor
Δ	difference between the exchanger outlet and inlet conditions
δ	thickness of the exchanger sheets [m]
ε_L	latent effectiveness [%]
ε_s	sensible effectiveness [%]
ε_T	total effectiveness [%]
θ	normalized temperature
ρ	density [$kg \cdot m^{-3}$]
τ	time constant of exchanger response [s]
ψ	angle ratio
Ω	accumulative moisture uptake/removal
ω	wheel angular speed [s^{-1}or rpm]

SUBSCRIPTS

a	Airflow
ads	Adsorption
b	breakthrough point
CF	counter-flow
c	cold airstream
ch	Channels
cr	Critical
des	desiccant (or desorption)

e	exhaust point
final	test final conditions
FD	fully-developed
h	hot airstream
ht	heat transfer
i	exchanger inlet
init	test initial conditions
M	Matrix
m	mass transfer
o	exchanger outlet
PF	parallel-flow
reg	regeneration
St	step change
W	Wheel
YN	Yoon-Nelson model

SUPERSCIPTS

′	heat loss/gain indicator

CHAPTER 1

INTRODUCTION

1.1 Motivation

The growth in world energy demand, depletion of fossil fuels, increased CO_2 emissions, and lack of alternative promising energy resources have motivated engineers to adopt more energy-efficient technologies. A study from the World Energy Council (WEC) estimates that with no change in the energy consumption rate, the energy consumption in 2020 would be 50-80 % higher than in 1990 (Omer, 2008). Recent statistical data reveal that buildings are responsible for about 40% of national energy consumption in North America (Natural Resources Canada, 2011; U.S. Energy Information Administration (EIA), 2015). More than 50% of this energy is used by heating, ventilating, and air conditioning (HVAC) systems to achieve thermal comfort in industrial and commercial buildings. Furthermore, energy cost has always been a matter of concern for both HVAC designers and consumers. In 2009, Canadians spent about $16 billion to maintain the indoor thermal comfort conditions in buildings (Natural Resources Canada, 2011). As a result, engineers are continuously working towards buildings with reduced sensible and latent loads and equipped with more energy-efficient HVAC systems with lower capital and operational costs. In the past few decades, energy efficient HVAC systems are being equipped with air-to-air heat or energy exchangers which recover a large portion of the energy from the exhaust or the supply airstreams. These exchangers can substantially decrease the cooling and heating load and reduce the capacity of the HVAC equipment installed in commercial and industrial buildings.

Among conventionally available air-to-air heat/energy exchangers, rotary wheels (heat wheels and energy wheels) are the most common exchangers used in the North American HVAC market. The main advantages of rotary wheels are their high energy recovery effectiveness, ease

of manufacturing, low installation, operational, and maintenance cost, and short (2-4 years) payback periods (Asiedu et al., 2004, 2005). Since rotary wheels play an important role in the performance and energy savings of HVAC systems, much attention has been placed on wheel performance testing, enhanced matrix materials, and wheel designs. The main goal of this Ph.D. study is to reduce the time and cost required to test rotary wheels by developing a new method of performance testing, known as transient component testing. The hypothesis is that the transient heat and moisture transfer measurements taken from testing the basic components of wheels can be used to predict the steady-state performance of rotary wheels. This novel method can eventually help to enhance the effectiveness of wheels by facilitating the wheel design process and expediting the performance testing of prototypes.

1.2 Background

1.2.1 Indoor Air Quality Control

An activity pattern study in North America shows that Canadians and Americans spend about 90% of their time indoors (Leech et al., 2002). Due to the amount of time that occupants spend indoors, indoor air quality (IAQ) and thermal comfort of buildings are directly related to occupants' health and productivity (Yu et al., 2009). The main factors that affect thermal comfort and IAQ are temperature, humidity, ventilation rate, and concentration of particles and pollutant gases. The worldwide energy crisis in the 1970s drew public attention towards energy saving strategies. Since then, airtight buildings with enhanced insulation materials and lower ventilation rates have been constructed. However, several studies reveal the adverse effects of low ventilation rates on the well-being and performance of occupants, especially in workplaces and schools (Mendell & Heath, 2005; Sundell et al., 2011). It was reported that the prevalence of sick building syndrome (SBD) is 30%-200% higher in buildings with natural ventilation compared to the buildings equipped with air-conditioning systems (Seppanen & Fisk, 2002). Although the

importance of indoor thermal comfort has been recognized for centuries, the influence of indoor humidity on occupants' health have often been underestimated. The impacts of indoor humidity level on occupants' health are shown in Figure 1.1 which shows that humidity levels between 40-60% are recommended for human health.

In the past few decades, many countries have introduced new regulations, standards, and codes for buildings that require HVAC systems to be equipped with air-to-air heat/energy exchangers (Ashrae & Ies, 2011) to reduce the overall energy consumption while maintaining acceptable IAQ (Ashrae & Ies, 2011). The research in this thesis focuses on a specific type of air-to-air heat/energy exchanger known as *heat wheel* and *energy wheel*. In the next sections, different types of rotary wheels (heat wheels, energy wheels, and desiccant wheels) will be described.

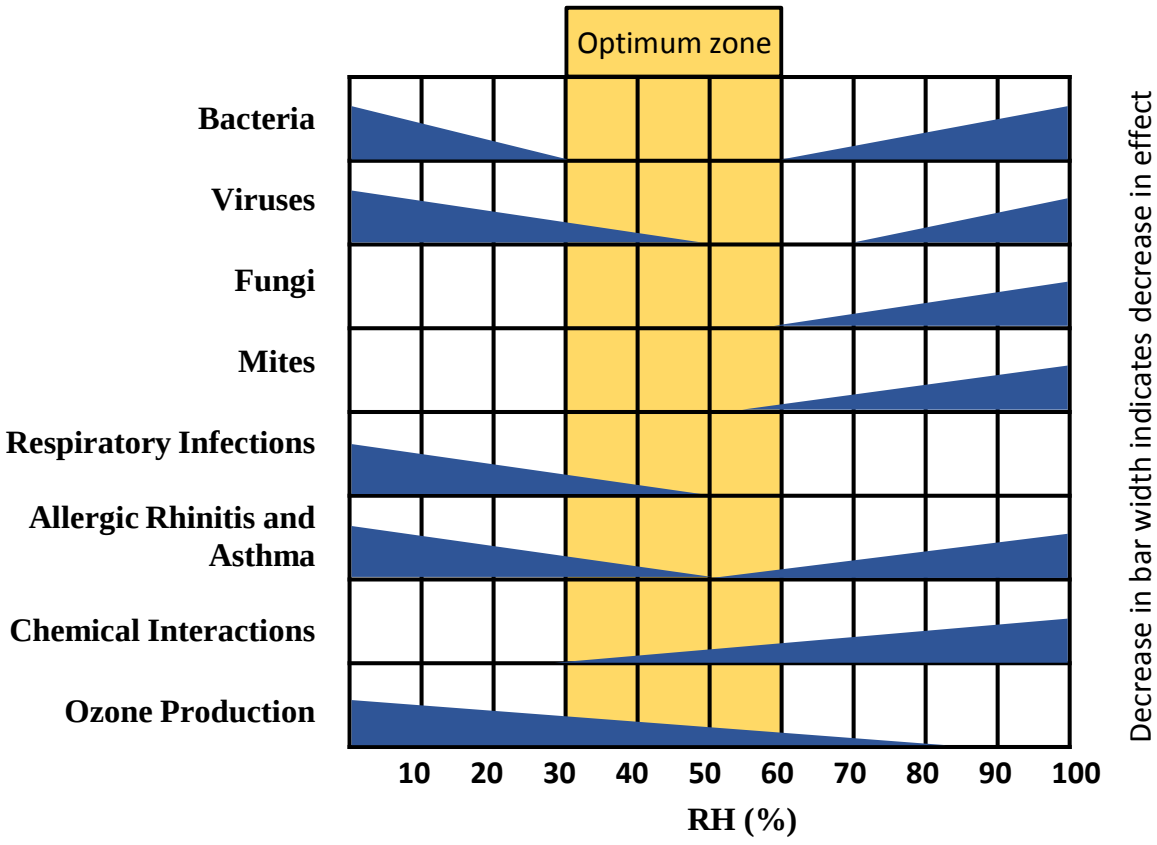

Figure 1.1-Influence of indoor air humidity level on human health and its optimum range (Sterling et al., 1985)

1.2.2 Heat Wheel (Sensible Energy Recovery)

Heat wheels are one of the most effective sensible energy (heat) recovery exchangers. Figure 1.2 shows a schematic of the heat wheel with the supply and exhaust airstreams. Heat wheels consist of a cylindrical matrix with thousands of honeycomb or corrugated flow channels. The matrix is made up of a heat-adsorbing material such as aluminum. As the wheel rotates, heat is continuously transferred between the supply and exhaust airstreams with different temperatures. Heat is absorbed by the wheel matrix as the hot airstream, the supply air in the summer or the exhaust air in the winter, passes through the wheel flow channels, presented in Figure 1.3. The stored heat in the wheel matrix is transferred to the cold airstream as the wheel rotates and the channel is exposed to the cold airstream. This phenomenon repeats as the wheel rotates continuously which leads to continuous heat recovery with an effectiveness of 70-80% (ASHRAE, 2008). Moreover, in a recent application of heat wheels, they are combined with other types of energy exchangers (energy wheels, air-to-air membrane, liquid-to-air membrane) to enhance the coefficient of performance (COP) of the system and prevent frost formation in energy exchangers (Rafati Nasr et al., 2014). Although heat wheels are still of great interest for HVAC designers, heat wheels are not capable of transferring moisture (latent recovery) between air streams unless condensation or frosting occurs in the wheel.

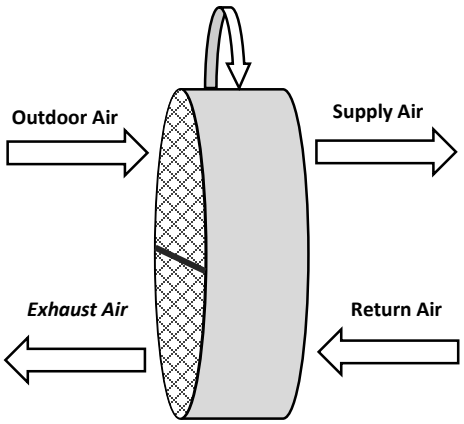

Figure 1.2-Schematic of the heat wheel with supply and exhaust airstreams

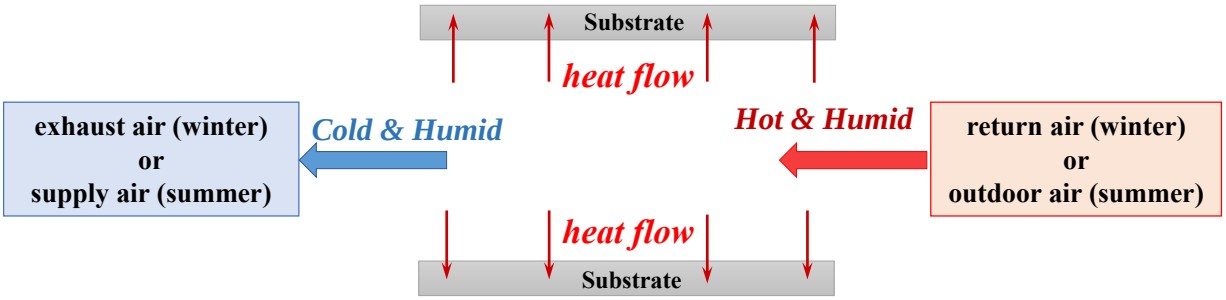

Figure 1.3-Schematic of heat transfer in a channel of heat wheels with no moisture transfer

1.2.3 Energy Wheel (Sensible and Latent Energy Recovery)

While heat wheels are used to transfer sensible energy, energy (enthalpy) wheels are capable of recovering a large portion of sensible (heat) and latent (moisture) energy from the exhaust airstream. Similar to heat wheels, energy wheels have a heat-adsorbing (mainly metallic) cylindrical matrix that consists of a large number of honeycomb or corrugated flow channels. To make the moisture transfer possible, the energy wheel channels are coated with micron-sized highly-porous desiccant particles with strong affinity for water vapor. Silica gel, molecular sieves, activated alumina, and zeolites are extensively used to coat the wheels due to their high surface area, low cost, and low regeneration temperature (Zheng et al., 2014). A schematic of an energy wheel with coating is shown in Figure 1.4. While hot and humid air passes through the wheel channels, heat is mainly stored in the metallic substrate and water vapor is adsorbed by the desiccant particles. As the wheel rotates and the channels are exposed to the cold and dry airstream, the accumulated heat and moisture in the wheel matrix are released into the airstream. As a result of the continuous rotation of the wheel, heat and moisture are transferred between the supply and exhaust airstreams periodically.

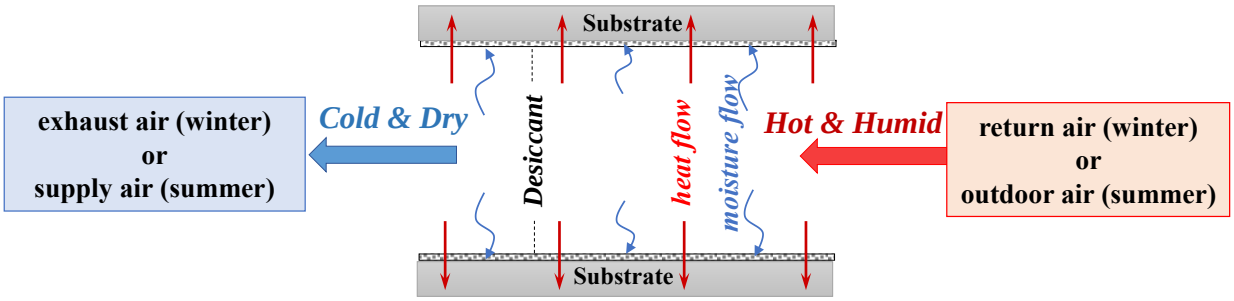

Figure 1.4-Schematic of heat and moisture transfer in a desiccant coated channel of energy wheels

1.2.4 Desiccant Wheels

Desiccant wheels, or desiccant drying wheels, are mainly used as dehumidifiers in HVAC systems in order to remove moisture from the supply air. Compared to conventional dehumidification systems, such as cooling coils, desiccant wheels are beneficial when the required dew point is low (~less than 4°C). In desiccant cooling systems, the desiccant wheel is mainly placed before a direct/indirect evaporative cooling system to decouple the latent and sensible loads for the system. Similar to energy wheels, the matrix of desiccant wheels is coated with micron size desiccant particles; whereas, the matrix substrate is made of materials with low heat capacity, such as plastic. As a result, desiccant wheels have high latent recovery efficiency with low sensible energy recovery. Unlike the regeneration process in energy wheels which takes place at moderate temperature (T_{reg} = 20-35 °C), the desiccant is regenerated at elevated temperatures in desiccant wheels (T_{reg} = 60-90 °C). A heating device, such as electrical or gas heater, is commonly coupled with a desiccant wheel to provide the energy required for the regeneration process. Another difference between energy wheels and desiccant wheels comes from the wheel angular speed. Desiccant wheels typically operate at low angular speeds, 0.1 rpm < ω < 1 rpm, whereas energy wheels and heat wheels angular speed are relatively higher, 10 rpm < ω < 20 rpm.

1.2.5 Wheel Performance Testing

There are several parameters that quantify the performance of rotary wheels. Among them, the effectiveness is the most important factor that identifies the energy recovery efficiency of the heat/energy wheels. The heat recovery performance in rotary wheels is quantified by sensible effectiveness. The sensible effectiveness is defined as the ratio of the actual heat transfer rate between the supply and exhaust airstreams to the maximum possible heat transfer rate between the supply and exhaust airstreams (Kays & London, 1984). Similarly, the moisture recovery performance in energy wheels is indicated by the latent effectiveness. The latent effectiveness is the ratio of actual moisture transfer rate to the highest possible moisture transfer rate between the humid and dry air streams.

The total effectiveness represents the transfer of enthalpy in the energy wheels which is the ratio of actual enthalpy transfer rate to the highest possible enthalpy transfer rate between the supply and exhaust air streams. According to data in the literature, wheel effectiveness values can be determined through experimental, empirical-analytical, or numerical methods. Although numerical simulations are mostly successful in predicting wheel effectiveness, experimental approaches are still the most reliable testing methods to obtain wheel effectiveness values. The following is a brief description of experimental methods for testing wheels.

1.2.5.1 Steady-State Testing Method

In the steady-state testing method, the sensible and latent effectiveness are measured while the wheel operates at steady-state conditions. The steady-state tests are conventionally used to certify wheels at specified operating conditions. Several standards, such as AHRI certification 1060-2011 (ANSI/AHRI, 2014) and ANSI/ASHRAE standard 84-2013 (ANSI/ASHRAE, 2013), provide the specific conditions and stepwise procedure to obtain the effectiveness of the wheels

within acceptable uncertainty limits. AHRI test conditions are listed in Table 1.1. In fact, maintaining the standard conditions requires a large test facility with the ability to provide conditioned air flow. Moreover, obtaining the effectiveness within the acceptable uncertainty limits is reported to be expensive and time consuming which requires extensive online data analysis (Ciepliski, 1997; 1998).

Table 1.1- AHRI standard 1060-2014 test conditions for steady-state testing of energy wheels

Airstream	Conditions	
	Heating	*Cooling*
Supply air		
Dry bulb temperature	1.7 ± 1°C	35.0 ± 1°C
Relative humidity	82.5% ± 2%	82.5% ± 2%
Exhaust air		
Dry bulb temperature	21.1 ± 1°C	23.9 ± 1°C
Relative humidity	49.2% ± 2%	51.2% ± 2%

1.2.5.2 Transient Testing Method

To reduce testing time and cost, Abe et al. (Abe et al., 2006a, 2006b) proposed a testing method which measures the sensible and latent effectiveness from the transient response of the wheel to a step change in the inlet flow properties (temperature or humidity ratio). They suggested that wheels with different matrices and coatings respond to the inlet step change differently and, consequently, each wheel has distinctive transient characteristics. They developed an analytical model that correlates the wheels transient characteristics (time constants and weighting factors) to the effectiveness. In their method of testing, a wheel was subjected to a step change in the inlet airflow temperature and/or humidity ratio while the airflow properties (temperature and humidity) were measured at the inlet and outlet sections. Analyzing the data obtained from transient test, Abe et al. (2006) calculated the effectiveness with acceptable uncertainty from their transient analytical

model. Since then, several researchers studied the transient response of wheel at different operating conditions (Abe et al.2006a, 2006b; Shang & Besant, 2009a, 2008, 2009c). The obtained sensible and latent effectiveness agreed with the steady-state test results within the uncertainty bounds at most of the tested conditions.

The transient testing method has several advantages over the steady-state method, listed in Table 1.2. Since the transient test is performed on part of a stationary wheel, the air supply system and the entire test facility can be scaled down. Moreover, the transient test duration is substantially shorter than conventional steady-state testing. As a result, the cost per test can be effectively reduced for the transient test. In addition, transient testing can effectively be used for performance comparison of the wheels and quality control purposes.

Table 1.2-Comparison between the steady-state and the transient test for determination of the wheels effectiveness

Parameter	Steady state test	Transient test	Factor
Test time	5-10 hours	1 hour	5-10
Equipment cost	$1-2,000,000	$50,000	20-40
Space	1-2,000 ft^2	100 ft^2	10-20
Cost per test	$5-10,000	$500-1,000	10
Uncertainty	±5% (sensible) ±7% (latent)	±4% (sensible) ±5% (latent)	Slight improvement

1.2.6 Literature Overview

Since the invention of desiccant coated wheels (energy wheels and desiccant wheels) in the 1980s, wheels have become the most common air-to-air energy exchangers in HVAC systems. In addition, several desiccant cooling evaporative systems (direct and indirect) have been designed that employ desiccant wheels as a dehumidifier and energy and/or heat wheel as air-to-air energy exchangers (Rafique et al., 2015). As another application in the food and mining industries, new configurations have been developed for desiccant wheels as an industrial dryer (Chua & Chou,

2003). With more emphasis on renewable energy, solar desiccant integrated A/C systems use solar energy to assist the regeneration of desiccant wheels (Ge et al., 2014). Numerous studies have been conducted to study the wheel operation and investigate methods to improve their performance. In this section, a brief statistical overview of data published on wheels (as a single device or as a system component) between 1990 and 2015 is given; whereas, more details on the most related literature are provided at the introduction sections of chapters 2-5. The results have been collected by searching the words *"Energy Wheel"*, *"Enthalpy Wheel"*, *"Desiccant Wheel"*, and *"Heat Wheel"* through the online databases: Engineering Village (www.engineeringvillage.com), Scopus (www.scopus.com), Science Direct (www.sciencedirect.com), and ASME (asmedigitalcollection.asme.org). Figure 1.5 shows the number of published journal articles per year from 1990 to 2015. It should be noted that duplicate papers from the different databases are removed from the search results.

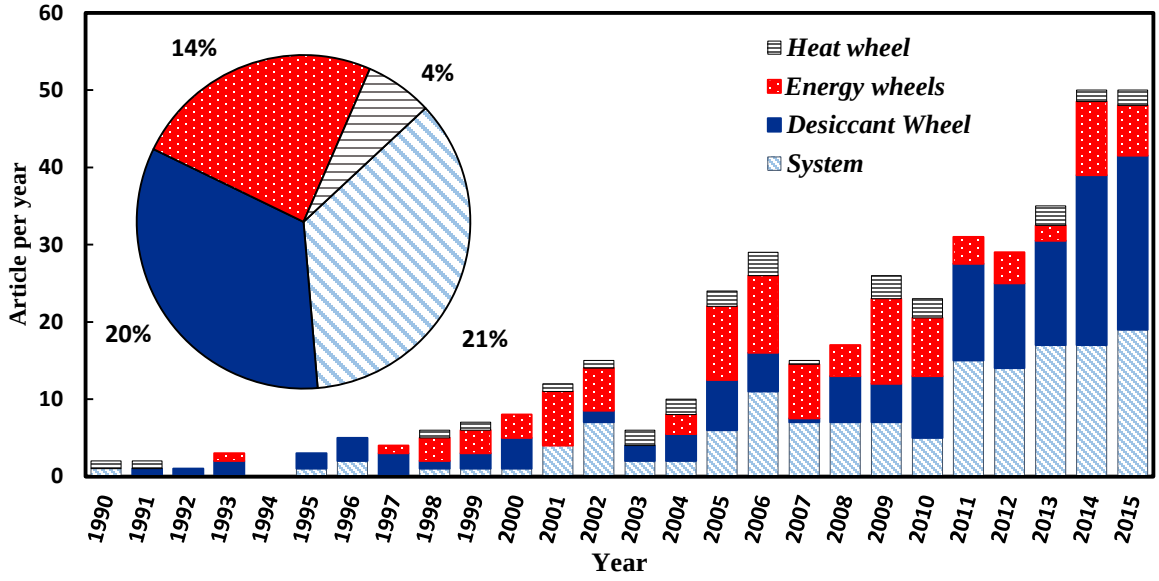

Figure 1.5-Classification of the 416 journal papers on rotary wheels as a single device or a systems component published between 1990 and 2015 as found in Engineering Village, Scopus, Science Direct, and ASME databases

The results in Figure 1.5 clearly indicate an increasing trend in the number of articles, especially after 2010. Although numerous investigations have been conducted on wheel integrated systems, studying the wheel as a single device has the highest contribution. This fact reflects the overall complexity of coupled heat and moisture transfer in the desiccant coated wheels which remains to be fully understood. Figure 1.6 gives a statistical overview of the methodologies used in the wheel studies as a single device. Although several enhanced analytical models and numerical simulations have been proposed throughout these years, experimental investigations are still very common, 39%, where more than 90% of the experiments were performed on full-scale wheels. As discussed in section 1.2.4, full-scale testing has several practical challenges and experimental limitations, such as constructing a full-scale wheel and providing the testing conditions according to standards AHRI conditions, given in Table 1.1. Therefore, developing an alternative small-scale testing methods would be beneficial for wheel performance testing which has received relatively little attention.

A breakdown of the major topics and objectives with the portion of contribution covered in the previous wheel studies is given in Figure 1.7. The papers are divided into three main categories *Operation (50%)*, *Testing (5%)*, and *Design (45%)*. In addition, a list of the main parameters investigated in each category is given in Figure 1.7. Based on Figure 1.7, much focus has been on the design and the operating conditions of wheels with little emphasis on the testing. According to the design parameters listed in Figure 1.7, studying the design parameters at different operating conditions requires hundreds of tests which equates with huge amount of testing time and cost. Therefore, this Ph.D. thesis targets the gap in the literature and attempts to develop an alternative testing method (known as transient component testing) based on the transient method presented in section 1.2.4.

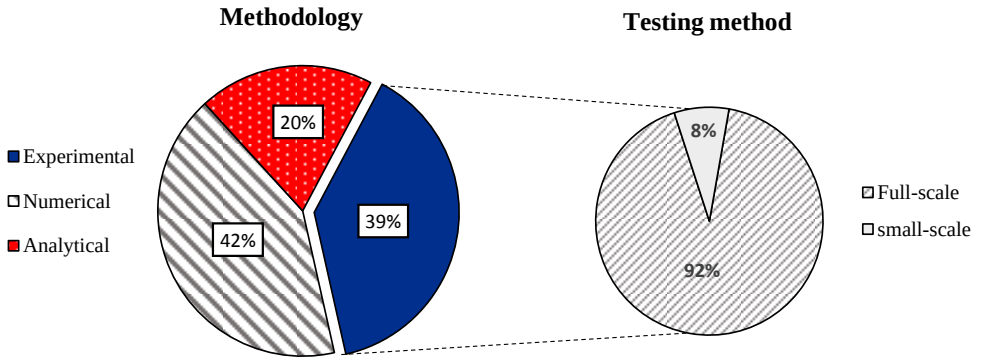

Figure 1.6-A classification for the methodologies used to study the rotary wheels in the majority of journal papers published between 1990 and 2015

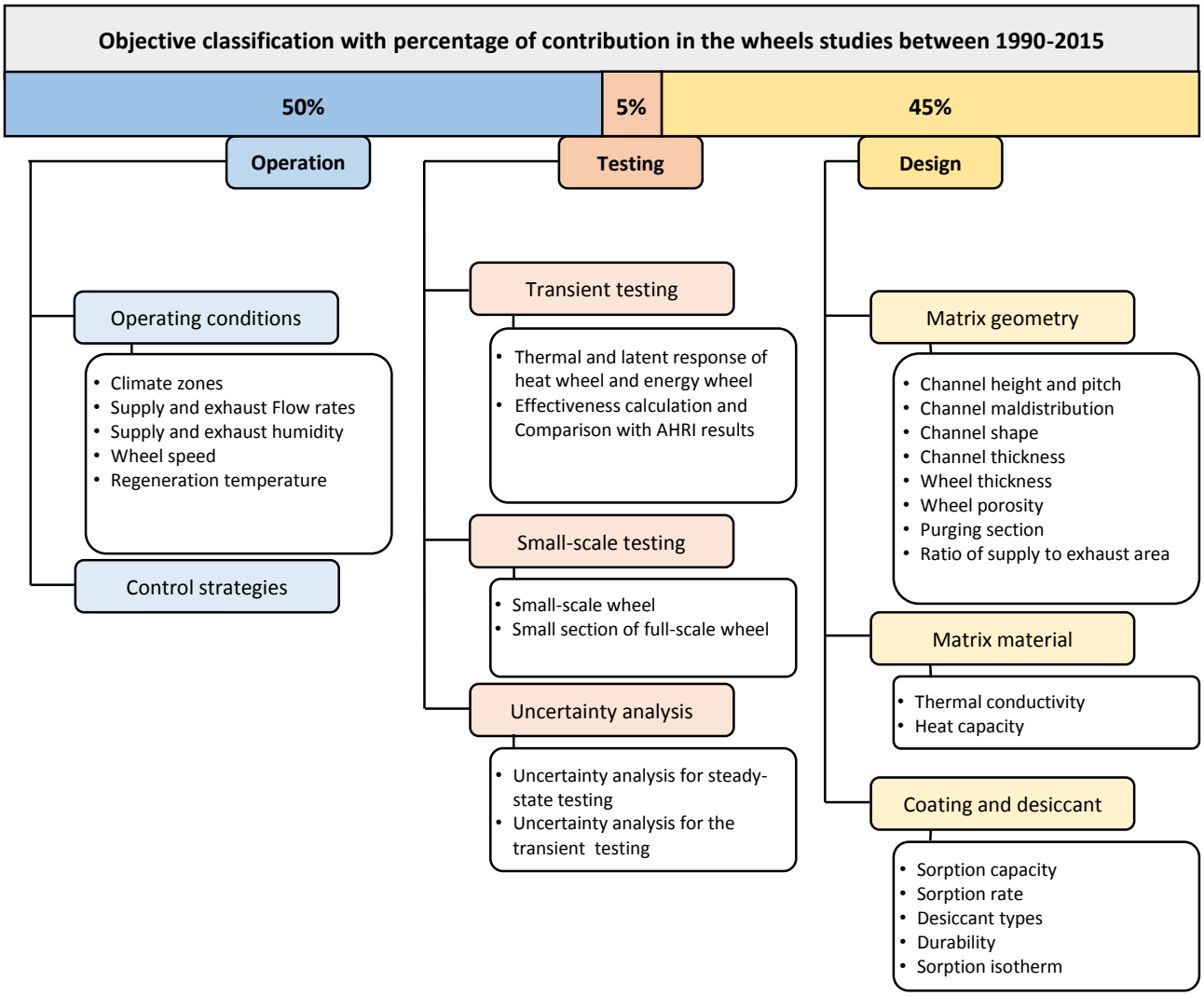

Figure 1.7-A breakdown of common topics reported in the majority of published journals on wheel studies between 1990 and 2015

1.3 Objectives

The main aim of this Ph.D. study is to develop a transient method for testing components of heat wheels and energy wheels. The hypothesis is that it is possible to predict accurately the performance of a full-scale wheel by conducting small-scale transient tests on the wheel components (i.e. materials and coating). For heat wheels, the component is a few sheets of the heat wheel; whereas, the sheets are coated with the desiccant material in the case of energy wheels. A modified version of the transient testing method, mentioned in section 1.2.4, is used in this study. This method of component testing is novel and has not been reported elsewhere in the literature. Transient testing of components enables one to quantify the effects of the desiccant physical and sorption properties on the wheel performance with reduced testing time and cost. It is believed that such a fundamental investigation would be beneficial for better understanding the operation and design of wheels. Therefore, the objectives of this Ph.D. study are defined as follows:

1. To develop a novel testing facility for performing the transient testing on *heat* and *energy wheel* components.
2. To predict the full-scale *heat wheel* effectiveness with its uncertainty and to investigate the relationship between the sensible effectiveness and operating conditions.
3. To predict the full-scale *energy wheel* effectiveness with its uncertainty and to investigate the relationship between the latent effectiveness and operating conditions.
4. To identify the effects of physical, chemical, and sorption properties of the desiccant on the latent effectiveness of energy wheels.

1.4 Publications

The outcome of the current Ph.D. study have been presented in 6 peer-reviewed journal papers, 1 conference paper, and 1 poster presentation. Four of the journal papers are published and two are under review.

1.4.1 Refereed Journal Papers

1. F. Fathieh*, R. W. Besant, R. W. Evitts, C. J. Simonson, "Determination of air-to-air heat wheel sensible effectiveness using temperature step change data", *International Journal of Heat and Mass Transfer*, 2015, **87**, pp 312-326.
2. F. Fathieh*, R. W. Besant, R. W. Evitts, C. J. Simonson, "The effects of Heat Loss/Gain on the Sensible Effectiveness of Heat Wheels Determining from Transient Single Step Testing", *ASME Journal of Thermal Science and Engineering Application*, 2016, **8**, 0311003-1-12.
3. F. Fathieh*, M. Rafati Nasr, S. Sadeh, R. W. Besant, R. W. Evitts, J. Müller, C. J. Simonson, "Determination of Air-to-Air Energy Wheels Latent Effectiveness Using Humidity Step Test Data", *International Journal of Heat and Mass Transfer*, Accepted, July 2016.
4. F. Fathieh*, M. Nezakat, R. W. Evitts, C. J. Simonson, "Effects of Physical and Sorption Properties of Mesoporous Silica Gel on Dehumidification Performance of Energy Wheels", *ASME Journal of Heat Transfer*, Submitted, March 2016.
5. F. Fathieh*, L. Dehabadi, L. D. Wilson, R. W. Besant, R. W. Evitts, C. J. Simonson, "Sorption Study of a Starch Biopolymer as an Alternative Adsorbent for Energy Wheels", *ACS Sustainable Chemistry & Engineering*, 2016, **4**, issue 3, pp 1262-1273.
6. L. Dehabadi, F. Fathieh*, L. D. Wilson, R. W. Evitts, C. J. Simonson, "Study of Dehumidification and Regeneration in a Starch Coated Energy Wheel", *ACS Sustainable Chemistry & Engineering*, Submitted, June 2016.

* *Corresponding author*

1.4.2 Conference Papers and Posters

1. F. Fathieh, R. W. Besant, R. W. Evitts, C. J. Simonson, "Sorption Changes after Milling Silica Gel Particles to Micron Sizes", *Proceedings of the 24th CANCAM*, Saskatoon, SK, Canada, June 2013.
2. F. Fathieh, R. W. Besant, R. W. Evitts, C. J. Simonson, "Effects of Physical and Sorption Properties of Silica Gel on the Performance of Energy Wheels", Poster Presentation, *ASHRAE Saskatoon Chapters Regional Conference*, Saskatoon, SK, Canada, May 2016.

1.5 Thesis Outline

The current thesis is a collection of the refereed journals listed in section 1.4. Each chapter of the thesis is comprised of a separate publication that addresses one or more of the thesis objectives, Figure 1.8. Manuscripts are slightly modified to present the material in a logical sequence and to follow the thesis formatting style. In order to avoid repetition, the background, overview, and applications are omitted from the introduction section of each paper as they are thoroughly presented in chapter 1 of the thesis. In addition, the experimental facility is only described in chapter 2 (for heat transfer) and chapter 4 (for mass transfer). The analytical analysis is presented only in chapter 2 and 3 and is referenced in the other chapters. Figure 1.8 shows the outline of the thesis with the objectives addressed in each chapter. A brief overview of each chapter and the authors' contributions to each paper are also given at the beginning of each chapter. Note that the authors' contributions are included only when the paper is co-authored by more than one graduate student.

CHAPTER 1: INTRODUCTION

CHAPTER 2: TRANSIENT TESTING OF HEAT WHEELS
Manuscript: Determination of Air-to-Air Heat Wheel Sensible Effectiveness Using Temperature Step Change Data
Objective #1: To developing a novel testing facility for performing the transient testing on *heat wheels* component

CHAPTER 3: HEAT LOSS/GAIN IN TRANSIENT TESTING OF HEAT WHEELS
Manuscript: Effects of Heat Loss/Gain on the Transient Testing of Heat Wheels
Objective #2: To predict the full-scale *heat wheel* effectiveness with its uncertainty and to investigate the relationship between the sensible effectiveness and operating conditions

CHAPTER 4: TRANSIENT TESTING OF ENERGY WHEELS
Manuscript: Determination of Latent Effectiveness in Regenerators Using Humidity Step Test Data
Objective #1: To developing a novel testing facility for performing the transient testing on *energy wheels* component
Objective #3: To predict the full-scale *energy wheel* effectiveness with its uncertainty and to investigate the relationship between the latent effectiveness and operating conditions.

CHAPTER 5: EFFECTS OF DESICCANT PHYSICAL PROPERTIES ON MOISTURE RECOVERY
Manuscript: Effects of Physical and Sorption Properties of Mesoporous Silica Gel on Dehumidification Performance of Energy Wheels
Objective #4: To identify the effects of physical, chemical, and sorption properties of desiccant on the latent effectiveness of *energy wheels*

CHAPTER 6: EFFECTS OF DESICCANT CHEMICAL COMPOSITION ON MOISTURE RECOVERY
Manuscript: Sorption Study of a Starch Biopolymer as an Alternative Desiccant for Energy Wheels
Objective #4: To identify the effects of physical, chemical, and sorption properties of desiccant on the latent effectiveness of *energy wheels*

CHAPTER 7: SUMMARY, CONCLUCIOSN AND RECOMMENDATIONS FOR FUTURE WORK

APPENDIX A: COPY RIGHT PERMISSIONS

Figure 1.8-Thesis outline with the objectives and manuscript title for each chapter

CHAPTER 2

TRANSIENT TESTING OF HEAT WHEELS

2.1 Overview

This chapter mainly addresses the first objective of this Ph.D. research which is "to develop a novel testing facility for performing the transient testing of *heat wheel* components*".* In this chapter, the heat wheel component, a small-scale parallel-plate heat exchanger, is introduced and the experimental facility with instrumentation are thoroughly described. Sensors calibration, uncertainty analysis, and experimental validation are also presented in this chapter. The chapter focuses on heat transfer (no moisture transfer) while the extension of the test facility and study of moisture transfer in energy wheels will be presented in chapter 4.

In addition to the first objective, the second objective, "to predict the full-scale *heat wheel* effectiveness with its uncertainty and to investigate the relationship between the sensible effectiveness and operating conditions" is partially addressed in this chapter. To address the second objective of this Ph.D. thesis, this chapter studies the effects of operating conditions (including airflow velocity, wheel speed, and temperature difference) on sensible effectiveness. In addition, cyclic tests are conducted to validate the predicted results obtained from transient testing. Finally, a comparison between the sensible effectiveness obtained from the transient component testing and the literature correlations are presented at the end of the chapter. This manuscript was published in the International Journal of Heat and Mass Transfer in August 2015.

Determination of Air-to-Air Heat Wheel Sensible Effectiveness Using Temperature Step Change Data

Farhad Fathieh *, Robert. W. Besant, Richard. W. Evitts, Carey. J. Simonson

2.2 Abstract

The determination of the effectiveness of large heat wheels using standard measured data and test conditions can be very expensive and time consuming. The main contribution of this chapter is to test heat wheel components rather than the wheel itself. In addition, this chapter discusses the uncertainty in sensible effectiveness obtained by performing a transient step change on the exchanger matrix materials. In this chapter, the sensible effectiveness of heat wheels was predicted by performing a number of cyclic and single step change transient experiments on a wheel component (i.e. parallel-plate heat exchanger). A new experimental facility was developed to cause a step change for the inlet air temperature of the exchanger. In the cyclic tests, the heat exchanger was exposed to a periodic inlet temperature steps; afterward, the sensible effectiveness of parallel-flow and counter-flow heat wheel, comprised of the same material as parallel-plate exchanger was determined using the obtained temperature profiles. It was found that the cyclic test can be used to determine the sensible effectiveness of heat wheels with a parallel-flow arrangement for a range of angle ratios ($1 < \psi < 20$). However, a high uncertainty (±20%) was found in the sensible effectiveness of counter-flow heat wheels when $\psi > 2$. In the single step-change test, a time constant was assigned to the exchanger response when it was subjected to a step change in the inlet temperature. The time constant was obtained by fitting the experimental data to a first order exponential time response curve. An analytical solution states that the effectiveness of the heat wheel depends only on the product of the time constant and the wheel angular speed, or angle

ratio. Comparing values of the sensible effectiveness calculated through available empirical correlations and the ones obtained by single step change experiment showed less than 3% difference in results when the heat capacity rate ratio is greater than 5. It was concluded that due to simplicity, accuracy, and low cost of the single step change experiments, it could be an alternative testing method to determine the effectiveness of heat wheels operating at a specified range of angular speed, provided the flow channel geometries and Reynolds numbers for both the wheel and the small-scale test cell.

2.3 Introduction

Many studies have been done to investigate the sensible effectiveness of heat recovery wheels both theoretically and numerically. Some researchers attempted to solve the partial differential governing equation applied within the wheels' flow channels under simplifying assumptions (Baclic, 1985; Romie, 1988). However, due to complexity and inaccuracy in the results, the solutions were not appreciated by wheel designers and manufacturers. Instead, most of the reliable data is in the form of a correlation proposed by Kays and London (Kays & London, 1984). They derived a correlation based on the results of a comprehensive study on heat regenerative wheels done by others (Lamberston, 1958; Bahnke & Howard, 1964). For the same supply and exhaust air heat capacity rate, their correlation can be simplified as follow:

$$\varepsilon = \left(\frac{NTU}{1+NTU}\right)\left(1-\frac{1}{9C_r^{*1.93}}\right) \tag{2.1}$$

where a dimensionless term $NTU = (hA_{ht})/(\dot{m}_a c_{p,a})$ is number of transfer unit in which h is the convective heat transfer coefficient, A_{ht} is heat transfer surface area, $\dot{m}_a$ and $c_{p,a}$ are the mass flow rate and specific heat capacity of the air, respectively. The heat capacity rate ratio, C_r^* is defined as follows:

$$C_r^* = \frac{\left(MC_{p,m}\right)\omega}{\dot{m}_a C_{p,a}} \tag{2.2}$$

and M and $c_{\mathrm{p.m}}$ are the mass and specific heat capacity of the matrix, respectively. The symbol ω represents the angular frequency of the wheel.

Even though the Kays and London correlation provides useful information about performance of the wheels, its application is limited to high rotational speeds, $C_r^* > 1$. More recently, a simpler analytical solution for the effectiveness of heat wheels was presented in 2002 (Buyukalaca & Yilmaz, 2002, 2003) which can be applied to all wheel rotational speeds.

$$\varepsilon = \frac{C_r^*}{\left[1+3\left(\frac{NTU.C_r^*}{1+NTU}\right)^2+\left(\frac{NTU.C_r^*}{1+NTU}\right)^4\right]^{1/4}} \tag{2.3}$$

The accuracy of these models strongly depends on the convective heat transfer coefficient inside the wheel channels. An analytical study was done to determine the Nusselt number and convective heat transfer coefficient inside a constant wall temperature channel from the literature (Yilmaz & Cihan, 1993). Applying this theory to determine convective heat transfer coefficient, Yilmaz and Buyukalaca (Yilmaz & Büyükalaca, 2003) found a good agreement between the experimental and analytical sensible effectiveness of the heat wheel.

Because standard steady-state tests are costly and time consuming, researchers have been seeking new transient methods to measure data and determine wheel effectiveness (Abe et al., 2006a, 2006b; Shang & Besant, 2009a, 2009c). They suggested that as a wheel rotates between supply and exhaust airstreams, the inlet condition can be modeled by a series of increasing and decreasing step changes in temperature and relative humidity. They developed an analytical model which can predict the sensible and latent effectiveness of the wheel with acceptable uncertainties

by subjecting the wheel to a step change in temperature and/or relative humidity, respectively. They also conducted a set of experiments on a section of a wheel to determine sensible and latent effectiveness and verify the analytical model. A good agreement was seen by comparing the predicted sensible and latent effectiveness to standard steady-state test results. Shang and Besant (Shang & Besant, 2009a, 2009c) made some corrections to the transient model presented by Abe et al. (Abe et al., 2006a, 2006b). The modified transient analytical model predicted sensible effectiveness of energy wheels with corrections for flow entrance effects, axial heat conduction, carryover, water vapor phase change, and flow channel variations due to manufacturing tolerances. It was observed that these corrections improved agreement between the transient and steady-state results. The corrections were seen to be important and small in most cases except for phase change which can be large for some test inlet conditions.

The main goal of this chapter is to predict the sensible effectiveness of a heat wheel by performing transient step change experiments on a wheel component (a small-scale, parallel-plate heat exchanger). The small-scale heat exchanger used in this study was made of an identical material to an industrial heat wheel matrix. Testing a small-scale exchanger is beneficial for paramet studies and allows the researchers and designers to test a proposed wheel matrix material before constructing a wheel and before building a wheel cassette with all the sealing, casing, and external driving systems. In addition, the transient test can be performed by a more convenient testing facility compared to standard steady-state tests. Another contribution of this chapter is to assess different testing conditions, including the amplitude of step change and air flow rate, for transient tests. In this chapter, the uncertainty analysis for the transient test was studied which have not been accurately addressed in previous studies. The same theoretical relations and experimental

procedure proposed for energy recovery wheels by others (Shang & Besant, 2009a, 2009c, Abe et al., 2006a, 2006b).

For wheel component testing, an experimental test cell was described with all the measurement instrumentation. The effects of the supply and exhaust flow rate and amplitude of step change on effectiveness were also investigated through a set of experiments. Furthermore, a comprehensive uncertainty analysis was conducted for different operating conditions. A comparison between the results of single and cyclic step changes and their uncertainties were investigated. Finally, the sensible effectiveness found by single step change experiment was compared to results determined using correlations in literature.

2.4 Theory

As discussed, the inlet condition of heat wheels varies as it rotates between the supply and exhaust airstreams. These variations in inlet conditions can be mathematically modeled by a series of step changes. An analytical solution was presented in the literature to model transient response of a heat (energy) wheel by integrating the governing equations (continuity, momentum, energy, and state equations for both flow and matrix) within its channel (Abe et al., 2006a, 2006b; Shang & Besant, 2009c). It was shown that the airflow temperature at the outlet of rotary wheels behaves similar to a first order linear system with the forcing function of inlet temperature In their analysis, they assumed that the entrance effects, carry-over of air flow due to wheel rotation, axial heat conduction in the matrix, and flow channel hydraulic diameter variations are small which can be accounted for as small corrections to the linear theory. Based on their studies, the analytical model can successfully describe the heat transfer in both heat wheels and energy wheels. They mathematically modeled the temperature response of the rotary heat wheel as follows:

$$\tau \frac{d\theta}{dt} + \theta = f(t) \tag{2.4}$$

where τ is the time constant and θ is the normalized temperature given by

$$\theta(t) = \left(T_o - T_i\right) / \Delta T_{st} \tag{2.5}$$

in which ΔT_{st} is the amplitude of the step change and T_o (t=0) – T_i ($t \to \infty$) is the maximum temperature difference. For a parallel-flow heat wheel where both the supply and exhaust airstreams enter the wheel at the same side, the periodic forcing function $f(t)$ is expressed as follows:

$$f(t) = \begin{cases} 1, & 0 \le t \le \pi/\omega \\ 0, & \pi/\omega \le t \le 2\pi/\omega \end{cases} \tag{2.6}$$

The steady-state solution of Eq. (2.4) with periodic step change forcing function, Eq. (2.6) was found (Kaplan, 1962) as follows:

$$\theta(t) = \begin{cases} \left(\dfrac{1-e^{-\frac{1}{\psi}}}{1-e^{-\frac{2}{\psi}}}\right) e^{-\frac{t}{\tau}}, & 0 \le t \le \pi/\omega \\ 1-\left(\dfrac{1-e^{-\frac{1}{\psi}}}{1-e^{-\frac{2}{\psi}}}\right) e^{-\frac{t}{\tau}}, & \pi/\omega \le t \le 2\pi/\omega \end{cases} \tag{2.7}$$

where $\psi = \omega\tau/\pi$ is defined as an angle ratio that has the typical range of $1 < \psi < 20$ in heat wheels (Shang & Besant, 2008). The normalized inlet and outlet temperature profiles obtained respectively by Eqs. (2.6) and (2.7) are shown in Figure 2.1. This figure shows that the outlet air temperature of the wheel cycles through a range of values much smaller than the step size, e.g. about 50% of the step change amplitude.

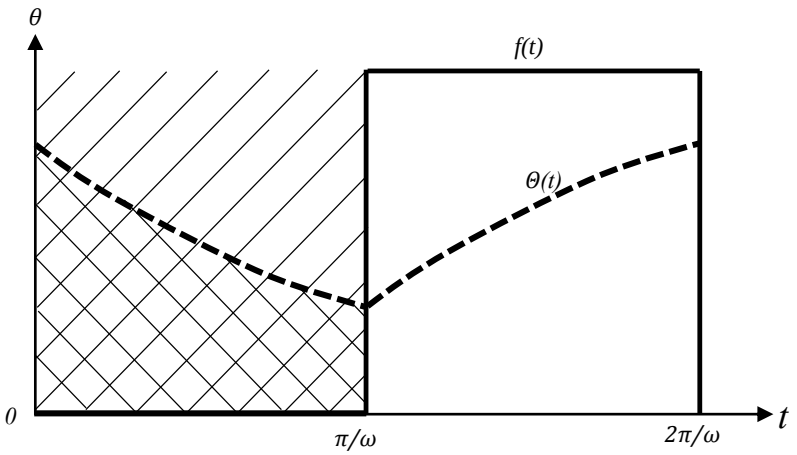

Figure 2.1- Normalized inlet and outlet temperature profiles for parallel-flow heat exchangers.

In case of a single step change instead of periodic series of step changes, Eq. (2.4) is still applicable with the new forcing function described as follow:

$$f(t)=\begin{cases}1, & 0\le t\le\infty \quad step\,increase\\ 0, & 0\le t\le\infty \quad step\,decrease\end{cases} \tag{2.8}$$

The solution for the ordinary differential, Eq. (2.4), with the forcing function given by Eq. (2.8) is found as:

$$f(t)=\begin{cases}1-e^{-\frac{t}{\tau}}, & 0\le t\le\infty \quad step\,increase\\ e^{-\frac{t}{\tau}}, & 0\le t\le\infty \quad step\,decrease\end{cases} \tag{2.9}$$

Therefore, the same time constant can be achieved through periodic and single step changes though there might be small deviations due to experimental uncertainties.

The sensible effectiveness of heat wheels is defined as the ratio of the averaged actual heat transfer rate in each half cycle (double shaded area shown in Figure 2.1) to the maximum possible heat transfer rate (shaded area shown in Figure 2.1). If the flow temperature profile at the steady-

state conditions is known, then the effectiveness can be calculated by integrating the area between the input and output curves by Eq. (2.10) (Abe et al., 2006a; Shang & Besant, 2009c).

$$\varepsilon = \frac{\omega}{\pi}\int_0^{\frac{\pi}{\omega}} \theta dt \tag{2.10}$$

Using the temperature profile given by Eq. (2.7), the sensible effectiveness for fully-developed parallel-flow within the channel is found as (Shang & Besant, 2009c):

$$\varepsilon_{PF} = \psi \frac{\left(1-e^{-\frac{1}{\psi}}\right)^2}{\left(1-e^{-\frac{2}{\psi}}\right)} \tag{2.11}$$

It is known that for parallel-flow heat exchangers with equal supply and exhaust flow rates, the effectiveness can be expressed only as a function of number of transfer units as (Shah & Sekuli, 2003):

$$\varepsilon_{PF} = \frac{1}{2}\left(1-e^{-2NTU}\right) \tag{2.12}$$

Combining Eqs. (2.11) and (2.12), the *NTU* can be expressed by (Shang & Besant, 2009c):

$$NTU = -\frac{1}{2}\mathrm{Ln}\left[1-2\psi\frac{\left(1-e^{-\frac{1}{\psi}}\right)^2}{\left(1-e^{-\frac{2}{\psi}}\right)}\right] \tag{2.13}$$

The *NTU* has the same value for fully-developed flow in both parallel-flow and counter-flow exchangers with the same inlet condition and channel geometry. For balanced supply and exhaust flows, the effectiveness of counter-flow exchangers is given by (Shah & Sekuli, 2003):

$$\varepsilon_{\mathrm{CF}} = \frac{NTU}{1+NTU} \tag{2.14}$$

The theoretical effectiveness for counter-flow exchangers, given in Eq. (2.14), states that the sensible effectiveness is related to the number of transfer units, which in turn is a function of angle ratio, ψ. As the supply and exhaust airstreams flow in opposite directions in heat wheels, therefore, Eq. (2.14) can be used to determine the sensible effectiveness of heat wheels when the angle ratio is known. Since the response of the wheel is expressed by a single exponential relation, the analytical model presented above is referred to as the single exponential model (SEM) through this thesis.

Figure 2.2 depicts the sensible effectiveness with respect to angle ratio for a heat wheel with equal supply and exhaust airflow rates. It can be observed that the heat wheel has a higher effectiveness at the higher angle ratios. Consequently, the performance of the wheel can be improved by increasing either the angular speed of the wheel or its time constant. However, increasing the angular speed results in the adverse effect of increased carryover, the phenomenon in which a portion of the air at the exhaust side of the wheel is carried to the supply side or vice versa. Although carry-over physically increases the sensible effectiveness of the exchanger, it reduces the indoor air quality and is not desirable (Shang & Besant, 2008). It should be mentioned that the carry-over was not taken into consideration in determining the effectiveness in Figure 2.2 In addition to carry-over, more power is required to rotate the wheel at higher angular speeds, which may not be economical especially when the inlet temperature differences are small. Based on all these facts, it is preferred to have a wheel operating at lower angular speeds. However, there is another solution: i.e. making wheels with a larger time constant. In fact, the larger the time constant, the higher the angle ratio, and the higher wheel sensible effectiveness at the same angular speed. The time constant depends on the structure, geometry, and material thermal properties of the wheel as well as the heat convection properties of the airflow.

2.5 Experimental

2.5.1 Small-Scale Heat Exchanger

The wheel component used for transient testing was a small-scale parallel-plate heat exchanger. Figure 2.3 shows the parallel-plate heat exchanger with its dimensions. The parallel-plate exchanger used in the experiments was comprised of 16 sheets of Al-3003. Each sheet was 80 mm x 200 mm and 0.62 ± 0.05 mm thick. A plastic frame, made by 3D printing rapid prototyping held the sheets in parallel and formed 15 flow channels that had 4 mm height. Thus, the parallel-plate heat exchanger had an airflow channel hydraulic diameter of 7.2 mm. The geometric dimensions of the channels with physical and thermal properties of the matrix is given in Table 2.1.

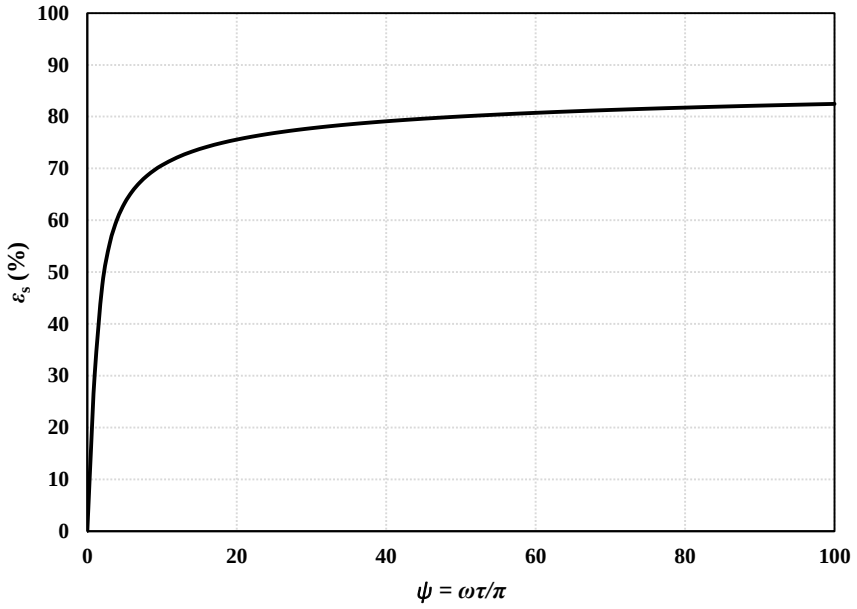

Figure 2.2- Theoretical sensible effectiveness versus ψ for a heat wheel with equal supply and exhaust airflow rates

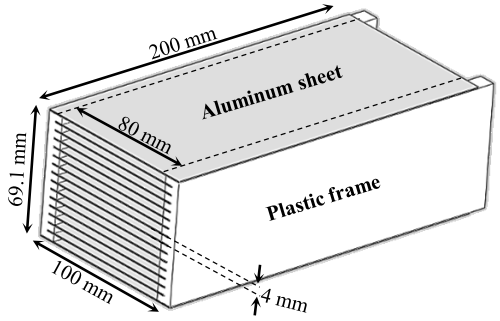

Figure 2.3-The small-scale heat exchanger geometry with the supporting frame and geometrical dimensions

Table 2.1-Geometric dimensions of flow channels with the physical and thermal properties of the sheets

Channel				Sheets			
Width (mm) b	Length (mm) L	Height (mm) h	Hydraulic diameter (mm) d_h	Material	Thickness (mm) δ_m	Specific heat capacity (J.kg^{-1}K^{-1}) $C_{p,m}$	Density (m^3/kg) ρ_m
80	200	4	7.6	Al-3003	0.62	893	2730

2.5.2 Transient Test Facility

The test facility, shown in Figure 2.4, was designed to measure the transient response of the parallel-plate exchanger (wheel component) after exposure to a step change in airflow temperature at the inlet. The transient testing facility consisted of (1) the supply air system, (2) the test section, and (3) the sliding and supporting plates.

Supply Air System: An air compressor in line with an industrial dryer provided dry air (3%-5% RH) to the test section through 25.4 mm (1 inch) inner diameter PVC tubes. To perform the transient test, two airstreams with different temperature were needed. Thus, the supply air was split into two airstreams where the flow rate of each was adjusted by a flow controller (MKS-Type 1559A). Depending on flow rates required for each test, three flow controllers with capacities (in L/min) of 0-50, 0-200, and 0-400 and an accuracy of 2% of the full-scale were used. In addition, to adjust the temperature of each airstream, two electric heaters with maximum power of 110 W

were placed after the flow controllers, where variable transformers (variac) were used to regulate the supply power of each. The heated air passed through PVC tubes surrounded by 12.5 mm insulation to minimize heat loss.

The air supply tubes terminated at two 12.5 mm (1/2 inch) Plexiglas ducts of 500 mm length, shown as duct I and duct II in Figure 2.4. Since the exchanger had a rectangular cross section, rectangular ducts with the same inner dimensions were installed upstream of the test section. One inch of extruded polystyrene insulation was put around the ducts to ensure minimal heat loss or gain during the experiments. In all the tests, the airflow in duct II had ambient temperature whereas the airflow with elevated temperature passed through duct I. To provide more uniform bulk temperature in duct I, two stationary air mixers were installed 100 mm from the top of the duct. In addition, a flow straightener was placed before the exchanger inlet to provide a uniform velocity profile. The flow straightener was composed of hundreds of 2mm x 3mm rectangular channels with a length of 100 mm. This setup provided a uniform airflow with the desired temperature to pre-condition and change the inlet condition of the exchanger.

2.5.3 Test Section

The test section with its dimension is shown in Figure 2.5. The test section was made of extruded polystyrene insulation which substantially reduced the heat transfer to the surroundings. The test section consisted of three flow passages. The parallel-plate exchanger was placed at the middle passage which was the test cell and two other passages were used to bypass the airflow.

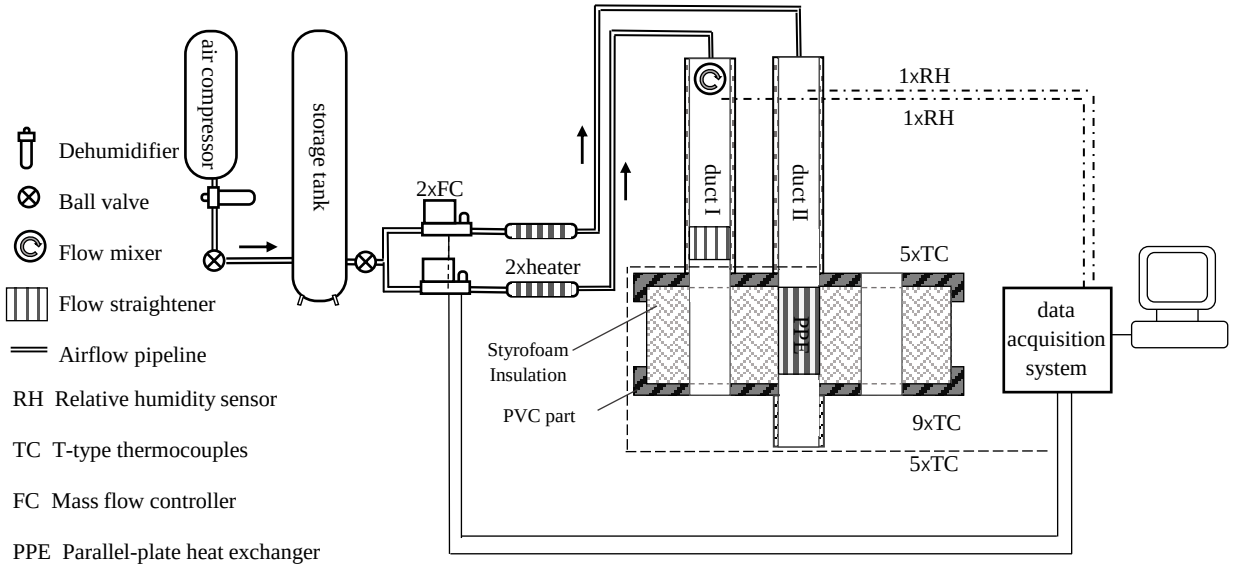

Figure 2.4-Schematic of the testing facility with the airflow lines, the measurement instrumentations, and the test section.

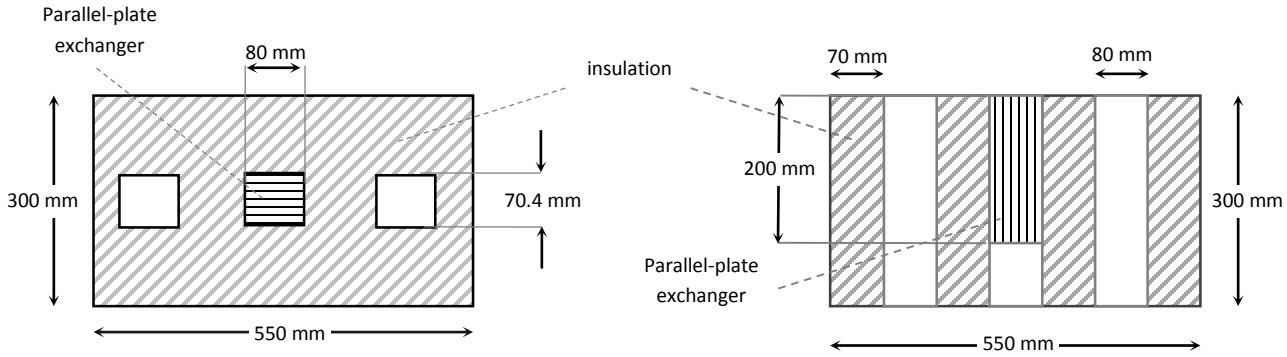

Figure 2.5-Test section with the insulation (a) top view (b) side view.

2.5.4 Sliding and Supporting Plates

To subject the parallel-plate exchangers to a step change in inlet air temperature, the inlet condition must be changed as fast as possible. Thus, the Plexiglas air ducts were designed to be capable of sliding horizontally. The Plexiglas ducts were attached to a Plexiglas sliding plate from the bottom. This plate was capable of quick linear motion between two Plexiglas rail-bars and over a PVC supporting plate, shown in Figure 2.6. The PVC supporting plate with three air passages

was placed on top of the test section. This PVC plate held the rail-bars and provided a flat and rigid base for the sliding plate to move on. The Plexiglas rail-bars supported the linear motion of the sliding plate and prevented any lateral movement. To avoid any misalignment of the ducts before and after a step change, two stoppers were installed at each side of the rail-bars, not shown in the Figure 2.6. To ensure no airflow leakage through the sliding plate, two toggle clamps were used to force the sliding plate down onto the PVC plate. The bottom PVC supporting plate, similar to the top PVC supporting plate, was placed beneath the insulation and fastened to the upper PVC plate by means of eight threaded rods.

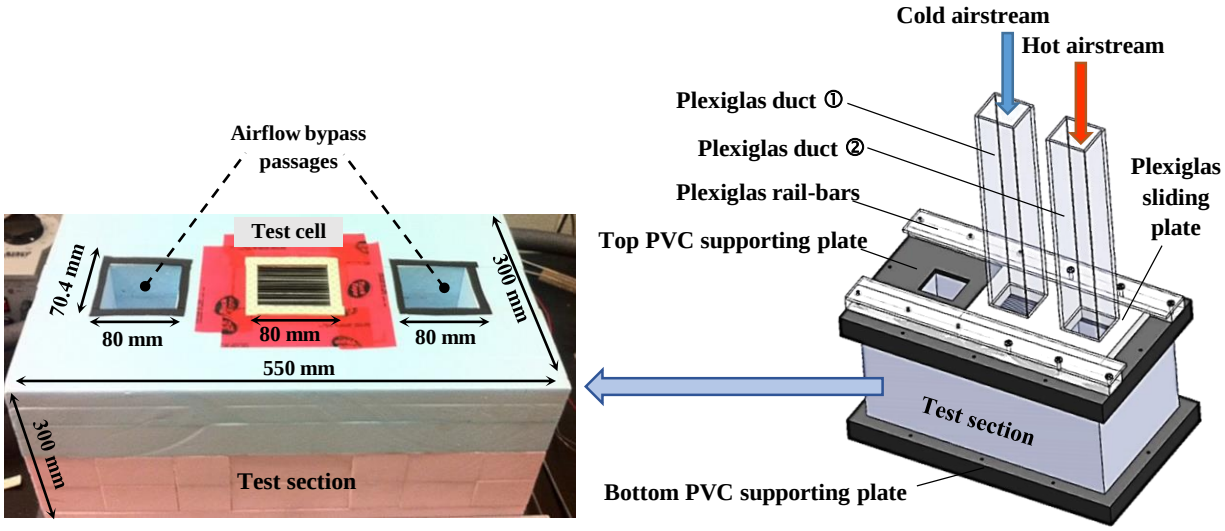

Figure 2.6-Sliding and supporting plates, air ducts, and test section.

2.6 Measurements and Data Acquisition System

To determine the transient response and then effectiveness of a parallel-plate exchanger, the temperature should be measured at locations upstream and downstream of the exchanger. Five T-type thermocouples installed 5 cm upstream of the exchanger measured the inlet temperature. The outlet temperature was monitored by nine thermocouples 1 cm downstream of the exchanger. The arrangement of these thermocouples is shown in Figure 2.7. All the thermocouples were

calibrated using a Hart Scientific Dry-well Calibrator (model 9107) with a transfer standard bias uncertainty of ±0.1 °C. The total uncertainty in temperature for the calibration range of 15 to 85 °C was found to be ±0.2 °C. The measured temperatures and flow rates were acquired using a National Instruments data acquisition system (NI-CDAQ 9174); these were monitored and recorded each second through Lab View 2010 software.

2.7 Experimental Procedure and Test Conditions

In this study two different tests, named *cyclic* and *single step change*, were performed on the wheel component. The same test facilities were used for both tests where the only difference was inlet conditions. In the single step change test, the heat exchanger inlet temperature was altered in less than a second and then kept constant through the end of the experiment. In the cyclic test, the inlet temperature was changed periodically through a number of step changes. In this section the procedure for each of these tests will be discussed.

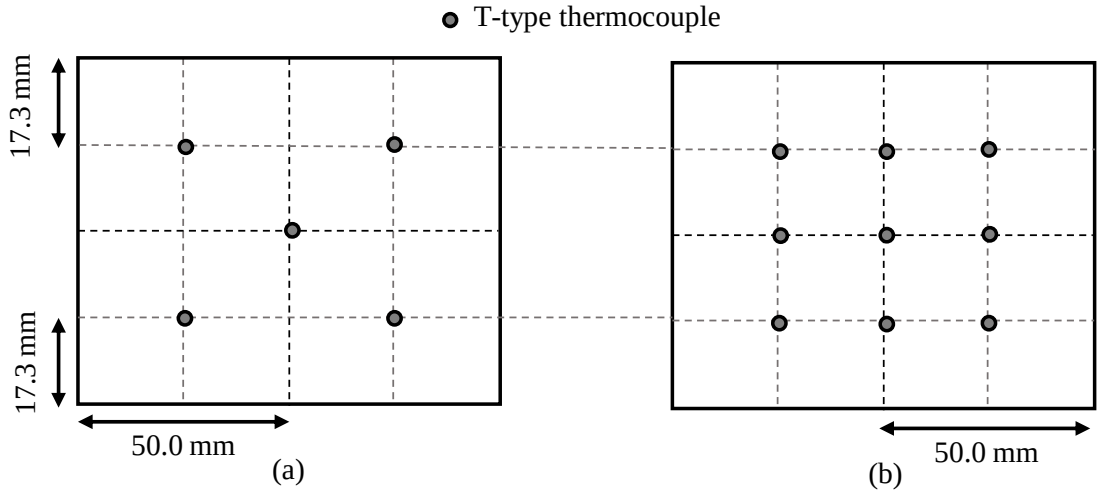

Figure 2.7-Schematic of the ducts cross-section with thermocouples arrangement at (a) duct inlet and (b) exchanger outlet.

2.8 Single Step Change Test

In the single step tests, the air inside ducts I and II had different conditions which are given in Table 2.2 and Table 2.3. To perform the transient single step change experiment, the following step-wise procedure was followed:

- *Pre-conditioning period*: Conditioned air passed through the ducts for at least one hour before the step change. Thus, the steady-state condition was achieved at the exchanger outlet. The steady-state was defined as the condition under which the temperature variation remains within the thermocouples' uncertainty, ±0.2 °C, for a period of 30 minutes.
- *Step change:* After pre-conditioning, the step change in temperature was made. In this step, the inlet temperature was changed in less than one second by sliding the ducts rapidly. The stoppers put on the rail-bars prevent any misalignment of the ducts. As a result, the pre-conditioned airflow in duct I passed through the test cell and the heat exchanger whereas the airflow in duct II purged into the ambient through the bypass flow passage.
- *Transient period:* The ducts remained in their positions until the outlet temperature reached the inlet temperature so that the new equilibrium conditions were obtained. Monitoring the temperature at the inlet and outlet of the test cell during the test, the response of the heat exchanger was studied.

As discussed in section 2.4, the amplitude of the step change represents the temperature difference between the supply and exhaust airstreams passing through a wheel. In fact, the temperature of the supply and exhaust airstreams has different values during the summer and winter, their difference is not constant throughout wheel operation. In the first set of experiments,

the effects of the amplitude of step change on the time constant and the sensible effectiveness were studied. To alter the step change amplitude, airflow temperatures were adjusted to different values in duct I while the temperature of airflow in duct II was kept constant at room temperature. The air condition at the exchanger inlet and the flow rates in each duct are provided in Table 2.2.

It was reported that the flow rate can also alter the time constant and sensible effectiveness of the heat exchanger (Abe et al., 2006b; Wu et al., 2006). To investigate the effect of flow rate on the performance of the parallel-plate heat exchanger, a number of step change experiments were performed at different flow rates. Table 2.3 shows the airflow conditions for these tests.

Table 2.2-Air condition at duct inlet for different amplitude of step change

Volumetric flow rate (± 2 L/min)	Face velocity (± 0.01 m/s)	Re_{dh} (± 4)	Air relative humidity (± 3%)	Cold airstream temperature (± 0.2 °C)	Hot airstream temperature (± 0.2 °C)	Step change amplitude (± 0.3 °C)
100	0.34	174	< 4%	23.1	60.6	37.5
				23.7	50.7	27.0
				22.8	42.9	20.1
				24.1	39.9	15.8
				22.8	30.1	7.3
				23.5	28.3	4.8

Table 2.3- Air flow rates for the step change tests with cold airstream temperature T_c = 22.9 °C and hot airstream temperature T_h = 29.8 °C, ΔT_{st}= 6.9 °C.

Volumetric flow rate (L/min)	Volumetric flow rate bias error (L/min)	Face velocity (m/s)	$Re_{channel}$
15	1	0.05	26
25	1	0.09	43
50	1	0.17	87
75	1	0.26	130
100	2	0.34	174
120	2	0.41	209
150	2	0.51	261
200	4	0.68	348
250	4	0.86	434
300	4	1.03	521
350	4	1.20	608

2.9 Cyclic Test

In the cyclic tests, the exchanger was exposed to a series of step changes in inlet temperature as given in Table 2.4. The cyclic test provided inlet conditions very similar to heat wheel operating conditions with a parallel-flow arrangement. The test cell and heat exchanger were pre-conditioned with the same procedure used for the single step change test. As before, the steady-state condition was defined where the temperature changes no more than ±0.20 °C for a period of 30 minutes. Then, the cycles of step changes was made by rapidly interchanging duct ① and duct ② in each half a period. In this set of tests, four different periods of 2 min (ω = 3.14 rpm), 4 min (ω = 1.57 rpm), 8 min (ω = 0.78 rpm), and 16 min (ω = 0.39 rpm) were considered for the cyclic experiments. For a period of less than 2 min the changes in outlet temperature could not be detected by the measurement system as the changes were smaller than the uncertainty range of the thermocouples.

2.10 Results and Discussion

In this section, the results of cyclic and single step change experiments are presented and compared. The effects of flow rate and step change amplitude on the time constants and the sensible effectiveness are also provided in this section. Uncertainty analysis results are presented for both cyclic and single step change results. Moreover, a comparison with the correlations in the literature is presented.

Table 2.4-Airflow conditions in the ducts for cyclic step changes

Volumetric flow rate (±2 lit/min)	Air relative humidity (± 3%)	Cold airstream temperature (± 0.2 °C)	Hot airstream temperature (± 0.2 °C)	Step change amplitude (± 0.4 °C)	*T* (min)	*ω* (rpm)
100	< 4%	22.9	50.5	27.6	2	3.14
					4	1.57
					8	0.78
					16	0.39

2.10.1 Single Step Test Results

2.10.1.1 Exchanger Transient Response

Figure 2.8 provides an example of the exchanger response in terms of outlet temperature profile normalized by Eq. (2.5). In this test, the inlet temperature was changed through 27 °C, ΔT_{st} = 27 °C, where the face velocity was 0.34 m/s. The experimental data was correlated using an exponential function given in Eq. (2.9) using the trust-region optimization algorithm with MATLAB R2013a (Moré and Sorensen, 19883). The Levenberg-Marquardt method was used to fit test data by minimizing the sum of squares of the difference between the measured and calculated temperatures. For the case shown in Figure 2.8, the time constant was found to be 470 s. The coefficient of determination (R^2) was found to be 0.993 which indicates how precisely the single exponential model fits the experimental data.

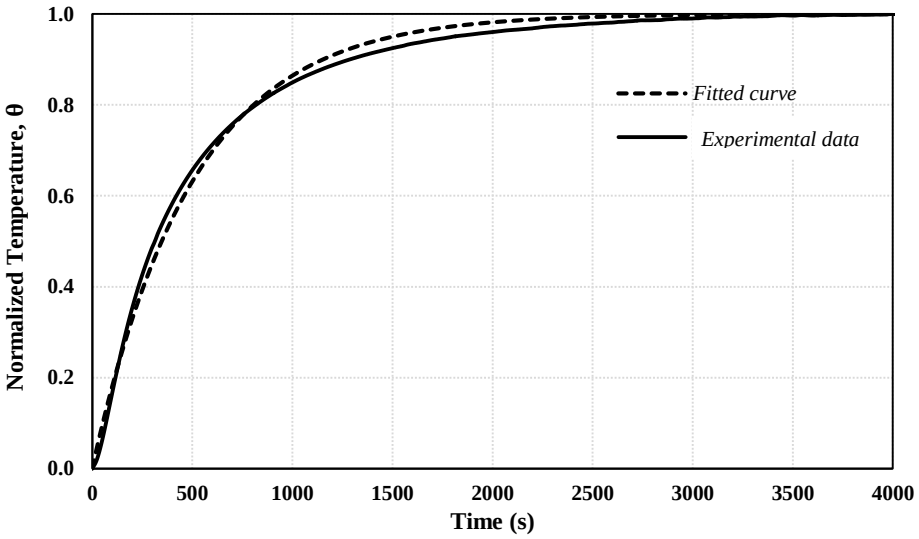

Figure 2.8-Normalized temperature profile of small-scale heat exchanger with theoretical fitted curve for a step increase in the inlet temperature (ΔT_{st} = 27 °C, and V_f = 0.34 m/s, maximum uncertainty in the experimental data is U_θ = ±0.01)

2.10.1.2 Effect of Step Change Amplitude on Transient Response

To determine the performance of a wheel through steady-state tests, the temperature of the supply and exhaust airstreams should be adjusted according to NSI/AHRI 1060-2011 (ANSI/AHRI, 2014), presented in Table 1.1. A question may be raised about testing conditions for wheel transient testing. Based on the analytical results, it is believed that the time constant must be independent of the step change amplitude; this in turn means that the obtained effectiveness is valid for any temperature difference between the supply and exhaust airstreams. To investigate the effects of step change amplitude on the time constant and the effectiveness, the heat exchanger was tested under six different step change amplitudes with the conditions listed in Table 2.2. This set of amplitudes covered the range of temperature difference normally experienced by wheels at different operating conditions, i.e. 5-35 °C temperature difference between the supply and exhaust streams.

The time constant and the sensible effectiveness for different step change amplitudes are listed in Table 2.5 for an angular speed of ω = 0.75 rpm. This value of angular speed is chosen to maintain the angle ratio within the conventional operating range for heat wheels, $1 < \psi < 20$. It can be observed that changing the step change amplitude from 4.8 to 37.5 leads to a 70 s change in the time constant which leads to about 0.2% variation in the sensible effectiveness. The difference between results can be related to the effects of heat loss or even small variations in the inlet air conditions, such as moisture content or flow rate. Since the sensible effectiveness variations are very small by changing the amplitude of the step change, it is suggested that an average value can be assigned for the time constant and the sensible effectiveness with the relative precision uncertainty. The average values for time constant, angle ratio, and the sensible

effectiveness are also given in Table 2.5. The precision of sensible effectiveness, $U_{p,amp}$, can be determined by the following relation:

$$U_{p,amp} = St \tag{2.15}$$

Where *S is* the precision index defined as the square root of data points standard deviation and *t* is the student t-factor based on the 95% of uncertainty bounds on both sides of mean value (Figliola & Beasley, 2006). For the total number of 6 data points the student t-factor is 2.571.

Figure 2.9 depicts the precision uncertainty coming from step change amplitude for different values of angle ratio. Different values of angle ratio were calculated by assigning different values to the wheel angular speed. Then, the precision was determined based on the six values of sensible effectiveness corresponding to each step change amplitude. It is observed that the uncertainty increases as the wheel has a lower angle ratio, however, the uncertainty remains less than 0.5% for $\psi > 4$. It should be noted that the ± 0.2 K uncertainty in temperature coming from T-type thermocouples imposes insignificant uncertainty on final results. This is due to the fact that bias uncertainty in temperature measurement changes the step change amplitude only by a maximum value of ±0.4 K. A change in the step change amplitude by 32.5 °C caused the uncertainty of 0.1% in the sensible effectiveness, therefore, the bias uncertainty in temperature measurement did not affect results by more than 0.1%, which was included in the uncertainty of 0.2% in the sensible effectiveness.

Table 2.5-Time constant, *NTU*, and ε_s of the equivalent full-scale heat wheel obtained by performing the transient test on the small-scale heat exchanger at different step change amplitudes, (V_f = 0.34 m/s, ω = 0.75 rpm)

ΔT_{st} (± 0.4 °C)	τ (± 6.7 s)	R^2	ψ	*NTU*	ε_{CF}
37.5	488	0.995	12.2	3.74	78.9
27.0	501	0.993	12.5	3.77	79.0
20.1	494	0.993	12.4	3.76	79.0
15.8	485	0.993	12.1	3.74	78.9
7.3	470	0.996	11.8	3.71	78.8
4.8	431	0.999	10.8	3.62	78.4
Average	**478**	**-**	**11.9**	**3.72**	**78.8**

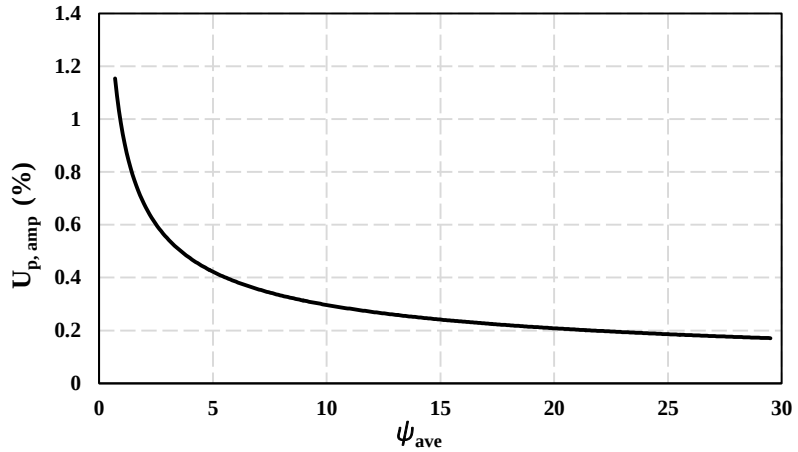

Figure 2.9-Precision uncertainty in the sensible effectiveness due to temperature difference between exhaust and supply airstreams (step change amplitude) obtained by the transient test

Based on the above discussion, the value of temperature difference between the supply and exhaust airstreams does not play an important role at an angle ratio of greater than 5. In fact, a precision uncertainty can be assigned to sensible effectiveness to account for step change amplitude effects.

2.10.1.3 Effect of Flow Rate on the Transient Response

The supply and exhaust flow rates must be kept constant during the test period. The sensible effectiveness has different values for each specified equal supply and exhaust flow rate that should be studied. To investigate the effects of flow rates on the time constant and effectiveness, the single

step change experiment was conducted at eleven different flow rates, or face velocities. For all the tests step change amplitude was ΔT_{st} = 6.9 ± 0.2 °C, as indicated in Table 2.3. Figure 2.10 shows the time constant found by fitting the experimental data at each face velocity. It can be seen that the time constant increases rapidly at lower values of face velocities, V_f < 0.1 m/s. On the other hand, the time constant approaches an almost constant value of 100 s at higher face velocities.

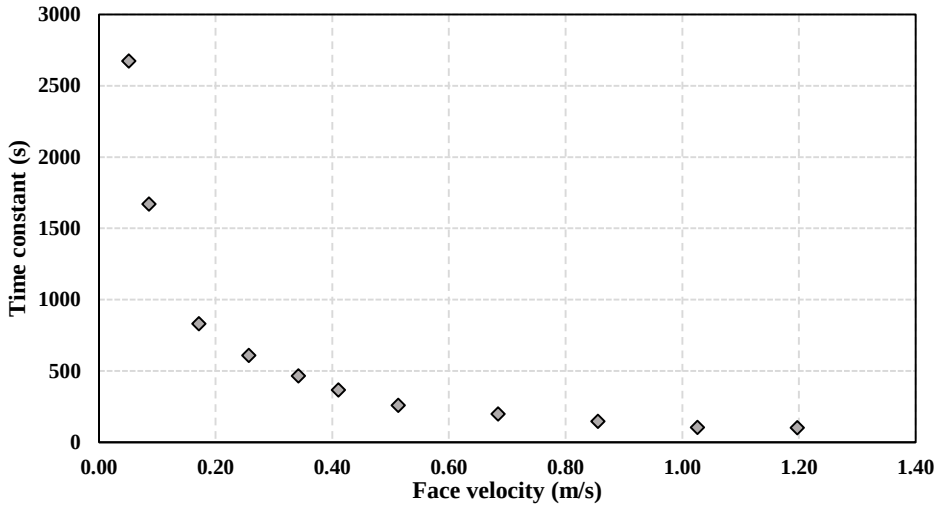

Figure 2.10-Time constants for the parallel-plate heat exchanger response for different values of face velocities at (ΔT_{st} = 6.9 °C)

The sensible effectiveness at different angular speed is plotted in Figure 2.11. It can be seen that for all wheel angular speeds, sensible effectiveness decreases as the face velocity increases. This decrease in the effectiveness is due to the fact that at higher face velocities there is less flow residence time, which reduces the amount of heat transferred within the wheel channel. In other words, the *NTU* is lower at higher face velocities that leads to lower sensible effectiveness. Based on the results in Figure 2.11, it is preferable for heat wheels to operate at higher angle ratios. For a built wheel, a larger angle ratio can be achieved by rotating the wheel at higher angular speeds. However, this amplifies carryover which is not preferable. The amount of carryover is generally different from wheel to wheel, depending on the wheel design and manufacturing

quality. Therefore, the optimal angular speed can be found for each wheel (Simonson, 1998). Small systematic deviations in flow rate measurements, due to flow controller inaccuracies, can lead to bias uncertainty in the sensible effectiveness of the wheel. In order to take this uncertainty into account, a power function was determined to be a proper choice to represents the sensible effectiveness as a function of face velocity. Therefore:

$$\varepsilon\left(V_{\mathrm{f}}\right) = aV_{\mathrm{f}}^{b} + c \tag{2.16}$$

Where, Table 2.6 depicts the values of fitting parameters *a* and *b* at various wheel angular speeds.

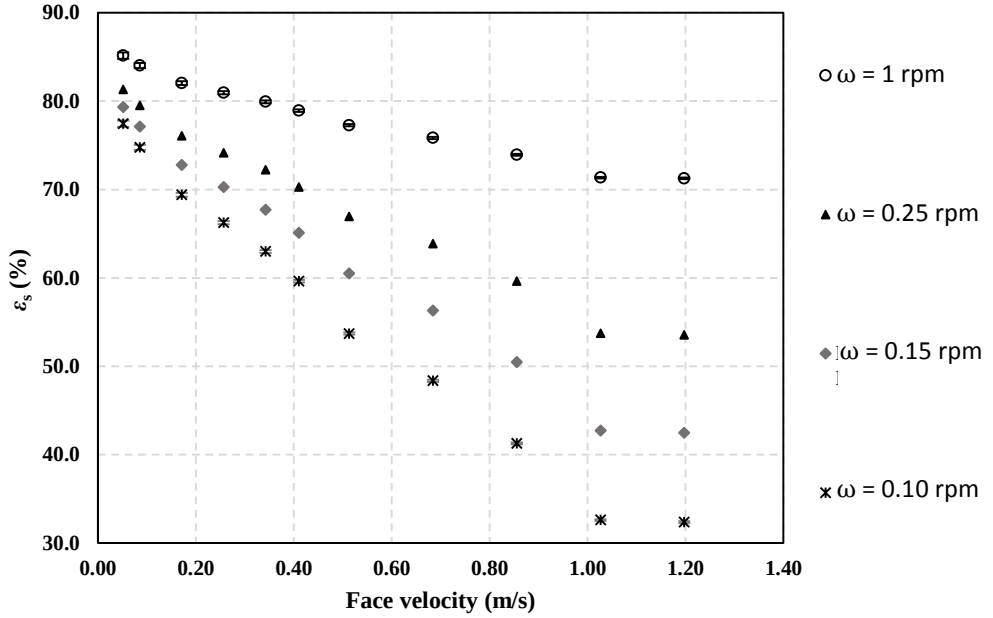

Figure 2.11-Sensible effectiveness with respect to face velocity obtained by performing the transient test on the small-scale heat exchanger (ΔT_{st} = 6.9 °C)

Table 2.6-Fitting constant and R-squared for power fitting on the sensible effectiveness versus face velocity for different wheel angular speeds

Angular Speed ω (rpm)	$\varepsilon(V_f) = aV_f^b + c$			
	a	*b*	*c*	R^2
1	-15.1	0.60	87.5	0.9939
0.5	-19.9	0.68	86.0	0.9932
0.25	-27.7	0.75	84.1	0.9924
0.15	-36.5	0.78	82.8	0.9923
0.1	-45.9	0.74	82.5	0.9927

With the bias uncertainty of flow controllers, bias uncertainty in the sensible effectiveness can be calculated by:

$$U_{\mathrm{B},\varepsilon\mathrm{Qf}} = \frac{\partial \varepsilon(V_{\mathrm{f}})}{\partial Q_{\mathrm{f}}} U_{\mathrm{B},\mathrm{Q_f}} = \frac{\partial \varepsilon(V_{\mathrm{f}})}{\partial V_{\mathrm{f}}} \frac{U_{\mathrm{B},\mathrm{Q_f}}}{A_{\mathrm{duct}}} = abV_{\mathrm{f}}^{\,b-1} \frac{U_{\mathrm{B},\mathrm{Q_f}}}{A_{\mathrm{duct}}} \tag{2.17}$$

Figure 2.12 shows the bias uncertainty in the sensible effectiveness coming from the uncertainty in flow rates measurement with respect to face velocities at different angular speeds. It can be seen that the uncertainty decreases as the flow rate increases and rises at the lower angular speeds. For the typical angle ratio of more than 5 and within the range of face velocities tested, the bias uncertainty in the sensible effectiveness is less than 1%.

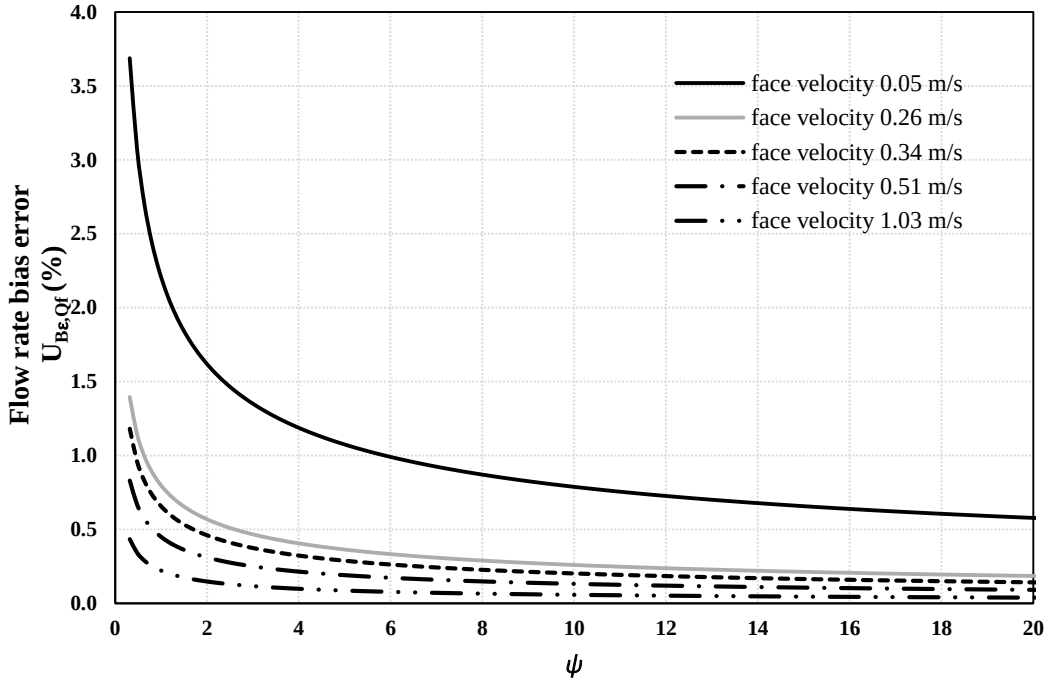

Figure 2.12-Bias uncertainty in sensible effectiveness due to systematic error in flow rate measurements ($U_{B\varepsilon,Qf}$) with respect to angle ratio ψ for different values of the supply and exhaust flow rate

2.10.1.4 Transient Test Uncertainty Analysis

With regard to the ANSI/ASHRAE 84-2013 standard of testing air-to-air heat/energy exchangers, the uncertainty in measuring the sensible effectiveness found by the steady state test should not exceed 5% (ANSI/ASHRAE, 2013). Therefore, any alternative testing method must have a uncertainty of less than 5%. For the single step change transient method presented in this thesis, the two sources of uncertainty come from fitting the experimental data and systematic uncertainty of the flow rate and temperature measurements. In this chapter, the regression curves were determined with 95% confidence bounds, which causes an uncertainty of less than 1.5 s in the time constant, $U_{\tau 95\%} = \pm 1.5$ s. A bias uncertainty was imposed in the calculated effectiveness due to curve fitting which was determined using the method of error propagation (Figliola & Beasley, 2006). It was found that the uncertainty in sensible effectiveness within the tested flow rates was less than 0.1%. In addition, the bias uncertainty in flow rate measurement was determined in section 6.1.2. Thus, the total bias uncertainty in sensible effectiveness can be determined as:

$$U_{\mathrm{B}} = \sqrt{U_{\mathrm{fit}}^2 + U_{\mathrm{B,Q_f}}^2} \tag{2.18}$$

Total bias uncertainty versus angle ratio for different face velocities is plotted in Figure 2.13. The bias uncertainty increases with lowering the face velocity. In addition, for high angle ratio, $\psi > 5$, the uncertainty decreases to less than 1% for all the face velocity except for $V_{\mathrm{f}} = 0.05$ m/s.

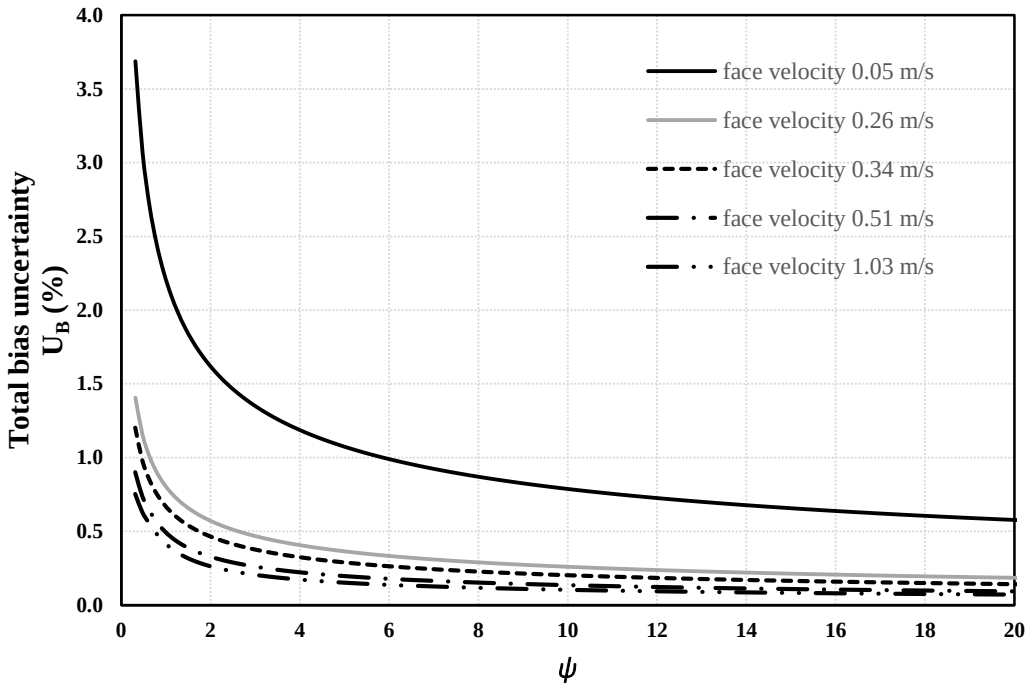

Figure 2.13-Total bias uncertainty in sensible effectiveness with respect to angle ratio ψ for different values of supply and exhaust air face velocities obtained through small-scale transient test (ΔT_{st} = 6.9 °C)

In addition, the temperature difference between the supply and exhaust air imposes a precision uncertainty of $U_{p,amp}$= 0.2-05% on the sensible effectiveness. These values include the uncertainty due to temperature measurements as well. Finally, the total uncertainty, U_T, is comprised of bias and precision uncertainty can be calculated as:

$$U_{t,\varepsilon} = \sqrt{U_B^2 + U_{p,amp}^2} \tag{2.19}$$

Since the bias and precision uncertainties are functions of face velocity and wheel angular speed, the total uncertainty also depends on these two parameters. The total uncertainty in the sensible effectiveness with respect to angle ratio for a face velocity of 0.34 m/s is given in Figure 2.14. The uncertainty of less than 2.5% for $1 < \psi < 20$ confirms the high accuracy of the single step change testing method in determining the sensible effectiveness. The results are within

the 5% uncertainty bounds required by ANSI/ASHRAE 84-2013 standard (ANSI/ASHRAE, 2013). For the ψ <1 the uncertainty in sensible effectiveness raises to more than the acceptable 5%, however, this is not a conventional range of angle ratio for heat wheels to operate.

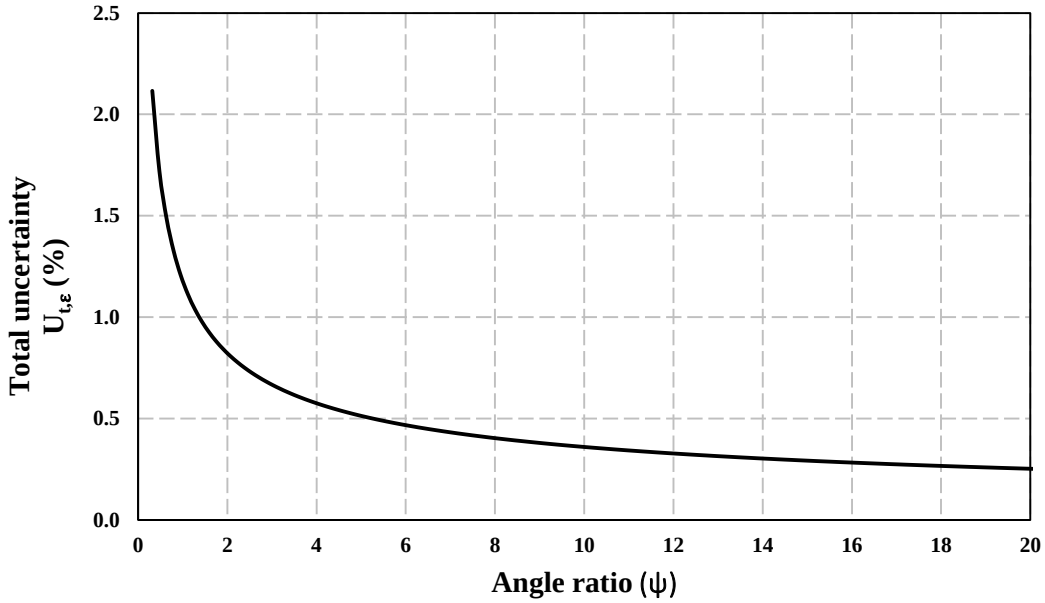

Figure 2.14-Total uncertainty in sensible effectiveness with respect to angle ratio ψ obtained though small-scale transient test at supply and exhaust air face velocity 0.34 m/s.

2.10.2 Cyclic Test Results and Uncertainty Analysis

Periodic step change tests were performed with the cold and hot airstreams at a constant face velocity of V_f = 0.34 m/s and air conditions, as indicated in Table 2.4. Periodic tests have different periods of 2 min (ω = 3.14 rpm), 4 min (ω = 1.57 rpm), 8 min (ω = 0.78 rpm), and 16 min (ω = 0.39 rpm). It should be noted that these angular speeds were relatively low compared to typical heat wheel operating speeds, ω = 10-30 rpm. In fact, the sheets of wheel material were about 20-50 times thicker than the foils used to construct the wheel matrix. The thicker sheets overcome the maldistribution of the tested wheel components. As a result, the time constants for the parallel-plate exchanger are 10-100 times larger than the values for conventional heat wheels.

Thus, considering relatively low angular speeds but large time constants for the wheel component (parallel-plate exchanger), the angle ratio would be within the range of $1 < \psi < 10$. This range corresponds to conventional range for heat wheels $1 < \psi < 20$ (Shang & Besant, 2008).

The normalized temperature profile for three cycles of step change with a period of 16 min is shown in Figure 2.15. The temperature profile was obtained after the exchanger was exposed to a sufficient number of cycles (more than 30 cycles). Thus, the steady-state temperature profile was achieved at the exchanger outlet. The temperature was normalized using Eq. (2.5) where ΔT_{st} = 27.6 °C. The bold line shows the inlet temperature profile, which varies between hot and cold air streams corresponding to 1 and 0, respectively. It can be observed that the normalized outlet temperature varies between 0.25 and 0.74, which results in an amplitude of oscillation equal to 0.49. Based on the time constant obtained through a single step change experiment, given by Eq. (2.9), it was possible to predict the periodic temperature profile by Eq. (2.7). Taking the average time constant from Table 2.5, the predicted temperature profile was calculated and is shown with a dashed line in Figure 2.15. The comparison proves a good agreement between the temperature profiles. Small differences between the results can be attributed to heat loss or gain during the experiments. In addition, the flow within the channels is developing, both thermally and hydrodynamically with the developing length of $x_{th,FD}/L$=0.21 and $x_{h,FD}/L$=0.30, respectively. Thus, assuming the fully developed flow in the transient testing given in section 2.4 may cause small deviations in results.

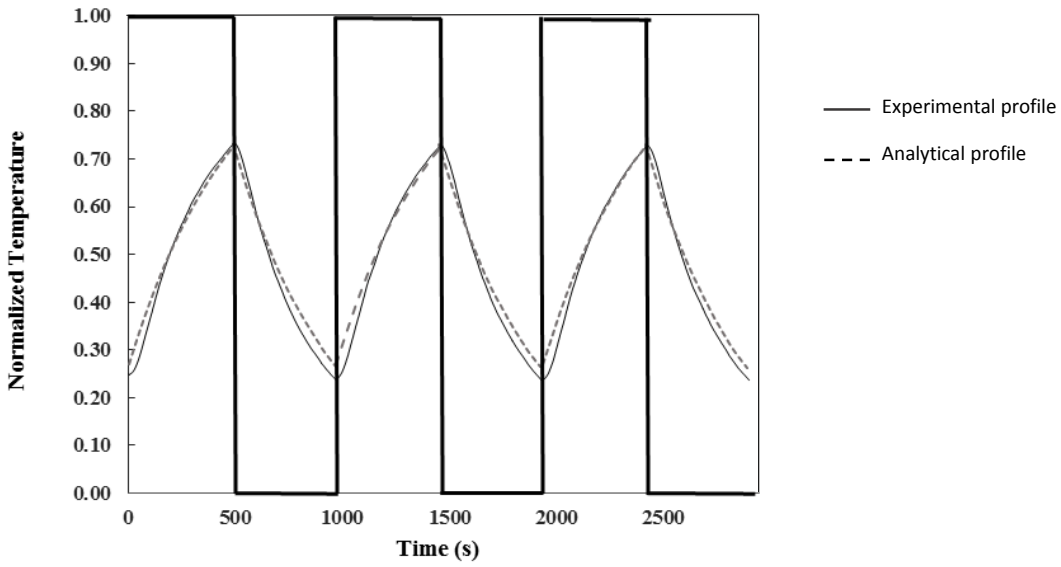

Figure 2.15-Normalized experimental and theoretical temperature profiles for cyclic test (with 16 min period of oscillations and ΔT_{st} = 27 °C, and V_f = 0.34 m/s, maximum uncertainty in the experimental data is U_θ = ±0.01)

To determine the effectiveness based on the periodic temperature profile, Eq. (2.7) was used to find the area between the output and input curve within each half a cycle. A ninth order polynomial is used to precisely fit the the temperature profile. Then, the obtained curve was integrated. Finding the sensible effectiveness in parallel-flow arrangement, the *NTU* was determined from Eq. (2.12). Considering that the *NTU* was independent of the flow arrangement, the sensible effectiveness of the counter-flow arrangement was calculated by using Eq. (2.14). To show the repeatability of the result in different cycles, effectiveness was calculated within 6 half-cycles at each period by numerical integration of temperature profiles. Then, the precision uncertainty was calculated by Eq. (2.15) where the student t-factor is 2.571 for six data points.

In addition to precision uncertainty, the bias uncertainty of the area integration should be taken into consideration. In this set of tests, the bias uncertainty mainly resulted from uncertainty in temperature profiles, which can be calculated based on calibration results. The bias uncertainty of ±0.2 K for temperature measurements caused the changes in integration area resulting in bias

uncertainty in the sensible effectiveness of the parallel-flow exchanger. To determine the bias uncertainty of sensible effectiveness in a counter-flow exchanger (heat wheel), the method of propagation of error was used. Detailed calculations are provided in Appendix A. Consequently, the total uncertainty can be obtained as a combination of precision and bias uncertainty by Eq. (2.19).

The average value of sensible effectiveness with its total uncertainty at each angular speed is presented in Table 2.7. In addition, a comparison between the measured effectiveness, determined by periodic temperature profile of the cyclic test, and the predicted effectiveness, calculated by time constant obtained through single step change experiment, is given in Figure 2.16. The predicted values of effectiveness for the parallel and counter flow exchangers are determined through Eqs. (2.11) and (2.14), respectively, where the angle ratio, ψ, was obtained from single step change experiments, Table 2.5. The results show that for both flow arrangements increasing angular speed causes higher sensible effectiveness. In addition, there is good agreement between cyclic test results and the sensible effectiveness predicted from single step change results for both parallel-flow and counter-flow exchangers. It can be seen that the sensible effectiveness of parallel flow can be measured with adequate accuracy with an uncertainty of less than 1.5%. However, considerable uncertainty can be seen in the effectiveness of the counter-flow exchanger at higher angular speeds, i.e. U_T = 32.5% at ω = 3.14 rpm. The high amount of uncertainty is an indicator of the propagation of error in calculations. Even though the uncertainty for the parallel-flow effectiveness is less than 1.5%, the maximum theoretical effectiveness for parallel-flow exchanger approaches 50% when *NTU* is infinite. As a result, for an effectiveness of more than 48.5% even a small uncertainty leads to a large variation in *NTU*, which in turn causes a large variations in the counter-flow exchanger effectiveness. Even though decreasing the angular speed

reduces the uncertainty in a counter-flow exchanger, this can be applied to the cases where the counter-flow effectiveness is less than 55%, which is far below the performance of industrial counter-flow exchangers (heat wheels) available on the market. Thus, it can be concluded that finding the effectiveness of a heat wheel through cyclic step changes performed on a parallel-flow exchanger with the same geometry and material is not practical.

Table 2.7-Sensible effectiveness of the heat exchanger response found through cyclic test, (ΔT_{st}= 27 °C, and V_f = 0.34 m/s)

T (min)	ω (rpm)	ε_{PF} (%)	$U_{\varepsilon,PF}$(%)	ε_{CF} (%)	$U_{\varepsilon,CF}$(%)
2	3.14	49.8	1.4	74.5	32.5
4	1.57	49.6	1.4	70.7	15.2
8	0.78	49.0	1.4	66.92	8.1
16	0.39	45.8	1.3	55.37	3.6

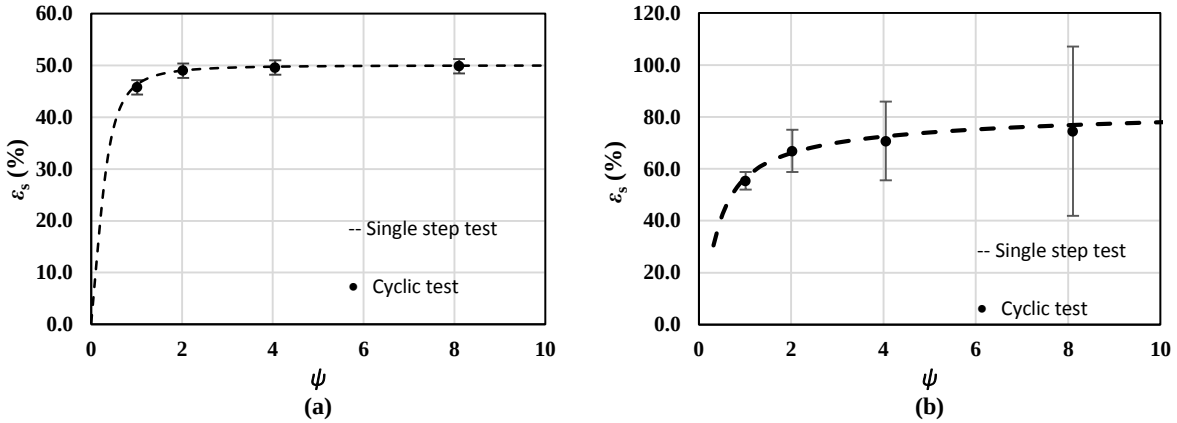

Figure 2.16-Sensible effectiveness obtained by cyclic and single step tests a heat wheel with (a) parallel-flow and (b) counter-flow flow arrangement (ΔT_{st} = 27 °C, and V_f = 0.34 m/s)

2.10.3 Comparison with the Literature Data

No data was found for a full-scale wheel with the same geometry and materials as in the small-scale exchanger tested in this chapter. On the other hand, building a full-scale wheel and carrying out full-scale performing testing was not economically and technically feasible. Thus, in this section, the predicted sensible effectiveness of the equivalent heat wheel is compared to results obtained by empirical correlations in the literature (Kays & London, 1984; (Buyukalaca & Yilmaz, 2002). Eqs. (1-3). Measuring airflow rate, mass of sheets, and area of heat transfer, the sensible effectiveness can be determined by correlations if the convective heat transfer coefficient is known. In the tests performed in this study, the flow within the exchanger channels was laminar, i.e. $26 < Re < 626$, therefore, the convective heat transfer coefficient value can be taken from the literature by knowing the channel aspect ratio. It should be noted that at face velocities less than 0.2 m/s, entrance effects were insignificant as the flow was assumed to be both thermally and hydrodynamically fully developed, $x_{h,FD}/L = 0.12$ and $x_{th,FD}/L = 0.04$; whereas, at higher face velocities there was developing flow through all the channel length, $x_{h,FD}/L = 1.99$ and $x_{th,FD}/L = 1.42$. To account for the changes in convective heat transfer coefficient for both thermally and hydrodynamically developing flow, the tabular results of the average Nusselt number for simultaneously developing flow were utilized (Shah & London, 1978). The obtained sensible effectiveness from experiment and correlations are plotted in Figure 2.17. a. It can be seen that the results show good agreement for high C_r^* values, however, the difference between the results increases as C_r^* decreases. To get more information, the difference between the predicted and correlated sensible effectiveness is given in Figure 2.17.b. Comparing to either of the correlations, the difference in the sensible effectiveness increases to more than 5% at $C_r^* < 4$. This is expected since the analytical solution used to predict sensible effectiveness of rotary wheels is developed for the cases that $C_r^* > 5$. For $C_r^* = 5$, about 5% and 3% discrepancy is observed comparing the

results to Kays and London and Yilmaz and Buyukalaca correlations, respectively. At higher heat capacity rate ratio, $C_r^* > 5$, the difference between results reduces to less than 3% and approaches about 1% at $C_r^* = 20$. It should be noted that these values should not be interpreted as the actual uncertainty in the sensible effectiveness found by the single step change testing method. In fact, an accurate uncertainty study was not applicable since the literature did not specify the uncertainty bounds for the sensible effectiveness correlations. The Kays and London correlation is based on the numerical study of Lamberston (Lamberston, 1958) which does not include any uncertainty in its tabular results. Yilmaz and Buyukalaca validated the proposed empirical correlations with their experimental data and reported 2.8-10% difference in the results increasing *NTU* from 1.2 to 2.3. However, the comparison was made based on their experiment with specified conditions that were not the same as this study. Also, the uncertainty in the sensible effectiveness obtained from experiment was not mentioned, which is normally within the range of ±5%. Considering all these facts, it can only be claimed that the single step change testing method on stationary parallel-plate heat exchanger is applicable for predicting the performance of the rotary wheels with $C_r^* > 5$ by which the predicted sensible effectiveness of the wheel has the uncertainty of less than 3% compared to that obtained by available correlations. It should be noted that heat loss (or gain) to the surroundings during the transient test can change the thermal response of the exchanger which was not considered in the transient model. Further studies are required to fully describe these effects in the transient testing.

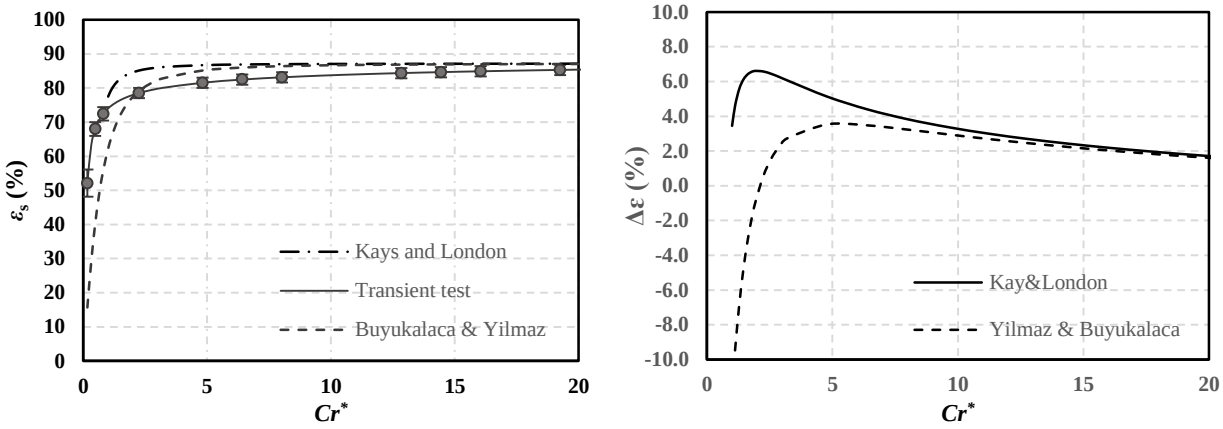

Figure 2.17-(a) Sensible effectiveness of the heat wheel obtained by transient experiment and the literature correlations. (b) Difference between the transient and correlated sensible effectiveness (ΔT_{st} = 27 °C, and V_f = 0.34 m/s)

2.11 Summary and Conclusions

In this chapter, a set of transient experiments was performed on a parallel-plate heat exchanger to predict the effectiveness of an equivalent heat wheel comprised of the same material and hydraulic diameter. In the transient tests, the inlet temperature of the exchanger changed through a step increase/decrease and the step response of the exchanger was studied by monitoring its outlet temperature. A time constant was determined for response of heat exchanger by fitting the normalized temperature profile at different airflow rates. Then, the wheel angle ratio was defined as a ratio of wheel time constant to half of its rotation period. An analytical solution represented the sensible effectiveness of heat wheels as a function of the angle ratio. Obtaining the time constant through transient experiment and considering the wheel angular speed, the sensible effectiveness was calculated at different air flow rates. The results stated that the effectiveness decreased as the face velocity increased. In addition, increasing angular speed of the wheel led to an increase in the sensible effectiveness. The uncertainty analysis was performed on the results to find the uncertainty imposed on the sensible effectiveness due to systematic uncertainty in flow rate measurements, curve fitting, and changes in amplitude of step change. When V_f = 0.34 m/s,

the uncertainty analysis determined the total uncertainty to be less than 5% when the angle ratio was between 5 and 20. Finally, the sensible effectiveness of the heat wheel obtained by the transient test was compared to the sensible effectiveness calculated by empirical correlations in the literature. It was observed that there was less than 3% difference in results for heat capacity rate ratio of greater than 5. The difference between the sensible effectiveness values is higher at low capacity rate ratio, $C_r^* < 5$, which may be due to the uncertainty involved in the transient experiments, such as heat loss to the surroundings. In general, the outcomes demonstrated that the single step change transient experiment could predict the effectiveness of heat wheels within certain operating conditions.

In addition, the sensible effectiveness of parallel-flow and counter-flow heat wheel configurations was determined by performing a cyclic test on the parallel-plate exchanger. In this experiment, the inlet condition was changed through a series of step cycles, similar to what occurs in an actual heat wheel. It was observed that at a constant airflow rate, the effectiveness for both the parallel-flow and counter-flow heat wheels increased as the periods of the cycles decreased. The uncertainty analysis showed that the uncertainty in the effectiveness of the parallel-flow wheels was less than 1.5%. However, the uncertainty in the sensible effectiveness of the counter-flow wheels, was found to be large, $\varepsilon = 74.5 \pm 32.5\%$. The high values of uncertainty illustrated that the cyclic test performed in this study could not determine the effectiveness of counter-flow heat wheels with low uncertainty.

CHAPTER 3

HEAT LOSS/GAIN IN TRANSIENT TESTING OF HEAT WHEELS

3.1 Overview

The results in chapter 2 revealed that although the component transient testing has great potential for heat wheel testing, the predicted sensible effectiveness values are lower than the literature correlations. It was hypothesized that this discrepancy was due to heat loss/gain occurring during the transient test. Therefore in this chapter, the analytical model is extended to consider heat transfer with the surroundings. Thus, the main purpose of this chapter is to satisfy the second objective of the thesis, "to predict the full-scale *heat wheel* effectiveness with its uncertainty and to investigate the relationship between the sensible effectiveness and operating conditions", which was partially addressed in chapter 2. The first part of this chapter discusses the modification of the transient analytical model to consider the influence of heat loss/gain and determines the criteria within which the model is valid. In addition, the effects of heat loss are experimentally investigated at different step change amplitudes, air flow velocities, and wheel angular speeds. Finally, a correlation is proposed based on the extended model to determine the sensible effectiveness as a function of operating conditions, within the tested range.

The manuscript in this chapter was published in the ASME Journal of Thermal Science and Engineering Applications in February 2016. It should be noted that slight changes have been applied to the original manuscript to avoid repetition. In particular, the experimental facility and introduction are not presented in this chapter as they were thoroughly described chapter 2.

Effects of Heat Loss/Gain on the Transient Testing of Heat Wheels

Farhad Fathieh, Robert. W. Besant, Richard. W. Evitts, Carey. J. Simonson

3.2 Abstract

Heat wheels are used in ventilation systems to recover a considerable amount of sensible energy required for providing indoor thermal comfort. The transient single step test is a new testing method developed to determine the sensible effectiveness of heat wheels. In practice, heat loss/gain may create large uncertainty in the sensible effectiveness obtained through transient testing. In this chapter, the transient analytical model in the literature was extended to account for heat loss/gain effects in the transient testing. The results state that in particular operating conditions, the sensible effectiveness can be affected by more than 10% due to heat loss/gain. The transient testing facility (introduced in chapter 1) was used to investigate the effects of heat loss/gain on the sensible effectiveness through transient testing of a small-scale heat exchanger. After decoupling heat loss/gain effects from transient test data, less than 2% difference was observed in the sensible effectiveness while the supply and exhaust flow rate was small (Re < 209) and the temperature difference was ΔT_{st} < 7.0 °C. However, the sensible effectiveness decreased by more than 9% when ΔT_{st} > 37.5 °C or Re > 600. An empirical correlation was proposed based on the transient test data that correlates the sensible effectiveness with the heat capacity rate ratio. Comparing the results of the proposed correlation with data in the literature, less than 2% difference was observed at a heat capacity rate ratio greater than 0.5 after the heat loss/gain effects were decoupled from transient test data.

3.3 Introduction

Fathieh et al. conducted the transient single step tests on a heat wheel component to predict the sensible effectiveness of a full-scale wheel (Fathieh et al., 2015). The heat wheel component

in their work, was a parallel-plate exchanger made up of identical materials to industrial heat wheels. Comparing the sensible effectiveness with the experimental data in the literature, the results were in good agreement at moderate and high angular speeds and while the heat capacity of the matrix is relatively large compared with the heat capacity of airflow. However, a 5-10% discrepancy was seen compared to the steady state results in some testing conditions. It was reported that the difference could be due to heat loss/gain.

Although the second mode was observed in the transient results (Bolster, 2012; Fathieh et al., 2015), its effects on the results have not been considered until now. Therefore, the main objective of this study is to take the effects of the second mode on the sensible effectiveness into consideration. For this reason, the transient analytical model in the literature is extended to consider the effect of second mode, in the presence of heat loss/gain. In addition, the effects of heat loss/gain on the sensible effectiveness is investigated by conducting a series of transient tests with the same procedure provided in the literature (Fathieh et al., 2015). In this research, a test facility was developed to perform the transient single-step experiment on a small-scale heat exchanger and predict the sensible effectiveness of a full size heat wheel with the same material. The small-scale testing facilitate the experiments by reducing the testing time and allowing to provide and maintain test conditions with laboratory scale facilities. The sensible effectiveness is modified due to heat loss/gain and a detailed comparison with literature data was carried out. In addition, an empirical correlation is proposed for the sensible effectiveness with respect to the capacity rate ratio.

3.4 Theory

In practice, a second mode of heat transfer was observed in transient test data which could be attributed to heat loss/gain during the test (Fathieh et al., 2015). This would change the temperature profile and, consequently, the sensible effectiveness determined through the transient

single exponential model (SEM), discussed in section 2.4. A double exponential model (DEM) is introduced in this chapter to account for the changes in the temperature due to heat loss and gain. In this regard, a second term was added to the normalized temperature response of the heat wheel, Eq. (2.4), that gives:

$$\theta(t) = \gamma_w \theta_w(t) + \gamma' \theta'(t) \tag{3.1}$$

The subscript *w* and superscript $'$ represent the response parameters for heat wheel and heat loss/gain, respectively, that satisfy the energy balance for both heating and cooling period as follows:

$$\gamma_w + \gamma' = 1, \qquad \gamma_w \geq 0 \tag{3.2}$$

The sign of γ' can be evaluated from the criterion given in Eq. (3.2). If heat loss occurs during the test, γ' is negative. On the other hand, heat gain results in positive γ'. With the periodic forcing function, given by Eq. (2.6), the solution of Eq. (2.4) with the modification due to heat loss/gain effect becomes:

$$\theta(t) = \begin{cases} \gamma_{\mathrm{w}} \left(\dfrac{1 - e^{-\frac{1}{\psi_{\mathrm{w}}}}}{1 - e^{-\frac{2}{\psi_{\mathrm{w}}}}} \right) e^{-t/\tau_{\mathrm{w}}} + \gamma' \left(\dfrac{1 - e^{-\frac{1}{\psi'}}}{1 - e^{-\frac{2}{\psi'}}} \right) e^{-t/\tau'} & 0 \leq t \leq \pi/\omega \\ 1 - \gamma_{\mathrm{w}} \left(\dfrac{1 - e^{\frac{1}{\psi_{\mathrm{w}}}}}{1 - e^{-\frac{2}{\psi_{\mathrm{w}}}}} \right) e^{-t/\tau_{\mathrm{w}}} - \gamma' \left(\dfrac{1 - e^{\frac{1}{\psi'}}}{1 - e^{-\frac{2}{\psi'}}} \right) e^{-t/\tau'} & \pi/\omega \leq t \leq 2\,\pi/\omega \end{cases} \tag{3.3}$$

In which the subscript "w" and superscript "′" represent wheel and heat loss/gain, respectively. With the equal heat capacity rate of supply and exhaust airstreams, the sensible effectiveness for cooling or heating periods is calculated by dividing the integral of the normalized temperature response by the integral of the forcing function within each period (O. Abe et al., 2006a):

$$\varepsilon = \frac{\omega}{\pi}\int_{0}^{\frac{\pi}{\omega}} \theta dt \tag{3.4}$$

Replacing normalized temperature, θ, from Eq. (3.3), the sensible effectiveness of the parallel-flow heat wheel can be expressed by:

$$\varepsilon_{\mathrm{PF}} = \varepsilon_{\mathrm{PF,w}} + \Delta\varepsilon'_{\mathrm{PF}} = \gamma_{\mathrm{w}}\psi_{\mathrm{w}}\frac{\left(1-e^{-\frac{1}{\psi_{\mathrm{w}}}}\right)^2}{1-e^{-\frac{2}{\psi_{\mathrm{w}}}}} \pm \gamma'\psi'\frac{\left(1-e^{-\frac{1}{\psi'}}\right)^2}{1-e^{-\frac{2}{\psi'}}} \tag{3.5}$$

where ε_{PF} is the sensible effectiveness when heat loss/gain occurs within the wheel and $\varepsilon_{PF,w}$ is the sensible effectiveness of heat wheel alone with no heat loss/gain. The term $\Delta\varepsilon'_{PF}$ represents the uncertainty in the sensible effectiveness due to heat loss/gain. The sensible effectiveness of a stationary parallel-flow heat wheel with equal supply and exhaust flow rates can be expressed in terms of NTU as follows (Shah & Sekuli, 2003):

$$\varepsilon_{\mathrm{PF,w}} = \frac{1}{2}\left(1-e^{-2NTU_{\mathrm{w}}}\right) \tag{3.6}$$

Combining Eqs. (3.5) and (3.6), NTU_{w} can be given in terms of angle ratio as:

$$NTU_{\mathrm{w}} = -\frac{1}{2}Ln\left(\varepsilon_{\mathrm{PF,w}}\right) = -\frac{1}{2}\mathrm{Ln}\left[1-2\gamma_{\mathrm{w}}\psi_{\mathrm{w}}\frac{\left(1-e^{-\frac{1}{\psi_{\mathrm{w}}}}\right)^2}{1-e^{-\frac{2}{\psi_{\mathrm{w}}}}}\right] \tag{3.7}$$

Thus, the sensible effectiveness of the counter-flow heat wheel can be obtained as follows:

$$\varepsilon_{\mathrm{CF,w}} = \frac{NTU_{\mathrm{w}}}{1+NTU_{\mathrm{w}}} \tag{3.8}$$

According to DEM, the time constant of the heat wheel is the property of the system which is independent from the forcing function. In fact, in the case of heat loss/gain, the sensible

effectiveness can be determined only if the corresponding time constants and weighting factors of the wheel and heat loss/gain are known. The time constants and weighting factors can be obtained by performing the single step test. Considering DEM, the solution of Eq. (2.4) is as follows:

$$\theta(t) = \begin{cases} 1 - \gamma_w e^{-t/\tau_w} - \gamma' e^{-t/\tau'}, & 0 \le t \le \infty \quad step\ increase\ (heating) \\ \gamma_w e^{-t/\tau_w} + \gamma' e^{-t/\tau'}, & 0 \le t \le \infty \quad step\ decrease\ (cooling) \end{cases} \tag{3.9}$$

In the transient single step test, the inlet and outlet temperature are monitored and the normalized temperature is determined. Then, the time constants and weighting factors are found by fitting DEM to the experimental data using Eq. (3.9). Finally, the sensible effectiveness is determined through Eqs. (3.7) and (3.8).

3.5 Experimental

The same small-scale exchanger and experimental facility, as described in section 2.5.1 and 2.5.2., were used in this chapter. The test procedure was also identical to the procedure described in section 2.7.

3.5.1 Test Conditions

It was believed that changing the amplitude of the step change may alter the heat loss/gain during the experiment. In this regard, the transient single step change test was performed at six different amplitudes. The amplitude of the step change was adjusted by changing the hot and cold airstream temperatures at each constant flow rate given in Table 2.2. The face velocity may also affect heat loss/gain and, consequently, the sensible effectiveness of the heat wheels (Abe et al., 2006b; Fathieh et al., 2015; Wu et al., 2006). In this chapter, step change experiments were performed at eleven different flow rates at two amplitudes of step change, ΔT_{st} = 4.8 °C and ΔT_{st} = 7.0 °C. The face velocities and volumetric flow rates for each test are also provided in Table 2.3.

3.6 Results and Discussion

3.6.1 Analytical Results

The double exponential model (DEM), provided in section 3.4, was used to obtain the normalized temperature profile and sensible effectiveness of full-scale, parallel-flow and counter-flow heat wheels. According to Eq. (3.6) and (3.7), the sensible effectiveness of heat wheels is only a function of angle ratio. Figure 3.1 shows the sensible effectiveness as a function of wheel angle ratio, ψ_w, for the parallel-flow and counter-flow heat wheels with equal supply and exhaust airflow rates. It can be observed that the sensible effectiveness for both the parallel-flow and counter-flow rotary exchangers increases as the angle ratio increases. The maximum effectiveness of parallel-flow wheels is 50% while 100% effectiveness is theoretically achievable for counter-flow wheels. In practice, conventional heat wheels operate at a counter-flow arrangement with the angle ratio within the range of $1 < \psi_w < 20$ and a sensible effectiveness of 70-80% (Shang & Besant, 2008). As shown in Figure 3.1, a wheel is capable of recovering more sensible energy by increasing its angular speed and/or time constant. It is reported that increasing the wheel angular speed leads to higher amount of carryover (Shang & Besant, 2008). Carryover occurs if a portion of the exhaust air is carried to the supply side. Although carryover slightly increases the sensible effectiveness of the wheel, it reduces the indoor air quality. Thus, it is preferred to lower the wheel angular speeds and increase the time constant by proper selection of the matrix thermal properties, air channels geometry, and airflow rate. Moreover, heat loss/gain may considerably change the time constant in small-scale testing (Shang & Besant, 2009b).

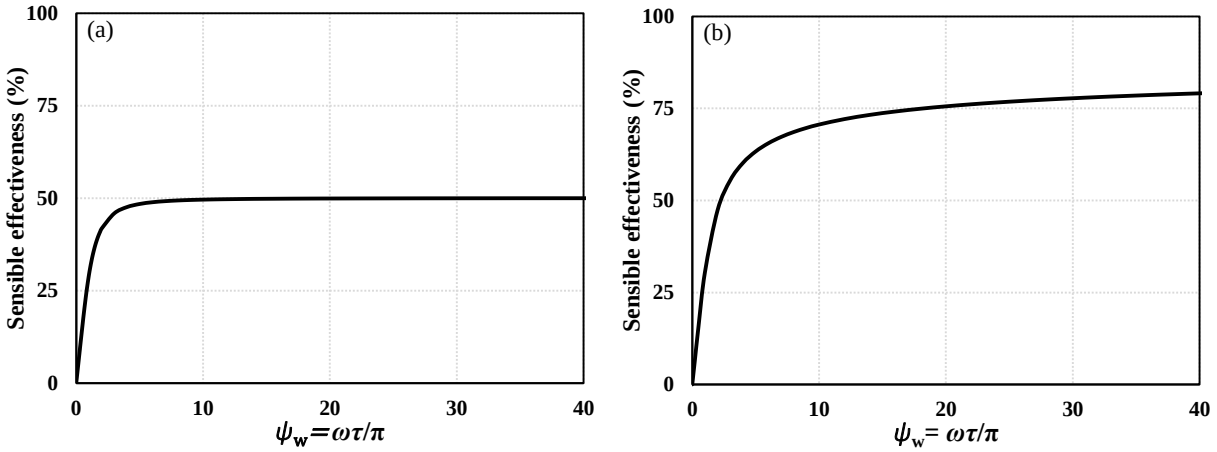

Figure 3.1-Sensible effectiveness versus angle ratio (ψ_w) for (a) parallel-flow and (b) counter-flow heat wheel with the equal supply and exhaust airflow rates

Figure 3.2 shows the normalized temperature profile for the parallel-flow heat wheel at different wheel angle ratios calculated from Eq. (3.5) while no heat loss/gain occurs, $\gamma' = 0$. It can be observed that as the wheel rotates, the normalized temperature increases during the heating period and then decreases in cooling periods. For the case shown in Figure 3.2, the wheel angular speed was kept constant and the angle ratio was changed by increasing/decreasing the time constant. Reducing the angle ratio of the wheel leads to larger variations in the normalized temperature. Moreover, increasing the angle ratio from 10 to 20 has a small impact on the temperature profile. For extremely large angle ratios, the temperature profile becomes horizontal and its value approaches 0.5. This would result in the sensible effectiveness of 50% which is the maximum value for parallel-flow heat wheels, see Figure 3.1.

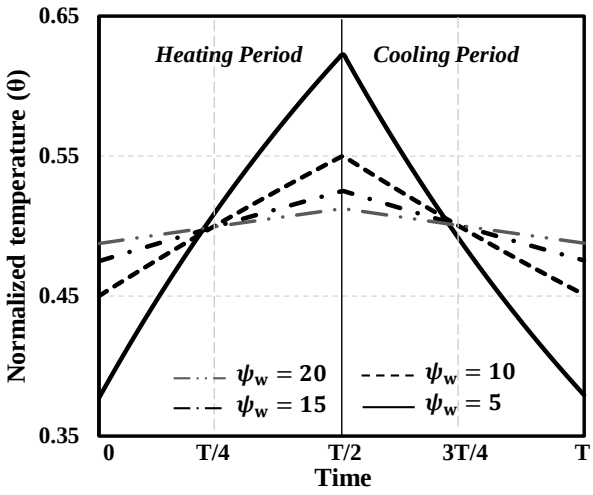

Figure 3.2-Normalized temperature for a parallel-flow heat wheel with equal supply and exhaust air flow rates at different angle ratios

The effects of heat loss/gain on the temperature profile of a parallel-flow wheel with equal supply and exhaust airflow are plotted in Figure 3.3. The profiles were computed for two loss time constants and weighting factors, while the wheel angle ratio was $\psi_w = 20$ ($\tau_w = 2.5$ s and $\omega = 15$ rpm) and the results were compared to the case without heat loss/gain, $\gamma' = 0$. It can be observed that once γ' increases the temperature profile changes remarkably. For instance, the maximum difference in normalized temperature increases from 0.001 to 0.005 as γ' increases from 0.1 to 0.4 for $\tau_w/\tau' = 0.5$. It should be noted that even this small difference in normalized temperature would be considerable if the amplitude of the step change is large. For small values of loss weighting factor, $\gamma' < 0.1$, the temperature profile variations are trivial for a wide range of loss time constants. However, the variations in the temperature profile with the loss time constant becomes significant for larger loss weighting factors.

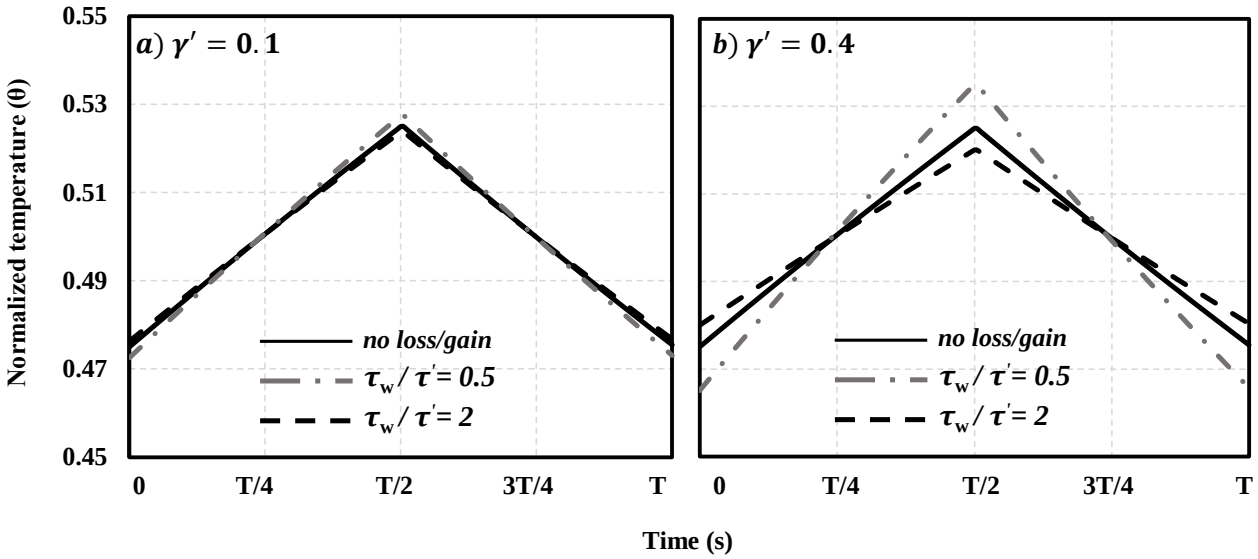

Figure 3.3-Normalized temperature profile (θ) of a parallel-flow heat wheel with the equal supply and exhaust airflow rate for different values of loss weighting factors

The double exponential model (DEM) was used to determine the sensible effectiveness of a counter-flow exchanger for loss/gain weighing factors of $\gamma' = 0.1$ and $\gamma' = 0.4$. The effectiveness was calculated for three values of wheel angle ratio (ψ_w) and the results are graphed as a function of τ_w/τ' in Figure 3.4. For each angle ratio, two curves were plotted corresponding to the upper and lower bounds for the sensible effectiveness. Depending on the direction of the heat (heat loss or gain), the effectiveness would increase or decrease. However, the absolute value of the changes in effectiveness increases as the ratio of τ_w/τ' decreases. The upper and lower bounds of sensible effectiveness approach the wheel effectiveness at high time constant ratios, $\tau_w/\tau' >> 1$. This implies that the heat loss/gain effects are insignificant when the second time constant is a few times larger than the wheel time constant. In addition, the effectiveness increases with the wheel angle ratio which is in accordance with the results of Figure 3.1.

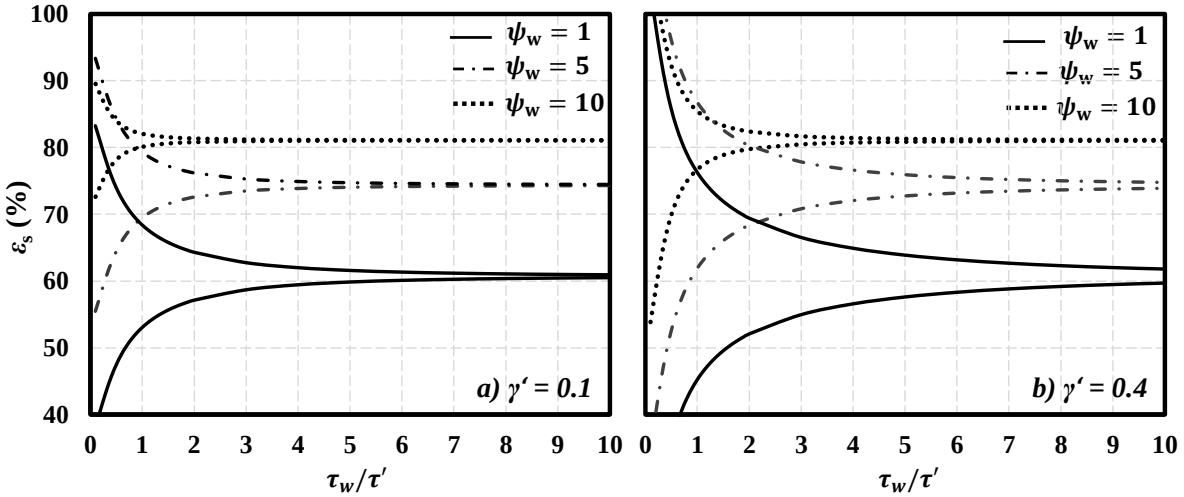

Figure 3.4- The upper and lower limits for the sensible effectiveness of a counter-flow heat wheel with the equal supply and exhaust airflow rate with respect to the wheel time constant for different weighting factors and wheel angle ratio ψ_w

According to the results of Figure 3.4, a critical time constant ratio, $(\tau_w/\tau')_{cr}$, can be defined above which less than 2% uncertainty is expected in the sensible effectiveness. In fact, 2% uncertainty coming from heat loss/gain combined with 2-3% uncertainty in the transient testing would result in the total uncertainty of less than 5% which is still acceptable according to the standards. The critical time constant ratio with respect to the loss weighting factor is plotted in Figure 3.5 for different wheel angle ratios. It can be seen that $(\tau_w/\tau')_{cr}$ increases with loss weighting factor. In addition, the $(\tau_w/\tau')_{cr}$ is higher if the wheel has a higher angle ratio. In fact, above the critical point, the heat loss/gain is relatively slow compared to the heat transfer which occurs between the airflow and the wheel matrix. Consequently, the heat loss/gain has small effects on the sensible effectiveness. Figure 3.5 gives the critical time constant ratio if the wheel and heat loss/gain time constants and weighting factors are known. A few analytical studies (Abe et al., 2006a, 2006b; Shang & Besant, 2009b, 2008) were conducted to relate the wheel time constant to the matrix thermal properties, channel geometry, and face velocity. Due to the simplifying assumptions in these works, the results cannot accurately predict the wheel time constant and

examine the effects of heat loss/gain on wheel time constant. Therefore, a set of transient experiments was carried out to study the effects of heat loss/gain on wheel time constant and the results were presented in the next section.

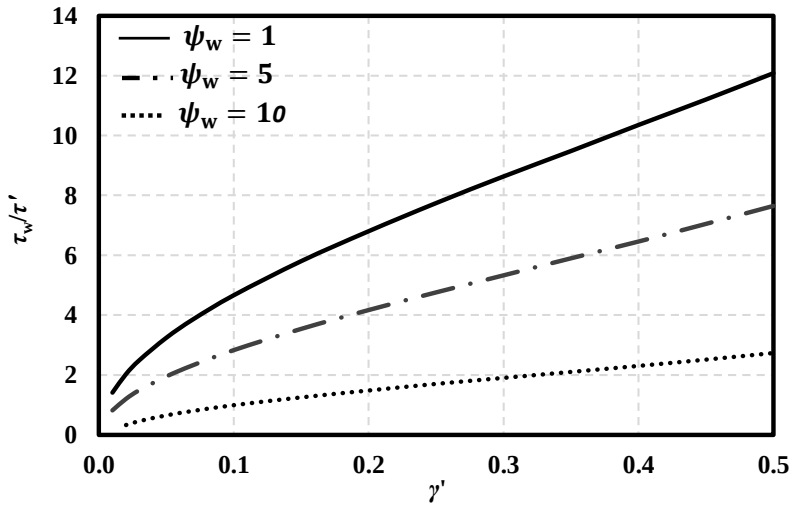

Figure 3.5-The critical ratio of wheel to heat loss/gain time constant (τ_w/τ') above which less than 2% uncertainty is expected in the sensible effectiveness

3.6.2 Transient Test Results

3.6.2.1 Effects of Step Change Amplitude on the Second Transient Mode

Figure 3.6 shows the transient normalized temperature profile of the small-scale heat exchanger at different values of step change amplitude. It can be seen that increasing the amplitude of the step change slightly alters the exchanger temperature response. To quantify the response variations, the single exponential model (SEM) was used to fit the experimental data with Eq. (2.7). The data was fitted using the trust-region optimization algorithm in MATLAB R2014a. It should be noted that SEM does not take the effects of heat loss/gain into account since the loss weighting factor is equal to zero in this model, $\gamma'=0$. The time constant, weighting factors, and coefficient of determination (R^2) obtained through SEM are given in Table 3.1.

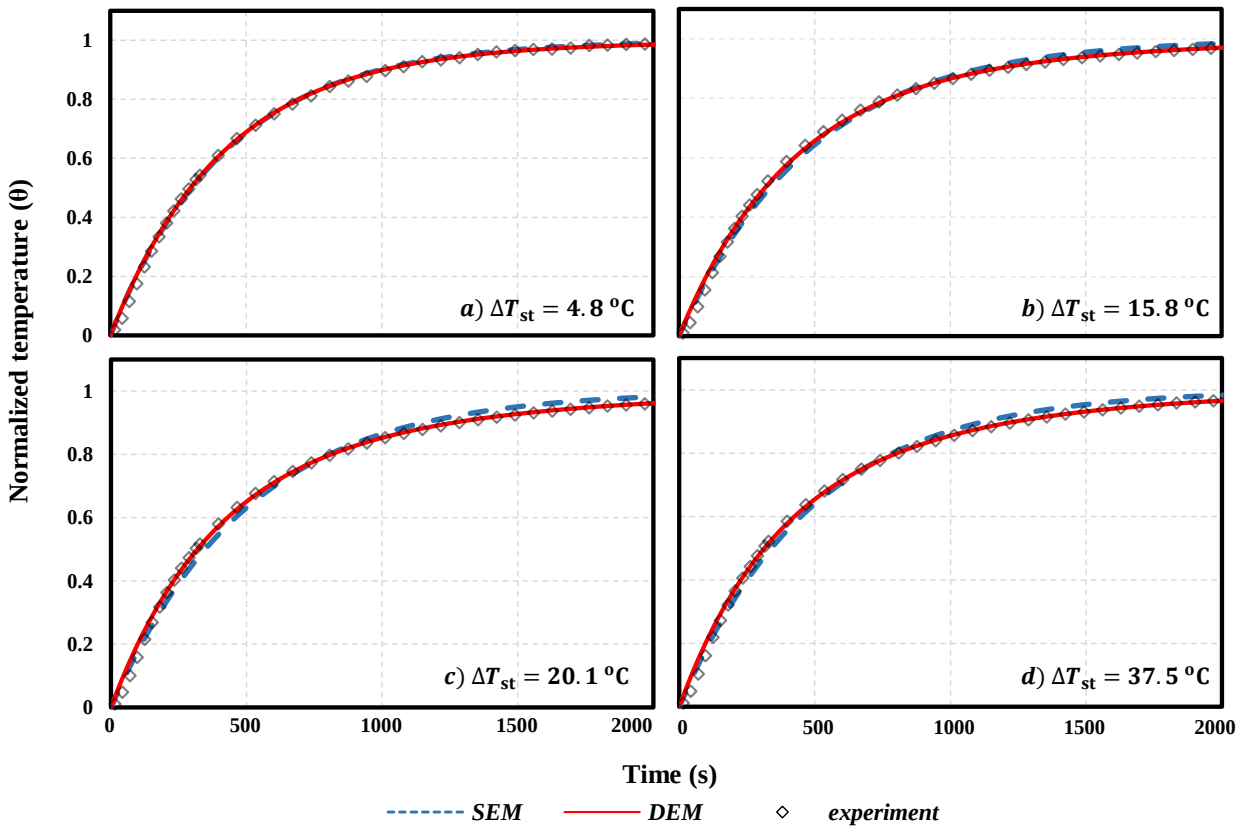

Figure 3.6-Normalized temperature response of the small-scale heat exchanger obtained through transient testing at different step change amplitudes (V_f = 0.34 m/s, maximum uncertainty in the experimental data is U_θ = ±0.06 and ±0.01 at ΔT_{st} = 4.8 °C and 37.5 °C, respectively)

Table 3.1-Response characteristics of the small-scale heat exchanger obtained through transient testing at different step change amplitudes (V_f = 0.34 m/s, Re_{dh} = 174)

ΔT_{st} °C	SEM		DEM				
	τ_w (s)	R^2	τ_w(s)	γ_w	τ'(s)	γ'	R^2
4.8	431	0.999	430	0.99	1136	0.01	0.999
7.0	470	0.996	430	0.89	989	0.11	0.999
15.8	485	0.993	430	0.86	1077	0.14	0.998
20.1	494	0.993	430	0.85	1310	0.15	0.998
27.0	501	0.993	430	0.81	1071	0.19	0.998
37.5	488	0.995	430	0.54	1074	0.16	0.997

In fact, the wheel time constant depends on the wheel structure and should not change with the amplitude of the step change at certain face velocity and angular speeds. However, it was found that the time constant varies 14% while the amplitude of the step change increases from 4.8 °C to

37.5 °C. This could be due to the heat loss to the surroundings which is more significant at higher temperature. To consider the heat loss effects, the double exponential model (DEM) was also used to fit the experimental data using eq. (3.9) and eq. (3.3). It was found that at the lowest amplitude of the step change, ΔT_{st} = 4.8 °C, the fitting parameters obtained through DEM and SEM are almost identical which states that the heat loss/gain effects are negligible. Therefore, the wheel time constant is specified with negligible uncertainty due to heat loss/gain at ΔT_{st} = 4.8 °C. With the fixed wheel time constant obtained at ΔT_{st} = 4.8 °C, DEM model was used to determine the weighting factors and loss time constant. Table 3.1 lists the time constant, weighting factors, and coefficient of determination (R^2) obtained through DEM. The plots in Figure 3.6 and coefficient of determination given in Table 3.1 state that both SEM and DEM fit the experimental data accurately at low amplitude of step change, ΔT_{st} < 15.8 °C. However, at higher amplitudes of the step change, DEM fits the experimental data better. The values given in Table 3.1 show that heat loss/gain intensifies remarkably as γ' increases with the step change amplitude. On the other hand, the loss time constant slightly changes by increasing step change amplitude. In conclusion, the amplitude of the step change has a significant impact on the amount of the loss/gain in transient testing but it does not alter the rate of loss/gain effectively.

With the time constants and weighting factors given in Table 3.1, the sensible effectiveness was calculated at different step change amplitudes through SEM, described in section 2.4, and DEM, described in section 3.4. The difference in the SEM and DEM sensible effectiveness is calculated at each angular speed and the results are plotted in Figure 3.7. The results illustrate that the difference in sensible effectiveness is less than 2% for the given range of step change amplitude if ω > 0.7 rpm. However, for 0.1 < ω < 0.7 rpm, more than 5%, appears in the sensible effectiveness as the amplitude of step change increases, ΔT_{st} > 7.0 °C.

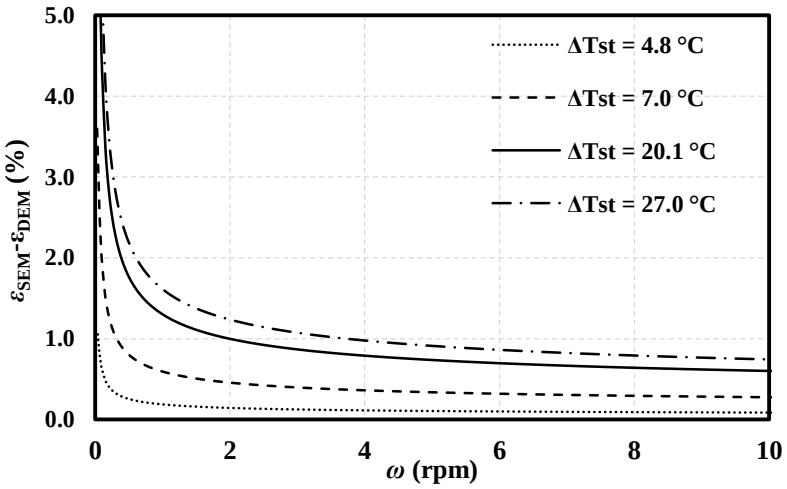

Figure 3.7-The difference in the sensible effectiveness of the small-scale heat exchanger calculated by DEM and SEM (V_f = 0.34 m/s, Re_{dh} = 174)

3.6.2.2 Effects of Flow Rate on the Second Transient Mode

The effects of supply and exhaust flow rate on the time constant is presented in Figure 3.8. According to the weighting factor values for ΔT_{st} = 7.0 °C, given in Table 3.1, the effects of heat loss are expected to be small enough so that the linear superposition model presented in section 2.2 should be valid. Thus, the amplitude of step changes for flow rate tests was set to 7.0 °C. In addition, to find the wheel time constant while heat loss effects are insignificant, the tests were also performed at ΔT_{st} = 4.8 °C at each flow rate. In Figure 3.8, it can be seen that as the flow rate increases, the outlet temperature reaches its final value faster. The experimental data was correlated using SEM and DEM and the results are presented in Table 3.2. The results in Table 3.2 clearly state that changing the flow rate alters heat loss/gain effects in transient test. Observing the SEM correlated curves, it can be found that the model can precisely describe the exchanger's response at low Reynolds number, $Re < 261$. At higher Reynolds number, a second mode appears which cannot be correlated accurately by SEM while the DEM can precisely correlate the experimental data even at high Reynolds number. The time constants, weighting factors, and

coefficients of determination (R^2) are listed in Table 3.2. When SEM was used to correlate the temperature profile, low values of R^2 at higher face velocities were found. In contrast, R^2 of higher than 0.99 was seen for DEM at all the flow rates. Moreover, increasing the face velocity amplifies the heat loss weighting factor, γ', for the most of the cases.

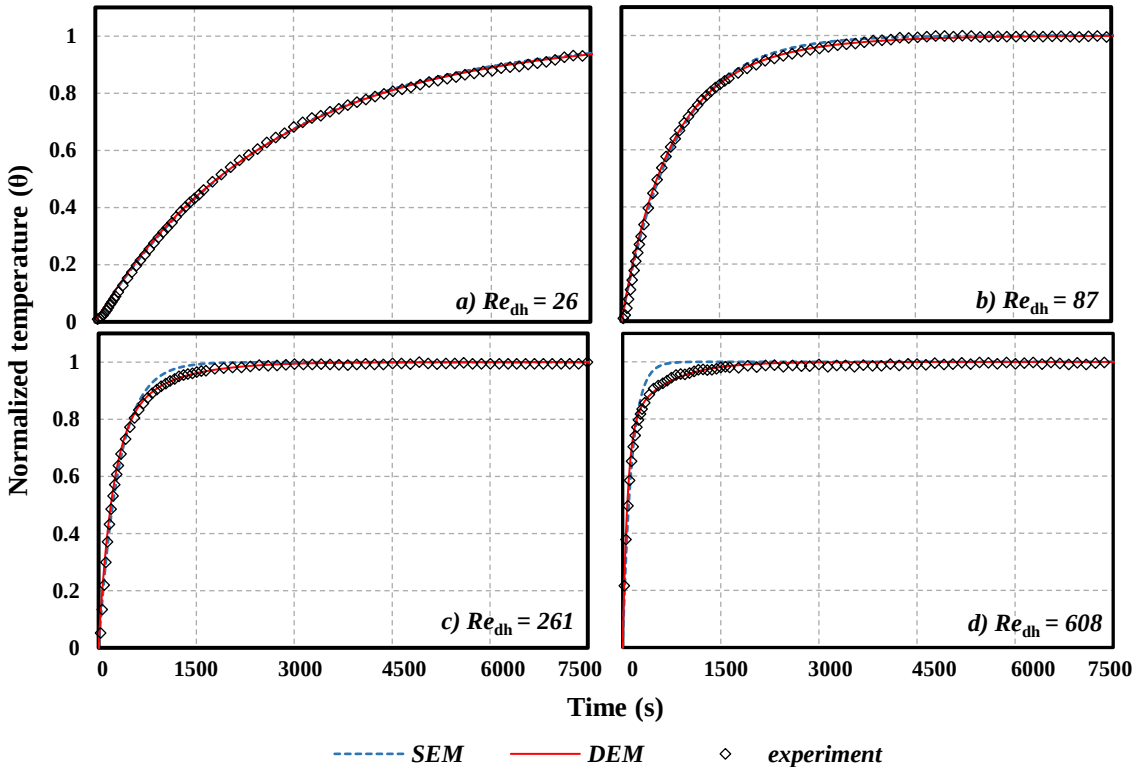

Figure 3.8-Normalized temperature response of small-scale heat at different flow rates of the (ΔT_{st} = 7.0 °C, maximum uncertainty in the experimental data is U_θ = ±0.03)

Table 3.2-Response characteristics of the small-scale heat exchanger obtained though the transient testing at different air flow rates, (ΔT_{st} = 7.0 °C)

Re_{dh}	$V_f(m/s)$	SEM		DEM				
		τ_w (s)	R^2	τ_w (s)	γ_w	$\tau'(s)$	γ'	R^2
26	0.05	2676	0.999	2784	0.98	8004	0.02	0.999
43	0.09	1672	0.999	1670	0.96	5155	0.04	0.999
87	0.17	832	0.996	745	0.92	2408	0.08	0.999
130	0.26	610	0.997	553	0.91	1686	0.07	0.998
174	0.34	468	0.996	430	0.89	989	0.11	0.999
209	0.41	441	0.958	293	0.81	1706	0.19	0.998
261	0.51	312	0.984	207	0.74	781	0.26	0.998
348	0.68	241	0.907	158	0.85	1696	0.15	0.998
434	0.86	180	0.888	114	0.84	1315	0.16	0.997
521	1.03	139	0.924	69	0.72	470	0.28	0.997
608	1.20	134	0.905	73	0.77	590	0.23	0.997

It should be noted that the time constant of the small-scale exchanger may be different from the commercial wheels depending on wheels matrix structure and geometry. It was stated that the time constant is proportional to the heat capacitance of the exchanger (Shang & Besant, 2008); therefore, with thicker sheets and greater heat capacity, a larger time constant is expected for small-scale exchangers. The time constant of the small-scale exchanger was compared to the thermal response of three commercial wheels tested using a single step test in literature (Abe et al., 2006b). The comparison shows that the time constant of the small-scale exchanger is about 5.6 times larger than the time constant of commercial wheels at a face velocity of 0.3 m/s.

With the time constants and weighting factors given in Table 3.2, the sensible effectiveness was determined through SEM and DEM at specified wheel angular speeds. Figure 3.9 shows the sensible effectiveness with respect to Reynold number at four different wheel angular speeds. The angular speeds presented in Figure 3.9 are relatively low, ω = 0.1-1 rpm, compared to the angular speeds of a practical heat wheels, ω = 10-30 rpm. In fact, due to the larger heat capacity of the small-scale exchanger, its time constant is about 10 times larger than the time constant of the conventional heat wheels. For similarity study, with the larger time constant, lower angular speeds are required to limit the angle ratio of small-scale exchanger to that of conventional wheels, $1 < \psi_w < 10$. According to the results in Figure 3.9, the sensible effectiveness decreases as Reynolds number increases. In fact, as flow rate increases, *NTU* decreases which in turn lowers the sensible effectiveness. Comparing the sensible effectiveness obtained by SEM and DEM in Figure 3.9 shows that the difference in the sensible effectiveness is insignificant at low Reynolds numbers, Re < 209 within the range of the given angular speeds. For instance, at ω = 1 rpm and *Re* = 130 (ψ_w = 18), a maximum difference of less than 0.4% in the sensible effectiveness is seen, whereas,

the difference increases to 1.6% when the angular speed is reduced to ω = 1 rpm (ψ_w = 18). However, the difference in sensible effectiveness increases more than 9% when *Re* > 608.

3.6.3 Comparison with Literature Data

To study the effects of heat loss/gain in small-scale transient testing, the calculated effectiveness through the SEM and DEM models were compared to correlations proposed in the literature (Kays & London, 1984; Buyukalaca & Yilmaz, 2002; Yilmaz & Cihan, 1993), given by Eq. (2.1) and Eq. (2.3). Moreover, the sensible effectiveness obtained through SEM and DEM in this study were used to develop a correlation as follows:

$$\varepsilon/\varepsilon_0 = 1 - \frac{1}{aC_r^{*b}} \tag{3.10}$$

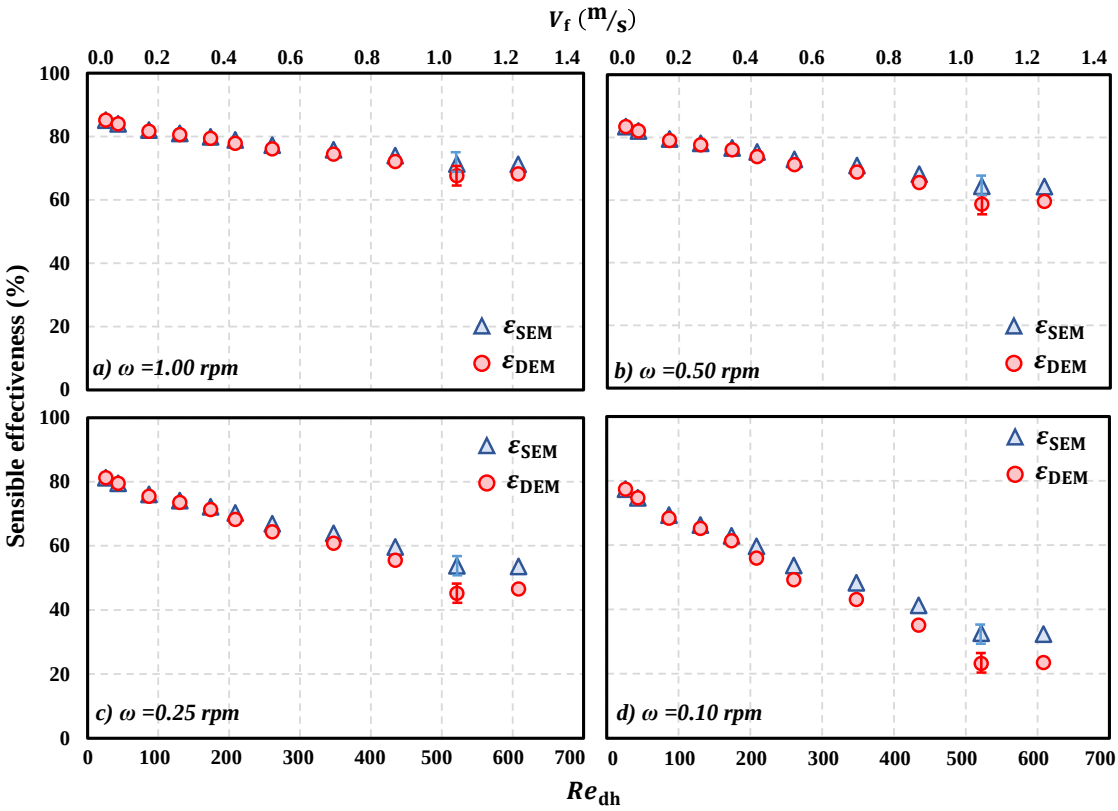

Figure 3.9-Comparison of the sensible effectiveness calculated by SEM and DEM at different flow rates and wheel angular speeds (ΔT_{st} = 7.0 °C, sample error bars show the maximum uncertainty in the effectiveness values obtained from SEM and DEM)

The effectiveness of the stationary wheel (ε_0) can be determined if the number of transfer units of the stationary wheel $NTU = (hA_{\mathrm{ht}})/(\dot{m}C_p)_a$ is known. With the known flow rate and total heat transfer surface area, *NTU* could be calculated if the convective heat transfer coefficient was known. In this set of experiments, the flow inside the channels was laminar and developing, both thermally and hydrodynamically. To account for the changes in convective heat transfer coefficient due to entrance effects, the tabular results of the average Nusselt number for simultaneously developing flow in literature was used (Shah & London, 1978). The calculated NTU_0 values are given in Table 3.3.

Table 3.3-Fitting parameters and coefficient of determination (R^2) for Eq. (3.10)

Re	Ntu_0	SEM			DEM		
		a	***b***	R^2	***a***	***b***	R^2
26	43.3	3.9 ± 0.3	1.20 ± 0.02	0.956	3.9 ± 0.3	1.20 ± 0.02	0.956
43	26.0	3.8 ± 0.3	1.24 ± 0.02	0.957	3.8 ± 0.3	1.26 ± 0.02	0.964
87	13.1	4.1 ± 0.3	1.34 ± 0.03	0.982	3.3 ± 0.3	1.35 ± 0.03	0.986
130	8.8	5.4 ± 0.4	1.44 ± 0.03	0.996	5.1 ± 0.4	1.45 ± 0.04	0.998
174	6.7	7.0 ± 0.5	1.58 ± 0.05	0.993	6.4 ± 0.5	1.52 ± 0.04	0.995
209	5.5	9.2 ± 0.7	1.65 ± 0.05	0.992	6.6 ± 0.5	1.54 ± 0.04	0.966
261	4.4	11.0 ± 0.8	1.75 ± 0.06	0.991	6.5 ± 0.5	1.52 ± 0.04	0.973
348	3.3	15.0 ± 1.1	1.59 ± 0.05	0.982	6.9 ± 0.4	1.51 ± 0.04	0.987
434	2.7	12.5 ± 0.9	1.68 ± 0.06	0.940	6.6 ± 0.4	1.48 ± 0.03	0.950
521	2.3	19.1 ± 1.3	1.87 ± 0.07	0.961	5.4 ± 0.4	1.43 ± 0.03	0.988
608	2.0	18.2 ± 1.3	1.86 ± 0.07	0.953	5.9 ± 0.4	1.43 ± 0.03	0.979
	Average	**9.9 ± 3.9**	**1.56 ± 0.16**		**5.4 ± 0.9**	**1.43 ± 0.08**	

With the transient test data and the sensible effectiveness obtained through SEM and DEM, Eq. (3.10) was used to determine fitting parameters *a* and *b*. Table 3.3 lists the values of *a* and *b* at different *Re* numbers. For all the cases, the coefficients of determination exceeds 0.95, for 95% confidence bounds, which represents a strong fitting. It can be seen that while Eq. (3.10) was used to correlate SEM results, the values of fitting parameters increased with flow rate. However, there was only a slight change in the values of *a* and *b* while DEM results were used. At the lower flow rates with trivial heat loss/gain, the values for fitting parameters are almost identical for both SEM and DEM. Nevertheless, a large discrepancy is seen between SEM and DEM fitting parameters at

higher flow rates when heat loss/gain is considerable. According to the results of Table 3.3, average values can be assigned to fitting parameters obtained by DEM. In contrast, due to large variations in the SEM results, averaging the values for fitting parameters would result in a high uncertainty in the averaged values.

A comparison between the values of sensible effectiveness calculated from correlations in the literature and the new correlation is shown in Figure 3.10. Moreover, the differences between the correlated values are plotted in Figure 3.11. According to the results, good agreement is seen between the SEM and Kays and London correlated effectiveness values, whereas, more than 5% difference is observed at $C_r^* < 2$. In contrast, the effectiveness values obtained from the DEM correlation follow the Yilmaz and Buyukalaca correlation which is more accurate. For the range of the NTU_0 tested, the DEM correlation gives more accurate effectiveness within the range of $0.5 < C_r^* < 10$, while, at $C_r^* > 10$ less than 2% difference in SEM and DEM correlated effectiveness is achieved. In fact, the fitting parameters vary with the air and matrix heat capacity, convective heat transfer coefficient, heat transfer area, and the wheels angular speed. A detailed study is needed to relate fitting parameters to wheel physical and thermal properties.

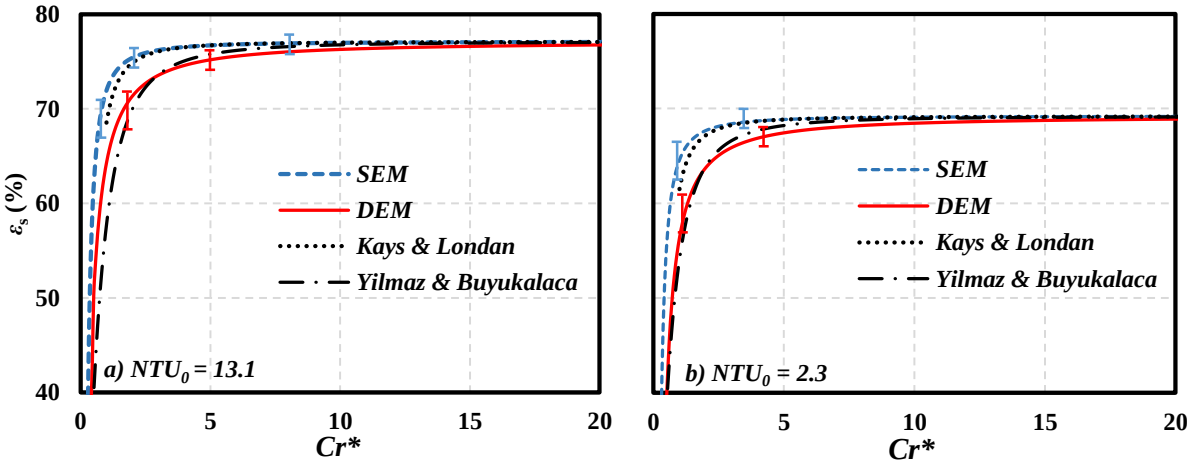

Figure 3.10-Comparison between the sensible effectiveness of the heat wheel calculated from Eq. (3.10) and the correlations in literature for a) NTU_0 = 13.1 and b) NTU_0 =2.3

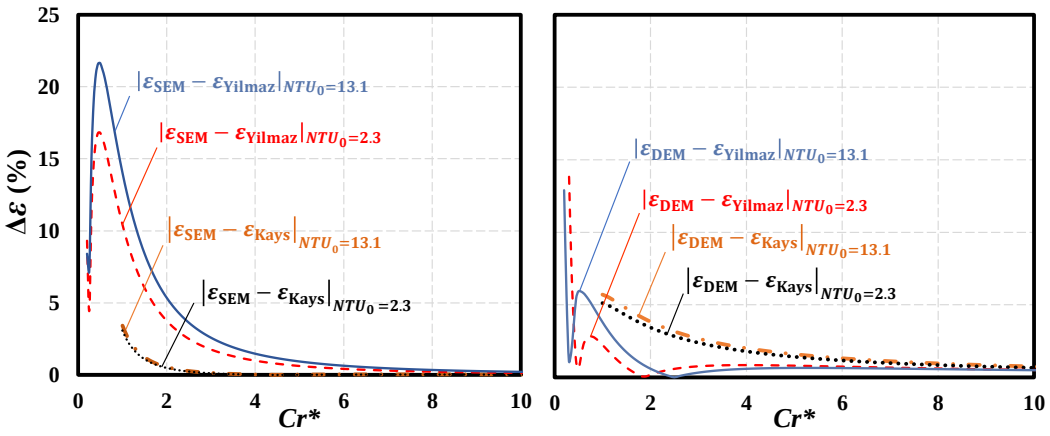

Figure 3.11-The difference between the sensible effectiveness of a heat wheel obtained through literature correlations and the correlation in Eq. (3.10) using a) SEM b) DEM

3.7 Summary and Conclusions

The transient single exponential model (SEM) relates the sensible effectiveness of a rotary heat wheel to its angular speed and time constant, τ_w. The time constant of a wheel can be obtained through its temperature response to a step change in the wheel inlet temperature. In this chapter, a double exponential model (DEM) was presented to modify the SEM due to the heat loss/gain occurring during the transient testing. The loss time constant, τ', and weighting factors, γ', were assigned to heat loss/gain. In addition, the wheel weighting factor, γ_w, should be defined to satisfy the energy balance. According to the analytical solution, the heat loss/gain would substantially change the sensible effectiveness at high loss time constant and weighting factors.

Transient tests were performed on a small-scale heat exchanger to determine the sensible effectiveness from the transient test data. The small-scale heat exchanger was comprised of the same materials as conventional heat wheels. It was observed that, increasing the amplitude of the step change led to higher heat loss and, consequently, a larger loss weighting factor. The DEM was used to decouple heat loss effects from the test data. It was found that the DEM fit the experimental data more accurately compared to SEM, especially at higher step change amplitude, $\Delta T_{st} > 4.1$ °C.

Comparison of the sensible effectiveness obtained through SEM and DEM showed that at Re < 209, heat loss reduced the effectiveness less than 0.4% whereas 9% difference was seen in the sensible effectiveness at Re = 608. An empirical correlation was developed to correlate the sensible effectiveness with capacity rate ratio. More than 40% uncertainty was found in correlation parameters when SEM results were used; whereas the uncertainty in parameters reduced to less than 17% for DEM results. Comparison showed a good agreement between effectiveness calculated through the DEM correlation and the results obtained through correlation in the literature while heat capacity rate ratio is higher than 0.5. Moreover, if the heat capacity rate ratio is higher than 10, both the DEM and SEM result in the same effectiveness with less than 2% uncertainty bounds. The outcome of this research showed that the transient single step test can be used to determine the sensible effectiveness of parallel-plate exchanger accurately at a certain range of operating conditions.

CHAPTER 4

TRANSIENT TESTING OF ENERGY WHEELS

4.1 Overview

This chapter completes the first objective of the thesis, "to develop a novel testing facility for performing the transient testing on *energy wheel* components*",* by modifying the transient test facility (presented in chapter 2) to measure the latent energy transfer in energy wheel components. The humidifying/dehumidifying systems, humidity sensors calibrations, detailed uncertainty analysis, and the procedure for coating a small-scale parallel-plate exchanger are presented in this chapter. The physical and sorption properties of desiccants are also obtained and used to calculate the full-scale energy wheel latent effectiveness using a correlation in the literature. The correlated latent effectiveness is used to verify the latent effectiveness obtained from the transient testing. With the results presented in this chapter, the third objective is also fully addressed which is "to predict the full-scale *energy wheel* effectiveness with its uncertainty and to investigate the relationship between the latent effectiveness and operating conditions".

To fulfill the objectives addressed in this chapter, a Ph.D. student (Mr. M. Rafati Nasr) assisted the author of this Ph.D. thesis (Farhad Fathieh) with uncertainty analysis and performing cyclic tests. In addition, the desiccant preparation for water sorption isotherm measurements was done with the help of Dr. S. Sadeh and Dr. J. Müller from the Department of Chemistry, University of Saskatchewan. Except for these parts, all the experiments, data acquisition, and data analysis were conducted by Farhad Fathieh, the lead author of the paper. Farhad Fathieh wrote the manuscript, integrated comments from the co-authors, and submitted it for review for publication to the International Journal of Heat and Mass Transfer in February 2016.

Determination of Air-to-Air Energy Wheel Latent Effectiveness in Using Humidity Step Test Data

Farhad Fathieh, Mohamad Rafati Nasr, Saied Sadeh, Robert W. Besant, Richard W. Evitts, Jens Müller, Carey J. Simonson

4.2 Abstract

Desiccant wheels are capable of recovering a considerable amount of the moisture difference between two air streams. This chapter is aimed at determining the latent effectiveness of a rotary desiccant wheel through small-scale, transient testing. A coating of mesoporous silica gel particles (55 μm particle size- pore width 77.5 Å) was deposited on an aluminum substrate. The physical properties (particle size, pore width, surface area, and surface functional groups) of the silica gel were characterized and its sorption properties were investigated by nitrogen gas adsorption at 77 K. In addition, the equilibrium condition and the kinetics of water vapor sorption on the silica gel sample were studied at 23 °C. A test facility was developed to obtain the exchanger transient response during the dehumidification process and the data was used to determine the latent effectiveness of a regenerator constructed with the silica gel coated aluminum. Moreover, the latent effectiveness was determined using a cyclic test with both dehumidification and regeneration cycles. Good agreement was observed between the latent effectiveness values obtained through the single dehumidification and cyclic tests. A correlation from the literature was used to calculate the latent effectiveness of the silica gel coated regenerator. Comparison between the latent effectiveness determined by transient test data and the correlation showed good agreement when $NTU_m < 4.3$ and $\omega > 4$ rpm.

4.3 Introduction

During the past decades, extensive research has been carried out to model heat and mass transfer in rotary wheels (Golubovic et al., 2006; Nia et al., 2006; Nóbrega & Brum, 2009; Simonson & Besant, 1998; Sphaier & Worek, 2004; Wu et al., 2006; Zhang & Niu, 2002; Zhang et al., 2003). It has been found that the sorption properties of desiccant material have a large influence on the performance of wheels. In these studies, it was assumed that the driving force for moisture transfer was proportional to the gradient of water vapor partial pressure (relative humidity) in the air stream and the moist air in the vicinity of the adsorbent surface. The relative humidity at the desiccant surface was determined using the equilibrium sorption isotherm. However, during transient sorption processes in wheels, the moisture content in the desiccant may be different than its equilibrium sorption capacity as the sorption kinetics are reduced by water vapor in-pore diffusion and access to the internal sorption sites. In fact, the gas diffusion coefficient in microporous and mesoporous desiccants is significantly lower when the average pore width is reduced (Satoh et al., 1995). Another challenge in this research is that the heat of sorption calculation depends on surface functional groups of adsorbent material. A few correlations have been developed based on numerically simulated data that relate the performance of the wheels to the matrix thermal and physical properties, moisture diffusivity, desiccant sorption isotherms, and heat of sorption at different operating conditions (Jeong & Mumma, 2005; Simonson & Besant, 1999; Simonson & Besant, 1999). Due to these reasons, the proposed correlations in the literature are only valid for certain types of desiccant and specific ranges of operating conditions.

Over the past few years, numerous studies have been conducted to determine the latent (moisture recovery) effectiveness through transient single step testing of rotary wheels (Abe et al., 2006a, 2006b; Shang & Besant, 2009a, 2008). During the transient single step testing, a stationary wheel is subjected to a step change in the inlet humidity and the response of the wheel is monitored

by measuring the humidity at the outlet. It has been found that the wheel response to step changes in the inlet humidity can be modeled by a first order linear system. An analytical relation has been developed to relate the latent effectiveness to the response time constant of the wheel. Good agreement was seen between the latent effectiveness values obtained through transient testing (Abe et al., 2006a, 2006b) and ANSI/ASHRAE standard testing method 84 (2013). Most recently, Fathieh et al. (Fathieh et al., 2015) performed the transient single step test on a small-scale heat exchanger to predict the sensible (heat recovery) effectiveness of the full-scale heat wheel with the same matrix materials and physical properties. To account for heat loss/gain during the transient testing, they considered a second mode and extended the analytical relation for latent effectiveness calculations (Fathieh et al., 2016a). It was verified that the sensible effectiveness values predicted by the transient testing of small-scale exchanger were consistent with data in the literature.

In this chapter, the transient single step testing was applied to a desiccant coated small-scale energy exchanger to predict the full-scale wheel effectiveness with identical coating and channel geometry. A novel coating method was used to deposit mesoporous micron-size silica gel particles on the metallic substrate of an exchanger. Several tests were performed to determine the physical and sorption properties of silica gel. Moreover, the experimental facility (introduced in chapter 2) was modified to perform transient testing on the small-scale exchanger. The transient humidity measurements were corrected to account for the transient characteristics of the sensors and the latent effectiveness was predicted based on the wheel response. The second order linear model proposed for heat wheels (presented section 3.4) was applied to the energy exchanger to calculate the latent effectiveness. In addition to single step dehumidification and regeneration tests, the latent effectiveness values were obtained through several repeated cycles of dehumidification and regeneration steps (cyclic test) and the results were compared to the single step test. A

correlation in the literature (C.J. Simonson & Besant, 1999) was used to determine the latent effectiveness and the values obtained through the transient testing and the correlation were compared.

4.4 Theory

4.4.1 Transient Double Exponential Model (DEM)

Similar to heat wheels, the latent effectiveness of counter-flow energy exchangers for the balanced supply and exhaust air flow can be determined by (Shah & Sekuli, 2003):

$$\varepsilon_{\mathrm{L}} = \frac{NTU_{\mathrm{m}}}{1 + NTU_{\mathrm{m}}} \tag{4.1}$$

in which

$$NTU_{\mathrm{m}} = (h_{\mathrm{m}} A_{\mathrm{m}})/\dot{m}_{\mathrm{a}} \tag{4.2}$$

In Eq. (4.2), h_{m} is the convective mass transfer coefficient, A_{m} is the total area for mass transfer, and $\dot{m}_{\mathrm{a}}$ is air mass flow rate. In fact, determination of h_{m} is a practical challenge in wheels with coated channels. Since different mechanisms are responsible for heat and mass transfer in coated channels of rotary wheels, the heat and mass transfer analogy may not be applicable to find h_{m}. Furthermore, the coating pattern, maldistribution in hydraulic diameter of airflow channels, and entrance effects alter h_{m} and, consequently, NTU_{m} (Shang & Besant, 2005).

Fathieh et al. (2016a) showed that the heat wheel time constants and weighting factors can be determined by fitting the double exponential model (DEM) to the transient thermal response of the wheel. Similarly, the DEM can be used to express the humidity response of the energy wheel during the single step change in the inlet humidity. Thus, the humidity response of an energy wheel can be determined as follows:

$$W(t) = \begin{cases} 1 - \gamma_1 e^{-t/\tau_1} - \gamma_2 e^{-t/\tau_2}, & 0 \le t \le \infty \qquad step\ increase\ (dehumidification) \\ \gamma_1 e^{-t/\tau_1} + \gamma_2 e^{-t/\tau_2}, & 0 \le t \le \infty \qquad step\ decrease\ (regeneration) \end{cases} \tag{4.3}$$

where *W(t)* is the normalized humidity is:

$$W(t) = \frac{w_{out} - w_{init}}{w_{final} - w_{init}} \tag{4.4}$$

And $w = (kg_{\text{water vapor}})/(kg_{\text{air}})$ is the air humidity ratio.

In Eq. (4.3) τ is the time constant for wheel response to the step change in inlet humidity. Two time constants for wheel response are attributed to a fast mass transfer mode (for sorption on external surfaces and macro pores) followed by a slow mode (for sorption on micropore and mesopore sorption sites with large diffusion barriers). As for heat wheels, the mass transfer weighting factors (γ) satisfy the following equation:

$$\gamma_1 + \gamma_2 = 1 \tag{4.5}$$

Following the analogy presented for the heat wheels in section 2.4, NTU_{m} of an energy wheel can be expressed by:

$$NTU_{\text{m}} = -\frac{1}{2}\text{Ln}\left[1 - \left(\frac{2\omega}{\pi}\right)\gamma_1\tau_1\frac{\left(1 - e^{-\pi/\omega\tau_1}\right)^2}{1 - e^{-2\pi/\omega\tau_1}} - \left(\frac{2\omega}{\pi}\right)\gamma_2\tau_2\frac{\left(1 - e^{-\pi/\omega\tau_2}\right)^2}{1 - e^{-2\pi/\omega\tau_2}}\right] \tag{4.6}$$

Since the wheel rotates continuously, the inlet humidity alters between the supply and exhaust humidity values in a periodic manner. Based on the fact that the response characteristics should be independent of the number of cycles, Abe et al. (Abe et al., 2006a, 2006b) showed that the time constants and weighting factors obtained through the transient single step test can be used to predict the NTU_{m} and latent effectiveness of rotary wheels. Therefore, monitoring the humidity changes across the wheel during the step change, its response characteristics (time constant and weighting factors) can be determined through Eq. (4.3). Then, the latent effectiveness of a full-scale exchanger with same matrix materials and geometry can be predicted by Eq. (4.1). More

detail on the governing equations, simplifying assumptions, and analytical approach is available in the literature (Abe et al., 2006a; Fathieh et al., 2016a).

4.4.2 Latent Effectiveness Calculation for the Cyclic Tests

In addition to a single step test, the performance of a parallel-flow energy exchanger was also studied during dehumidification and regeneration cycles. The procedure for performing the cyclic experiment is provided in section 3.3.2. In addition, the uncertainty analysis is the same as section 3.3.2 (Appendix A). The latent effectiveness for the parallel-flow exchanger can be calculated as the ratio of the amount of moisture recovered in a half of the nth cycle (w_{out} - w_{init}) to the maximum possible moisture transfer between the dry and humid air streams (w_{humid} - w_{dry}) within the same period. With the known inlet and outlet humidity profiles, the effectiveness can be calculated by (Fathieh et al., 2015)

$$\varepsilon_{PF} = \begin{cases} \frac{\omega}{\pi} \int_{n}^{n+\frac{T}{2}} (1-W)dt & dehumidification \\ \frac{\omega}{\pi} \int_{n+\frac{T}{2}}^{n+T} W dt & regeneration \end{cases} \quad (4.7)$$

With the effectiveness of parallel-flow exchanger obtained from Eq. (4.7), NTU_m was determined by (R. K. Shah and D. P. Sekuli, 2003):

$$NTU_m = -\frac{1}{2}\mathrm{Ln}(1-2\varepsilon_{PF}) \quad (4.8)$$

It should be noted that the cyclic tests were performed on the parallel-flow exchanger whereas the rotary wheels operate under counter-flow conditions. However, since the NTU_m is independent of flow arrangement, Eq. (4.1) can still be applied to determine the latent effectiveness of the same energy exchanger with counter-flow arrangement. Therefore, finding the NTU_m from Eq. (4.8), the latent effectiveness of counter-flow exchanger can be calculated from Eq. (4.1).

4.5 Experimental

4.5.1 Materials and Characterization Methods

Silica gel is an amorphous form of silicon dioxide that is widely used as a solid desiccant for use in dehumidification processes. The Si-O-Si and Si-OH functional groups at the surface of silica gel adsorb water molecules by dispersion forces and polar forces (Ng et al., 2001). The highly porous structure of silica gel gives it a specific surface area of 400-700 m^2/g. With such a high specific surface area and a polar surface, silica gel exhibits an excellent adsorption capacity towards water vapor (0.05-0.30 $g_{water\ vapor}/g_{silica\ gel}$ at RH = 50%) (Li et al., 2007). In this chapter, mesoporous silica gel particles (Sigma- Aldrich, mesh 230-400) were used to coat the small-scale exchanger surface. To specify the surface functional groups of the silica gel, Fourier Transform infrared (FTIR) spectra were obtained via a BIO-RAD FTS-40 spectrophotometer (operating in diffuse reflectance mode). Multiple scans were obtained with a 4 cm^{-1} resolution and corrected against spectroscopic grade potassium bromide (KBr) background as the sample matrix over the spectral range of 400–4000 cm^{-1}.

A Mastersizer S Long Bench Particle Size Analyzer (PSA) (Malvern Instruments), was used to measure the silica gel particle size within a range of 0.05-880 μm. The particle diameter was obtained by collecting the scattering pattern from 15,000 particles passing through a laser beam. A range lens (300 RF) focused the scattered laser light onto the array of photo-diode detectors and the collected data was analyzed to determine the particle size. To determine the surface area and pore width distribution of silica gel, nitrogen gas adsorption tests were performed by using a Micromeritics ASAP 2020 (Norcross, GA). The surface area was obtained from the adsorption isotherms (Copeland et al, 2009) and the de Boer *t*-plot method was used to calculate the micropore surface area (Broekhoff, 1968).

Water vapor sorption isotherm on the silica gel was obtained by measuring mass of a 2 mg dry sample before and after moisture uptake at different relative humidity values. The silica gel was dried in a 1000 mL Schlenk flask equipped with a grease-less (CHEM-VAC^{TM}; bore size 0-8 mm) and solid cap with a PTFE-coated silicon seal (GL 45). The Schlenk flask was connected to a solvent trap (cooled with liquid nitrogen), which was connected to a vacuum Schlenk line, and is shown in Figure 4.1. The flask was slowly evacuated to avoid the silica gel fine powder being drawn into the vacuum pump. Using a heating mantle and a temperature controller, the evacuated flask was slowly heated to 300 ºC and then kept at this temperature for 24 h. Temperatures were measured with a flexible T-type thermocouple that was located between the heating mantle and the Schlenk flask. The pressure fluctuations of the vacuum line during the heating period indicate that significant amounts of volatile species vaporized. However, after 24 h at 300 °C high vacuum had been reached ($p \sim 10^{-2}$ Torr). The flask was filled with nitrogen, cooled to room temperature, and then transferred to a nitrogen-filled MBRAUN glovebox. Afterwards, 2 mg of dry silica gel were transferred to the 8 mL PTFE-coated silicon sealed chromatography vials inside the glovebox and their masses determined by an AB204-S Mettle Toledo balance. The vials were put inside a 20 mL bottle and then transferred to the saturated aqueous salt solution jars. According to the tabulated results in the literature (Greenspan et al., 1977), the equilibrium vapor pressure (relative humidity) has different values at the liquid-air interface of hygroscopic salt solutions. In this study, 12 hygroscopic salts were dissolved in de-ionized water inside a 50 mL sealed jar to cover the range of humidity values as listed in Table 4.1. A magnetic stirrer with a plate temperature of 25 °C was used for 24 h to achieve a homogenously saturated salt solution. A relative humidity of 100% was created by adding pure de-ionized water into the sealed jar. Figure 4.1(b) shows a picture of the sealed jar with the vials and the salt solution. The sealed salt solution jars with silica

gel samples remained within an environmental chamber with T = 23.0 ± 1.0 °C and RH = 45 ± 5%. The samples were kept inside the jars for 72 h since changes in mass of the samples were observed to be within the uncertainty bounds of the experiments after this period. The adsorption isotherm was obtained by measuring silica gel mass before and after the water uptake by using an analytical balance (Ohaus, Adventure^{TM} Balance, precision ±0.1 mg with 210 g full scale).

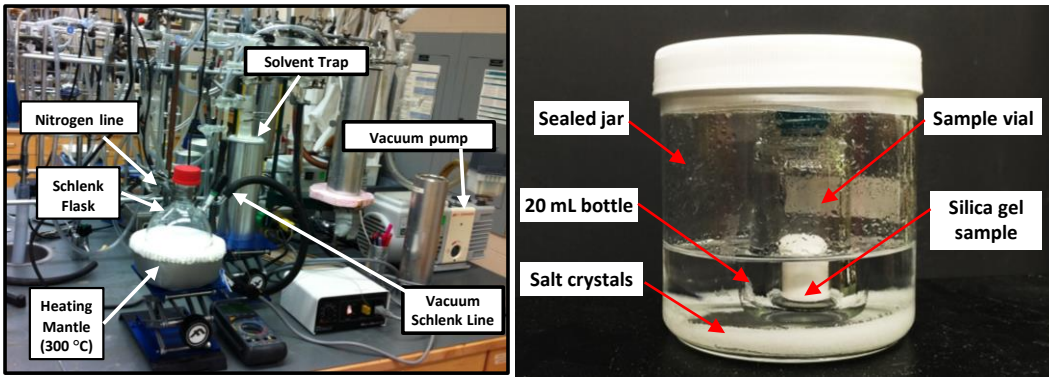

(a) **(b)**

Figure 4.1-The pictures of a) Schlenk line and b) sealed jar used to dry the silica gel

Table 4.1-Equilibrium relative humidity of saturated aqueous salt solutions (Greenspans et al., 1977)

Salt	LiBr	LiCl	$KC_2H_3O_2$	MgCl	KCO_3	$Mg(NO_3)_2$	NaBr	$CoCl_2$	NaCl	KCl	KNO_3	K_2SO_4	H_2O
RH (%)	6.37	11.30	22.51	32.78	43.16	52.89	57.57	64.92	75.29	84.34	93.58	97.30	100

4.5.2 Small-Scale Energy Exchanger

A schematic of the small-scale exchanger is shown in Figure 4.2. The small exchanger was a parallel-plate energy exchanger comprised of sixteen coated aluminum sheets held in parallel with a uniform spacing by means of a plastic frame. The exchanger had 15 flow channels, each 4 mm in height and 80 mm in width and a hydraulic diameter of 7.2 mm. The physical properties of the sheets are given in Table 2.1. The 0.62 mm thick sheet was considerably thicker than the thin metallic/plastic foil (~0.025 mm thick) substrate often used in industrial wheels. The thicker sheet avoided any maldistribution in the flow channel and provide a rigid and smooth coating surface.

The aluminum sheets were coated with silica gel particles on both sides. In conventional industrial coating methods, the particles are bonded to the surface of the substrate by means of a liquid bonding agent. This results in a multilayer desiccant coating in which a considerable number of particles are submerged into the bonding agent (Abe et al., 2006a). Consequently, a large fraction of sorption sites are inaccessible and interactions between the bonding agent and water vapor are more significant. Due to the aforementioned issue in industrial coatings, a powder coating method was used to create a monolayer desiccant coating with reduced interaction between water vapor and the bonding agent. A schematic of the coated surface with the substrate, bonding agent, and particles is shown in Figure 4.2. In the powder coating method, a 3M^{TM} Super 77 aerosol adhesive was uniformly sprayed on the surface of aluminum sheets which were cleaned inside an ultrasonic deionized-water bath for 5 minutes. Next, an annealed aluminum foil tape (3M^{TM} 3381-1.4 mil, 0.035 mm) backing with acrylic adhesive was attached to the sheet surface from the non-adhesive side of the tape. The aluminum foil tape created a durable barrier against moisture transfer over a wide range of temperature and humidity (-23 to 49 °C and 0 to 95% RH). Afterwards, a pneumatic gravity-fed spray gun (Mastercraft 058-9312-8 model) was used to spray the silica gel particles on the acrylic adhesive surface of the tape. During this process, the air back pressure was adjusted to 40 psi to force the particles to inject through ten air jet nozzles (1.4 mm diameter) towards the target surface located 30 cm away. Finally, a pressurized air jet was used to remove loose silica gel from the surface. Images of the coated surface were obtained using Hitachi FEG-SEM SU6600 scanning electron microscope (SEM).

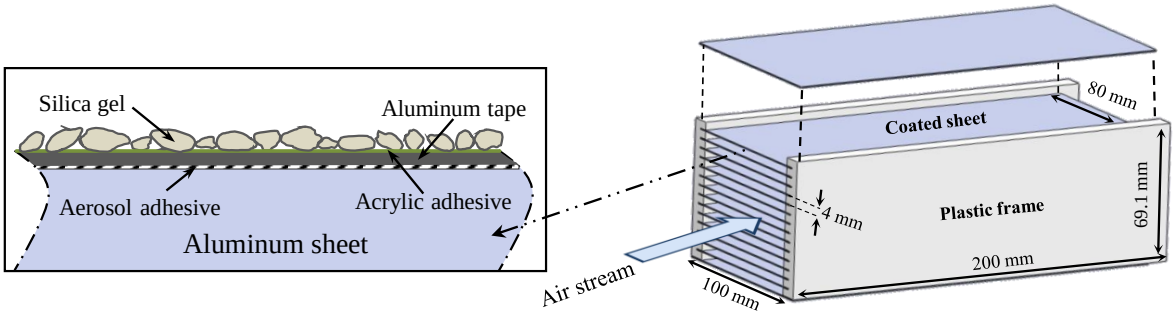

Figure 4.2-A schematic of a) coated exchanger and b) coated substrate front view

4.5.3 Test Apparatus and Experimental Procedures

A transient test facility was developed to subject the stationary coated energy exchangers to a sudden change in the inlet humidity. A schematic of the transient test setup is shown in Figure 4.3. The small-scale coated exchanger was placed into a test section made of extruded polystyrene insulation that prevented heat and mass transfer from the exchanger to the external surroundings. Air was provided by a reciprocating compressor (ITW Devilbiss 120 gal, 454 L) and then stored in pressurized tank (1800 L) to mitigate flow disturbances. The airstreams at fixed temperature and flow rate but different humidity values flowed through duct I (humid airstream) and duct II (dry airstream). These ducts were movable by sliding over a PVC plate located on the top of the test section. The air flow rates were controlled by a mass flow controller (MKS-Type 1559A) and the temperatures were adjusted by using electrical heaters. A 10 L bubble humidifier tank was used to humidify the airflow in duct I and the airflow in duct II was dehumidified (RH < 5%) by an industrial dehumidifier (ITW Devilbiss PRO dry).

Temperature measurements were carried out using T-type thermocouples located at the exchanger inlet and outlet with a sampling rate of 1 s. High accuracy humidity sensors (Honeywell type HIH-4021) were placed upstream and downstream of the exchanger. The experimental measurements were taken by a PC-based National Data Acquisition system (Type DAQ-9174).

The test data were monitored and recorded by a 2011 Lab View software with 1 s sampling rate. A detailed description of the testing apparatus, calibrations procedure, data acquisition, and uncertainty analysis is provided elsewhere (Fathieh et al., 2015).

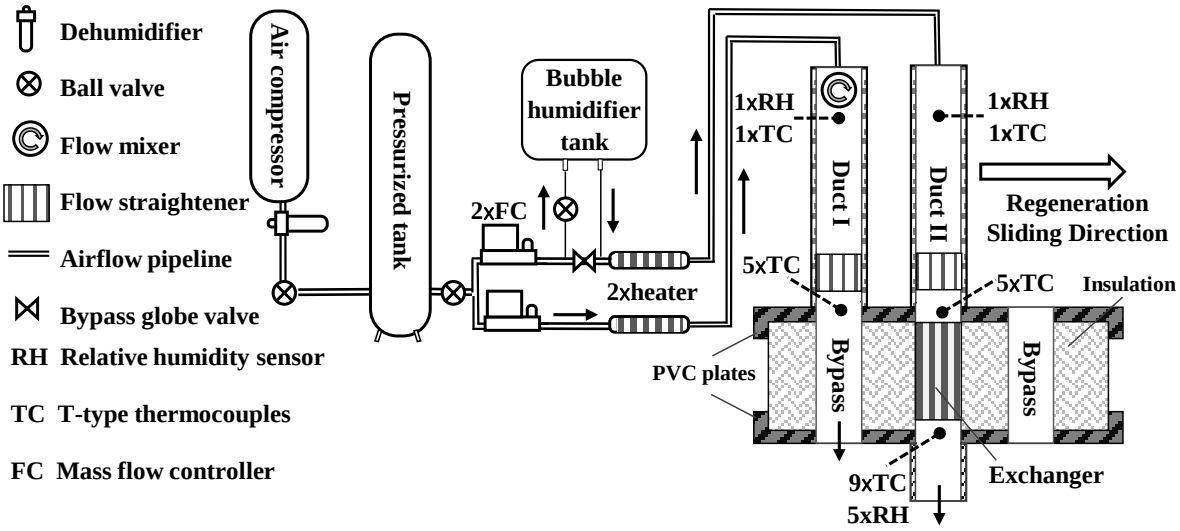

Figure 4.3-Schematic of the test facility with the airflow lines, the measurement instrumentation, and the test section

4.5.4 Single Step Test Procedure and Operating Conditions

The test conditions and flow rates for single step experiments are listed in Table 4.2. The following stepwise procedure was followed to perform the transient single step test:

1. *Pre-conditioning*: The air streams with specified temperature and humidity were passed through the ducts for at least one hour before the step change to achieve steady-state conditions in the facility. Steady-state conditions were defined as when the temperature and humidity variations remained within the sensor uncertainty for a period of 30 minutes. For the dehumidification tests, dry air (RH < 5%) was used for exchanger pre-conditioning whereas the pre-condition of the exchanger was done by the humid air (RH = 44%) for the regeneration tests.

2. *Humidity Step change:* In this step, the inlet humidity was altered in less than one second by sliding the ducts rapidly. For the regeneration tests, after pre-conditioning the exchanger with humid airflow, the ducts were slid to the right (as shown in Figure 4.3). As a result, the dry airflow in duct ① passed through the small-scale exchanger; whereas, the humid airflow in duct ② was delivered to the environment through the bypass flow passage. The dehumidification tests were done by changing the sliding direction.
3. *Transient Measurements:* The temperature and humidity at the inlet and outlet of the test section were recorded until the outlet humidity reached the inlet humidity. These data represent the transient response of the exchanger.

Table 4.2-Air conditions and the flow rates for the transient single increase (dehumidification) and step decrease (regeneration) tests

Q_a (L/min)	V_f (m/s)	Re_{dh}	T_{air} (°C)	RH_{dry} (%)	RH_{humid} (%)	ΔRH_{st} (%)
15 ± **1**	0.050 ± 0.001	26 ± 2				
25 ± **1**	0.091 ± 0.001	43 ± 2				
50 ± **1**	0.172 ± 0.002	87 ± 2	23.0 ± 0.5	4 ± 2	44 ± 2	40 ± 2
75 ± **1**	0.264 ± 0.003	130 ± 2				
100 ± **2**	0.344 ± 0.004	174 ± 4				

4.5.5 Cyclic Test Procedure and Operating Conditions

In the cyclic test, the small-scale exchanger was exposed to a series of step changes in the inlet humidity during a cyclic test where all the other conditions were kept constant. The humidity values, flow rates, and angular speed in the cyclic tests are given in Table 4.3. The cyclic test was performed by rapidly interchanging duct ① and duct ② with specified angular speeds as given in Table 4.3. The pre-conditioning step was carried out by performing enough cycles so that the outlet humidity profile became identical for each cycle. It was observed that at $\omega > 1.5$ rpm, the humidity variations remained within the uncertainty bounds of the humidity sensors.

Table 4.3-Airflow conditions and flow rate for the cyclic tests

ω (rpm)	Q_a (L/min)	V_f (m/s)	Re_{dh}	T_{air} (°C)	RH_{dry} (%)	RH_{humid} (%)	ΔRH_{st} (%)
0.50 ± 0.01							
0.75 ± 0.01	100 ± 2	0.344 ± 0.004	174 ± 2	23.0 ± 0.5	4 ± 2	44 ± 2	40 ± 2
1.50 ± 0.02							

4.5.6 Sensor Calibration and Uncertainty Analysis

The humidity sensors were calibrated at steady-state conditions for a range of RH (10% < *RH* < 90%, with 10% *RH* increments and at T = 23 °C) by using a Thunder Scientific 1200 mini two-pressure two-temperature humidity generator with a bias uncertainty of 0.5% *RH*. The *RH* values were measured 40 times at each equilibrium state with a sampling frequency intervals of 30 s. The hysteresis effects were studied by increasing and decreasing the reference *RH* values in one loop. Linear regression was used to convert sensor voltage reads to humidity, $R^2 > 0.99$. The precision uncertainty, U_p, of the time constants and weighting factors of humidity sensors were determined using:

$$U_p = St \tag{4.9}$$

where S is the precision index that equals the square root of standard deviation of data points and t is the two-tailed student t-factor, t = 2 for 40 data points (Figliola & Beasley, 2006). Using Eq. (4.9), the maximum precision uncertainty for humidity sensors were found to be ±0.01%. The bias uncertainty, U_B, in humidity measurements at steady-state conditions is due to data reduction, U_{fit}, and the bias uncertainty in the reference humidity, U_{ref}. The bias uncertainty was calculated by:

$$U_B = \left(U_{fit}^2 + U_{ref}^2\right)^{1/2} \tag{4.10}$$

A maximum bias uncertainty of ±1.5% was determined for the relative humidity measurements. At steady-state conditions, the maximum total uncertainty in the humidity sensor was found to be less than ±1.6% from the following equation:

$$U_{\mathrm{T,steady}} = \left(U_{\mathrm{P}}^2 + U_{\mathrm{B}}^2\right)^{1/2} \tag{4.11}$$

In addition to the steady-state calibration, transient calibration was required for transient tests in which the humidity varies with time. According to the literature (Kuse & Takahashi, 2000), the transient sorption of water vapor on a tin oxide semiconductor humidity sensor may impose an uncertainty in humidity measurements during the transient testing. Wang et al. (2005) presented an empirical relation to calibrate the humidity readings and to decouple the exchanger response from humidity sensor measurements downstream of the exchanger. The same approach was used in this study for humidity sensor calibration and correcting the exchanger response. In this method, the sensor time constant and weighting factors should be characterized by fitting the double exponential model (DEM) to humidity test data when the exchanger is not in the test cell. The trust-region optimization algorithm was applied to fit the DEM to the sensors data using MATLAB R2014 (a). For each case, the data reduction uncertainty values were taken from the fitting software in the 95% of trust-region. The transient characteristics of humidity sensors were also obtained at each flow rate in Table 4.3. More details on the transient calibration method can be found in the literature (Wang et al., 2005). To study the repeatability of humidity sensor readings, the sensors were tested three times at different amplitudes of step change (ΔRH = 10, 20, 30, 40, 50%). Eq. (4.9) was used to calculate the precision uncertainty of the time constants and the weighting factors of the humidity sensors. The bias uncertainty in humidity sensor time constants and weighting factors is due to data reduction, U_{fit}, and the error in flow rate measurements uncertainties, U_Q. Thus, the bias uncertainty in τ (or γ) was calculated by:

$$U_{\mathrm{B},\tau} = \left(U_{\mathrm{fit},\tau}^2 + U_{\mathrm{Q},\tau}^2\right)^{1/2} \tag{4.12}$$

Propagation of error analysis was used to determine $U_{Q,\tau}$ for the time constant and weighting factor as follows:

$$U_{\mathrm{FR},\tau} = \frac{\partial \tau}{\partial \mathrm{Re}} U_{\mathrm{Re}} \tag{4.13}$$

where U_{Re} is the uncertainty in Reynolds number given in Table 4.3. To calculate $\partial\tau/\partial Re$, the time constant was linearly interpolated between the *Re* intervals listed in Table 4.3. The same method and set of equations were used to determine the uncertainty in sensors weighting factors. The humidity sensor transient characteristics are further discussed in section 4.2.

T-type thermocouples were calibrated within the range of 15-85 °C with 5 °C increments by a Hart Scientific dry-well calibrator (Model 9107). At each reference temperature, 40 readings with sampling rate of 5 s were taken under steady-state conditions. The measurements were taken during increasing and decreasing temperature conditions to account for hysteresis effects. The bias uncertainty was determined from Eq. (4.10) and found to be ± 0.1 °C. A maximum precision error of 0.03 °C was calculated from Eq. (4.9). Using Eq. (4.11), the maximum total uncertainty in the thermocouples was found to be less than 0.2 °C.

4.6 Results and Discussion

4.6.1 Desiccant Properties and Coating

The IR spectra of silica gel sample is given in Figure 4.4. An intense adsorption band at 1092 cm^{-1} is seen in the IR spectra, which is attributed to the stretching vibration of the Si-O bond. In addition, the adsorption band at 803 cm^{-1} corresponds to the ring structure of SiO_4, and the 464 cm^{-1} band is due to deformation vibration of Si-O-Si (Decottignies et al., 1978; Gallas et al., 1997; Gillis-D'hamers et al., 1993; Maniar et al., 1990; Almeida & Pantano, 1990; Rumph & Schubert, 1978; Wood & Rabinovich, 1989). In addition to Si-O bands, a very wide band at 3440 cm^{-1} is related to the hydroxyl groups which may participate in water vapor sorption significantly. The IR spectra illustrate that the surface of silica gel used in this study is comprised of Si-O bonds with small fraction of hydroxyl groups.

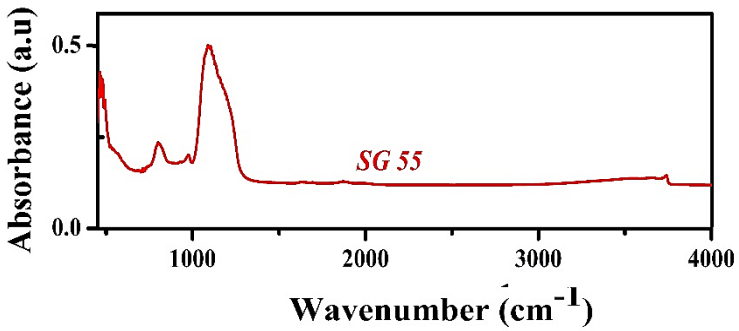

Figure 4.4-IR spectrum of silica gel (SG55-77)

The volume fraction of the samples at each the particle diameter obtained by using PSA is shown in Figure 4.5**.** The particle size measurements illustrate a narrow particle size distribution for silica gel with a mean particle diameter of 55 μm. The adsorption average pore width (P_w) and particle surface area (S_A), obtained through nitrogen gas adsorption tests are listed in Table 4.4. According to the pore size distribution (Rouquerol et al., 1994), the silica gel (P_w = 77.5 Å) is mesoporous. The high specific surface area of silica gel, 478 m^2/g, provides a large number of sorption sites for water vapor sorption.

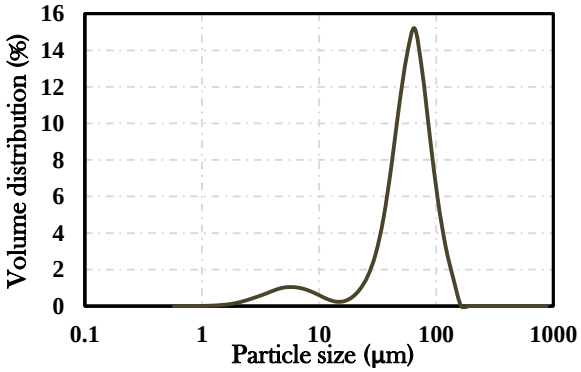

Figure 4.5-Particle size distribution of silica gel desiccant obtained from PSA

Table 4.4-Silica gel physical properties

Material	Density (m^3/kg) ρ_m	Average Particle Size (μm)	Adsorption average pore width (Å)	Available surface area (m^2/g)
Silica Gel	2730*	55	77.5	478

**Data from manufacturer*

The water vapor adsorption isotherm (at 23.0 °C) for the silica gel sample is shown in Figure 4.6. It can be seen that the sorption capacity increases almost linearly with relative humidity. The same trend was observed for mesoporous silica gel samples in the literature (Ng et al., 2001; Wang et al., 2007; Wang et al. 2004). At the maximum capacity, the silica gel can adsorb up to 0.27 (g_w/g_{SG}) at a relative humidity of 100%. However, the sorption isotherm does not provide any information about sorption kinetics and this plays a key role in moisture recovery in rotary wheels. In this regard, transient observations, such as single step testing, should be made to investigate the kinetics of sorption during the dehumidification and regeneration.

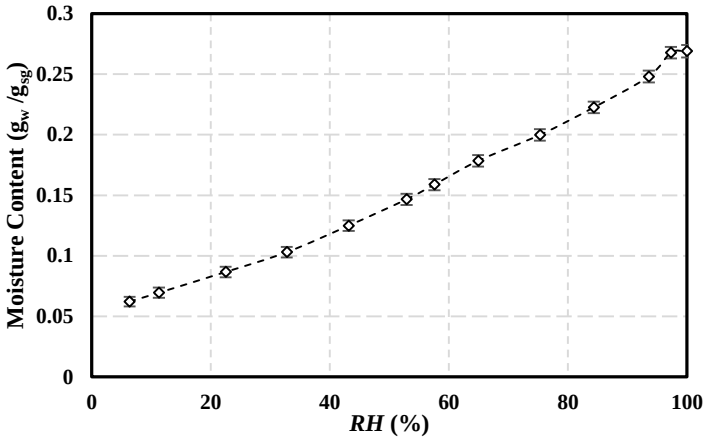

Figure 4.6-Adsorption isotherm of water vapor on the mesoporous silica gel at 23.0 °C

The SEM images of the aluminum sheets coated with silica gel particles through the powder coating method are shown in Figure 4.7. It can be seen that the silica gel particles are irregular in shape with narrow particle size distribution. Moreover, the SEM images illustrate that the powder coating method resulted in a uniform layer of coated particles in which the desiccant particles are not fully submerged into an acrylic bonding agent. In fact, SEM images from industrial coating in the literature showed a multilayer coating with desiccant particles submerged into the liquid binder (Shang, 2009c). The enhanced coating improves, both on a per unit mass of

particles and surface coverage, the amount of water adsorbed. The amount of silica gel coated on the exchanger is given in Table 4.5. It was found that the desiccant mass per unit area for the small-scale exchanger is 1.94 mg/cm^2, whereas, industrial wheels have a surface coverage of 0.8-1.6 mg/cm^2 (Jeong & Mumma, 2005). Thus, the powder coating technique can be used to effectively deposit silica gel on the surface of exchanger. Since a portion of substrate surface was not covered with silica gel particles, the water vapor molecules may also interact with polar groups in the acrylic resin. However, when testing the substrate covered with only the acrylic bonding agent, Fathieh et al. (2016b) showed that the bonding agent has insignificant effects on the moisture transfer during the dehumidification and regeneration processes.

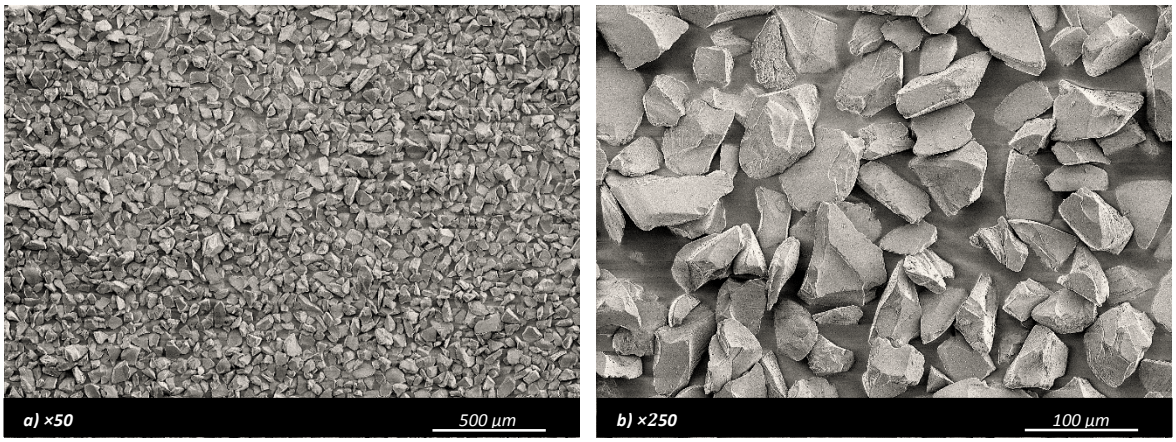

Figure 4.7-SEM images of aluminum substrate coated with silica gel particles through powder coating at two levels of magnification

Table 4.5-Amount of silica gel coated on the small-scale exchangers through powder coating

Sample	Total mass coated (g)	Mass coated per unit area (mg/cm²)	Mass of desiccant to mass of the matrix (%)
SG55	9.32 ± 0.02	1.941 ± 0.004	1.9

4.7 Transient Response of Humidity Sensors

Figure 4.8 depicts the normalized response of the humidity sensor alone (W) versus time during the single step increase and decrease of ΔRH = 40% and with Re = 87. The step change in

the humidity was made after pre-conditioning of the test section and humidity readings were carried out with sampling frequency interval of 2.5 s. For each case, the trust-region optimization algorithm was used to fit the double exponential model, Eq. (4.3), to the humidity data using MATLAB R2014 (a). From the results shown in Figure 4.8, it can be seen that the sensor has a fast response, with response time 15 s and 16 s (based on 90% of the output) for the increase and decrease step changes, respectively. The repeatability of the experiment was found by performing the test three times at different amplitudes of step change and the time constants, weighting factors, and coefficient of determination (R^2) are given in Table 4.6 and Table 4.7. The precision uncertainty of the humidity sensors was calculated using Eq. (4.9) where the two-tailed student t-factor has the value of 2.131 for 15 data points (based on 95% of uncertainty bounds) (Figliola & Beasley, 2006). The average values for the fitting parameters with their precision uncertainty are given in Table 4.6 and Table 4.7. An R^2 value of greater than 0.99 indicates that the DEM can precisely describe the transient characteristics of the sensors by considering two modes for mass transfer. The first mode (with smaller time constant and larger weighting factor) is the dominant process and it can be attributed to the water vapor diffusion from the air to the sensor surface. The second mode ($\tau_2 > 10\tau_1$ and $\gamma_2 < 0.1\gamma_1$) seems to be less important and probably is a consequence of the slow diffusion of water molecules into/out of the sensor material. Based on the results presented in Table 4.6 and Table 4.7, the time constant and weighting factors do not change significantly as the amplitude of humidity step change increases from 10 to 50 %.

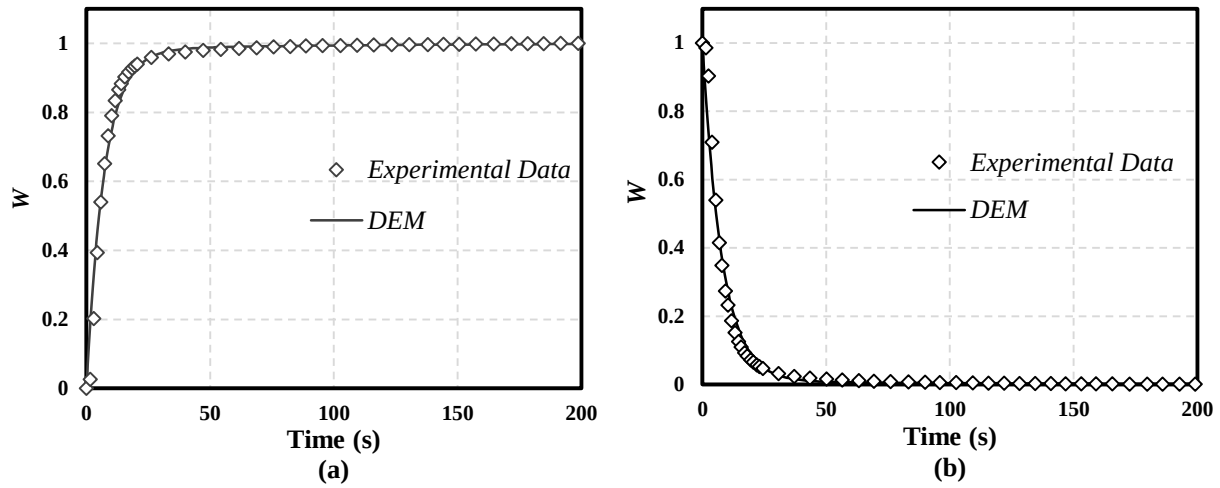

Figure 4.8-Normalized response of *RH* sensors to the step change in the humidity and fitted curve obtained through DEM for a) step increase and b) step decrease (ΔRH= 40%, and Re_{dh} = 87, maximum uncertainty in the experimental data is U_W = ±0.05)

Table 4.6-The average RH sensor response time constants and weighting factors obtained through three tests at each amplitude of step increase in the inlet humidity (Re_{dh} = 87 and T_{air} = 23 °C)

Number of tests	ΔRH_{step}	$\gamma_{1,s}$	$\tau_{1,s}$ (s)	$\gamma_{2,s}$	$\tau_{2,s}$ (s)	R^2
3	50 ± 1%	0.94	6.0	0.06	72.5	0.9923
3	40 ± 1%	0.96	6.4	0.04	77.6	0.9904
3	33 ± 1%	0.96	6.7	0.04	102	0.9889
3	20 ± 1%	0.95	6.6	0.05	124	0.9911
3	10 ± 1%	0.96	6.3	0.04	68.1	0.9951
15	**Average**	**0.95**	**6.4**	**0.05**	**88.8**	**0.9916**
	Precision	**±0.01**	**±0.3**	**±0.01**	**±21.4**	-

Table 4.7-The average *RH* sensor response time constants and weighting factors obtained through three tests at each amplitude of step decrease in the inlet humidity (Re_{dh} = 87 and T_{air} = 23 °C)

Number of tests	ΔRH_{st}	$\gamma_{1,s}$	$\tau_{1,s}$ (s)	$\gamma_{2,s}$	$\tau_{2,s}$ (s)	R^2
3	50 ± 1%	0.97	6.9	0.03	84.3	0.9926
3	40 ± 1%	0.98	7.2	0.02	104.8	0.9879
3	33 ± 1%	0.97	6.6	0.03	69.9	0.9960
3	20 ± 1%	0.97	7.5	0.03	70.3	0.9852
3	10 ± 1%	0.98	7.4	0.02	75.3	0.9918
15	**Average**	**0.97**	**7.1**	**0.02**	**80.9**	**0.9907**
	Precision	**±0.01**	**±0.5**	**±0.01**	**±13.4**	-

The transient characteristics of the humidity sensors were also obtained at different flow rates by fitting the DEM to humidity test data. The fitting parameters with their total uncertainty are given in Table 4.8 and Table 4.9. It can be seen that the time constants decrease as the Reynolds number increases, whereas, there is only slight change in weighting factors. With higher R^2 values, the fitting quality is better at higher Reynolds numbers. The total uncertainty (U_T) in the fitting parameters were calculated by Eq. (4.11). The data reduction uncertainty was obtained by the fitting software based on the 95% confidence interval and the values and the bias uncertainty were calculated by Eq. (4.12). Table A.1 and Table A.2 list the U_{fit}, U_{Q}, and U_{B} for sensor time constants and weighting factors. The total uncertainty in the time constant and weighting factors were determined by using Eq. (4.11), where the values are given in Table 4.8 and Table 4.9. In the uncertainty calculation, the precision of the sensors was assumed to be constant within the range of tested flow rates.

Table 4.8-*RH* sensor response to a step increase in the inlet humidity at different flow rates

Re	$\gamma_{1,s}$	$\tau_{1,s}$ (s)	$\gamma_{2,s}$	$\tau_{2,s}$ (s)	R^2
26	0.95 ± 0.01	9.9 ± 0.7	0.05 ± 0.01	146.5 ± 56.1	0.9766
43	0.95 ± 0.01	8.4 ± 0.6	0.05 ± 0.01	105.3 ± 54.5	0.9827
87	0.96 ± 0.01	6.4 ± 0.4	0.04 ± 0.01	77.6 ± 35.5	0.9904
130	0.95 ± 0.01	6.0 ± 0.4	0.05 ± 0.01	41.7 ± 12.6	0.9954
174	0.92 ± 0.02	6.0 ± 0.4	0.08 ± 0.02	53.4 ± 13.4	0.9948

Table 4.9-*RH* sensor response to a step decrease in the inlet humidity at different flow rates

Re	$\gamma_{1,s}$	$\tau_{1,s}$ (s)	$\gamma_{2,s}$	$\tau_{2,s}$ (s)	R^2
26	0.98 ± 0.01	9.9 ± 0.8	0.02 ± 0.01	300.0 ± 98.7	0.9796
43	0.98 ± 0.01	9.1 ± 0.7	0.02 ± 0.01	186.9 ± 66.1	0.9840
87	0.98 ± 0.01	7.2 ± 0.6	0.02 ± 0.01	104.8 ± 43.5	0.9876
130	0.95 ± 0.01	6.6 ± 0.6	0.05 ± 0.02	58.6 ± 20.4	0.9982
174	0.97 ± 0.01	7.0 ± 0.6	0.03 ± 0.01	75.4 ± 20.4	0.9940

4.8 Transient Response of the Exchanger plus Humidity Sensor

Transient single humidity step tests were performed on the small-scale energy exchanger for ΔRH = 40% and at T = 23.0 °C for various flow rates given in Table 4.2. The normalized humidity response of the small-scale exchanger for dehumidification and regeneration for several Reynolds numbers is plotted in Figure 4.9. It can be seen that as the Reynolds number increases, the outlet humidity reaches equilibrium faster. For Reynolds numbers greater than 130, only slight changes in the transient humidity profiles were observed for both dehumidification and regeneration. Figure 4.8 and Figure 4.9 show that the response time (based on 90% of ΔW) increases when the energy exchanger is placed in the test section. For instance, for dehumidification test at Re = 87, the response time of exchanger plus sensor is 94 s; whereas, the sensor response time is 15 s. This is an indication of water vapor sorption on the silica gel coated surface of the exchanger that delays the increase in outlet humidity during the transient period.

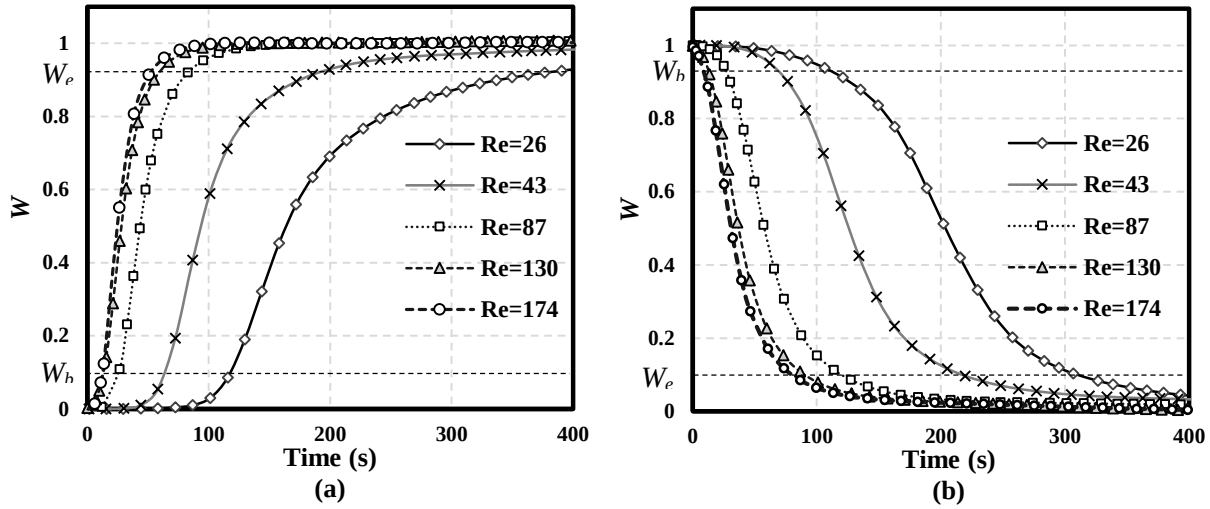

Figure 4.9-Normalized response of small-scale energy exchanger plus *RH* sensors to the step change in the inlet humidity during a) dehumidification and b) regeneration (ΔRH = 40%, and T_{air} = 23.0 °C, maximum uncertainty in the experimental data is U_W = ±0.05)

The exchanger plus sensor response was quantified by fitting the DEM to the normalized humidity profiles. Figure 4.9 (which is a breakthrough curve) shows that the humidity of the air at the outlet gradually changes to reach the humidity at the inlet. During dehumidification, as water vapor molecules are adsorbed on the sorption sites, the difference of water vapor concentration between the air flow and adsorbent surface is reduced and, consequently the driving force for mass transfer decreases. Thus the breakthrough curve for dehumidification, Figure 4.9(a), is conventionally divided into three distinct regions distinguished by breakthrough and exhaust points. The breakthrough point is the point on the breakthrough curves at which the normalized humidity is less than a specified value (W_b = 0.05-0.15) whereas at the exhaust point the normalized humidity is W_e = 0.9-0.95 (Eduardo & Nóbrega, 2014). In the primary sorption zone, $W < W_b$, a large fraction of moisture is adsorbed from the humid air stream so that the humidity at the outlet is has almost the same value as before the step change. Most practical adsorbent beds are designed to keep the humidity below the breakthrough point (Chang et al., 2005). While $W > W_e$, the moisture sorption occurs slowly, the desiccant is almost saturated, and the mass transfer driving force approaches zero. At this point, regeneration is required to remove the moisture from the desiccant. The outlet humidity raises substantially between breakthrough and exhaust points during which most of the sorption sites are occupied by adsorbate. It has been observed that in desiccant drying wheels, the temperature and/or humidity variations at the outlet are in the range of $W_b < W < W_e$ (Sphaier & Worek, 2004; Zhang & Niu, 2002). In a similar way, the breakthrough and exhaust points for regeneration were defined when the normalized humidity has the values of 0.95-0.85 and 0.05-0.1, respectively.

The breakthrough and exhaust time, t_b and t_e, of the small-scale exchanger based on W_b = 0.10 and W_e = 0.95 for dehumidification and W_b = 0.90 and W_e = 0.05 for regeneration are shown

in Figure 4.10. It can be seen that both t_b and t_e follow a similar decreasing trend with increasing Reynolds number. It can be seen that the exhaust time is one order of magnitude larger than the breakthrough time for both the dehumidification and regeneration tests. In addition, the breakthrough time for dehumidification is higher than the breakthrough time for regeneration which indicates that primary sorption process takes longer during the dehumidification process. In contrast, the exhaust time is larger for regeneration than dehumidification, except at Re = 15, which is probably due to the fact that the complete regeneration of the desiccant particles requires more time.

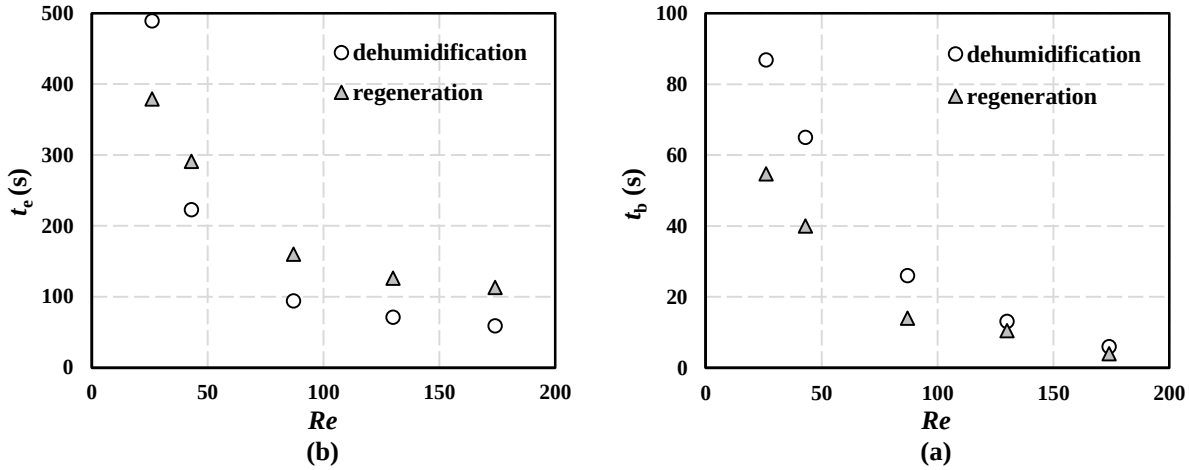

Figure 4.10-a) Breakthrough and b) exhaust time for the humidity response of the small-scale exchanger

It was found that the DEM was successful in describing the normalized humidity response between the breakthrough and exhaust point. Based on the fact that the selection of the breakthrough time is arbitrary, the starting point after which the DEM can be applied is not well-defined in this method. For this reason, the DEM was used to correlate the data by varying the starting point from 0 to 200 s and the coefficient of determination (R^2) was evaluated for each curve fit. Figure 4.11 shows the R^2 values as a function of the starting time at Re = 43. The maximum R^2 is at the starting time of 36 s. Since the primary moisture uptake zone is shorter at

higher *Re* values, the starting time at which R^2 reaches its maximum is reduced by flow rate, e.g. t_{max}= 4 s at *Re* = 174. The time constants and weighting factors were obtained using the starting time that resulted in the highest R^2.

To find the repeatability of the transient test and the precision uncertainty in the time constants and weighting factors, the transient test was performed six times at *Re* = 87. The precision of the fitting parameters for exchanger plus sensor were calculated by Eq. (4.9) with Student's *t* = 2.447. Moreover, an uncertainty in time constants and weighting factors was considered due to the uncertainty in the stating time for the curve fit. From a statistical point of view, the fitting with $R^2 > 0.99$ is considered a high quality correlation. Thus, comparing the time constant and weighting factors values obtained from R^2_{max} and $R^2_{0.99}$, the uncertainty was specified for the fitting parameters. The precision uncertainty and the averaged time constant and weighting factor values are listed in Table 4.10.

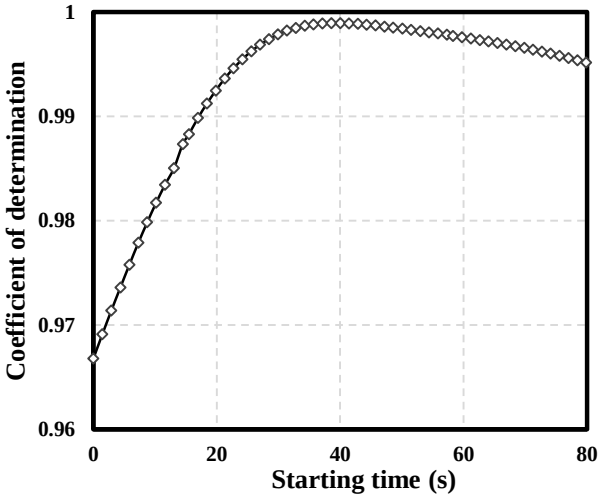

Figure 4.11-R-squared values obtained by applying DEM on the response of small-scale energy exchanger plus *RH* sensors to the step increase in the inlet humidity, (Δ*RH*= 40%, *Re* = 43, and T_{air} = 23.0 °C)

Table 4.10-Precision uncertainty in time constants and weighting factors of the exchanger plus RH sensor response to step increase in the inlet humidity (Re_{dh} = 87 and T_{air} = 23.0 °C)

Step type		$\gamma_{1,w+s}$	$\tau_{1,w+s}$ (s)	$\gamma_{2,w+s}$	$\tau_{2,w+s}$ (s)
Increase step	Average	0.99	22.3	0.01	100.1
	Precision	±0.01	±2.9	±0.01	±21.5
Decrease step	Average	0.90	29.8	0.10	234.3
	Precision	±0.01	±2.1	±0.01	±42.1

The humidity response at each Reynolds number was fitted by DEM and the fitting parameters were obtained at the highest value of R^2. The time constants, weighting factors, and R^2 for dehumidification and regeneration are given in Table 4.11 and Table 4.12. It is observed that both the time constants decrease as the Reynolds number increases. In the dehumidification process, the smaller the time constant, the faster the silica gel surface becomes saturated at the given relative pressure. Moreover, the first weighting factor increases with flow rate and the second mode diminishes at higher flow rates values. It should be noted that the first time constant is one order of magnitude larger than the first time constant of the humidity sensors, while the second time constant have similar order of magnitude values. Another observation is that the fitting parameters are different for dehumidification and regeneration so that the second mode of mass transfer is more effective in the desorption process. In Table 4.11 and Table 4.12, the total uncertainty was determined through the same analysis presented in section 3.3.1 where the precision errors were taken from Table 4.10.

Table 4.11-Exchanger plus RH sensors response to the step increase in the humidity at different flow rates (ΔRH = 40% and T_{air} = 23.0 °C)

Re_{dh}	$\gamma_{1,w+s}$	$\tau_{1,w+s}$ (s)	$\gamma_{2,w+s}$	$\tau_{2,w+s}$ (s)	R^2
26	0.85 ± 0.02	61.1 ± 6.0	0.15 ± 0.02	445.6 ± 50.2	0.9966
43	0.84 ± 0.01	33.2 ± 3.3	0.16 ± 0.01	162.5 ± 30.0	0.9989
87	0.99 ± 0.01	22.3 ± 2.1	0.01 ± 0.01	100.1 ± 21.5	0.9913
130	1.00 ± 0.00	18.1 ± 1.6	0.00 ± 0.00	-	0.9934
174	1.00 ± 0.00	12.2 ± 1.2	0.00 ± 0.00	-	0.9996

Table 4.12-Exchanger plus RH sensors response to the step decrease in the humidity at different flow rates (ΔRH = 40% and T_{air} = 23.0 °C)

Re_{dh}	$\gamma_{1,w+s}$	$\tau_{1,w+s}$ (s)	$\gamma_{2,w+s}$	$\tau_{2,w+s}$ (s)	R^2
26	0.78 ± 0.02	45.1 ± 4.8	0.22 ± 0.02	208.2 ± 45.9	0.9970
43	0.83 ± 0.01	38.6 ± 3.7	0.17 ± 0.01	285.8 ± 61.9	0.9990
87	0.90 ± 0.01	29.8 ± 2.6	0.10 ± 0.01	234.3 ± 50.9	0.9987
130	0.85 ± 0.01	23.7 ± 2.0	0.15 ± 0.01	129.8 ± 28.2	0.9993
174	0.81 ± 0.01	22.9 ± 1.9	0.19 ± 0.01	101.8 ± 22.2	0.9993

4.9 Energy Exchanger Response

The humidity sensor readings in the transient testing may affect the exchanger response and, consequently, alter the calculated time constants and weighting factors. Using the sensors transient characteristic data, found in Table 4.8 and Table 4.9, and exchanger plus sensor time constants and weighting factors, found in Table 4.11 and Table 4.12, the exchanger response was decoupled from sensor response by the method presented by Wang et al. (Wang et al., 2005). The exchanger response before and after the correction at Re = 87 is shown in Figure 4.12. It can be seen that the exchanger response is very close to the response of the exchanger plus sensor. This shows that the sensor response is much faster than the exchanger and the sensor dynamics have only a small impact on the humidity measurements. The corrected time constants and weighting factors of the exchanger are listed in Table 4.13 and Table 4.14. The same trend is seen for the fitting parameters as in Table 4.11and Table 4.12 while the values are slightly different. For instance, for dehumidification test at *Re* = 43, the first and second time constant change less than 2.5% and 0.7%, respectively, after decoupling the test data; whereas, the weighting factors are identical. The uncertainty in the exchanger time constants and weighting factors was calculated based on the highest uncertainty bounds in the response of the sensor and the exchanger plus sensor given in Table 4.8 to Table 4.12.

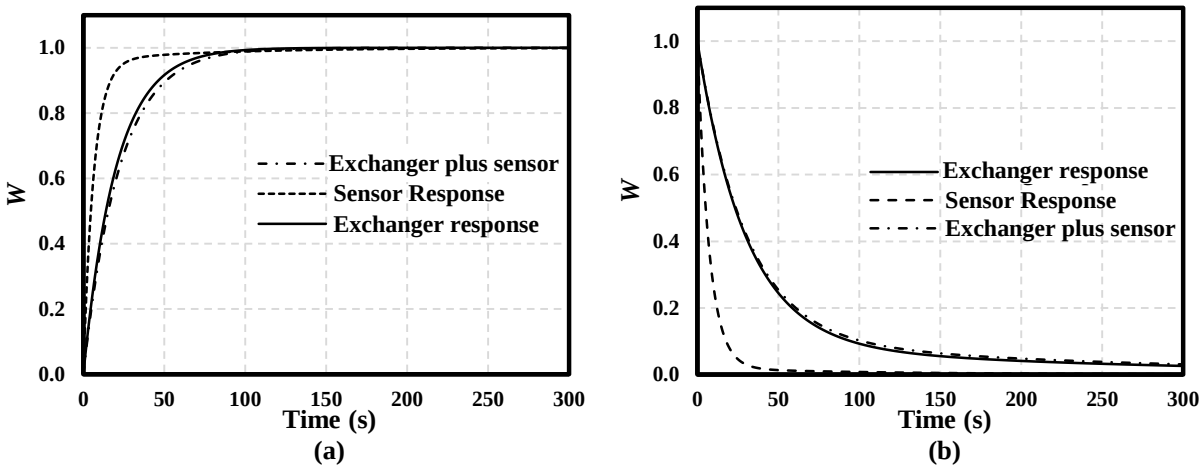

Figure 4.12-Decoupled response of the small-scale energy exchanger from humidity sensor response during a) dehumidification and b) regeneration single step test (ΔRH= 40%, Re_{dh} = 87, and T_{air} = 23.0 ºC)

Table 4.13-Exchanger response to the step increase in the inlet humidity at different flow rates

Re_{dh}	$\gamma_{1,w}$	$\tau_{1,w}$ (s)	$\gamma_{2,w}$	$\tau_{2,w}$ (s)	R^2
26	0.86 ± 0.02	60.2 ± 6.1	0.14 ± 0.02	469.3 ± 53.1	0.9998
43	0.84 ± 0.02	33.4 ± 3.4	0.16 ± 0.02	164.4 ± 30.1	0.9998
87	1.00	20.1 ± 2.2	-	-	0.9913
130	1.00	16.2 ± 1.6	-	-	0.9934
174	1.00	12.2 ± 1.3	-	-	0.9996

Table 4.14-Exchanger response to the step decrease in the inlet humidity at different flow rates

Re_{dh}	$\gamma_{1,w}$	$\tau_{1,w}$ (s)	$\gamma_{2,w}$	$\tau_{2,w}$ (s)	R^2
26	0.74 ± 0.02	45.0 ± 4.9	0.26 ± 0.02	202.8 ± 49.3	0.9997
43	0.81 ± 0.02	38.6 ± 3.8	0.19 ± 0.02	283.2 ± 62.3	0.9999
87	0.89 ± 0.01	29.7 ± 2.7	0.11 ± 0.01	237.7 ± 51.7	0.9999
130	0.84 ± 0.01	23.5 ± 2.1	0.16 ± 0.01	133.0 ± 29.1	0.9999
174	0.77 ± 0.01	22.3 ± 2.0	0.23 ± 0.01	145.1 ± 22.5	1.0000

4.10 Cyclic Test Results

The humidity profiles at *Re* = 174 and angular speeds ω = 0.5, 0.75, and 1.5 rpm for the dehumidification and regeneration cycles are shown in Figure 4.13. The humidity profiles in

Figure 4.13 were obtained when the system reached quasi-steady state. It can be seen that as the angular speed increases, the amplitudes of the humidity variations decrease, e.g. $\Delta W = 0.82$ at $\omega = 0.5$ rpm whereas $\Delta W = 0.22$ at $\omega = 1.5$ rpm. In addition, the humidity profiles show, during the cyclic operation, that the normalized humidity varies within $W_b = 0.1 < W < W_e = 0.95$. In contrast to the transient test, no primary moisture uptake takes place for $W < W_b = 0.1$. Primary moisture uptake was observed for the first few cycles when the desiccant was initially dry; however, the amount of moisture uptake diminished as the cycles were performed and the desiccant adsorbed moisture. It is suggested that only a portion of sorption sites were occupied during the primary moisture uptake and only a small fraction of adsorbent surface participates in the transient dehumidification/regeneration process. This indicates that the sorption process does not take place at the equilibrium condition as given by the sorption isotherm. Apparently, the intrapore diffusion time is long compared to the convective flow residence time and that makes a fraction of available surface area inaccessible during the cyclic sorption process.

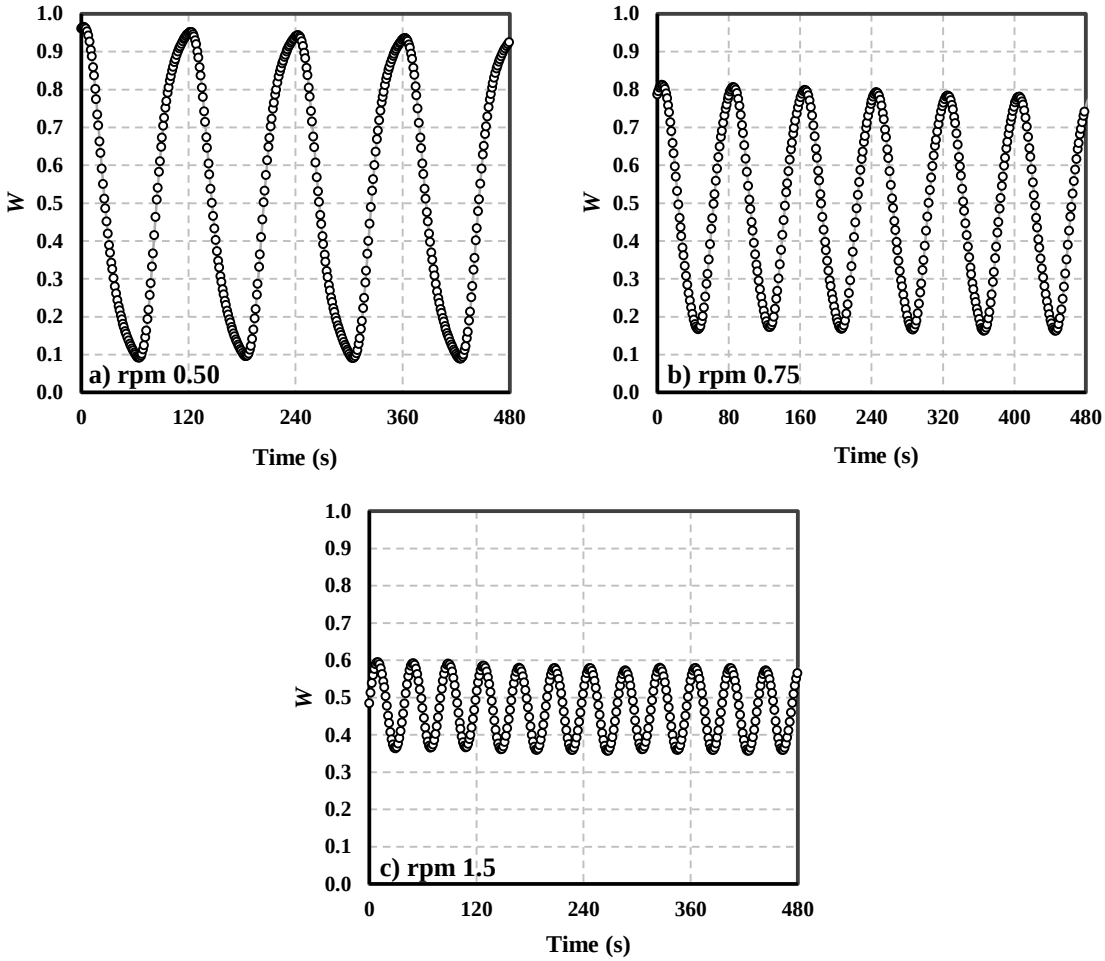

Figure 4.13-Response of the small-scale energy exchanger to the periodic step increase/decrease in the inlet humidity at different periods of excitation, (ΔRH = 40%, T_{air} = 23.0 °C, Re_{dh} = 174, maximum uncertainty in the experimental data is U_W = ±0.05)

4.11 Latent Effectiveness

The latent effectiveness of energy wheels with the same coating and channel geometry was predicted using the dehumidification and regeneration test data obtained from the transient testing of the small-scale energy exchanger. With the exchanger time constants and weighting factors given in Table 4.13 and Table 4.14 , eqs. (4.6) and (4.1) were used to find NTU_m and the latent effectiveness. The latent effectiveness at different Reynolds numbers is plotted within a conventional range of wheel angular speeds, 0.1 rpm < ω < 20 rpm, in Figure 4.14. The uncertainty bounds for latent effectiveness were calculated using the propagation of error analysis based on

the uncertainty in the exchanger time constants and weighting factors in Table 4.13 and Table 4.14. The results illustrate that as the wheel angular speed increases, the latent effectiveness increases. Furthermore, as the Reynolds number increases, latent effectiveness decreases. All these results are in agreement with the data available in the literature (Angrisani et al., 2012; Eicker et al., 2010; Enteria et al., 2012). At high angular speeds and Reynolds numbers, ω > 15 rpm and Re > 43, the effect of flow rate on the latent effectiveness is small and generally within the uncertainty bounds. It can also be observed that the latent effectiveness has different values for the dehumidification and regeneration tests. The difference between the regeneration and dehumidification effectiveness as well as the uncertainty bounds are shown in Figure 4.15. The results show that the regeneration effectiveness is considerably higher at low angular speeds, ω < 5 rpm. When the angular speed is greater than 10 rpm, the difference between the results is reduced to less than the experimental uncertainty bounds. Thus, the determination of the effectiveness by the transient test facility at ω < 5 rpm is a challenge since the regeneration and dehumidification effectiveness values are not identical.

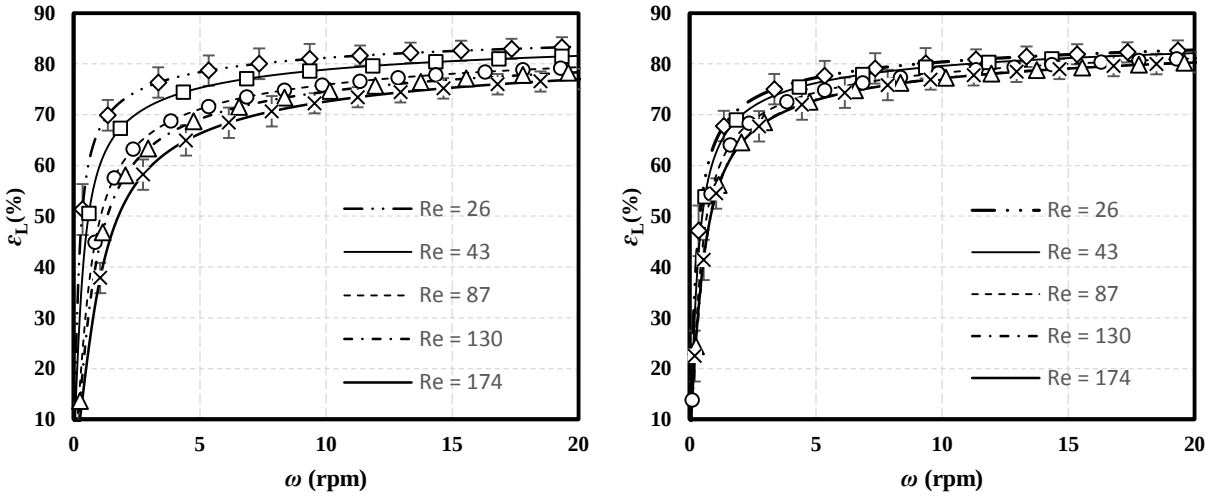

Figure 4.14-Latent effectiveness of the exchanger obtained through the step change in the inlet relative humidity during a) dehumidification and b) regeneration (ΔRH = 40% and T_{air} = 23.0 °C)

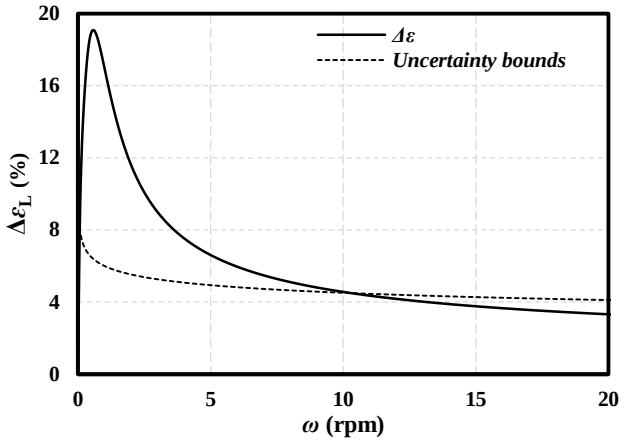

Figure 4.15-Difference between the latent effectiveness obtained from regeneration and dehumidification tests ($\Delta\varepsilon_L = \varepsilon_{L,reg} - \varepsilon_{L,deh}$)

To explore the effectiveness at lower angular speeds, the dehumidification and regeneration latent effectiveness obtained from single step tests were compared to the effectiveness values calculated from cyclic test data. The latent effectiveness of the exchanger was determined for the steady-state cyclic test using Eq. (4.7). In the Eq. (4.7), the integral corresponds to the area between the output humidity curve and the forcing function in each half period of excitation. This area was numerically calculated for six dehumidification and six regeneration cycles based on the results in Figure 4.13. The average latent effectiveness values for cyclic tests are listed in Table 4.15. The uncertainty analysis was done by considering the error in the numerical calculation of the area and the precision in the calculated effectiveness values. In addition, the uncertainty from the measurements on the cyclic humidity curves were also taken into account. A detailed description of the uncertainty analysis has been presented elsewhere. (Fathieh et al., 2015). Similar to the transient results, the latent effectiveness calculated from the regeneration cycles is greater than the effectiveness obtained from the dehumidification cycles. The difference between the dehumidification and regeneration effectiveness values increases as the angular speed increases from 0.5 to 1.5 rpm. Table 4.15 also includes the effectiveness values obtained from the single

step dehumidification and regeneration test at the same angular speeds. Comparing the effectiveness values calculated from the dehumidification test data of single step and cyclic tests, it can be seen that the results are consistent and the differences are within the experimental uncertainty bounds. Moreover, the effectiveness from regeneration tests are in good agreement as well. It can thus be concluded that the transient single step test is successful for predicting the moisture recovery in cycles of dehumidification and regeneration. In practice, it is common to report a single value as a latent effectiveness of rotary regenerators. Thus, the average value of effectiveness for the regeneration and dehumidification is also reported in Table 4.15.

Table 4.15-Comparison of the latent effectiveness of rotary wheel obtained through the transient single step test and cyclic test, (ΔRH = 40% and T_{air} = 23.0 °C)

ω (rpm)	ε_{step} (%)		ε_{cyclic} (%)		ε_{cyclic} - ε_{step} (%)		ε_{ave}	
	ε_{deh}	ε_{reg}	ε_{deh}	ε_{reg}	ε_{deh}	ε_{reg}	ε_{step}	ε_{cyclic}
0.50	20 ± 5	39 ± 5	23 ± 2	30 ± 2	3 ± 7	-9 ± 7	29 ± 5	26 ± 2
0.75	29 ± 5	48 ± 5	32 ± 3	42 ± 2	3 ± 8	-6 ± 7	39 ± 5	37 ± 3
1.50	46 ± 4	60 ± 4	41 ± 4	54 ± 3	-5 ± 8	-6 ± 7	53 ± 4	48 ± 4

4.12 Comparison with Literature Correlation

A correlation found in the literature (Simonson & Besant, 1999) was used to predict the latent effectiveness of rotary desiccant wheel with the same channel geometry and coatings as the small-scale exchanger. Using more than 600 simulated data points, Simonson & Besant (1999) developed a correlation for latent effectiveness that is given by:

$$\varepsilon_{\mathrm{L}} = \frac{NTU}{1+NTU}\left[1-\frac{1}{0.54\left(Cr_{\mathrm{mt}}^{*}\right)^{0.86}}\right]\times\left[1-\frac{1}{\left(NTU\right)^{0.51}\left(Cr_{\mathrm{mt}}^{*}\right)^{0.54}H^{*}}\right] \tag{4.14}$$

where

$$NTU = \frac{1}{\dot{m}c_{p,a}}\left[\frac{1}{(hA_{ht})_s} + \frac{1}{(hA_{ht})_e}\right]^{-1},\ 2 \le NTU \le 10 \tag{4.15}$$

$$Cr^* = \frac{Mc_{p,m}N}{\dot{m}c_{p,a}},\ 3 \le Cr^* \le 10 \tag{4.16}$$

$$Crm^* = \frac{M_{des,dry}N}{\dot{m}_a} \tag{4.17}$$

$$Cr_{mt}^* = (Crm^*)^{0.58} W_m^{0.33} \left(\left.\frac{\partial u}{\partial RH}\right|_{\phi_{ave}}\right)^{0.2} (Cr^*)^{1.13} \left[\frac{e^{1482/T_{ave}}}{47.9} - 1.26(RH_{ave})^{0.5}\right]^{4.66} \tag{4.18}$$

and

$$H^* = 2500\frac{\Delta W}{\Delta T},\ -6 \le H^* \le 6 \tag{4.19}$$

The description of the correlation parameters with their values for the small-scale exchanger are given in Table 4.16.

Using the correlation in Eq. (4.14) with the values given in Table 4.16, the latent effectiveness of the small-scale exchanger was calculated at two NTU_m values. It should be noted that in their analysis, Simonson and Besant assumed that the Lewis number was unity, which leads to the same number of transfer unit for heat and mass transfer ($NTU = NTU_m$). Figure 4.16 presents the results of the present study within the validity range of the correlation $3 \le Cr^* \le 10$. The uncertainty bounds for the correlated effectiveness were obtained by propagating the uncertainty of each parameter.

Table 4.16-The correlation parameters used to determine the latent effectiveness of small-scale exchanger

Parameter	Description	Values	Reference
h [W/(K.m^2)]	Convective heat transfer coefficient	28.0 ± 0.5	Ref. (Shah & London, 1978)
A_{ht} [m^2]	Total area of heat transfer	0.48 ± 0.008	Measured
M [g]	Mass of coated matrix	537.8 ± 0.1	Measured
$c_{p,m}$ [J/(kg.K)]	Specific heat capacity of matrix	893	Al-3003, Ref. (Bauccio, 1993)
$M_{des,dry}$ [g]	Total mass of dry desiccant coated on the matrix	9.32 ± 0.002	Measured
W_m [g/g]	Maximum moisture content of desiccant	0.27 ± 0.02	Fig. 6
RH_{ave} [%]	Average relative humidity	24 ± 2	Table 3
$(\partial u/\partial RH)_{ave}$	Slope of sorption isotherm at average relative humidity	0.23	Fig. 6
H^*	Operating condition factor	$H^* >> 1$	ΔT is zero

The latent effectiveness from the transient single step test, Table 4.16 **,** are included in Figure 4.16 for comparison. Comparing the results it is shown that for NTU_m = 3.5 the correlated effectiveness values lie between the transient test dehumidification and regeneration effectiveness. At NTU_m = 4.3, the difference between correlated and transient effectiveness reaches the uncertainty bounds of experiment at some angular speeds; however, results are still in agreement if they are compared to the regeneration results. The discrepancy becomes larger than uncertainty bounds at higher NTU_m where the correlation overestimates the effectiveness. The difference in the results may be attributed to the simplifying assumptions used in the correlated results. In fact, the heat and mass transfer analogy cannot fully describe the moisture sorption in the highly porous structure of silica gel in which Le > 1 (Golubovic et al., 2006). This means that during the regeneration and dehumidification process the moisture content in silica gel particles may be lower than its equilibrium value. Therefore, the convective mass transfer coefficient may be smaller than the convective heat transfer coefficient. In addition, finding the area for mass transfer is a practical

challenge, and it was assumed to be identical to the heat transfer area in the correlation. Furthermore, the heat of sorption was overestimated in their numerical simulation by assuming it to be equal to heat of phase change. The aforementioned assumptions with the experimental uncertainty and the error in correlation parameters are expected to be the main reasons for the deviations in the correlated and transient effectiveness at higher NTU_m. According to the correlated results, it can be concluded that the single step test can be performed on small-scale exchanger to predict the effectiveness of full-scale wheel when $NTU_m < 4.3$ and $\omega > 4$ rpm. For better validation of single step test, detailed studies are required at wide range of operating conditions.

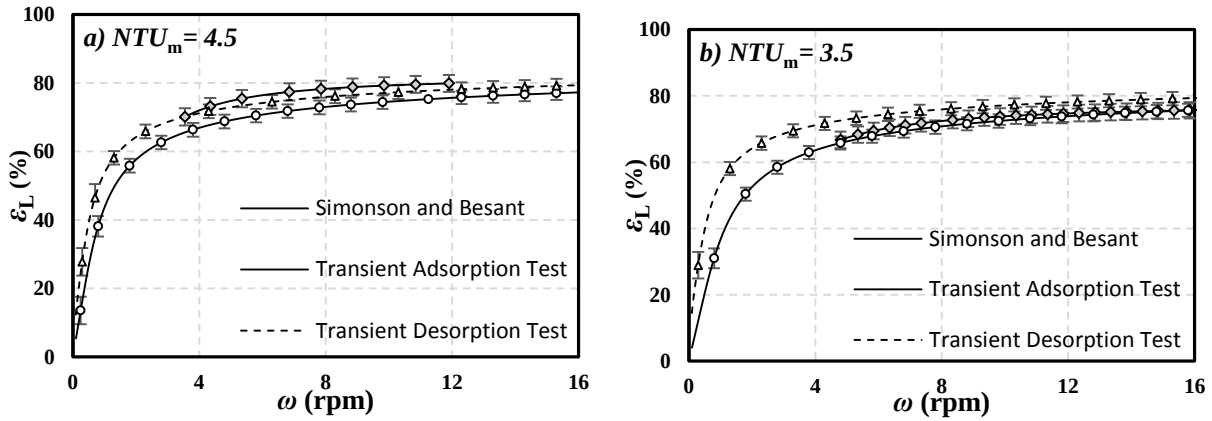

Figure 4.16-Comparison of the latent effectiveness obtained through the small-scale transient testing and the correlation in literature

4.13 Summary and Conclusions

In this work, the latent effectiveness of desiccant wheels was predicted by performing transient testing on a small-scale exchanger. The exchanger matrix is coated with silica gel particles with particle size of 55 μm and pore width of 77.5 Å. Water vapor adsorption isotherms on the silica gel showed almost a linear moisture uptake at 23.0 °C. The kinetics of water vapor sorption on the coated surfaces of an exchanger was studied experimentally using a single step and cyclic humidity change. Using the transient humidity test data during the single step and cyclic

test, the latent effectiveness was determined. The effectiveness values obtained by both tests were consistent proving that the transient single step test can produce the same results as steady-state cyclic operating conditions in rotary wheels. Furthermore, a correlation in the literature was used to determine the latent effectiveness of a wheel with the same coating and geometry. Good agreement was found between the effectiveness determined by transient testing and the correlation at the $NTU_m < 4.3$ and $\omega > 4$ rpm. The discrepancy at higher NTU_m is likely due to the simplifying assumptions in the numerical simulation used to develop the correlation. The uncertainties in the values of exchanger properties, such as effective area for mass transfer and convective mass transfer coefficient, have also significant effects on the correlated effectiveness.

CHAPTER 5

EFFECTS OF DESICCANT PHYSICAL PROPERTIES ON MOISTURE RECOVERY

5.1 Overview

In chapter 4, it was shown that transient component testing can be used to accurately predict the latent effectiveness of a full-scale wheel with the same materials and coating. In this chapter, the transient component testing is used to identify the influence of physical and sorption properties of desiccants on the latent effectiveness. Thus, this chapter addresses the fourth objective of the thesis, "To identify the effects of physical, chemical, and sorption properties of desiccant on the latent effectiveness of energy wheels". The performance of exchangers coated with silica gel samples with different particle sizes and pore widths are presented in this chapter. As in the other chapters, the effects of airflow rate and wheel angular speed are also studied.

In order to satisfy the goals of this chapter, Mr. M. Nezakat assisted the author in taking the scanning electron microscope (SEM) images, developing the powder coating method, and studying the surface morphology. Except the SEM imaging, all the experiments, data acquisition, and data analysis in this chapter were conducted by the author of the thesis (Farhad Fathieh). Farhad Fathieh wrote the manuscript and submitted it to the ASME Journal of Heat Transfer in March 2016. In order to avoid repetition, some parts of the experimental and theoretical analysis in the original manuscript are not included in this chapter.

Effects of Physical and Sorption Properties of Mesoporous Silica Gel on Dehumidification Performance of Energy Wheels

Farhad Fathieh, Majid Nezakat, R. W. Evitts, Robert W. Besant, Carey J. Simonson

5.2 Abstract

Silica gel coated energy wheels are widely used in ventilation systems to reduce the air conditioning load required for humidification/dehumidification of the supply air in industrial environments and commercial buildings. In this study, the effects of silica gel microphysical properties, i.e. pore width (P_w), specific surface area (S_A), and particle size (d_p), on the moisture recovery efficiency (latent effectiveness) of energy wheels are investigated. Three silica gels samples with different particle size and pore width (55 μm-77 Å, 150 μm-63 Å, 160 μm-115 Å) are selected to coat small-scale energy exchangers. The sorption performance of the exchangers are determined from their normalized humidity response to a step increase in the inlet humidity at different flow rates. The results demonstrate that the transient humidity response is mainly specified by the desiccant pore size distribution, specific surface area, and mass of the coating. The transient analytical model (DEM) is used to calculate the latent effectiveness (ε_L) of the exchanger from the transient humidity response. It was found that the exchanger coated with the smallest pore width (63 Å) has the highest available surface area and the highest latent effectiveness. With almost the same particle size (d_p = 150 μm and 160 μm), the latent effectiveness increases by 5% (at wheel speed of 20 rpm and Re = 174) as the silica gel pore width reduces from 150 Å to 63 Å. Increasing the particle size from 55 μm to 150 μm when the pore widths are almost identical (P_w = 63 Å and 77Å) results in a slight enhancement in the latent effectiveness. The Yoon-Nelson model is also applied on test data to correlate the adsorption

breakthrough curves. The ε_L values calculated from the measured and correlated data agreed within experimental uncertainty bounds.

5.3 Introduction

During the past decade, transient testing was proposed in the literature (Abe et al., 2006a, 2006b) to determine the moisture recovery performance (latent effectiveness) of energy wheels. The transient test is based on the analytical/empirical model that applies to the wheels response to a step inlet humidity change. The transient test was found to be faster, less expensive, and easier to perform with less uncertainty compared to the conventional steady-state test methods (ANSI/ASHRAE, 2013). Most recently, Fathieh et al. (2016c) performed the transient single step test on a small-scale exchanger coated with silica gel particles (d_p = 55 μm, P_w = 77 Å) to predict the latent effectiveness of a full-scale wheel with the same coating materials and matrix geometry. Verifying using correlations in the literature, it was shown that the small-scale transient test could successfully predict the latent effectiveness within the experimental uncertainty bounds at practical wheels operating conditions.

The moisture transfer occurs on the external surfaces and internal pores of the coating layer within the wheel channels. Silica gel is one of the most conventional desiccants for coating commercial wheels since it has a large specific adsorption surface area, low cost, non-hazardous interaction with water vapour, and low regeneration temperature (Zheng et al., 2014). Over the past decades, several works have been conducted to analytically/numerically study the latent effectiveness of the wheels (Golubovic et al., 2006; Nia et al., 2006; Nóbrega & Brum, 2009; Simonson & Besant, 1998; Sphaier & Worek, 2004; Wu et al., 2006; Zhang & Niu, 2002; Zhang et al., 2003). It has been reported that the sorption capacity of desiccants plays an important role in the performance of the wheels. In this regard, a desiccant with higher sorption capacity with a linear sorption isotherm is favorable (Simonson & Besant, 1999). It was also found that if the water

vapour diffusion into a porous desiccant is numerically modeled, a good agreement between the simulated results and experimental data is achievable (Sphaier & Worek, 2004). In fact, the accuracy of the numerical models in predicting the latent effectiveness strongly relies on desiccant equilibrium sorption capacity (isotherms) and sorption kinetics (rate of sorption). Several surveys (Gorbach et al., 2004; Harding et al., 1998; Li et al., 2007; Ng et al., 2001; Satoh et al., 1995; Wang et al., 2004) verify that both the sorption isotherms curves and sorption kinetics are specified by desiccant physical properties, i.e. particle size, pore width, and porosity. More importantly, functional groups on the surface of the adsorbate can significantly interact with adsorbate molecules and substantialy affect the sorption behavior (Bartell & Bower, 1952; Benesi & Jones, 1959; Brunauer et al., 1940). For this reason, the available numerical models in the literature for latent effectiveness determination are limited to certain types of desiccants with specified physical and sorptive properties.

In this chapter, three samples of mesoporous silica gel with different particle sizes and pore widths but the same surface functional groups were selected to construct small-scale coated exchangers. It is aimed to investigate effects of desiccant microphysical properties on the sorption characteristic (sorption capacity and kinetics) and the latent effectiveness of the exchangers. Several tests were performed to characterize the main physical and sorptive properties of the silica gel samples, i.e. particle size, pore width, sorption isotherm, and moisture removal rate. The latent effectiveness of energy wheels with the same coating materials and matrix geometry was also determined through the transient testing of the small-scale exchangers. The outcomes of this chapter relate the micro-scale desiccant properties to macro-scale performance of energy wheels.

5.4 Theory

5.4.1 Transient Double Exponential Model (DEM)

The double exponential model (DEM) developed in chapter 4 (section 4.4.1) was used to obtain the exchanger response and the latent effectiveness for different coated exchangers.

5.4.2 Yoon-Nelson Model

The Yoon-Nelson model (Yoon & Nelson, 1984) has been used to study the kinetics of water vapour adsorption on silica gel coated exchangers. This model states that the decrease in the adsorption probability of the adsorbate is proportional to the probability of adsorbate breakthrough. Compared to the other adsorption kinetics models that require extensive information about the adsorbate and adsorbent physical and sorption characteristics (Xu et al., 2013), the Yoon-Nelson model is simply based on two parameters k_{YN} (corresponding to the adsorption rate) and τ_{YN} (corresponding to the time when $W = 0.5$). Accordingly, the normalized humidity can be expressed by the Yoon-Nelson model as follows:

$$W(t) = \frac{e^{(k_{\mathrm{YN}}t - k_{\mathrm{YN}}\tau_{\mathrm{YN}})}}{1 + e^{(k_{\mathrm{YN}}t - k_{\mathrm{YN}}\tau_{\mathrm{YN}})}} \tag{5.1}$$

k_{YN} and τ_{YN} in Eq. (A.10) can be obtained by fitting the model to the humidity test data obtained through transient testing of the exchangers.

5.4.3 Moisture Uptake

Applying the moisture balance on the air flow and desiccant, the descant's moisture content (Ω) at time 't' can be calculated by:

$$\Omega_{\mathrm{ads}} = \frac{Q_{\mathrm{a}}\rho_{\mathrm{a}}(w_{\mathrm{final}} - w_{\mathrm{init}})}{M_{\mathrm{des}}} \int_0^t (1 - W)dt \tag{5.2}$$

in which Q_{a} and ρ_{a} are air flow rate and density, respectively. M_{des} corresponds to the total mass of desiccant coated on the exchanger matrix.

5.5 Experimental

5.5.1 Materials

Three samples of mesoporous silica gel (SG55-77, SG150-63, and SG 160-115) with different particle sizes (d_p) and pore widths (P_w) were selected for the sorption study. To make the comparison more convenient, the samples were named by their particle size and pore width through the study, e.g. SG55-77: $d_p = 55$ μm and $P_w = 77$ Å. Silica gel is an amorphous form of silicon dioxide with porous internal structure, Figure 5.1. The surface of silica gel is comprised of polar Si-O and Si-OH groups which adsorb adsorbates such as water and alcohol. The water molecules are physically bonded on the surface of silica gel by dispersion and polar forces. Due to the strong affinity of silica gel toward water vapour, silica gel is widely used as a solid desiccant in energy wheels. It has been reported that the pore width and available surface area are two main properties that affect the sorption performance of silica gels (Rouquerol et al., 2014). The smaller the pore width, the higher surface area, and consequently, a greater number of sorption sites. On the other hand, the kinetics of sorption is mainly limited by intrapore diffusion (Harding et al., 1998). Thus, sorption rate is lower for silica gel with smaller pore width as the internal diffusion resistance is larger for water vapour molecules to penetrate into its porous structure (Satoh et al., 1995). For this reason, a range of pore width values and particle sizes were selected to investigate the effects of desiccant properties on the performance of energy wheels.

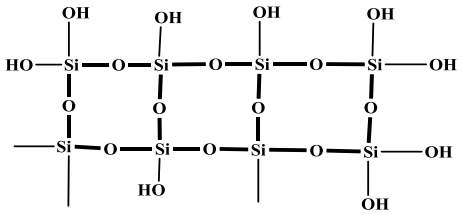

Figure 5.1-A conceptual view of the molecular structure of amorphous silica gel

The silica gel particles size was measured by using Mastersizer S Long Bench Particle Size Analyzer (Malvern Instruments, detecting range of 0.05-880 μm). A range lens (300 RF) focused the scattering pattern from 15,000 particles passing through a laser beam onto the photo-diode detectors. The collected data was processed and analyzing with Malvern data analysis software to determine the particle size. The surface area, pore width distribution, and sorption isotherms of the silica gels were obtained through nitrogen gas adsorption tests (at 77 K) using a Micromeritics ASAP 2020 (Norcross, GA) device. The adsorption isotherm data was used to calculated the surface area (Copeland et al., 2009) and micropore surface area was found by using the de Boer *t*-plot method (Broekhoff, 1968).

5.5.2 Small-Scale Energy Exchanger

Three small-scale energy exchangers were built by coating the silica gel samples on the aluminum substrate. The physical properties of the small-scale exchanger were the same as the exchanger described in section 4.5.2. To coat the exchangers with silica gel particles, the powder coating method, described in section 4.5.2 was used.

5.5.3 Transient Test Facility and Test Procedure

The transient test facility, described in section 4.5.3 was used for performing the transient test on the coated exchangers. The same test procedure was followed as given in section 4.5.4 with the testing conditions listed in Table 5.1.

Table 5.1-Air conditions and flow rates for the transient single step increase/decrease tests

Q_a (L/min)	V_f (m/s)	Re_{dh}	T_{air} (°C)	RH_{dry} (%)	RH_{humid} (%)	(RH_{humid} - RH_{dry})
15 ± 1	0.050 ± 0.001	26 ± 2				
25 ± 1	0.091 ± 0.001	43 ± 2				
50 ± 1	0.172 ± 0.002	86 ± 2	23.0 ± 0.5	4 ± 2	44 ± 2	40 ± 2
75 ± 1	0.264 ± 0.003	129 ± 2				
100 ± 2	0.344 ± 0.004	172 ± 4				

5.6 Results

The IR spectra of the three silica gel samples are presented in Figure 5.2. The IR spectra of all the samples are very similar which indicates that the silica gels are comprised of the same surface functional groups. A sharp adsorption band at 1092 cm $^{-1}$ is for the stretching vibration of the Si-O bond; whereas, the adsorption band at 803 cm^{-1} is attributed to the ring structure of SiO_4. The deformation vibration of Si-O-Si was detected through adsorption band at 464 cm^{-1}. A very wide band at 3440 cm $^{-1}$ is seen, which can be related to the hydroxyl groups. Hydroxyl groups may contribute in water vapor sorption significantly through hydrogen bonding. Similar observations have been reported in the literature (Decottignies et al., 1978; Gallas et al., 1997; Gillis-D'hamers et al., n.d.; Kamitsos et al., 1993; Maniar et al., 1990; RM & CG, 1990; Rumph & Schubert, 1978; Wood & Rabinovich, 1989).

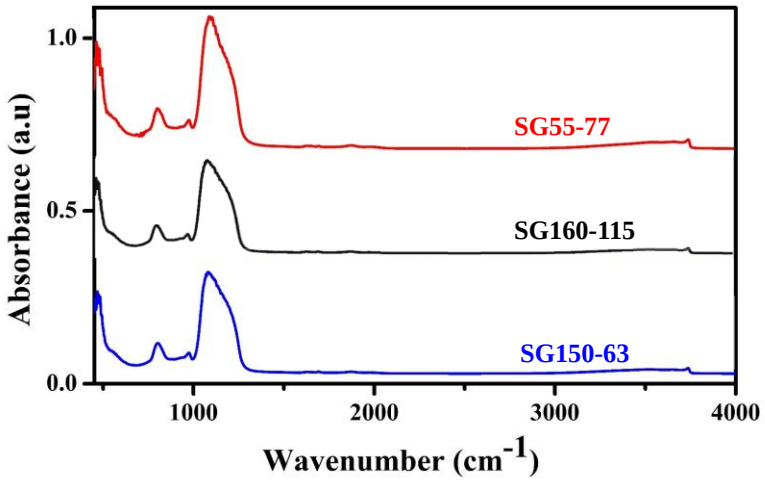

Figure 5.2-IR specta of the silica gel samples

The volumetric distributions of the silica gels particle with their particle sizes are presented in Figure 5.3. The results show a narrow and almost normal distribution for the size of the silica gel particles. SG150-63 and SG160-115 have almost the identical particle size distributions with

average particle diameter of 150 μm and 160 μm, respectively. SG55-77 has the smallest particle size among the tested silica gels.

The silica gel specific surface area (S_A), average pore width (P_w), and average pore volume (P_v) obtained through nitrogen gas adsorption at 77 K are listed in Table 5.2. According to the pore width classification recommended by International Union of Pure and Applied Chemistry (IUPAC), the silica gel samples are all mesoporous (20 Å < P_w < 500 Å) (Rouquerol et al., 1994). Although smaller particle sizes lead to higher external surface area, the surface area of the mesoporouse silica gels is mainly due to their internal surfaces. That is why SG150-63 with the smaller pore width has the a 13% higher S_A than SG55-77, even though the particle size of SG150-63 is nearly three times larger than the particle size of SG55-77. Table 5.2 also shows that the larger the pore width, the higher the pore volume per unit mass of the silica gels. Accordingly, SG160-115 has the largest pore volume; whereas, SG150-63 and SG55-77 have almost identical pore volumes.

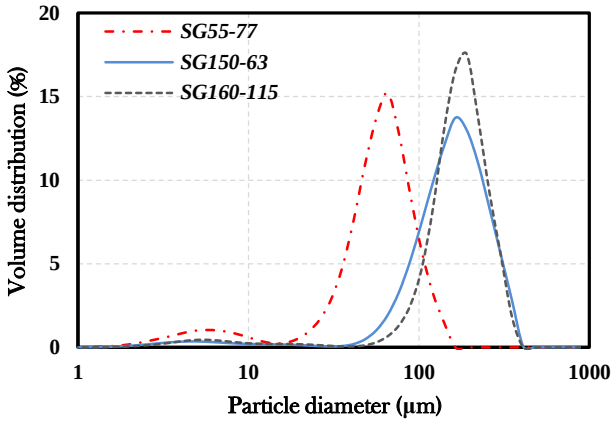

Figure 5.3-Particle size distribution of silica gel desiccants obtained from particle size analyzer

Table 5.2-Physical properties of the amorphous silica gel samples obtained by laser particle size analyzer and N_2 gas adsorption

Sample	Average Particle Size d_p (µm)	Adsorption pore width P_w (Å)	Accessible surface area S_A (m^2/g)	Volume of pores P_v (cm^3/g)
SG55-77	55	77	392	0.759
SG150-63	150	63	442	0.702
SG160-115	160	115	345	0.992

To quantify the influence of pore width, pore volume, and specific surface area, the nitrogen gas sorption isotherms for the silica gels at 77 K are presented in Figure 5.4. It can be seen that all the sorption isotherms represent type IV which is common for mesoporous materials (Haul, 1982). A hysteresis loop in the sorption isotherm is due to the capillary condensation within the mesopores. At lower partial pressures ($P/P_0 < 0.6$), the sorption process is mainly driven by interaction between the adsorbent surface and adsorbate molecules that form a monomolecular layer of adsorbate (Donohue & Aranovich, 1999). Therefore, an adsorbent with relatively higher specific surface area should exhibit a better sorption performance. This is why the SG160-115 with the largest P_w and the smallest S_A has the lowest sorption capacity at $P/P_0 < 0.6$. On the other hand, at the higher relative pressures ($P/P_0 > 0.9$), the sorption capacity of silica gels is limited by their pore volume (Li et al., 2007). Thus, SG160-115 with the largest pore width and pore volume has the highest sorption capacity for $P/P_0 < 0.9$. This illustrates the importance of internal porosity on the sorption performance of mesoporous silica gel which may affect the energy wheel performance operating at climate zones with different moisture partial pressures (relative humidity).

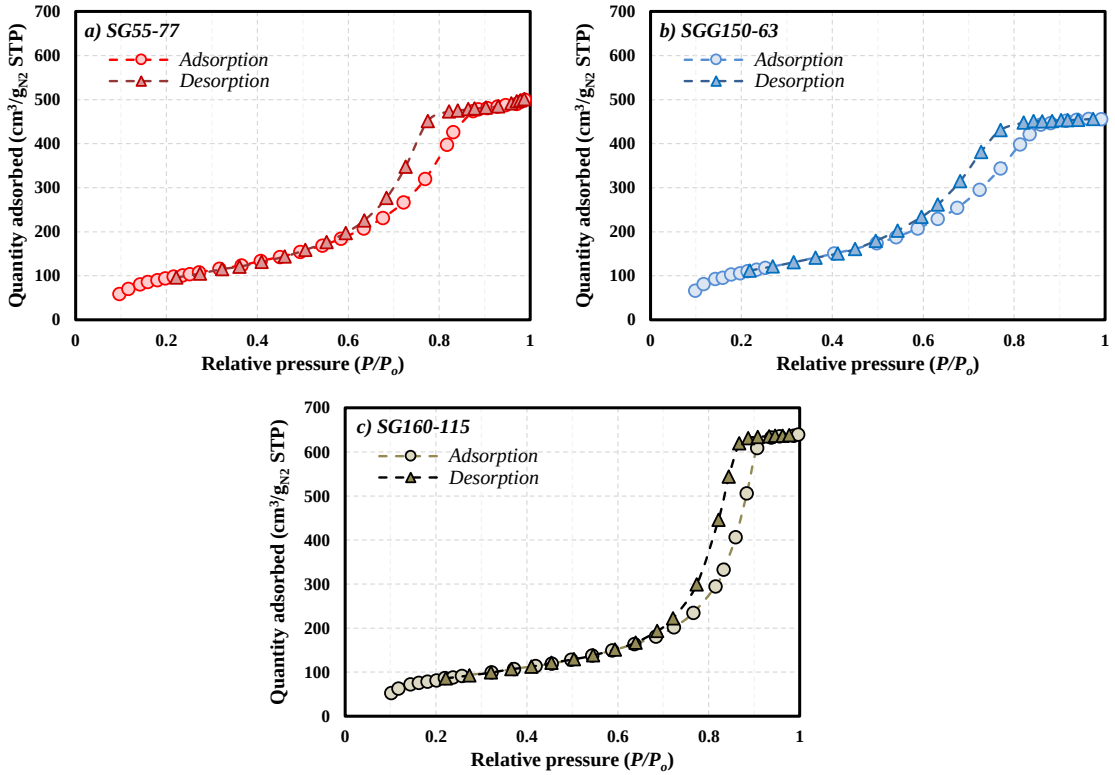

Figure 5.4-Sorption isotherms for a) SG55-77, b) SG150-63 and c) SG160-115 obtained through N_2 gas sorption at 77 K

Figure 5.5 shows SEM images of aluminum sheets coated with the silica gel particles. It can be see that all three silica gel samples have irregular particle shapes and a narrow range of particle sizes. This narrow particle size distribution was also verified by particle size measurements. It should be noted that the nanometer-sized pores of silica gel cannot be observed in SEM images as higher magnification levels are required to visualize the pores. The SEM images of coated samples also show a monolayer coating with uniform particle distribution. Unlike the industrial coatings in which a considerable number of desiccant particles are submerged into the bonding agent (Shang & Besant, 2009c), the powder coating creates an enhanced layer of coating on the acrylic bonding agent. Partial or full pore blockage, caused by the bonding agent in industrial coatings, increases the diffusion barriers and substantially reduces the mass transfer in the pores of desiccant.

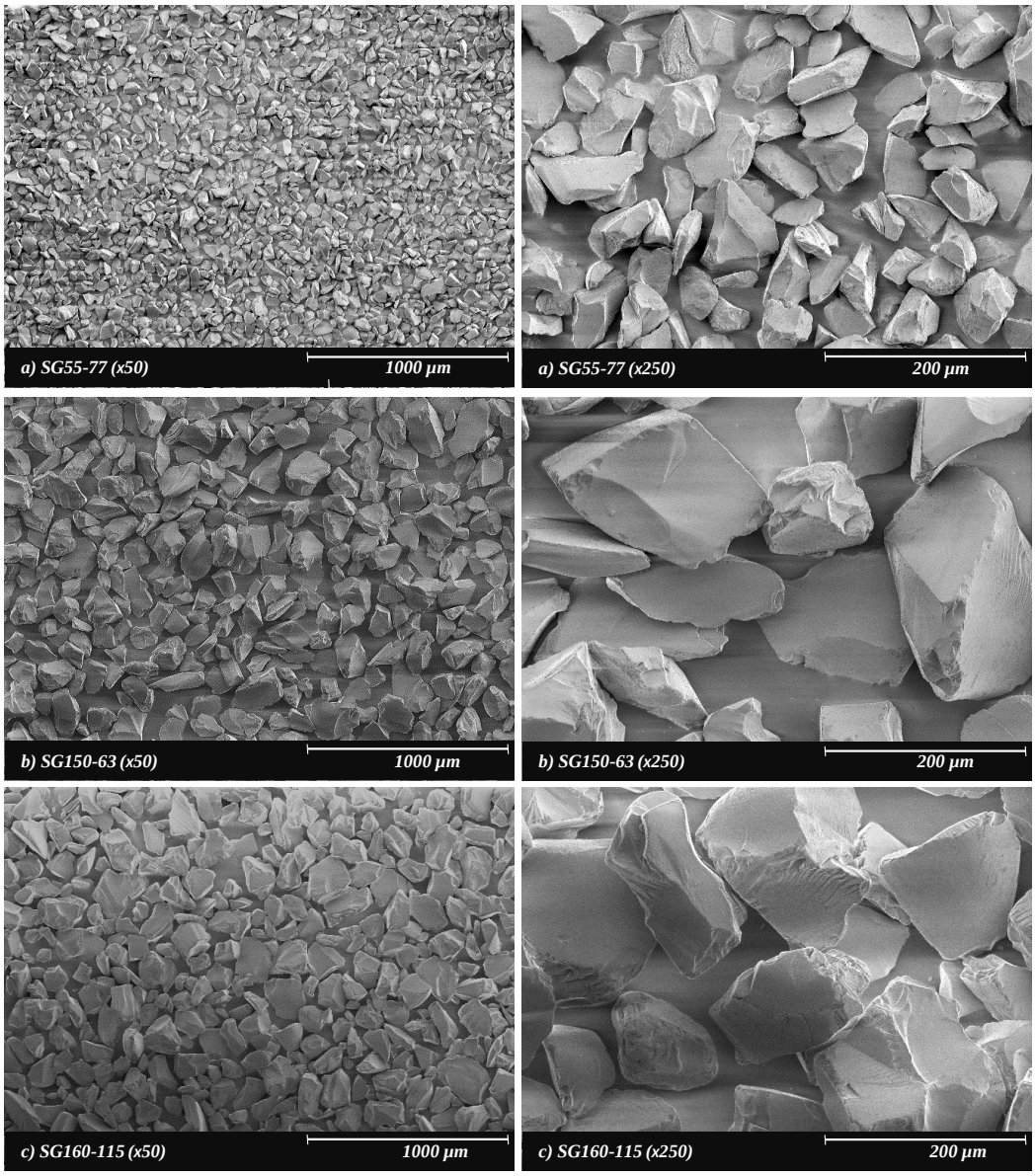

Figure 5.5-SEM images of silica gel particles coated on an aluminum substrate

In contrast to industrial coating the powder coating minimizes the pore blockage and interaction between bonding agent and desiccant by making almost all the sorption sites available for water vapor sorption. This enables the investigation of the influences of the desiccant internal pores on the overall performance of the small-scale energy exchanger with minor effects of the bonding agent. Moreover, the SEM images demonstrate that not all the surface of the substrate is

covered with the silica gel particles which may intensify the interaction between the polar groups in the acrylic resin and the water vapor molecules. Fathieh et al. (2016c) performed a set of transient humidity step tests on a small-scale exchanger comprised of sheets covered only with a layer of acrylic bonding agent and found that the bonding agent has a negligible effect on the sorption process during air dehumidification and desiccant regeneration.

Table 5.3 provides quantified information about the amount of desiccant used to coat the small-scale exchangers. It was found that when larger particles were used for powder coating, more mass of desiccant was deposited on the exchanger matrix. The observed effect is in agreement with the data in the literature on efficacy of powder coating for larger particles (Maniar et al., 1990). The coating to matrix mass ratio for the small-scale exchangers was determined by dividing the coated mass by the total mass of the sheets. It should be noted that the mass of desiccant to matrix is about 20% in commercial wheels but the available coating resulted only in a mass of 1.9 - 4.5%. In fact, the aluminum sheets used in the small-scale exchanger is 0.60 mm thick which is considerably thicker than the 0.02 aluminum foil in the commercial wheels. The thicker aluminum substrate provided a flat and rigid surface for coating and making the parallel-plate exchanger. However, considering the coating mass to matrix area ratio is between 0.8-1.6 mg/cm^2 in commercial wheels, the powder coating results in a higher amount of desiccant coating per unit area. A higher amount of coated desiccant along with a lower number of submerged particles into the bonding agent, reveals a good potential for powder coating to be used in the wheel manufacturing process. However, further studies are required to investigate the stability and durability of the coating during the production of energy wheels from flat materials and also over the life span of the wheel in operation.

Table 5.3-Mass of coated particles on the sheets of parallel-plate energy exchangers

Exchanger	Coated Desiccant	Total mass of desiccant coated (g)	Mass of desiccant coated per unit area (mg/cm²)	Mass of desiccant to mass of the matrix (%)
EX55-77	SG55-77	9.32 ± 0.02	1.941 ± 0.004	1.9
EX150-63	SG150-63	22.12 ± 0.02	4.604 ± 0.004	4.5
EX160-115	SG160-115	19.07 ± 0.02	3.969 ± 0.004	3.9

5.7 Energy Exchanger Response

In this section, the transient response of the small-scale exchangers to a step change in humidity at different flow rates is presented. The measured humidity downstream of the exchanger is the coupled response of the exchanger and the humidity sensors using an analytical/empirical relation presented in the literature (Wang et al., 2005). The transient response of the humidity sensors was determined elsewhere (Fathieh et al., 2016c) at different flow rates and humidity step change amplitudes when the exchanger was not in the test section. They used the DEM to determine the sensor response characteristics and their results are summarized in Table 5.4**.** The humidity sensors were found to have a dominant fast mode followed by a slow mode during the transient humidity measurements ($\tau_{1,s} < 0.1\tau_{2,s}$ and $\gamma_{1,s} > \gamma_{2,s}$). The sensor response is faster at higher flow rates and the second mode weighting factor increases with flow rate. In this study, the data in Table 5.4 was used to decouple the small-scale exchangers responses from the coupled response of the exchanger and the humidity sensors.

Table 5.4-RH sensor response to a step increase in the inlet humidity at different flow rates

Re	$\gamma_{1,s}$	$\tau_{1,s}$ (s)	$\gamma_{2,s}$	$\tau_{2,s}$ (s)	R^2
26	0.95 ± 0.01	9.9 ± 0.7	0.05 ± 0.01	146.5 ± 56.1	0.9766
43	0.95 ± 0.01	8.4 ± 0.6	0.05 ± 0.01	105.3 ± 54.5	0.9827
87	0.96 ± 0.01	6.4 ± 0.4	0.04 ± 0.01	77.6 ± 35.5	0.9904
130	0.95 ± 0.01	6.0 ± 0.4	0.05 ± 0.01	41.7 ± 12.6	0.9954
174	0.92 ± 0.02	6.0 ± 0.4	0.08 ± 0.02	53.4 ± 13.4	0.9948

The normalized humidity responses (breakthrough curves) obtained from the transient testing of the small-scale exchangers at different flow rates are shown in Figure 5.6. In this set of tests, the inlet humidity of the exchangers was increased in less than a second at time zero and the gradual changes in the outlet humidity were monitored. This gradual increase in humidity is attributed to the water vapor adsorption on the desiccant coated exchangers. As the moist air passes through the exchanger, the higher concentration of water vapor in the air flow forces the water vapor molecules to diffuse towards the adsorbent surface. When the water vapor molecules are in the vicinity of the adsorbent polar surface, they are attracted by dispersion and polar forces (Van der Waals forces) toward the sorption sites on the adsorbent surface. The driving force for mass transfer reduces with time as more sorption sites are occupied by adsorbate molecules, and consequently, the water vapor concentration on the adsorption surface approaches the value of the air stream. The transient behavior of breakthrough curves is commonly described based on the *breakthrough point* (W_b = 0.05-0.15) and *exhaust points* (W_e = 0.9-0.95) (Eduardo & Nóbrega, 2014). With these points, the breakthrough curves can be divided in three regions, primary sorption zone ($W < W_b$), transition zone ($W_b < W < W_e$), and saturation zone ($W > W_e$). Within the primary sorption zone, the normalized humidity changes are insignificant, most of the desiccant sorption sites are unoccupied and the desiccant is able to adsorb almost all the moisture from the humid air stream. Most commercial packed beds used for dehumidification purposes are operated in this region (Chang et al., 2005). In the transition zone, the slope of the breakthrough curve gradually decreases as it approaches the exhaust point. In contrast to packed beds, energy wheels and drying wheels outlet humidity variations are within the transition zone $0.35 < W < 0.65$ (Fathieh et al., 2016c; Sphaier & Worek, 2004; Zhang & Niu, 2002). In the saturation zone ($W > W_e$), most of the sorption sites are occupied, the desiccant is nearly saturated, and a regeneration process is required.

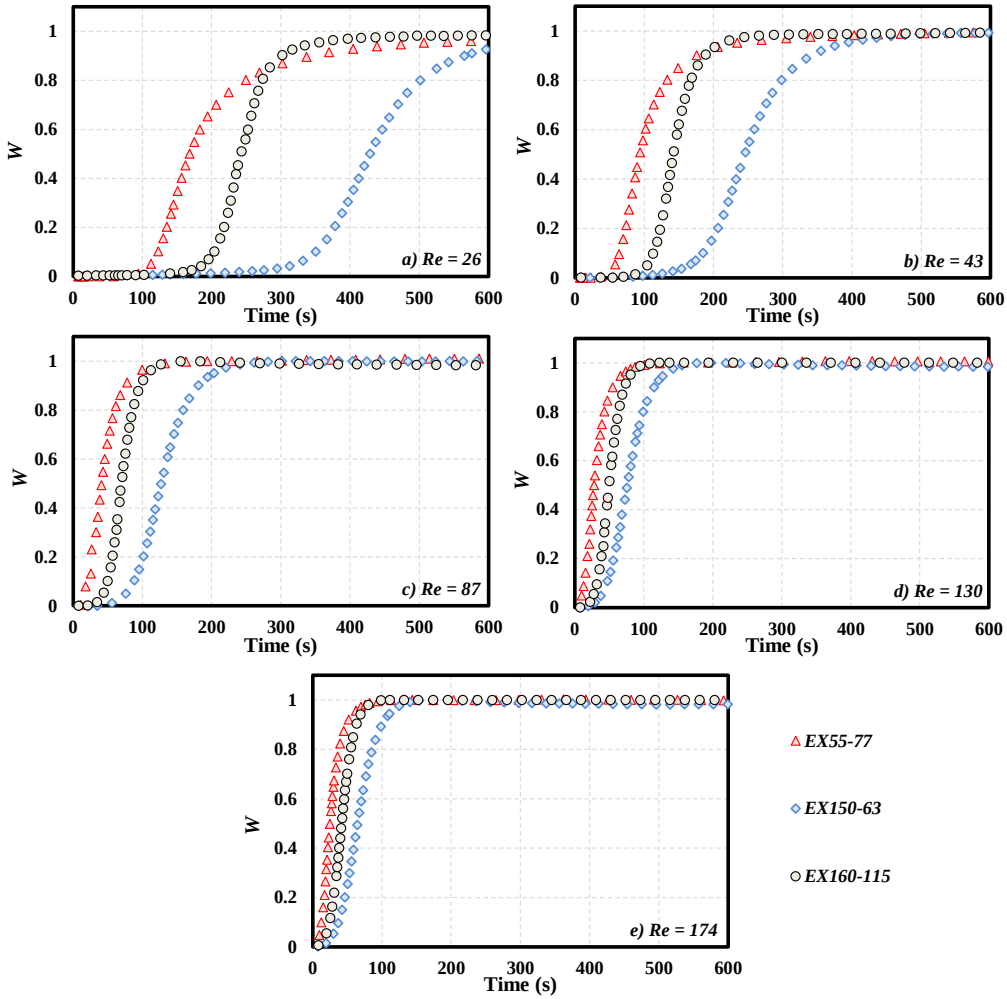

Figure 5.6-Breakthrough curves for water vapor adsorption on the mesoporous silica gels in the small scale exchangers at different flow rates (ΔRH= 40%, and T_{air} = 23.1 °C, maximum uncertainty in the experimental data is U_W = ±0.05)

Figure 5.6 also demonstrates a similar trend for all the exchanger breakthrough curves but different quantities at the given flow rates. For all the exchangers, the outlet humidity reaches equilibrium conditions sooner as the Reynolds number increases. The duration of the primary sorption and transition zones become shorter as *Re* increases. However, influence of flow rate on the breakthrough curves diminishes as *Re* increases to more than 130. Comparing the breakthrough curves of the small-scale exchangers, EX150-63 (the exchanger coated with SG150-63) has the slowest response at a specified *Re*. This implies that EX150-63 can adsorb a greater amount of

moisture from the humid airstream during the dehumidification process. The large dehumidification capacity of EX150-63 can be attributed to the greater specific surface area of SG150-63 particles (Table 5.2**)** and the higher amount of desiccant coated on EX150-63, Table 5.3. The poorest performance is found to be for EX55-77 as it becomes saturated prior to the other exchangers at the same flow rate. EX55-77 has the smallest mass of desiccant coated on its matrix which reduces its dehumidification capacity and, consequently, EX55-77 has the shortest primary zone. However, the duration of the transition zone for EX55-77 is longer compared to that of EX160-115. It is believed that the sorption sites of EX160-115, with the largest pore width, are easily accessible and mainly occupied during the primary sorption zone. On the other hand, diffusion barriers is in larger in the smaller pores of SG55-77, and consequently, the transition zone is longer for EX55-77. This can explain why the duration and curve slope in transition zones for EX55-77 and EX150-63, with almost identical pore width but different coating mass, are very close to each another. Based on the observation from breakthrough curves, following conclusions can be drawn:

1. The mass of coated desiccant plays a key role in moisture recovery by increasing the primary sorption zone duration and the dehumidification capacity of the exchangers.
2. The transition sorption zone is mainly controlled by pore width distributions and accessible sorption sites. The smaller the pore width and the larger specific surface, the longer the duration of the transition zone.
3. Although the particle size does not affect the sorption properties of materials significantly, it may substantially change the coating mass which in turn alters the exchanger dehumidification capacity. With a single layer of desiccant particles, the larger the particles, the greater the coating mass.

To investigate the moisture uptake per unit mass of desiccant, Eq. (5.2) was used to determine the moisture content of the desiccant (Ω) during the dehumidification test and the results are shown in Figure 5.7. With the desiccant in equilibrium with the dry air ($RH_{dry} < 5\%$) at the beginning of the tests, the moisture content values given in Figure 5.7 are relative to the desiccant moisture content at $RH = 5\%$. It can be seen that increasing *Re* shortens the transition period; nevertheless, it does not alter the specific sorption capacity of the exchanger (the moisture content at equilibrium conditions). This is a reasonable observation as the sorption capacity of materials at a specific relative humidity only depends on its sorption properties, but not the air flow rate. The moisture content curves verify that SG150-63 with the largest specific surface area has the highest sorption capacity. In contrast, SG160-115 has the lowest specific surface area and sorption capacity. The kinetics of adsorption can also be studied by comparing the slope of moisture uptake (rate of adsorption) within the transition region in Figure 5.7. In porous materials, the rate of adsorption is controlled by gas diffusion in the pores which is limited by the pore width (Satoh et al., 1995). On the other hand, the probability for adsorbate molecules to reach the adsorbent sorption site increases as the pore width becomes smaller and the surface area increases. Thus, a higher sorption rate is expected for a desiccant with higher specific surface area (smaller pore width) and smaller diffusion resistance (larger pore width). It is expected that a certain range of pore width would results in highest rate of sorption. Accordingly, SG55-77 with larger pore width (but smaller specific surface area) has higher sorption rate compared to SG150-63 with smaller pore width (but higher specific surface area), Table 5.2. On the other hand, although SG150-115 has larger pore width than SG55-77, its smaller surface area results in the reduced sorption rate.

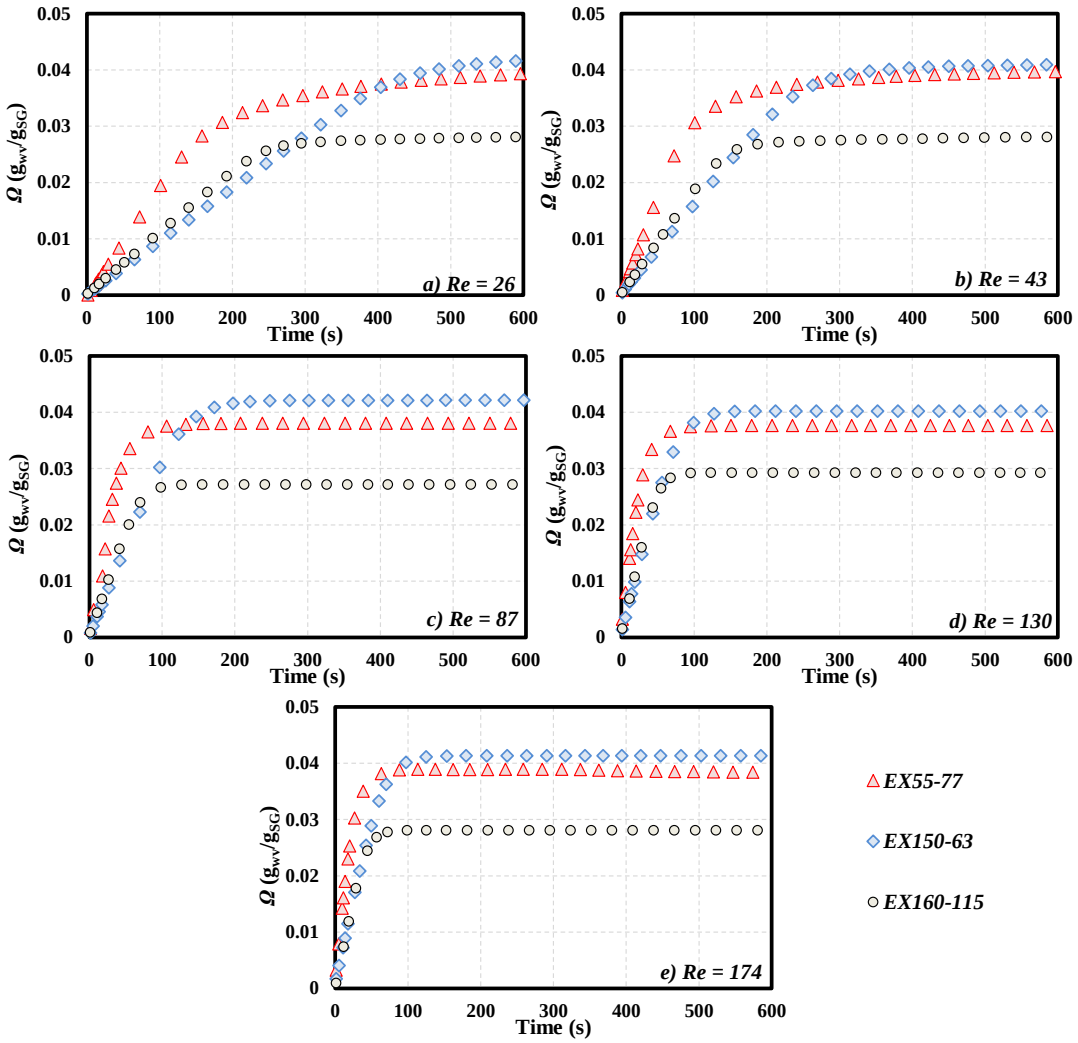

Figure 5.7-Moisture content in the small scale exchanger with time during the dehumidification at different flow rates (ΔRH= 40%, and T_{air} = 23.1 °C)

In order to quantify the transient response of the small-scale exchangers and determine their latent effectiveness, the DEM and the Yoon-Nelson models were used to fit the breakthrough curves in Figure 5.6**.** The trust-region optimization algorithm was applied to obtain the best fit using MATLAB R2014. Detailed information about the fitting procedure and relevant uncertainties are provided elsewhere (Fathieh et al., 2016c). The regression curves with the test data for EX160-115 at different flow rates are shown in Figure 5.8. As discussed, the humidity response of the wheels during the dehumidification and regeneration cycles are within the range

of $0.35 < W < 0.65$. Considering this fact, the DEM was developed to correlate the wheels' transient response in this range but the model is not accurate in correlating the humidity data close to the primary sorption zone. This is clearly shown in Figure 5.8 as the DEM successfully fits the test data at $W > 0.3$. As the flow rate increases and primary moisture uptake zone diminishes, DEM seems to be better in describing the breakthrough curves.

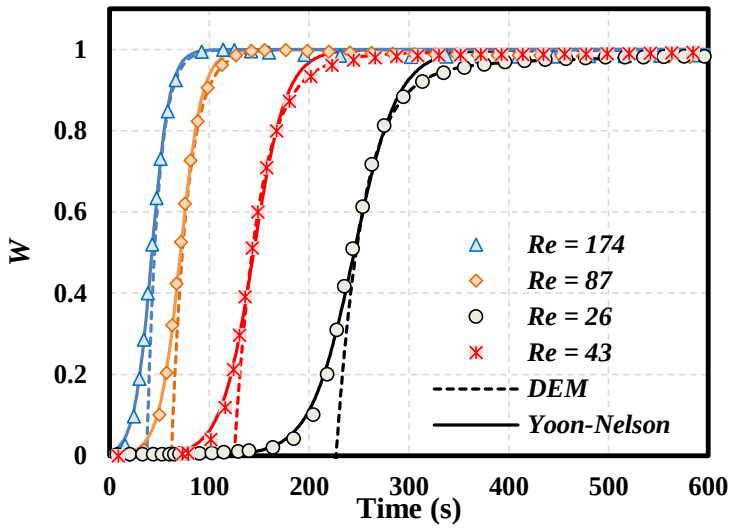

Figure 5.8-Breakthrough curves of water vapor on silica gel coated exchanger EX160-115 at different flow rates (ΔRH= 40%, and T_{air} = 23.1 °C, maximum uncertainty in the experimental data is U_W = ±0.05)

Table 5.5-5.7 list the time constants, weighting factors, and coefficients of determination (R^2) for the small-scale exchangers obtained from fitting the DEM to the breakthrough curves in Figure 5.6. Since the DEM cannot model the test data within the primary sorption zone, a start time should be specified for the DEM. In this regard, a start time was determined that resulted in the highest fitting R^2 and then, the time constants were calculated relative to this starting time (Fathieh et al., 2016c). It was found that the starting time corresponding to normalized response between $0.2 < W < 0.4$ led to the highest R^2. The R^2 values are calculated by comparing the correlated points and test data within the range of $0.25 < W \leq 1$. At $Re \leq 43$, the adsorption occurs

with two modes within all the exchangers. The first mode is observed to be relatively fast ($\tau_1 << \tau_2$) and dominant as its weighting factor is considerably greater than the second mode weighting factor ($\gamma_1 > \gamma_2$). The second mode diminishes as *Re* increases which means that the exchanger responds similar to a linear system to the step change in inlet humidity. As observed in the breakthrough curves of Figure 5.6, the exchangers reach the saturation zone faster at higher *Re* that leads to smaller time constants at higher flow rates. Among the exchangers, EX150-63 has the largest time constants which are due to the largest amount of coating on this exchanger. The shortest transition duration and the smallest time constant are for EX160-115 with the largest particle size and pore width. As discussed previously, the short transition period for EX160-115 may be attributed to SG160-115 with largest pore width and smallest diffusion barriers inside the pores.

Table 5.5-EX55-77 response characteristics to the humidity step increase at different flow rates (ΔRH = 40% and T_{air} = 23 °C)

Re_{dh}	γ_1	τ_1 (s)	γ_2	τ_2 (s)	R^2
26	0.86 ± 0.02	60.2 ± 6.1	0.14 ± 0.02	469.3 ± 53.1	0.9998
43	0.84 ± 0.02	33.4 ± 3.4	0.16 ± 0.02	164.4 ± 30.1	0.9998
86	1.00 ± 0.01	20.1 ± 2.1	0.00 ± 0.00	-	0.9913
129	1.00 ± 0.00	16.2 ± 1.6	0.00 ± 0.00	-	0.9934
172	1.00 ± 0.00	12.2 ± 1.2	0.00 ± 0.00	-	0.9996

Table 5.6-EX150-63 response characteristics to the humidity step increase at different flow rates (ΔRH = 40% and T_{air} = 23 °C)

Re_{dh}	γ_1	τ_1 (s)	γ_2	τ_2 (s)	R^2
26	0.96 ± 0.02	74.7 ± 5.3	0.04 ± 0.02	1314.0 ± 89.1	0.9999
43	0.98 ± 0.01	57.5 ± 4.1	0.02 ± 0.01	523.4 ± 48.6	0.9994
86	1.00 ± 0.01	29.3 ± 2.3	0.00 ± 0.00	-	0.9993
129	1.00 ± 0.00	20.1 ± 1.8	0.00 ± 0.00	-	0.9995
172	1.00 ± 0.00	16.2 ± 1.4	0.00 ± 0.00	-	0.9996

Table 5.7-EX160-115 response characteristics to the humidity step increase at different flow rates (ΔRH = 40% and T_{air} = 23 °C)

Re_{dh}	γ_1	τ_1 (s)	γ_2	τ_2 (s)	R^2
26	0.89 ± 0.02	26.9 ± 2.2	0.11 ± 0.01	315.7 ± 32.1	0.9990
43	0.95 ± 0.01	25.1 ± 2.1	0.05 ± 0.01	145.9 ± 16.3	0.9997
86	1.00 ± 0.01	15.9 ± 1.3	0.00 ± 0.00	-	0.9994
129	1.00 ± 0.00	12.5 ± 1.2	0.00 ± 0.00	-	0.9995
172	1.00 ± 0.00	8.6 ± 0.7	0.00 ± 0.00	-	0.9986

Although the DEM describes the exchanger response precisely above the breakthrough point, it cannot provide any information on humidity below the breakthrough point. Thus, if the primary sorption zone is of interest, another model should be employed to accurately predict the full range of breakthrough curves during the step change. For this reason, the Yoon-Nelson model was also applied to correlate the breakthrough curves in Figure 5.6 using the trust-region optimization algorithm MATLAB R2014. The correlated curves for EX160-115 are also shown in Figure 5.8**.** It can be seen that the Yoon-Nelson model fits the humidity data very well even in primary moisture uptake zone; however, the model cannot precisely correlate the test data between $0.9 < W < 0.95$ at lower *Re* ($Re \leq 43$). This is probably due to the second mode of sorption, as observed by DEM, that cannot be correlated by the Yoon-Nelson model. The fitting parameters for the Yoon-Nelson model are presented in Table 5.8. Similar to the DEM time constants, τ_{YN} reduces considerably as *Re* increases. On the other hand, the values of k_{YN} increase with *Re*. EX150-63 has the greatest τ_{YN} which can be explained by its highest coating mass among the exchangers and the largest specific sorption capacity of SG150-63.

Table 5.8-Yoon-Nelson fitting parameters for adsorption of water vapor on the mesoporous silica gel samples at different flow rates

Re	EX55-77			EX150-63			EX160-115		
	k_{YN}	τ_{YN} (s)	R^2	k_{YN}	τ_{YN} (s)	R^2	k_{YN}	τ_{YN} (s)	R^2
26	0.024 ± 0.001	182 ± 1.4	0.9789	0.021 ± 0.0003	435 ± 0.7	0.9976	0.046 ± 0.002	245 ± 0.4	0.9984
43	0.046 ± 0.002	99 ± 0.9	0.9876	0.029 ± 0.0004	249 ± 0.5	0.9985	0.061 ± 0.002	144 ± 0.4	0.9984
86	0.080 ± 0.003	42± 0.5	0.9933	0.048 ± 0.0005	129 ± 0.2	0.9993	0.094 ± 0.002	71 ± 0.3	0.9991
129	0.110 ± 0.004	30 ± 0.5	0.9936	0.065 ± 0.0010	77 ± 0.3	0.9995	0.110 ± 0.001	51 ± 0.2	0.9992
172	0.129 ± 0.004	26 ± 0.3	0.9925	0.071 ± 0.0010	66 ± 0.2	0.9995	0.114 ± 0.001	42 ± 0.2	0.9994

5.8 Latent Effectiveness

The latent effectiveness of an energy wheel with the same coating materials and matrix geometry as the small-scale exchangers was calculated with the DEM. With the known time constants and weighting factors given in Table 5.5-5.7, Eq. (4.6) was used to calculate NTU_m and ε_L was determined by Eq. (4.1). The latent effectiveness of the exchangers at tested flow rates and four wheel angular speeds are presented in Figure 5.9. It can be seen that as the *Re* (or face velocity) increases, the effectiveness decreases. This reduction in the effectiveness is less significant at lower angular speeds. For instance, when *Re* increases from 46 to 172 in EX150-63, latent effectiveness increases by 25% at ω = 0.5 rpm and by 5% at ω = 20 rpm. The same trend is seen for the other exchangers. The exchanger effectiveness increases substantially as angular speed increases from 0.5 to 5 rpm, but changing the angular speeds from 5 to 20 causes a minor enhancement in the effectiveness specially at low face velocities (*Re* < 43).

It has been observed in the breakthrough curves that EX150-63 has better performance due to having the greatest coating mass and the largest desiccant specific surface area among the tested exchangers. In addition, the highest time constant was found for EX150-63 since it has the longest transition period. According to Eq. (4.6), the greater the time constant, the larger the NTU_m, and the higher the latent effectiveness. This is why EX150-63 has the highest latent effectiveness among the tested exchangers. On the other hand, EX160-115 has the lowest latent effectiveness even though the coating mass in EX160-115 is very close to EX150-63 and it has about twice the

coating mass of EX55-77. This could be attributed to the lower specific surface area of EX160-115 compared to the other sample. Even though EX55-77 has less coating mass than EX150-63, the latent effectiveness of both exchangers are very close at higher angular speeds. This states the significant effects of pore width and available specific surface area rather than particle size. These outcomes clearly state that a proper selection of desiccant may result in the same or enhanced energy wheel with less cost for desiccant materials.

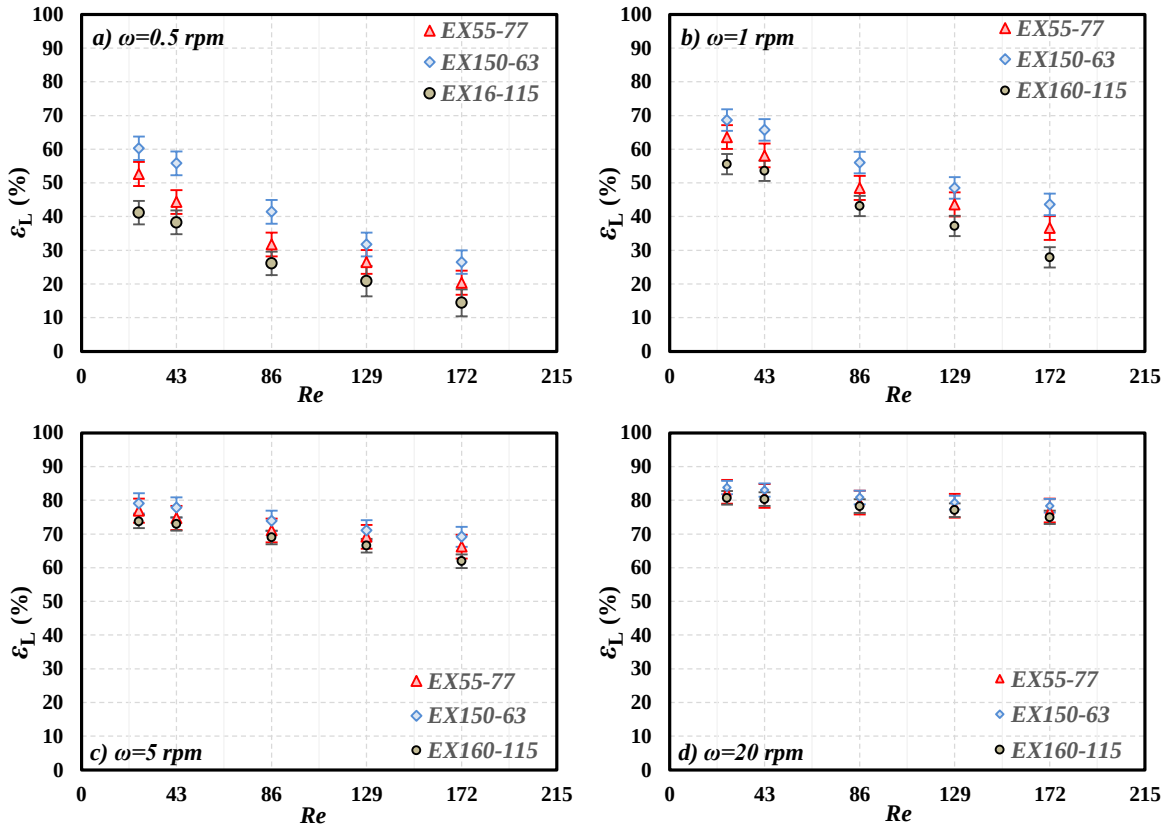

Figure 5.9-Latent effectiveness an equivalent wheel with the matrix coated with the same desiccant particles at different angular speeds and balanced supply and exhaust flow rate

Numerous data are available in the literature that provide the Yoon-Nelson fitting parameters for various desiccant packed beds at different operating conditions (Qiu et al., 2009; Xu et al., 2013). However, more investigations are required to determine the Yoon-Nelson parameters for desiccant coated matrix and calculate the wheel effectiveness from these data. For

this reason, the DEM was also applied on correlated humidity data predicted by the Yoon-Nelson model to predict the latent effectiveness. Figure 5.10 presents the latent effectiveness obtained from transient test data and Yoon-Nelson correlated values at different *Re* for ω = 0.5 rpm. Good agreement is seen between the effectiveness values at $Re \geq 86$. For lower *Re* numbers the discrepancy is within the experimental uncertainty bounds except for EX55-77 at *Re* = 26. The difference between the effectiveness values reduces below the uncertainty bounds at higher wheel angular speeds. This states that if the Yoon-Nelson model parameters are known for a desiccant coated exchanger, the DEM can be applied on the correlated results to predict the wheel's latent effectiveness at different angular speeds.

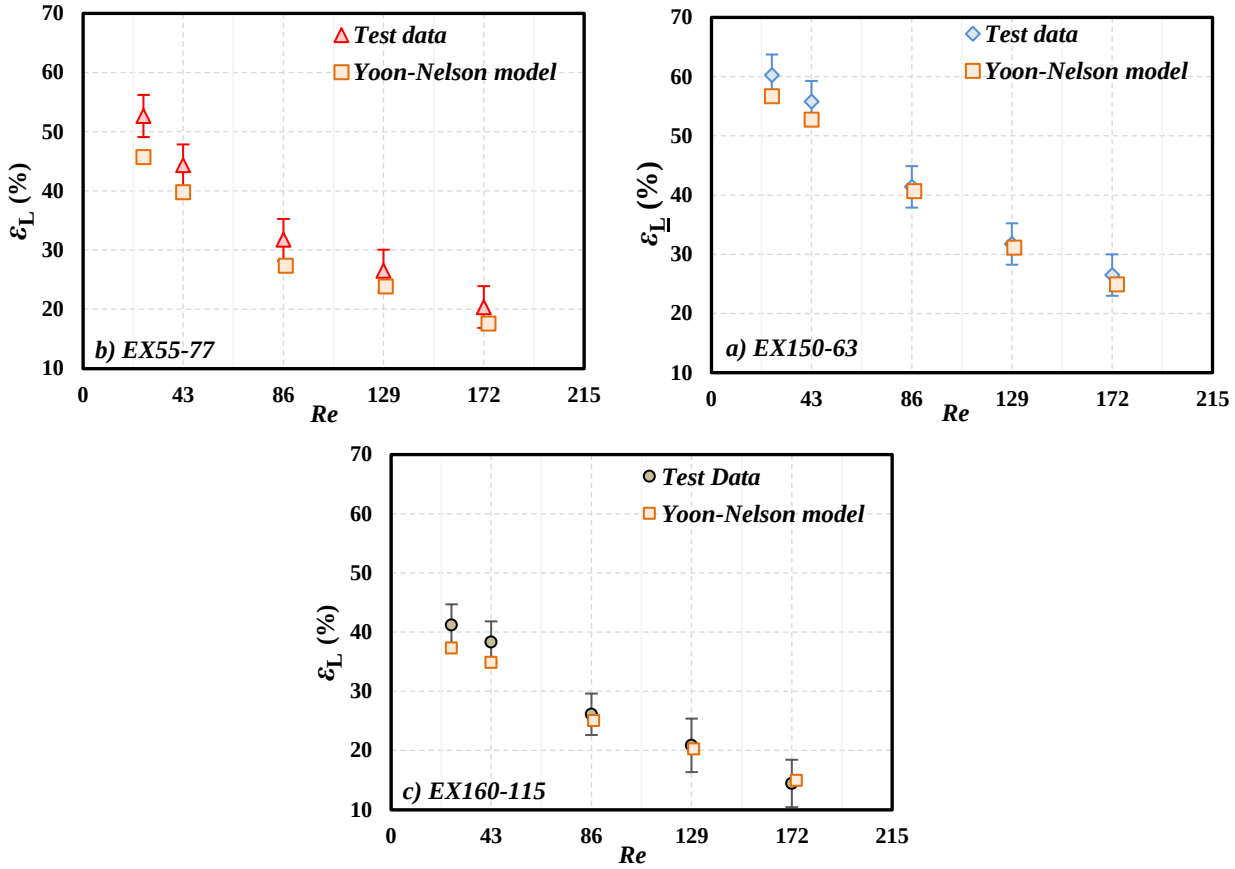

Figure 5.10-The latent effectiveness of tested exchangers obtained by applying DEM on the transient test data and Yoon-Nelson correlated data at different *Re* numbers and wheel angular speed of ω = 0.5 rpm.

5.9 Summary and Conclusions

In this study, the influence of pore width, specific surface area, and particle size of silica gel on the performance of energy wheels were investigated experimentally. Three samples of silica gel (SG55-77, SG150-63, and SG160-115) were coated on small-scale exchangers. The sorption performance of the coated exchangers were examined through their transient response (breakthrough curves) to the inlet humidity step increase at different flow rates during dehumidification. Using transient analytical/empirical model (DEM), the latent effectiveness of energy wheels comprised of the same coating and matrix geometry were obtained. The observations and outcomes of this research lead to the following conclusions:

- For the tested silica gel samples with the same functional groups, the size of the particles has insignificant influence on sorption properties of micron sized, mesoporous silica gels. However, the larger the particle size, the greater the mass of desiccant that can be deposited through the powder coating method and, consequently, the higher amount of moisture removed from the air. However, the effective diffusion coefficient is higher for larger particles which in turn lower the sorption rate.
- Pore width and specific surface area affect the sorption rate, sorption capacity, and the breakthrough curves. The smaller the pore width and larger the specific surface area, the longer transition zone in the breakthrough curves. It was suggested that the appropriate selection of pore width and specific surface area (or desiccant porosity) may lead to an optimum performance of wheels with economical considerations.
- In general, the latent effectiveness increases as the desiccant pore width reduces and the specific surface area increases. For the silica gel with close pore width (SG55-77 and SG150-63) the latent effectiveness slightly increases as the desiccant particle size increases

from 55 μm to 150 μm. This is due to the greater mass of coating for EX150-63 though the effective diffusion coefficient is larger in SG150-63.

- The latent effectiveness increases when the face velocity reduces or wheel angular speed increases. At angular speeds of ω > 20 rpm and *Re* > 129, the difference in latent effectiveness between the three tested exchangers reduces to less than 4%. This implies that at higher angular speeds and face velocity, a small enhancement in the latent effectiveness is achieved where different silica gel were used. However, in the case of drying wheels with low angular speed and face velocity (ω = 1 rpm and *Re* = 26), more than 15% enhancement was observed in the latent effectiveness of exchanger when the silica pore size reduced from 115 Å to 63 Å.
- The Yoon-Nelson model can precisely correlate the breakthrough curves of silica gel coated exchangers at different flow rates. In addition, good agreement was seen between the latent effectiveness values obtained from the measured data and Yoon-Nelson correlated results.

Although the outcomes of this research provide fundamental insights into the sorption process occurring within energy wheels, the results are only limited to mesoporous silica gel desiccant.. It should be noted that the surface groups in other desiccant may exhibit different sorption behavior toward water vapor molecules. In addition to moisture uptake, the regeneration of the desiccant is as important as dehumidification process in energy wheels. Therefore, the authors suggest more experimental/numerical studies to fully-understand the transient sorption process in desiccant wheels.

CHAPTER 6

EFFECTS OF DESICCANT CHEMICAL COMPOSITION ON MOISTURE RECOVERY

6.1 Overview

Chapter 6 completes the fourth objective of this research, "to identify the effects of physical, chemical, and sorption properties of desiccant on the latent effectiveness of *energy wheels*". In chapter 5, the influences of physical properties of desiccant particles on the latent effectiveness were studied; whereas, chapter 6 studies the effects of chemical properties of the desiccants on moisture transfer. A sample of biopolymer starch was selected for coating the exchanger and transient testing results were compared to the silica gel coated exchangers. With different chemical functional groups on the surfaces of starch and silica gel, chapter 6 discusses the chemical composition effects on the sorption process.

Since the investigation of surface functional groups requires a deep knowledge in surface chemistry, this part of the research was done through a collaborative research with Department of Chemistry, University of Saskatchewan. Dr. L. Wilson and a Ph.D. student, Ms. L. Dehabadi, collaborated in this research by providing the starch samples and performing nitrogen gas adsorption and infrared spectroscopy tests. Moreover, they assisted the thesis author (Farhad Fathieh) in analyzing the test results. The rest of the tests and data analysis mentioned in this chapter are performed by Farhad Fathieh. As the lead author of the paper, Farhad Fathieh prepared and wrote the manuscript which was published in ACS, Sustainable Chemistry & Engineering in February 2016. It worth mentioning that this collaborative research has resulted in one more manuscript which has been submitted to ACS, Sustainable Chemistry & Engineering for review, not included in this Ph.D. thesis.

Sorption Study of a Starch Biopolymer as an Alternative Desiccant for Energy Wheels

Farhad Fathieh, Leila Dehabadi, Lee D. Wilson, Robert W. Besant, Richard W. Evitts, Carey J. Simonson

6.2 Abstract

The sorption of water vapor on high amylose starch was investigated as an alternative desiccant for air-to-air energy exchangers used in ventilation units. Sorption performance of micron size mesoporous high amylose starch (HAS15, 15 µm-46 Å) and two mesoporous silica gel samples (SG13, 13 µm-62 Å and SG55, 55 µm-77 Å) were studied and compared. Transient water vapor sorption tests were performed using small-scale energy exchangers coated with HAS15 and the silica gel samples. Although N_2 gas adsorption tests showed lower sorption capacity for HAS15 compared to the silica gel samples, higher sorption rates and uptake capacity were shown for HAS15, when measured by water vapor transient sorption results. In addition, the latent effectiveness, an indicator of moisture recovery efficiency for exchangers was calculated for each exchanger. With the same amount of desiccant coated on the energy exchanger channels, the latent effectiveness of the HAS coated material was 2-13% greater than that of the silica gel materials, depending on the operating conditions.

6.3 Introduction

The moisture recovery efficiency in energy wheels is typically quantified by latent effectiveness. The latent effectiveness refers to the actual rate of moisture transfer between the supply and exhaust airstreams divided by the maximum possible rate of moisture transfer between the airstreams (Kays & London, 1984). Over the past few decades, numerous theoretical and experimental studies were carried out to investigate the performance of desiccant coated wheels at different operating conditions (Angrisani et al., 2012; Eicker et al., 2012; Enteria et al., 2010;

Goldsworthy & White, 2012; Narayanan et al., 2011; Nóbrega & Brum, 2009; Zhang & Niu, 2002). In addition, several empirical correlations have been proposed to estimate the effectiveness of hygroscopic wheels with specific matrix geometry and material composition at defined operating conditions (Jeong & Mumma, 2005; Nia et al., 2006). Although extensive data is available on the performance of hygroscopic wheels in the literature, very few investigations have considered the role of desiccant sorption characteristics (Golubovic, et al., 2006; Simonson & Besant, 1998; Simonson & Besant, 1999; Simonson & Besant, 1999). However, due to the complexity of the sorption process, molecular interactions between the adsorbent and adsorbate were not modeled in these simulations. As a result, the simulated outcome and empirical correlations are limited to the specified coating pattern and desiccant material. It has been reported that the desiccant sorption capacity, regeneration temperature, and sorption rate play a key role in recovering the latent energy in hygroscopic wheels (Colliers et al., 2014). In this regard, extensive research efforts have been directed toward new types of desiccants with improved sorption capacity, regeneration ability, and long-term stability. Comparatively few studies have considered biomaterials as an alternative desiccant (Zheng et al., 2014). It has been reported that polysaccharides such as starch and cellulose, have great tendency to adsorb water and organic chemicals in the liquid and vapor phase (Beery & Ladisch, 2001; Westgate & Ladisch, 1993). In a recent study, Dehabadi and Wilson (Dehabadi & Wilson, 2014) demonstrated that the linear form of starch displayed greater adsorption capacity with water relative to branched forms of starch.

Most recently, Fathieh et al. (2015) performed transient tests on a energy wheel component (small-scale heat exchanger) to predict the sensible effectiveness of a full scale energy wheel with the same matrix geometry, materials, and coating pattern. Without having to construct a full-scale wheel matrix and a cassette with the sealing, casing, external driving systems, and air ducts, the

small-scale transient testing substantially reduces the difficulties associated with the full-scale testing protocol.

According to a survey of the literature, it is believed that starch may serve as a promising adsorbent for desiccant energy wheels due to its unique sorption behavior and low cost. In spite of these considerations, few studies have been carried out to investigate the performance and stability of starch in this regard. Many previous studies have focused on the measurement of the sorption performance of different types of starch at equilibrium conditions, however; the moisture uptake/removal for energy wheels is a transient process. The main objective of this chapter is to compare the performance of wheels coated with a mesoporous high amylose starch (HAS) and mesoporous silica gel samples. The physical and sorption properties of the desiccants were characterized through several methods. In addition, nitrogen and water vapor adsorption was studied for the desiccant particles and coated exchangers, respectively. Moreover, the latent effectiveness of the energy wheels was predicted by performing the transient test on the small-scale exchangers coated with HAS and silica gel samples.

6.4 Experimental

6.4.1 Materials

A sample of high amylose starch (HAS15, d_p = 15 μm, P_w = 46 Å) was considered for the water vapor sorption study due to its high water vapor sorption capacity compared to the other types of starch (Dehabadi & Wilson, 2014). As reference materials for sorption study, two mesoporous silica gel samples, SG55 (d_p = 55 μm, P_w = 77 Å) and SG13 (d_p = 13 μm, P_w = 62 Å) with different particle sizes and pore width were selected. Figure 6.1 shows the molecular structure of high amylose starch and amorphous silica gel.

Starch is polysaccharide available in two structural forms (i.e. amylose and amylopectin). The composition of amylose (25%) and amylopectin content (75%) is *ca*. 1:3 (w/w). Amylose

consists of D-glucopyranose monomers connected *via* α-1,4 glycosidic bonds (Manners, 1985). Amylopectin has similar molecular structure as amylose but it differs in the position of the glycosidic linkages (α-1,6) that contributes to branching of the polysaccharide chain (every 25–30 units). This is the main reason for the crystallinity of starch. The ability of starch to adsorb water is attributed to its interaction with accessible -OH groups along the polysaccharide backbone. In the case of linear starch, it can adopt a helical arrangement, as evidenced by the formation of supramolecular complexes in aqueous solution (Vårum & Smidsrod, 2004). The helical assembly of linear starch involves cooperative electrostatic interactions such as hydrogen bonding, although capillary condensation makes partial contribution to adsorption of water vapor at specific conditions (Kulik et al. , 1994; Rebar et al. , 1984; Sair & Fetzer, 1944). Silica gel is an amorphous form of silicon dioxide which exhibits a very strong affinity for water (Abere et al., 2007). The surface of silica gel is polar and comprised of Si-O-Si and Si-OH groups that can adsorb water molecules by dispersion forces and polar forces (Ng et al., 2001). The high porosity of silica gel particles affords a relatively high surface area (400-600 m^2/g) with favourable adsorption capacity toward water vapor (0.30-0.45 $g_{water\ vapor}/g_{silica\ gel}$). In addition to its high adsorptive characteristics, silica gel can be regenerated by low grade heat sources in the range 50-90 °C, illustrating its utility as a good adsorbent for energy wheels.

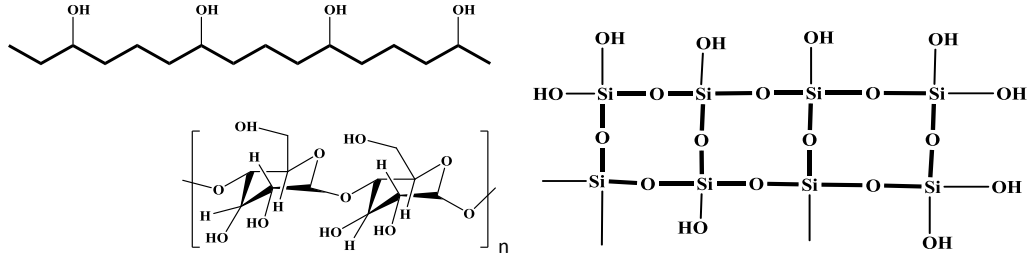

(a) (b)

Figure 6.1-A conceptual view of the molecular structure of a) high amylose "linear" starch where the unit in parentheses show the glycosidic linkage of a disaccharide fragment of starch and the various hydroxyl groups (n reflects the chain length of starch) , and b) a 2-D perspective of the framework and surface structure of an amorphous silica gel.

6.5 Characterization of the Samples

In order to specify the surface functional groups of HAS and silica gel samples, Fourier Transform infrared (FTIR) spectra were obtained with a BIO-RAD FTS-40 spectrophotometer operating in diffuse reflectance mode. Multiple scans were obtained with a 4 cm^{-1} resolution and corrected against spectroscopic grade potassium bromide (KBr) background as the sample matrix over the spectral range of 400–4000 cm^{-1}. The particle size of the samples were measured by Mastersizer S Long Bench Particle Size Analyzer (PSA), Malvern Instruments. The particle size was detected by capturing of the scattering pattern from the sample once they passed through a laser beam.

To obtain the surface area and pore width distribution of the adsorbents, nitrogen gas adsorption tests were performed by using a Micromeritics ASAP 2020 (Norcross, GA). The surface area was calculated from the adsorption isotherm (Copeland et al., 2009) and the micropore surface area was determined using the de Boer *t*-plot method (Broekhoff, 1968). Images of the surface morphology of the exchanger sheets coated with the desiccant materials were obtained using a scanning electron microscope (SEM) using a Hitachi FEG-SEM SU6600.

6.6 Small-Scale Exchanger

To study the transient behavior of the energy wheel, three small-scale exchangers were built which were coated with HAS15, SG13, and SG55 particles. The geometry and dimensions of the exchangers were illustrated by the schematic in Figure 4.2. The powder coating method, discussed in section 4.5.2 was used to coat the aluminum substrate of the exchangers.

6.7 Transient Test Facility

The transient test facility, presented in section 4.5.3. was used to subject the stationary coated energy exchangers to a sudden change in the inlet humidity. The schematic of the transient

test setup was shown before in Figure 4.3. To perform the single step transient tests, dry and humid airstreams were provided, as listed in Table 6.1.

Table 6.1-Air condition properties and the flow rates for the transient adsorption/desorption tests

Volumetric flow rate (L/min)	Face velocity (m/s)	Re_{dh}	Air temperature (°C)	P_{atm} (bar)	Dry airstream RH (%)	Humid airstream RH (%)	ΔRH_{st} (%)
15 ± 1	0.05 ± 0.005	26 ± 1	22.5 ± 0.5	1.01	4 ± 2	44 ± 2	40 ± 2

6.8 Results and Discussion

6.8.1 Desiccant and Coated Sheets

The IR spectra of silica gel samples and high amylose starch are shown in Figure 6.2. The following characteristic IR bands for high amylose starch are observed: O-H stretching ~3400 cm^{-1}, C-H stretching ~2900 cm^{-1}, and C-C stretching ~1600 cm^{-1} (Crini, 2005). Characteristic ring vibrations and anomeric C-H deformation bands are observed between 900 and 550 cm^{-1}. The IR results for the silica gel materials show an intense band at 1092 cm^{-1} which relate to the stretching vibration of the Si-O bond, 803 cm^{-1} band according to the ring structure of SiO_4, along with a 464 cm^{-1} band due to deformation vibration of Si-O-Si (Decottignies et al., 1978; Gallas et al., 1997; Gillis-D'hamers et al., 1993; Maniar et al., 1990; Almeida & Pantona, 1990; Rumph & Schubert, 1978; Wood & Rabinovich, 1989). In addition to Si-O bands, there is a broad band at 3440 cm^{-1} due to the presence of hydroxyl groups. The spectral frequencies and features for high amylose starch and silica gel are in agreement with a reported study (Costa et al., 1997).

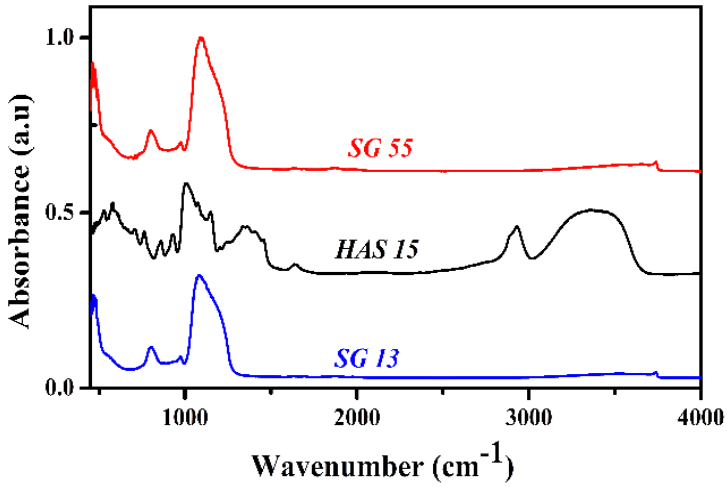

Figure 6.2-IR spectra of the silica gels and high amylose starch samples

Figure 6.3 shows the volume distribution of the samples with respect to the particle size where the average particle diameter (d_p) values are listed in Table 6.2. Based on the particle size measurements, SG55 has the largest average particle diameter (55 μm); whereas, the particle diameter of SG13 and HAS15 are nearly identical (13-15 μm). In Figure 6.3, the results for SG55 and HAS55 indicate a relatively narrow particle size distribution (PSD). The greater band width observed for SG13 reveals a PSD with a wider range as compared with HAS15 and SG55 in Table 6.2. Although the samples show mesoporous character, the available S_A of HAS15 is considerably less than the silica gel samples. The nitrogen adsorption isotherms are displayed in Figure 6.4 where comparatively steep hysteresis loops occur at the relative pressure P/P^0= 0.6 for SG15 and SG13, in agreement with the mesoporous network structure of silica gel. Although the chemical composition of the silica gel materials are similar, SG13 adsorbs more N_2 uptake compared to SG55 at relative pressures (P/P^0) below 0.8. This is attributed to the monolayer adsorption of N_2 onto the silica gel surface. As a result, SG13 with its larger S_A (478 m^2/g), greater uptake was observed relative to SG55 (S_A = 392 m^2/g). On the other hand, at higher relative pressures (P/P^0 > 0.8), the sorption capacity of SG55 increased and converged to values observed

for SG13. The results coincide with the larger pore width and pore volume of SG55, which are the key parameters for such sorption processes at higher P/P^0 values (Li et al., 2007). In comparison to SG samples, the HAS15 shows lower N_2 uptake at each P/P^0 value, in accordance with its lower S_A. Consequently, reduced interactions may occur between N_2 and the HAS15 surface. At $P/P^0 \sim 0.8$, greater adsorption of N_2 occurs due to adsorption at the grain boundaries. At $P/P^0 < 0.8$, the hysteresis is seen in the sorption isotherms occur such that the moisture content is lower for desorption curves compared to the adsorption curve at the same P/P^0 value. This could be attributed to shrinkage of the HAS15 polymer framework at low relative pressures and expansion of the framework at higher relative pressures due to pore filling of the adsorption sites with nitrogen. This behavior is common for analogous types of network polymers (Ayoub & Rizvi, 2009).

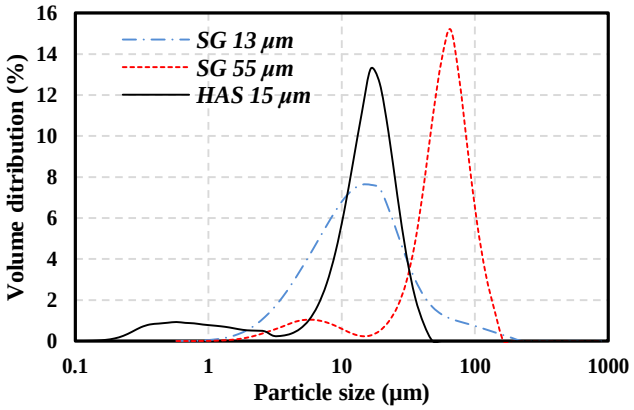

Figure 6.3-Particle diameter distribution of silica gel desiccant obtained from laser particle size analyzer

Table 6.2-Physical properties of the desiccant samples obtained by laser particle size analyzer* and N_2 gas adsorption†

Sample ID	*Material*	*d_p (µm)*	*Average P_W† (Å)*	*Accessible S_A† (m^2/g)*	*Pore volume P_v† (cm^3/g)*
HAS15	High Amylose Starch	15	46	0.56	0.0006
SG13	Silica Gel	13	62	478	0.7409
SG55	Silica Gel	55	77.5	392	0.7595

The average pore width (P_W) and particle surface area (S_A), obtained through N_2 gas adsorption tests are listed

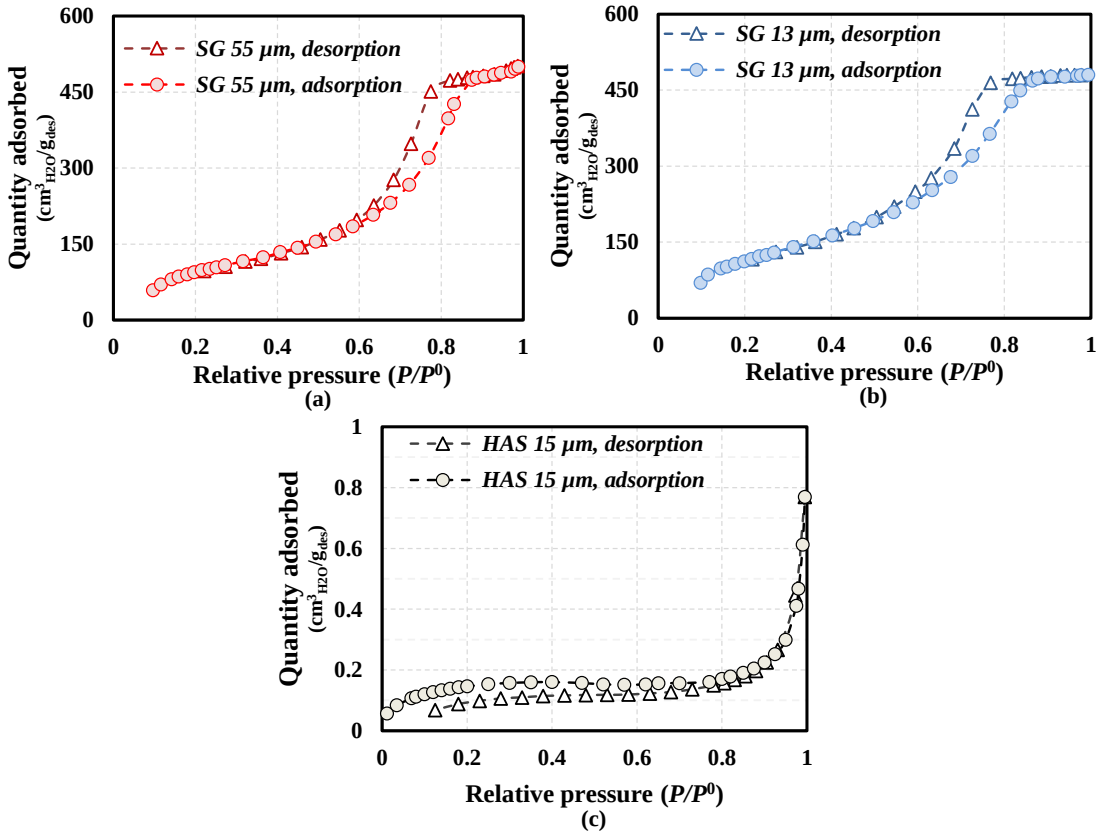

Figure 6.4-Sorption isotherms for a) SG 55, b) SG13 and c) HAS15 obtained through N_2 gas sorption test at 77 K (Solid lines serve as an illustrative guide)

Figure 6.5 shows the SEM images of the coated surface of the aluminum sheets used in the small-scale exchangers. Accordingly, the silica gel particles have irregular shapes with sharp edges while the starch particles are smoother in shape. The SEM images also show a layer of coated particles with almost uniform coating pattern for each of the samples. With this coating method, the particles are not fully submerged into the acrylic bonding agent. The improved coating method enables investigation of the sorption properties of the particles whilst minimizing small effects due to the bonding agent. However, the surface of the substrate was not entirely coated with desiccant particles, potentially contributing to water vapor sorption *via* polar groups of the acrylic resin. The effects of bonding agent on the sorption during the dehumidification and regeneration steps are discussed further in section 3.2.

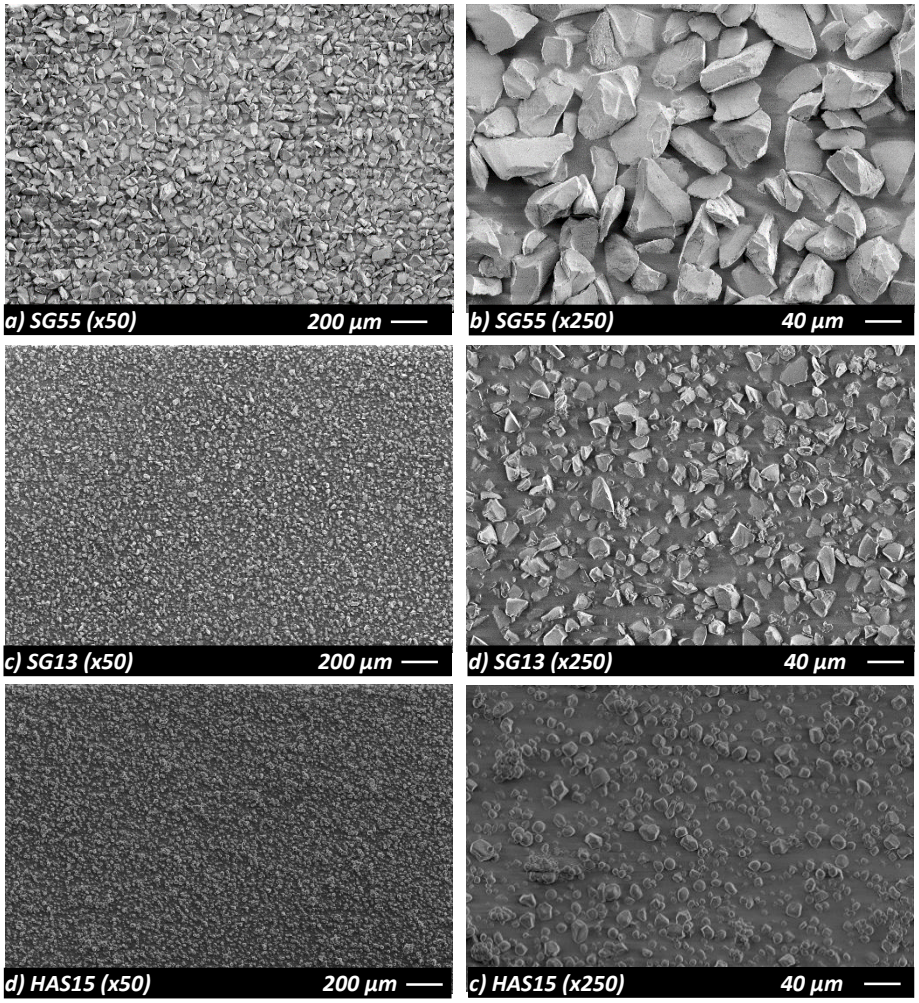

Figure 6.5-SEM images of aluminum substrate coated with HAS15, SG13, and SG55 at two levels of magnification

Table 6.3 gives the total mass of desiccant particles coated onto each exchanger. The amount of SG55 coated on the sheets is about three-fold larger than SG13 and HAS15. The observed effect is also supported from a study that relates coating efficacy to particle textural properties since there is a greater number of particles with fine powder grains, compared with coarse particle grains (Zhu, & Zhang, 2005). It should be noted that the level of coating for industrial energy wheels is about 0.8-1.6 mg/cm^2 (Jeong & Mumma, 2005) which indicates that the coating level for the small-scale exchanger described herein is within the acceptable range.

Table 6.3-Mass of coated particles on the small-scale coated exchangers

Sample	Total mass coated (g)	Mass coated per unit area (mg/cm²)	Mass of desiccant to mass of the matrix (%)
HAS15	3.20 ± 0.02	0.667 ± 0.004	0.6
SG13	3.12 ± 0.02	0.650 ± 0.004	0.6
SG55	9.32 ± 0.02	1.941 ± 0.004	1.9

6.8.2 Transient Test

The transient relative humidity and temperature curves during the dehumidification and regeneration tests are shown in Figure 6.6. It can be seen that the relative humidity gradually increases (for dehumidification test in Figure 6.6 (a)) or decreases (for regeneration test in Figure 6.6 (b)), it approaches the equilibrium and reaches the inlet relative humidity ($RH_{\text{inlet, deh}}$ = 44 ± 2% and $RH_{\text{inlet, reg}}$ = 4 ± 2%). The temperature profiles for dehumidification and regeneration are also presented in Figure 6.6 (c) and Figure 6.6 (d)**,** respectively. A temperature increase during the dehumidification in Figure 6.6 (c) is a result of heat of adsorption, whereas; the temperature decreases during the desorption process, Figure 6.6 (d). Based on the results in Figure 6.6, the temperature at the outlet of SG55 exchanger varies by 1.1 ± 0.2 °C which is substantially larger than the temperature variations for HAS15 (0.5 ± 0.2 °C) and SG13 (0.1 ± 0.2 °C), which within the thermocouple uncertainty bounds. This is due to the fact that a higher amount of SG55 was coated onto the sheets and, consequently, greater moisture sorption occurred within the SG55 exchanger. However, if the sorption temperature variations for SG13 and HAS15 (with only 2.5% different in their coating mass) are compared, it is realized that the temperature variations are *c.a.* 4-5 times larger in HAS15. This implies that the enthalpy of the sorption process is greater for HAS15 which may be due to the stronger bonds between the adsorbed water vapor molecules and hydroxyl groups on the HAS15 surface. It should be noted that further analytical study can be applied on the results to determine the enthalpy of sorption for the tested desiccant through the methods presented in the literature (Tao et al., 1992).

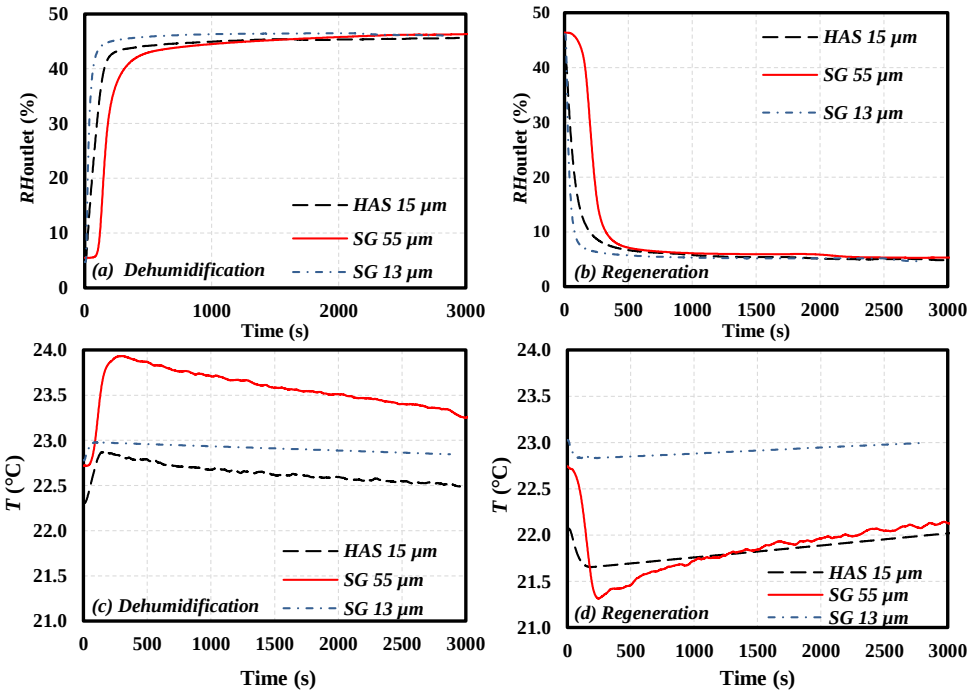

Figure 6.6-Relative humidity and temperature variations at the outlet of the exchangers during the dehumidification and regeneration tests (maximum uncertainty in the experimental data is U_{RH} = ±2 % and U_T = ±0.2 °C)

For each test, the exchanger response was decoupled from the humidity response of the sensors through the method proposed by Wang, et al. (2006). The response of the humidity sensors was measured by monitoring the readings of the hollow test cell as it was subjected to the step humidity increase/decrease. The humidity sensor response is illustrated by Figure 6.7. The sensor response time (based on 90% of output) was estimated to be 22 s for dehumidification and 21 s for regeneration. To determine if the aluminum substrate and acrylic adhesive participate in the sorption of water vapor to variable extents, the response of non-coated exchangers with aluminum sheets and sheets covered with bonding agent are shown in Figure 6.7. The trends demonstrate that the transient response for both the aluminum sheets and sheets with acrylic adhesive are nearly identical to the humidity sensor response. This implies that the sheets and adhesive bonding do not contribute significantly to water vapor sorption for the dehumidification process.

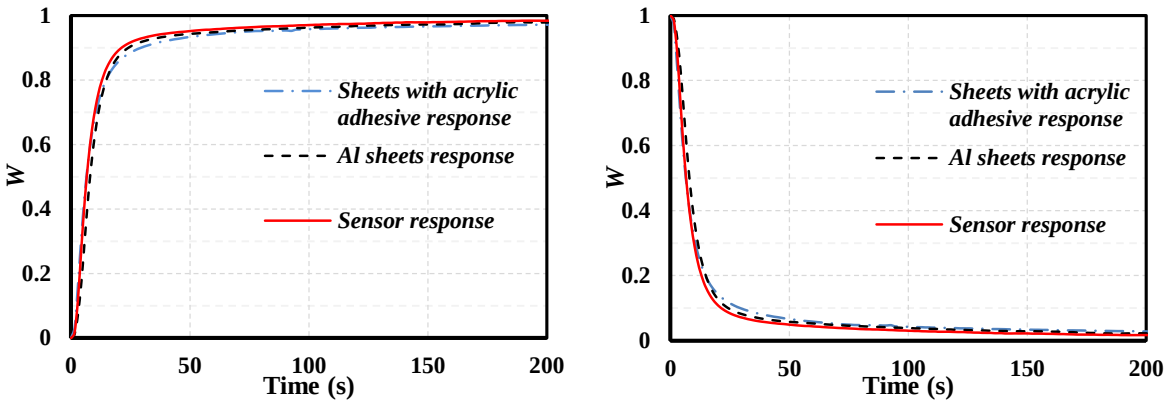

Figure 6.7-The normalized humidity ratio (*W*) for sensor, aluminum substrate and acrylic adhesive agent during the a) dehumidification and b) regeneration transient testing (maximum uncertainty in the experimental data is U_W = ±0.05)

Breakthrough curves were obtained for each exchanger by plotting the normalized humidity ratio versus testing time. The response *via* the breakthrough curves of the coated exchangers (SG55, SG13, and HAS15) during the dehumidification and regeneration period are shown in Figure 6.8**.** Accordingly, the air humidity ratio at the outlet of the exchanger gradually increased/decreased until it approached the inlet air humidity ratio during the dehumidification and regeneration processes. At the initial stage of the test, the desiccant particles can adsorb/desorb nearly all the water vapor in the airflow and, consequently, no apparent changes in the normalized humidity are observed. During dehumidification, Figure 6.8 (a), the air humidity ratio at the outlet of SG55 exchanger has the lowest value compared to SG13 and HAS15, indicating that more water vapor is adsorbed by SG55 desiccant particles. Hence, higher performance is expected for the SG55 exchanger coating, while SG13 shows the least optimal performance. The same trend is observed for the regeneration cycle (*cf.* Figure 6.8 (b)) where the SG55 material displays an optimal regenerative performance. In fact, the greater sorptive uptake of SG55 is attributed to the greater mass of SG55 particles coating onto the sheets (*cf.* Table 6.3). Thus, a better comparison

is made when the sorption characteristics were reported according to a mass basis (per unit mass of desiccant).

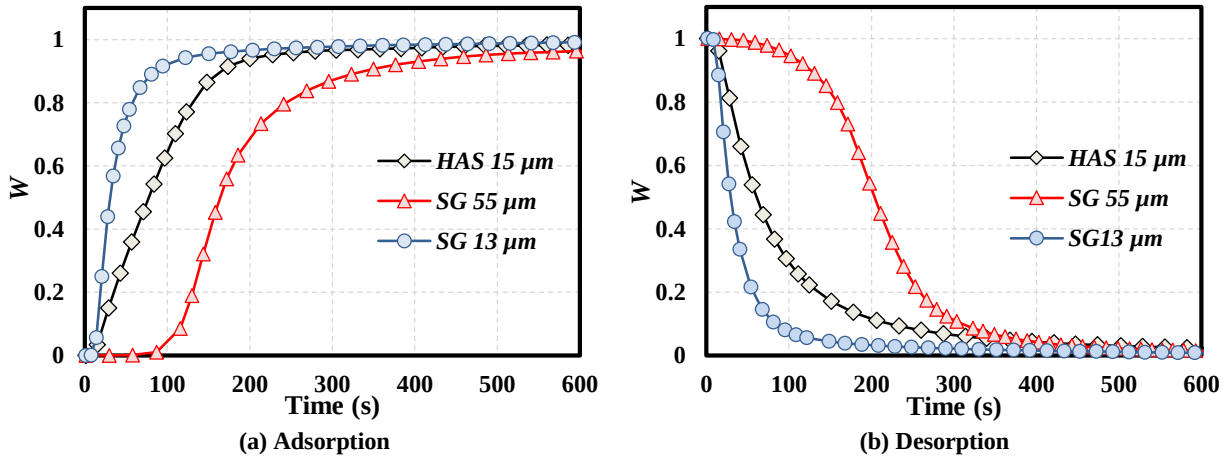

Figure 6.8-The response (breakthrough curves) of small-scale exchangers a) dehumidification (*RH* = 44% and T_{air}= 22.5 °C) and b) regeneration transient testing (*RH* = 4% and T_{air} = 22.5 °C) (maximum uncertainty in the experimental data is U_W = ±0.05)

To express the results based on unit mass of desiccant, the moisture uptake (Ω_{upt}) and moisture removal (Ω_{reg}), the amount of water vapor adsorbed/desorbed by per gram of desiccant during the dehumidification and regeneration cycle, were calculated by (5.2) The moisture uptake and removal for coated exchangers is shown in Figure 6.9. Accordingly, it can be seen that the silica moisture uptake of SG13 is higher than that of SG55 at the beginning of the test, t < 200 s (Figure 6.9 (a)). Thereafter, the moisture uptake of both the silica gel samples becomes almost identical, where the effect agrees with the results for the N_2 gas uptake isotherms, where SG13 reveals slightly greater N_2 uptake at P/P^o = 0.45 and T = 77 K. However, a direct comparison between the N_2 and water vapor adsorption is not readily comparable due to difference in size and dipolar character of each gas along with the relative temperature conditions for the isotherms.

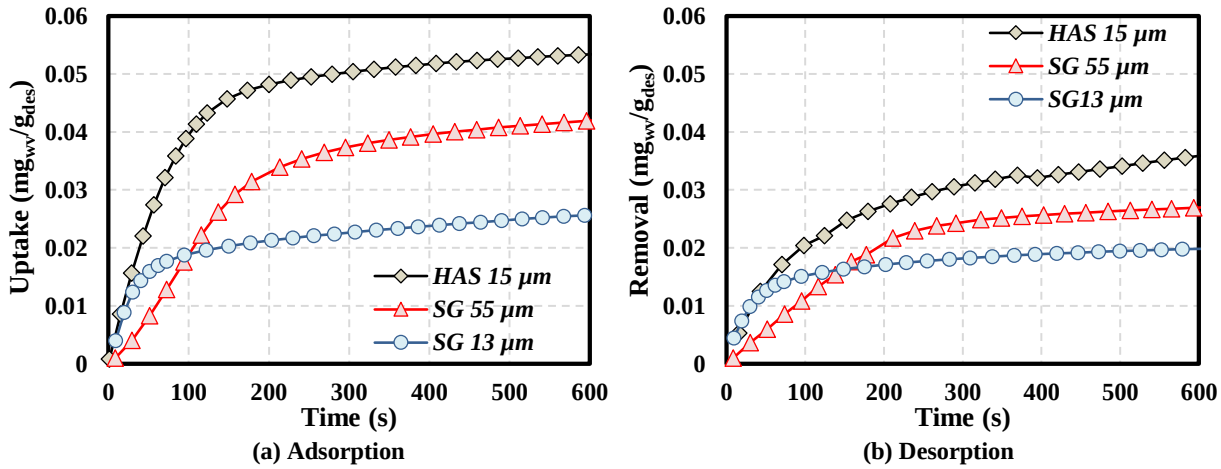

Figure 6.9-Moisture uptake/removal with time during the a) dehumidification and b) regeneration transient testing

Despite the fact that HAS15 showed poor performance for N_2 gas sorption, it has greater water vapor sorption capacity compared to the both silica gel samples. This phenomenon cannot be readily explained due to the microstructure of HAS15 since its pore size closely matches the silica gels samples, however; the accessible surface area is much lower. In fact, the high moisture uptake of the starch may be due to the strong dipolar interactions between the hydroxyl functional groups in HAS15 and the adsorbed water. In addition, new sorption sites would be formed by expansion of the framework and surface deformation of starch as hydrogen bonding likely occurs between starch particles and adsorbed water (Ayoub & Rizvi, 2009). It should be noted that the measured sorption capacities for the samples are typically underestimated since the adsorbents were not fully evacuated at the start of the adsorption test. The dehumidification and regeneration capacity can also be determined from Figure 6.9 by examining the moisture uptake and removal at the equilibrium condition (t > 600 s). The observed HAS15 dehumidification capacity is about 140% greater than that of the silica gel samples over the test period. Another observation from Figure 6.9 is the difference between the dehumidification capacity (sorption capacity) and regeneration capacity over the test period at the specified operating condition. In fact, the

dehumidification and regeneration capacity is expected to be identical (for no capillary condensation), but most of the time this was achieved by performing the test for longer duration with elevated regeneration temperature. In hygroscopic wheels, a desiccant with better regeneration transient performance is preferred due to the cyclic nature of the adsorption-desorption cycle. Based on the results presented in Figure 6.9, the complete regeneration of the samples with air at 4% *RH* at 22.5 °C and the same flow rate used for dehumidification is not apparent which suggests capillary condensation within the desiccant pores. In this situation, a greater amount of energy (temperature, flow rate, or exposure time) is required to regenerate the samples. Among the samples, HAS15 revealed the highest regeneration capacity compared to the silica gel materials. The relatively high water vapor dehumidification and regeneration capacity of HAS15 compared to silica gel materials indicate that HAS15 is a suitable alternative for energy wheels.

In addition to sorption capacity, the kinetic rate of sorption for the desiccant plays an important role in the performance of energy wheels (Abe et al., 2006a, 2006b). From the slope of moisture uptake/removal curves in Figure 6.9, the sorption rate in all cases was observed to be highest at the beginning of the test which then decays to approximately zero value as the surface becomes saturated. With the same surface functional groups, the difference in sorption rate of silica gel samples are understood by differences in their microstructural features. The fast rate of sorption at the beginning of the uptake profile is likely due to favorable interactions between the water vapor and accessible sorption sites on the external sorbent surface (Qiu et al., 2009). The similar pore width for SG13 (62 Å) and for SG55 (77 Å) indicate that the higher sorption rate observed for SG13 may be attributed to its greater accessible surface area. As the accessibility of the sorption sites decrease as the monolayer surface coverage increases for each adsorbate (N_2 or H_2O), the

sorption process is governed by molecular diffusion into micropore domains (Satoh et al., 1995). For t >170 s, the SG13 and SG55 materials reveal similar kinetic profiles which suggest the role of intrapore diffusion of water vapor. The highest sorption rate is seen for HAS15 where its greater sorption rate cannot be accounted for by the microstructural features of the samples. As discussed above, the surface functional groups play a key role in sorption of water vapor molecules, as described for the starch-based materials (Rouquerol et al., 2014).

6.9 Latent Effectiveness

The time constants and weighting factors associated with the response of HAS15, SG13, and SG55 small-scale coated exchangers were determined by fitting the DEM, eq. (4.3) to the breakthrough curves in Figure 6.8. The weighting factors and time constants are listed in Table 6.4. Using eqs. (4.6) and (4.1), the latent effectiveness of the wheels coated with HAS15, SG13, and SG55 was predicted for the dehumidification and regeneration cycles at a face velocity of 0.05 m/s (Re=26) and at different angular speeds, as shown in Figure 6.10. At each angular speed, the SG55 wheel had the highest latent effectiveness compared to the SG13 and HAS15 wheels. According to the dehumidification results in Figure 6.10 (a), the latent effectiveness of the SG55 wheel is about 8% more than the HAS15 wheel at ω = 0.5 rpm, which represents a typical angular speed for such dehumidifiers. For energy wheels with higher angular speeds (ω > 10 rpm), the difference in the latent effectiveness reduces to less than 2% which is within the experimental bounds of uncertainty. Since the breakthrough curves cannot be expressed based on a per unit mass of desiccant, the obtained weighting factors, time constants, and latent effectiveness are estimated to be mass dependent. It should be noted that since the relative amount of SG55 coating is about 3× greater than that of SG13 and HAS15, the SG55 wheel is expected to have the highest effectiveness. As silica gel particles are more expensive relative to starch, a detailed study is

required to further optimize the wheel design based on the desiccant mass and effectiveness for greater improvements. Furthermore, if an alternative coating method is available to deposit more starch particles on the substrates, the effectiveness of HAS15 wheel could be substantially increased.

Table 6.4-Time constants, weighting factors, and coefficient of determinations (R^2) for the small-scale coated exchangers obtained by fitting the DEM to the breakthrough curves

Wheel	Dehumidification					Regeneration				
	τ_1 (s)	γ_1	τ_2 (s)	γ_2	R^2	τ_1 (s)	γ_1	τ_2 (s)	γ_2	R^2
HAS15	36.4	0.80	438	0.20	0.9996	29.9	0.78	337	0.22	0.9996
SG13	22.9	0.91	291	0.09	0.9997	23.4	0.88	269	0.12	0.9998
SG55	60.2	0.86	469	0.14	0.9998	45.0	0.74	203	0.26	0.9997

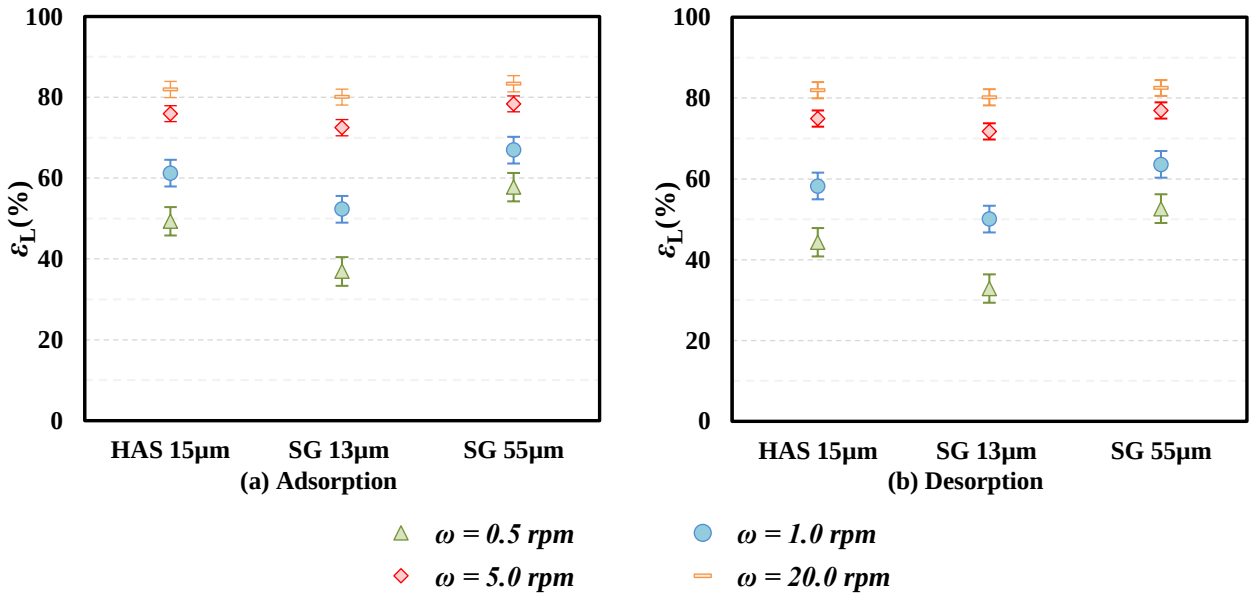

Figure 6.10-Latent effectiveness (ε_L) of energy wheels predicted through transient testing of the small-scale coated exchangers at variable conditions; a) dehumidification cycle b) regeneration cycle and for the balanced supply and exhaust flow rates

In comparison to the SG13 coated wheel, a significant improvement in the latent effectiveness of the HAS15 wheel coated was seen when using a similar amount of SG13 desiccant. When HAS15 is used instead of SG13 to coat the wheel, the latent effectiveness is enhanced by 13.0%, 8.3%, and 3.5% at ω = 0.5, 1.0, and 5 rpm, respectively. For ω > 20 rpm, the difference in the latent effectiveness of HAS15 and SG13 wheels is within the uncertainty bounds (*ca*. 2%), where the same trend is seen for the latent effectiveness estimation that was based on desorption data (regeneration cycle). Comparing the latent effectiveness in Figure 6.10 (a) and (b), it can be seen that the latent effectiveness during regeneration at ω = 0.5 rpm is *ca*. 4-5% lower than the latent effectiveness during the dehumidification step. This may be attributed to capillary condensation within the pores of desiccants which often requires more energy input when regenerating the desiccants. Based on these outcomes, it is suggested that the high amylose starch may serve as a promising alternative desiccant material for energy wheels. However, further studies are needed to investigate performance and stability of the starch and its modified forms (Dehabadi & Wilson, 2015) during the dehumidification and regeneration steps at variable operating conditions.

6.10 Summary and Conclusions

The goal of this chapter was to investigate the sorption performance of high amylose starch (HAS) as an alternative for energy wheels. N_2 and water vapor sorption isotherms were obtained for mesoporous HAS15 (d_p = 15 μm, P_w = 46 Å) and silica gel samples, SG55 (d_p = 55 μm, P_w = 77 Å) and SG13 (d_p = 13 μm, P_w = 62 Å). The N_2 gas adsorption isotherm showed that HAS15 has considerably fewer accessible sorption sites and, consequently, less sorption capacity compared to the silica gel samples. On the other hand, the transient water vapor sorption experiments at 22.5 ℃ were conducted on a small-scale exchanger coated with HAS15, SG13, and

SG55. The results illustrate that the sorption rate and capacity of HAS15 per unit mass are greater than the silica gel materials. This was likely the results of favorable electrostatic interactions between the polar hydroxyl groups on the surface of HAS with water vapor. Using the transient dehumidification and regeneration results at small-scale testing, the latent effectiveness of wheels with the same geometry and coating were predicted. It was found that the latent effectiveness was improved by 13% at angular speeds of 0.5 rpm by coating the wheel with HAS15 rather than SG13 particle grains. Compared to HAS15, the wheel coated with SG55 had a latent effectiveness *ca*. 8% higher at 0.5 rpm. The apparent difference was reduced to less than 2% as the angular speed increased to more than 5 rpm. The better performance of SG55 coated wheel is attributed to the higher mass of SG55 coated on the matrix. The good sorption behavior of high amylose starch along with its biodegradability, relatively low cost, and potential for chemical modification implies that this biopolymer desiccant represents a promising material for coating energy wheels. However, further research is needed to investigate the sorption performance of HAS at different operating conditions and its durability over a longer life cycle of the device. In addition, further studies are required to show the effects of HAS on heat transfer within the energy wheels.

CHAPTER 7

SUMMARY, CONCLUSIONS, CONTRIBUTIONS, AND FUTURE WORK

This Ph.D. thesis investigates the performance of heat/energy wheels by conducting transient testing on a component of the wheel (i.e. matrix). The main hypothesis is that the steady-state effectiveness of rotary wheels can be determined from transient measurements on stationary wheel components. To test the hypothesis, the thesis develops and validates a new transient facility and data analysis method (including uncertainty) to investigate the effects of operating conditions and desiccant properties (physical, chemical, sorption) on the performance of heat/energy wheels. The results in the thesis reveal that the hypothesis is valid for a certain range of operating conditions. In this chapter, a brief summary of the thesis, notable conclusions, and major contributions are presented. In addition, the promising topics for future work and further studies are provided.

7.1 Summary

Heat/energy wheels are commonly used in HVAC systems as a heat/energy recovery exchanger to reduce the sensible and/or latent load needed to achieve indoor thermal comfort. This Ph.D. research focuses on the feasibility of performing transient tests on a small component of the heat/energy wheel to predict the performance of a full-scale wheel comprised of the same components. Transient testing is an effective method to test wheels with reduced testing time and cost compared to conventional steady-state testing methods. The component used in this study is a few non-coated sheets for heat wheels and a few desiccant coated sheets for energy wheels.

In chapter 2, the test facility developed to perform the transient component testing on heat wheels was described. The sensors and data acquisition system were explained and the calibration process was discussed. In addition, the analytical method used to determine the sensible effectiveness from the transient data was presented and validated with correlations in the literature.

Studying transient heat transfer results with no moisture transfer, this chapter partially covered the first two objectives of the thesis, "*to develop a novel testing facility for performing the transient testing on heat wheel and energy wheel components"* and *"to predict the full-scale heat wheel effectiveness with its uncertainty and to investigate the relationship between the sensible effectiveness and operating conditions"*.

In chapter 3, the analytical model for transient testing was modified to account for a second mode of heat transfer observed in the transient testing. It was shown that this second mode can be attributed to the heat loss/gain that occurs during a test. The modified analytical model was used to decouple the second mode from the results and a sensitivity analysis was performed to study the effects of heat loss/gain on the sensible effectiveness obtained from the transient component testing. The effects of heat loss were also studied experimentally for different temperature differences between the hot and cold airstreams and various face velocities. Chapter 2 and 3, together, addressed the second objective of the thesis, *"to predict the full-scale heat wheel effectiveness with its uncertainty and to investigate the relationship between the sensible effectiveness and operating conditions".*

Chapter 4 focused on moisture transfer in energy wheel components while no heat transfer occurred during the tests. The transient test facility was modified to measure moisture transfer by adding humidity sensors and a humidifying/dehumidifying system. In addition, chapter 4 described a novel powder coating method that was used to coat the wheel component with mesoporous silica gel particles. The moisture uptake/removal occurring in the exchanger and the humidity response of the coated exchanger were studied during the transient test. With the humidity response of the wheel, the transient analytical model (developed in chapter 3) was used to analyze the data and determine the latent effectiveness. The sorption properties of the desiccant at equilibrium were

studied from nitrogen and water vapour sorption isotherms. A correlation in the literature was used to verify the transient testing results. This chapter combined with chapter 2, fully addressed the first objective of the thesis, "*to develop a novel testing facility for performing the transient testing on heat wheel and energy wheel components"*. In addition, the third objective, *"to predict the full-scale energy wheel effectiveness with its uncertainty and to investigate the relationship between the latent effectiveness and operating conditions",* was also fulfilled in this chapter.

In chapter 5, the transient component testing was used to investigate the effects of physical and sorption properties of desiccant materials on moisture recovery. Different mesoporous silica gel samples with a range of particle size and pore widths were coated on the exchanger matrix with the powder coating method. Similar to chapter 4, the humidity response of the exchangers to the inlet step humidity change and the transient moisture uptake/removal were obtained at room temperature (22 °C) and various air flow rates. Applying the modified transient model (developed in chapter 3), the latent effectiveness values were calculated for the exchangers coated with silica gel particles with different particle size and pore width. Chapter 5 focused on the fourth objective of this thesis, "t*o identify the effects of physical, chemical, and sorption properties of desiccant on the latent effectiveness of energy wheels"*.

In chapter 6, the effects of the chemical functional groups on the moisture sorption was investigated. A sample of starch was compared with two silica gel samples by coating the small-scale exchangers (energy wheel component) with the starch and silica gel samples. The transient component testing was performed on the coated exchangers. Chapter 5 addressed the fourth objective of this thesis, "*to identify the effects of physical, chemical, and sorption properties of desiccant on the latent effectiveness of energy wheels"*.

7.2 Conclusions

The following are the major conclusions and outcomes achieved through this Ph.D. research:

- The transient method of testing the heat wheel component can successfully predict the sensible effectiveness of full-scale wheels when the heat capacity rate ratio is higher than 10 and $2 < NTU < 13$. For heat capacity rate ratios of less than 0.5, the modified transient model should be used to account for heat loss/gain in the transient testing. Comparing the sensible effectiveness values calculated from the transient testing and the literature correlations, it is observed that the transient component testing results in the lower sensible effectiveness values (more than 5% difference at $C_r^* > 5$) if heat losses are not considered.
- The transient method of testing the energy wheel component can successfully predict the latent effectiveness at certain operating conditions. Good agreement is seen between the effectiveness valued determined by the transient test method and the literature correlation when $NTU_m < 4.3$ and $\omega > 4$ rpm. It should be noted that the discrepancy at low wheel angular speeds and higher NTU_m is likely due to the uncertainties involved in the calculation of the exchanger properties, such as effective area for moisture transfer and convective mass transfer coefficient.
- The sorption properties of desiccant particles can substantially affect the latent effectiveness of energy wheels. Analyzing the latent response of the silica gel coated exchangers, it was found that the latent effectiveness increases, especially at lower wheel speeds, as the desiccant pore width reduces and the specific surface area increases. At $\omega = 1$ rpm and $Re = 26$, the latent effectiveness increases by more than 15% when the pore width reduces from 115 Å to 63 Å; whereas, a small increase is observed in the latent effectiveness at $\omega = 20$ rpm.

- For the silica gels with similar pore widths (77 Å and 63 Å), the latent effectiveness slightly increases (3-5% at ω = 20 rpm) as the desiccant particle size increases from 55 μm to 150 μm. This is due to the greater mass of coating obtained through the powder coating for larger particles. In general, the influence of particle size on the latent effectiveness is less important than pore width for mesoporous silica gel samples.
- The sorption rate and capacity of high amylose starch per unit mass are greater than the mesoporous silica gel samples studied in this thesis. This was likely the results of favorable electrostatic interactions between the polar hydroxyl groups on the surface of starch and the water vapor molecule. The predicted latent effectiveness was 13% higher (at ω = 0.5 rpm) for a wheel coated with starch rather than silica gel. Almost the same latent effectiveness is observed for starch and silica gel coated exchangers when ω > 20 rpm. Considering that starch typically costs less than silica gel, the results show a good potential for the starch to be used as an alternative desiccant in the energy wheels.
- It is suggested that a desiccant material with a higher sorption rate and a higher sorption capacity will have a higher latent effectiveness. A small pore width and a high specific surface area will result in a high sorption capacity. However, the sorption rate reduces as the pore size decreases. For this purpose, the transient testing of wheel components can be used to test desiccants with a range of microstructure, and ultimately, would aid in the development of improved wheels without requiring an entire wheel to be constructed.

7.3 Contributions

The outcomes of this research contribute towards designing enhanced heat/energy wheels. The main contributions of this Ph.D. thesis are as listed below:

7.3.1 Transient Component Testing of Heat Wheels and Energy Wheels

- A novel test facility was developed to perform transient testing on the components of heat/energy wheels.
- The wheel components for transient tests were designed in the form of a small-scale parallel-plate exchanger and a powder coating method was developed to deposit micron size desiccant particles on a laboratory-scale wheel matrix with small interaction with bonding agent.

7.3.2 Performance Analysis for Wheel Component and Full-Scale Wheel

- The transient analytical model was modified and validated specifically for the transient component testing.
- The transient component test data were used to determine the sensible and latent effectiveness and the results were validated with effectiveness values determined from correlations of full-scale wheels with the same flow channel geometry, dimensions, and materials.
- The uncertainty bounds for the transient component testing were identified.
- The effects of air flow rate, temperature, and humidity on the heat and moisture transfer were investigated and validity ranges for the transient component testing were determined.

7.3.3 Desiccant Selection based on the Transient Component Testing of Energy Wheels

- The kinetics of sorption were investigated using the transient test. While standard equilibrium tests can determine the sorption capacity of desiccants, the transient test is a useful method to study the sorption rate and kinetics of moisture transfer.

- The transient moisture uptake/removal was correlated to the physical, chemical, and sorption properties of desiccants and the performance of wheels with different desiccant particles were compared.
- The thesis showed that the transient method can be used to study new materials (*e.g.* biopolymer starch) and alternative desiccants can be proposed to coat the energy wheels.

7.4 Future Work

7.4.1 Coupled Heat and Moisture Transfer Study

Since heat and mass transfer occur simultaneously in energy wheels, it is recommended to study coupled heat and moisture transfer in energy wheels by performing transient component testing. The heat of phase change during the sorption process can significantly alter the thermal response of the wheel. These effects were observed in some of the experiments which were not presented in this thesis. To account for the changes in sensible effectiveness due to heat of phase change, the analytical model should be modified. In addition, the influence of temperature on the sorption properties of desiccants (sorption rate, sorption capacity) could be investigated using the transient component testing. Further study is required to investigate the effects of thermal properties of the desiccant on the sensible effectiveness. Increasing the internal porosity while keeping the pore width constant is expected to reduce thermal conductivity of a desiccant. This may increase the thermal resistance for heat transfer, and consequently, reduces the sensible effectiveness.

7.4.2 Modification of Transient Analytical Model and the Test Facility for Counter-Flow Arrangement

The analytical model developed in this thesis corresponds to the experiments with parallel airflow. Then, the results were transformed to determine the effectiveness of the wheel with a counter-flow arrangement. This caused a large uncertainty at some specific operating conditions.

Therefore, it is suggested to modify the test facility to allow the component testing to be performed under a counter-flow arrangement. Furthermore, the analytical model should be modified in order to relate the thermal and latent response of the wheel component in the counter-flow arrangement to the sensible and latent effectiveness of full-scale wheels. This would also be beneficial for performing cyclic tests as the inlet conditions are similar to full-scale wheels.

7.4.3 Transient Component Testing for Desiccant Wheels

Since desiccant drying wheels are widely used in desiccant cooling and dehumidifying systems, it is recommended to extend the transient testing to study desiccant drying wheel components. The main challenge in this work would be modeling the significant heat of sorption. In the case of desiccant wheels, the temperature and humidity profiles along the wheel change significantly and these need to be accurately estimated. With the temperature and humidity profiles in the desiccant drying wheel, a similar analytical method, as given in Chapter 2, can be followed to develop a transient analytical model for desiccant drying wheels in a counter-flow arrangement.

7.4.4 Durability Tests and Life Cycle Analysis

The results presented in Chapter 7 showed that starch has great potential for coating energy wheels. However, factors such as the feasibility of using industrial processes to coat the starch on a wheel, the durability of the coating, and desiccant costs were not considered in this chapter. Further durability and economic studies are recommended for any proposed desiccants over a 5-10 year life cycle of wheels. In addition, testing the desiccant at extreme conditions (e.g. very hot and humid) is required to fully address the durability and performance of these materials.

REFERENCES

Abe, O. O., Simonson, C. J., & Besant, R. W. (2006a), Relationship between energy wheel speed and effectiveness and its transient response, part I: mathematical development of the characteristic time constants and their relationship with effectiveness. *ASHRAE Transactions, **112***, 89–102.

Abe, O. O., Simonson, C. J., & Besant, R. W. (2006b), Relationship between energy wheel speed and effectiveness and its transient response, part II: comparison between mathematical model predictions and experimental measurements and uncertainty analysis. *ASHRAE Transactions, **112***, 103–115.

Abe, O. O., Simonson, C. J.., Besant, R. W., & Shang, W. (2006a), Effectiveness of energy wheels from transient measurements. Part I: Prediction of effectiveness and uncertainty. *International Journal of Heat and Mass Transfer, **49*** (1–2), 52–62.

Abe, O. O., Simonson, C. J., Besant, R. W., & Shang, W. (2006b), Effectiveness of energy wheels from transient measurements: Part II—Results and verification. *International Journal of Heat and Mass Transfer*, ***49*** (1–2), 63–77.

Abere, T. A., Okeri, H. A., & Okafor, L. A., (2007), Comparative evaluation of selected starches as adsorbent for Thin-layer Chromatography, *Tropical Journal of Pharmaceutical,**4*** (1), 331-339.

Almeida, R. M., & Pantano, C. G., (1990). Structural investigation of silica gel films by infrared spectroscopy. *Journal of Applied Physics, **68*** (8), 4225–4232.

Angrisani, G., Minichiello, F., Roselli, C., & Sasso, M., (2012), Experimental analysis on the dehumidification and thermal performance of a desiccant wheel. *Applied Energy*, ***92***, 563–572.

ANSI/AHRI, (2014), *ARI Standard 1060-2011, Performance rating of air-to-air heat exchangers for energy recovery ventilation equipment*, Arlington: Air-Condition and Refrigeration Institute.

ANSI/ASHRAE, (2013), *Standard 84, Method of testing air-to-air heat/energy exchangers*, Atlanta.

ASHRAE, (2008). ASHRAE, HVAC systems and equipments. Atlanta.

Ashrae, & IES, (2011). *ANSI/ASHRAE/IES Standard 90.1-2010 Energy Standard for Buildings Except Low-Rise Residential Buildings*, *Ashrae Standard*.

Asiedu, Y., Besant, R. W., & Simonson, C. J., (2004), Wheel selection for heat and energy

recovery in simple HVAC ventilation design problems, *ASHRAE Transactions*, ***110*** (1), 381–398.

Asiedu, Y., Besant, R. W., & Simonson, C. J., (2005), Cost effective design of dual heat and energy recovery exchangers for 100% ventilation air in HVAC cabinet units, *ASHRAE Transactions*, ***111*** (1), 857–872.

Ayoub, A. S., & Rizvi, S. S., (2009), An Overview on the Technology of Cross-Linking of Starch for Nonfood Applications. *Journal of Plastic Film and Sheeting* , ***25*** (1), 25–45.

Baclic, B. S., (1985), The Application of Galerkin Method to the Solution of the Symmetric and Balanced Counterflow Regenerator Problem, *Transactions of ASME, Journal of Heat Transfer*, ***107***, 221–241.

Bartell, F. E., & Bower, J. E., (1952), Adsorption of vapors by silica gels of different structures. *Journal of Colloid Science*, ***7*** (1), 80–93.

Bauccio, M., (1993), *ASM Metals Reference Book*, 3rd Ed., Materials Park, OH.

Beery, K. E., & Ladisch, M. R., (2001), Chemistry and properties of starch based desiccants. *Enzyme and Microbial Technology*, ***28*** (7-8), 573–581.

Benesi, H. A., & Jones, A. C., (1959), An infrared study of the water-silica gel system. *The Journal of Physical Chemistry*, ***63*** (2), 179–182.

Bolster, J., (2012), *Improved desiccant coating for heat and water vapour transfer on the matrix surfaces of air-to-air regenerative wheels*, M.Sc. Thesis, University of Saskatchewan.

Broekhoff, J., (1968), Studies on pore systems in catalysts XI. Pore distribution calculations from the adsorption branch of a nitrogen adsorption isotherm in the case of ink-bottle type pores. *Journal of Catalysis*, ***10*** (2), 153–165.

Brunauer, S., Deming, L. S., Deming, W. E., & Teller, E., (1940), On a theory of the van der Waals adsorption of gases. *Journal of the American Chemical Society*, ***62*** (7), 1723–1732.

Buyukalaca, O., & Yilmaz, T., (2002), Influence of rotational speed on effectiveness of rotary-type heat exchanger, *Heat and Mass Transfer*, ***38***, 441–447.

Chang, K.-S., Chen, M. T., & Chung, T.W., (2005), Effects of the thickness and particle size of silica gel on the heat and mass transfer performance of a silica gel-coated bed for air-conditioning adsorption systems, *Applied Thermal Engineering*, ***25*** (14-15), 2330–2340.

Chua, K. J., & Chou, S. K., (2003), Low-cost drying methods for developing countries, *Trends in Food Science & Technology*, ***14*** (12), 519–528.

Ciepliski, D. L., (1997), *Testing an Air-to-Air Energy Recovery Device Using Performance Test Standards*. M.Sc. Thesis, University of Saskatchewan.

Collier, R. K. J., (1989), Desiccant properties and their effect on cooling system performance. *ASHRAE Transactions*, ***95***, 823–827.

Copeland, L., Blazek, J., Salman, H., & Tang, M. C., (2009), Form and functionality of starch. *Food Hydrocolloids*, ***23*** (6), 1527–1534.

Costa, T. M. H., Gallas, M. R., Benvenutti, E. V., & da Jornada, J. A. H., (1997), Infrared and thermogravimetric study of high pressure consolidation in alkoxide silica gel powders, *Journal of Non-Crystalline Solids*, ***220*** (2-3), 195–201.

Crini, G., (2005), Recent developments in polysaccharide-based materials used as adsorbents in wastewater treatment, *Progress in Polymer Science*, ***30*** (1), 38–70.

Decottignies, M., Phalippou, J., & Zarzycki, J., (1978), Synthesis of glasses by hot-pressing of gels, *Journal of Material Science*, ***13***, 2605–2618.

Dehabadi, L., & Wilson, L. D., (2014), Polysaccharide-based materials and their adsorption properties in aqueous solution, *Carbohydrate Polymers*, ***113***, 471–9.

Dehabadi, L., & Wilson, L. D., (2015), An NMR investigation of the fractionation of water-ethanol mixtures with cellulose and its cross-linked biopolymer forms, *Energy & Fuels*, ***29*** (10), 6512-6521.

Donohue, M. D., & Aranovich, G. L., (1999), A new classification of isotherms for Gibbs adsorption of gases on solids, *Fluid Phase Equilibria*, ***158-160***, 557–563.

Eduardo, C., & Nóbrega, L., (2014), *Desiccant-Assisted Cooling Fundumentals and Applictions*. London, Springer.

Eicker, U., Schürger, U., Köhler, M., Ge, T., Dai, Y., Li, H., & Wang, R., (2012), Experimental investigations on desiccant wheels, *Applied Thermal Engineering*, ***42***, 71–80.

Enteria, N., Yoshino, H., Satake, A., Mochida, A., Takaki, R., Yoshie, R., Baba, S., (2010), Experimental heat and mass transfer of the separated and coupled rotating desiccant wheel and heat wheel, *Experimental Thermal and Fluid Science*, ***34*** (5), 603–615.

Fathieh, F., Besant, R. W., Evitts, R. W., & Simonson, C. J., (2015), Determination of air-to-air heat wheel sensible effectiveness using temperature step change data, *International Journal of Heat and Mass Transfer*, ***87***, 312–326.

Fathieh, F., Besant, R. W., Evitts, R. W., & Simonson, C. J., (2016a), Effects of heat loss/gain on the transient testing of heat wheels, *ASME Journal of Thermal Science and Engineering Applications*, ***8*** (3), 1003-1015.

Fathieh, F., Dehabadi, L., Wilson, L. D., Besant, R. W., Evitts, R. W., & Simonson, C. J.,

(2016b), Sorption study of a strach biopolymer as an alternative desiccant for energy wheels, *ACS Sustainable Chemistry & Engineering*, ***4*** (3), 1262–1273.

Fathieh, F., Rafati Nasr, M., Sadeh, S., Besant, R. W., Evitts, R. W., Müller, J., & Simonson, C. J., (2016c), Determination of Air-to-Air Energy Wheels Latent Effectiveness Using Humidity Step Test Data. *International Journal of Heat and Mass Transfer*, Accepted manucript.

Figliola, R. S., & Beasley, D. E., (2006), *Theory and design for mechanical measurements*, New York: John Wiley & Sons, Inc.

Gallas, M. R., Rosa, A. R., Costa, T. H., & Jornada, J. A. H. da. (1997). High pressure compaction of nanosize ceramic powders, *Journal of Materials Research*, ***12*** (03), 764–768.

Ge, T. S. S., Dai, Y. J. J., & Wang, R. Z. Z., (2014), Review on solar powered rotary desiccant wheel cooling system. *Renewable & Sustainable Energy Reviews*, ***39***, 476–497.

Gillis-D'hamers, I., Vrancken, K. C., Vansant, E. F., & De Roy, G., Fourier-transform infrared photo-acoustic spectroscopy study of the free hydroxyl group vibration: dependence on the pretreatment temperature, *Journal of the Chemical Society, Faraday Transactions*, ***88*** (14), 2047–2050.

Goldsworthy, M., & White, S. D., (2012), Limiting performance mechanisms in desiccant wheel dehumidification, *Applied Thermal Engineering*, ***44***, 21–28.

Golubovic, M. N., Hettiarachchi, H. D. M. D. M., & Worek, W. M., (2006), Sorption properties for different types of molecular sieve and their influence on optimum dehumidification performance of desiccant wheels. *International Journal of Heat and Mass Transfer*, ***49*** (17-18), 2802–2809.

Golubovic, M. N., Madhawa Hettiarachchi, H. D., Belding, W., & Worek, W. M. (2006). A new method for the experimental determination of Lewis' relation. *International Communications in Heat and Mass Transfer*, ***33*** (8), 929–935.

Gorbach, A., Stegmaier, M., & Eigenberger, G., (2004), Measurement and Modeling of Water Vapor Adsorption on Zeolite 4A -Equilibria and Kinetics, ***10***, 29–46.

Greenspan, L., & others, (1977), Humidity fixed points of binary saturated aqueous solutions. *Journal of Research of the National Bureau of Standards*, ***81*** (1), 89–96.

Harding, A. W., Foley, N. J., Norman, P. R., Francis, D. C., & Thomas, K. M., (1998), Diffusion Barriers in the Kinetics of Water Vapor Adsorption/Desorption on Activated Carbons. *Langmuir*, ***14***, 3858–3864.

Haul, R., Gregg, S. J., Sing, K. S. W., (1982), *Adsorption, Surface Area and Porosity*. Auflage,

Academic Press, London.

Jeong, J.-W., & Mumma, S. A., (2005), Practical thermal performance correlations for molecular sieve and silica gel loaded enthalpy wheels, *Applied Thermal Engineering*, ***25*** (5-6), 719–740.

Kamitsos, E. I., Patsis, A. P., & Kordas, G. (1993), Infrared-reflectance spectra of heat-treated sol-gel-derived silica, *Physical Review B*, ***48*** (17), 12499–12505.

Kaplan, W., (1962), *Operational Method for Linear Systems*. Boston, Addison-Welsley Proffessional, Inc.

Kays, A. L., & London, W. M., (1984), *Compact heat exchanger*, New York: McGraw-Hill, Inc.

Kulik, A. S., de Costa, J. R. C., & Haverkamp, J., (1994), Water organization and molecular mobility in maize starch investigated by two-dimensional solid-state NMR, *Journal of Agricultural and Food Chemistry*, ***42*** (12), 2803–2807.

Kuse, T., & Takahashi, S., (2000), Transitional behavior of tin oxide semiconductor under a step-like humidity change, *Sensors and Actuators B: Chemical*, ***67*** (1-2), 36–42.

Lamberston, T. J., (1958), Performance Factor of a Periodic-Flow Heat Exchanger, *Transactions of ASME*, ***80***, 586–592.

Leech, J. A., Nelson, W. C., Burnett, R. T., Aaron, S., & Raizenne, M. E., (2002), It's about time: A comparison of Canadian and American time–activity patterns, *Journal of Exposure Analysis & Environmental Epidemiology*, *12* **(6)**, 427.

Li, X., Li, Z., Xia, Q., & Xi, H., (2007), Effects of pore sizes of porous silica gels on desorption activation energy of water vapour, *Applied Thermal Engineering*, ***27*** (5-6), 869–876.

Li, Z., Zhu, J., & Zhang, C., (2005), Numerical simulations of ultrafine powder coating systems. *Powder Technology*, ***150*** (3), 155–167.

Maniar, P. D., Navrotsky, A., Rabinovich, E. M., Ying, J. Y., & Benziger, J. B., (1990), Energetics and structure of sol-gel silicas, *Journal of Non-Crystalline Solids*, ***124*** (1), 101–111.

Manners, D., (1985), Some aspect of thr structure of starch, *Cereal Foods World*, ***30***, 461–467.

Mendell, M. J., & Heath, G. A., (2005), Do indoor pollutants and thermal conditions in schools influence student performance? A critical review of the literature, *Indoor Air*, ***15*** (1), 27–52.

Moré, J.J. & D.C. Sorensen, (1983), Computing a Trust Region Step, *SIAM Journal on Scientific and Statistical Computing*, **3**, 553–572.

Mujahid Rafique, M., Gandhidasan, P., Rehman, S., & Al-Hadhrami, L. M., (2015), A review on desiccant based evaporative cooling systems, *Renewable and Sustainable Energy Reviews*, ***45***, 145–159.

Narayanan, R., Saman, W. Y., White, S. D., & Goldsworthy, M., (2011), Comparative study of different desiccant wheel designs. *Applied Thermal Engineering*, ***31*** (10), 1613–1620.

Natural Resources Canada, (2011), *Energy Efficiency Trend in Canada 1990-2009*,.

Ng, K. C., Chua, H. T., Chung, C. Y., Loke, C. H., Kashiwagi, T., Akisawa, A., & Saha, B. B., (2001), Experimental investigation of the silica gel–water adsorption isotherm characteristics. *Applied Thermal Engineering*, ***21*** (16), 1631–1642.

Nia, F. E., van Paassen, D., & Saidi, M. H., (2006), Modeling and simulation of desiccant wheel for air conditioning. *Energy and Buildings*, ***38*** (10), 1230–1239.

Nóbrega, C. E. L., & Brum, N. C. L., (2009), Modeling and simulation of heat and enthalpy recovery wheels. *Energy*, ***34*** (12), 2063–2068.

Omer, A. M., (2008), On the wind energy resources of Sudan. *Renewable and Sustainable Energy Reviews*, ***12*** (8), 2117–2139.

Qiu, H., Lv, L., Pan, B., Zhang, Q., Zhang, W., & Zhang, Q., (2009), Critical review in adsorption kinetic models. *Journal of Zhejiang University Science*, ***10*** (5), 716-714.

R. K. Shah & D. P. Sekuli., (2003), *Fundamentals of heat exchanger design*, New York: John Wiley & Sons, Inc.

Rafati Nasr, M., Fauchoux, M., Besant, R. W., & Simonson, C. J., (2014), A review of frosting in air-to-air energy exchangers. *Renewable and Sustainable Energy Reviews*, ***30***, 538–554.

Rebar, V., Fischbach, E. R., Apostolopoulos, D., & Kokini, J. L., (1984), Thermodynamics of water and ethanol adsorption on four starches as model biomass separation systems. *Biotechnology and Bioengineering*, ***26*** (5), 513–517.

Romie, F. E., (1988), Transient Response of Rotary Regenerators, *Journal of Heat Transfer*, ***110*** (4a), 836–840.

Rouquerol, F., Rouquerol, J., Sing, K. S. W., Llewellyn, P., & Maurin, G., (2014), *Adsorption by Powders and Porous Solids*, 2nd Ed., Oxford: Academic Press.

Rouquerol, J., Avnir, D., Fairbridge, C. W., Everett, D. H., Haynes, J. H., Pernicone, N., Unger, K. K., (1994), Recommendations for the characterization of porous solids, *Pure and Applied Chemistry*, ***66*** (8), 1739–1758.

Rumph, H., & Schubert, H., (1978), *Ceramic Processing before Firing*, New York: Wiley.

Sair, L., & Fetzer, W. R., (1944), Water Sorption by Starches, *Industrial & Engineering Chemistry*, ***36*** (3), 205–208.

Satoh, S., Matsuyama, I., & Susa, K., (1995), Diffusion of gases in porous silica gel, *Journal of Non-Crystalline Solids*, ***190*** (3), 206–211.

Seppanen, O., & Fisk, W. J., (2002), Association of ventilation system type with SBS symptoms in office workers. *Indoor Air*, ***12*** (2), 98–112.

Shah, R. K., & London, A. L. (1978). *Advances in heat trnasfer, laminar flow forced convection in ducts*. New York: Academic Press.

Shang, W., & Besant, R., (2009a), Effectiveness of desiccant coated regenerative wheels from transient response characteristics and flow channel properties-Part II: predicting and comparing the latent effectiveness of dehumidifier and energy wheels using transient data and properties. *HVAC&R Research*, ***15*** (2), 346–365.

Shang, W., & Besant, R. (2009b), Performance and design of dehumidifier wheels, *HVAC&R Research*, ***15*** (3), 437–460.

Shang, W., & Besant, R. W., (2005), Effects of pore size variations on regenerative wheel performance. *Journal of Engineering for Gas Turbines and Power*, ***127*** (1), 121.

Shang, W., & Besant, R. W., (2008), Theoretical and experimental methods for the sensible effectiveness of air-to-air energy recovery wheels, *HVAC&R Research*, ***14*** (3), 373–396.

Shang, W., & Besant, R. W., (2009c), Effectiveness of desiccant coated regenerative wheels from transient response characteristics and Flow channel properties -part I: development of effectiveness equations. *HVAC&R Research*, ***15*** (2), 329–346.

Simonson, C.J. and Besant, R. W., (1999), Energy wheel effectiveness-part I: development of dimensionless groups. *International Journal of Heat and Mass Transfer*, ***42***, 2161–2170.

Simonson, C. J., (1998), *Heat and moisture transfer in energy wheels*, Ph.D. Thesis, University of Saskatchewan.

Simonson, C. J., & Besant, R. W., (1998), Heat and moisture transfer in energy wheels during sorption, condensation, and frosting conditions. *Journal of Heat Transfer*, ***120*** (3), 699–708.

Simonson, C. J., & Besant, R. W., (1999), Energy wheel effectiveness: part II-correlations. *International Journal of Heat and Mass Transfer*, ***42***, 2171–2185.

Sphaier, L. A., & Worek, W. M., (2004), Analysis of heat and mass transfer in porous sorbents used in rotary regenerators. *International Journal of Heat and Mass Transfer*, ***47*** (14-16), 3415–3430.

Sterling, E. M., Arundel, A., & Sterling, T. D., (1985), Criteria for human exposer to humidity in occupied buildings. *ASHRAE Transactions*, ***91*** (1), 611–622.

Sundell, J., Levin, H., Nazaroff, W. W., Cain, W. S., Fisk, W. J., Grimsrud, D. T., Weschler, C. J., (2011), Ventilation rates and health: multidisciplinary review of the scientific literature. *Indoor Air*, ***21*** (3), 191–204.

Tao, Y. X., Besant, R. W., & Simonson, C. J., (1992), Measurement of the heat of adsorption for a typical fibrous insulation. *ASHRAE Transactions*, ***6*** (3), 495–501.

U.S. Energy Information Administration (EIA), (2015), *Annual Energy Outlook 2015*.

Vårum, K., & Smidsrod, O., (2004), *Structure-Property Relationship in Chitosans, Polysaccharides*, CRC Press.

Wang, X. L., Chua, H. T., & L. Z, G., (2007), A thermogravimetric analyzer for condensable gas adsorption under subatmospheric conditions. *Journal of Thermal Analysis and Calorimetry*, ***90*** (3), 935–940.

Wang, X., Zimmermann, W., Ng, K. C., Chakraboty, A., & Keller, J. U., (2004), Investigation on the isotherm of silica gel+water systems, *Journal of Thermal Analysis and Calorimetry*, ***76*** (2), 659–669.

Wang, Y., (2005), *Transient characteristics of humidity sensors and their application to energy wheels*, M.Sc Thesis, University of Saskatchewan.

Wang, Y., Besant, R. W., Simonson, C. J., & Shang, W., (2006), Application of humidity sensors and an interactive device, *Sensors and Actuators B: Chemical*, ***115*** (1), 93–101.

Wang, Y. H., Besant, R. W., & Simonson, C. J., (2005),Transient Humidity Measurements for Flow Through an Energy Wheel, *ASHRAE Transactions*, ***111***, 353–369.

Westgate, P. J., & Ladisch, M. R., (1993), Sorption of organics and water on starch. *Industrial & Engineering Chemistry Research*, ***32*** (8), 1676–1680.

Wood, D. L., & Rabinovich, E. M., (1989), Study of alkoxide silica gels by infrared spectroscopy. *Applied Spectroscopy*, ***43***(2), 263–267.

Wu, Z., Melnik, R. V. N. N., & Borup, F., (2006), Model-based analysis and simulation of regenerative heat wheel. *Energy and Buildings*, ***38***(5), 502–514.

Xu, Z., Cai, J., & Pan, B., (2013), Mathematically modeling fixed-bed adsorption in aqueous systems. *Journal of Zhejiang University Science*, ***14*** (3), 155–176.

Yilmaz, T., & Büyükalaca, O., (2003), Design of Regenerative Heat Exchangers. *Heat Transfer Engineering*, ***24*** (4), 32–38. 4

Yilmaz, T., & Cihan, E., (1993), General equation for heat transfer for laminar flow in ducts of arbitrary cross-sections, *International Journal of Heat and Mass Transfer*, ***36*** (13), 3265–3270.

Yoon, Y. H. E. E., & Nelson, J. H., (1984), Application of gas adsorption kinetics: A theoretical model for respirator cartridge service life, *American Industrial Hygiene Association Journal*, ***45*** (8), 509–516.

Yu, B. F., Hu, Z. B., Liu, M., Yang, H. L., Kong, Q. X., & Liu, Y. H, (2009), Review of research on air-conditioning systems and indoor air quality control for human health, *International Journal of Refrigeration*, ***32*** (1), 3–20.

Zhang, L. Z., & Niu, J. L., (2002), Performance comparisons of desiccant wheels for air dehumidification and enthalpy recovery, *Applied Thermal Engineering*, ***22*** (12), 1347–1367.

Zhang, X. J., Dai, Y. J., & Wang, R. Z., (2003), A simulation study of heat and mass transfer in a honeycombed rotary desiccant dehumidifier. *Applied Thermal Engineering*, ***23*** (8), 989–1003.

Zheng, X., Ge, T. S., & Wang, R. Z., (2014), Recent progress on desiccant materials for solid desiccant cooling systems, *Energy*, ***74***, 280–294.

APPENDIX A

CYCLIC TEST UNCERTAINTY ANALYSIS

For the steady state test, the main source of uncertainty comes from the area integration. To integrate the area between the output and input temperature profiles, the normalized temperature was precisely fitted by a function f with its relevant uncertainty as:

$$\theta = f(t) \pm U_\theta \tag{A.1}$$

Where, $f(t)$ is a ninth order polynomial and $\delta\theta$ is the uncertainty in measuring normalized temperature. Considering normalized temperature defined by eq. (A.1), U_θ can be calculated as follows:

$$U_\theta = \frac{2U_T}{\Delta T_{st}} \tag{A.2}$$

Then, the sensible effectiveness can be found by:

$$\varepsilon_{PF} = \frac{\int_0^{\frac{\pi}{\omega}} \theta dt}{\frac{\pi}{\omega}} = \frac{\int_0^{\frac{\pi}{\omega}} f(t) dt}{\frac{\pi}{\omega}} \pm \frac{\int_0^{\frac{\pi}{\omega}} U_\theta dt}{\frac{\pi}{\omega}} \tag{A.3}$$

then,

$$U_{\varepsilon_{PF}} = \frac{\int_0^{\frac{\pi}{\omega}} U_\theta dt}{\frac{\pi}{\omega}} = U_\theta \tag{A.4}$$

Using calibration data for $U_{\mathrm{T}} = \pm 0.2$ °C and considering $\Delta T_{\mathrm{st}} = 27.6$ °C then U_{θ} is found to be 0.014. Consequently, the bias uncertainty in the sensible effectiveness can be determined as $U_{\mathrm{B},\varepsilon_{\mathrm{PF}}} = 1.4$ %. To find the bias uncertainty in the sensible effectiveness of a counter-flow wheel, the method of propagation of error is used as follows:

$$U_{B,\varepsilon_{CF}} = \sqrt{\left(\frac{\partial \varepsilon_{CF}}{\partial \theta}\right)^2 {U_{B,\theta}}^2} \tag{A.5}$$

The derivation of effectiveness with respect to normalized temperature can be found using the chain rule. Therefore,

$$\frac{\partial \varepsilon_{CF}}{\partial \theta} = \left(\frac{\partial \varepsilon_{CF}}{\partial NTU}\right)\left(\frac{\partial NTU}{\partial \varepsilon_{PF}}\right)\left(\frac{\partial \varepsilon_{PF}}{\partial \theta}\right) \tag{A.6}$$

where $\left(\frac{\partial NTU}{\partial \varepsilon_{PF}}\right)$ and $\left(\frac{\partial \varepsilon_{CF}}{\partial NTU}\right)$ are found based on Eqs. (2.9) and (2.11) as follows:

$$\frac{\partial NTU}{\partial \varepsilon_{PF}} = e^{2NTU} \tag{A.7}$$

And

$$\frac{\partial \varepsilon_{CF}}{\partial NTU} = \frac{1}{(1+NTU)^2} \tag{A.8}$$

Using the fact that $\frac{\partial \varepsilon_{PF}}{\partial \theta} = \frac{U_{B,\varepsilon_{PF}}}{U_{B,\theta}}$, then eq. (A.5) can be written as:

$$U_{B,\varepsilon_{CF}} = \sqrt{\left(\frac{e^{2Ntu}}{(1+NTU)^2}\right)^2 {U_{B,\varepsilon_{PF}}}^2} \tag{A.9}$$

This equation can be expressed in terms of sensible effectiveness of a parallel-flow exchanger by replacing NTU with $\varepsilon_{\mathrm{PF}}$ from eq. (2.9):

$$U_{B,\varepsilon_{CF}} = \sqrt{\left((1-2\varepsilon_{PF})^{-1}\left(1-\frac{1}{2}Ln(1-2\varepsilon_{PF})\right)^{-2}\right)^2 {U_{B,\varepsilon_{PF}}}^2} \tag{A.10}$$

APPENDIX B

COPYRIGHT PERMISSIONS

B.1 Permission for Manuscripts Used in Chapters 2

The Manuscript in chapter 2 is published by Elsevier. According to the Elsevier copyright policies, authors can use their publication for their thesis without a written permission from Elsevier. Following statement has been directly copied from Elsevier website:

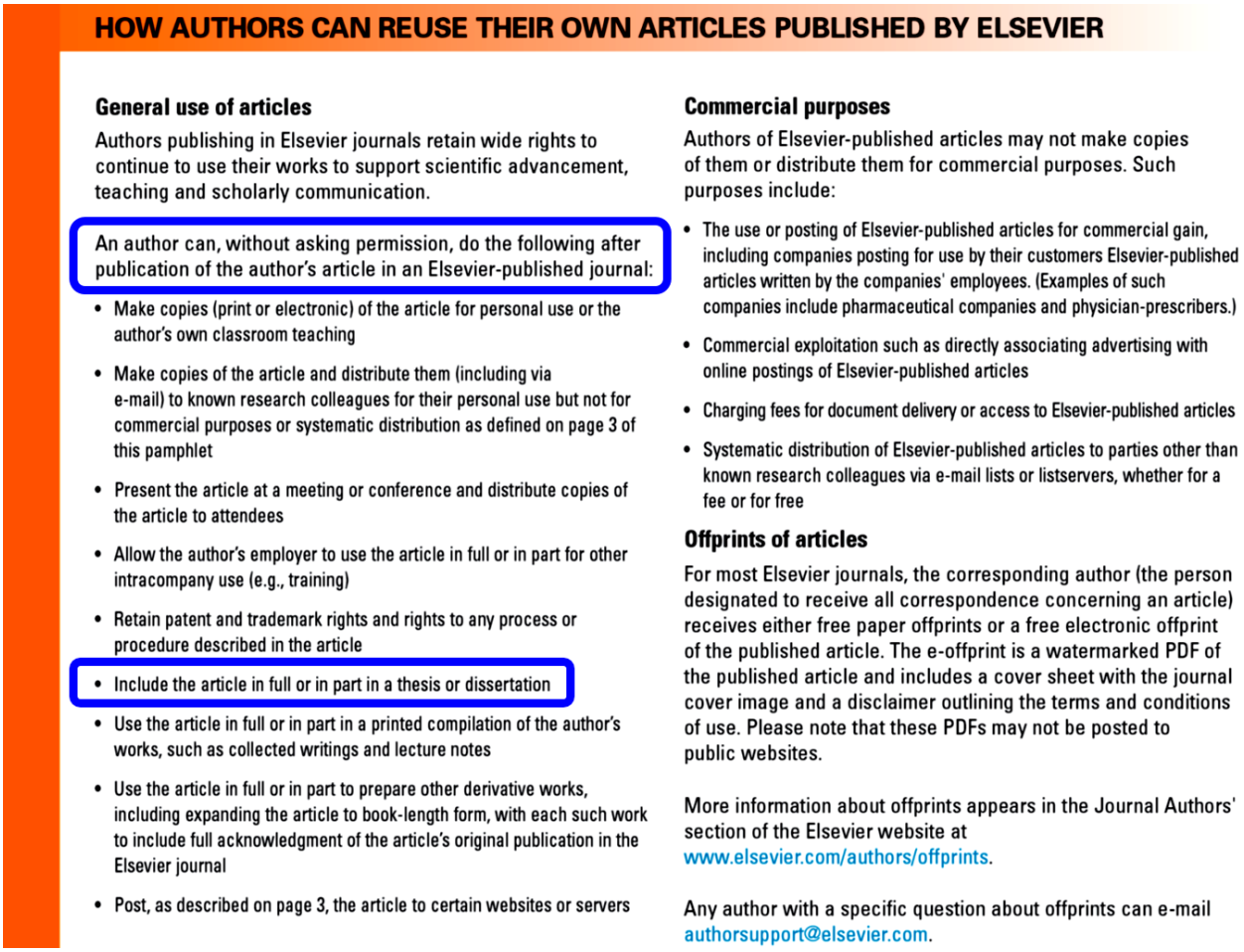

HOW AUTHORS CAN REUSE THEIR OWN ARTICLES PUBLISHED BY ELSEVIER

General use of articles

Authors publishing in Elsevier journals retain wide rights to continue to use their works to support scientific advancement, teaching and scholarly communication.

An author can, without asking permission, do the following after publication of the author's article in an Elsevier-published journal:

- Make copies (print or electronic) of the article for personal use or the author's own classroom teaching
- Make copies of the article and distribute them (including via e-mail) to known research colleagues for their personal use but not for commercial purposes or systematic distribution as defined on page 3 of this pamphlet
- Present the article at a meeting or conference and distribute copies of the article to attendees
- Allow the author's employer to use the article in full or in part for other intracompany use (e.g., training)
- Retain patent and trademark rights and rights to any process or procedure described in the article
- Include the article in full or in part in a thesis or dissertation
- Use the article in full or in part in a printed compilation of the author's works, such as collected writings and lecture notes
- Use the article in full or in part to prepare other derivative works, including expanding the article to book-length form, with each such work to include full acknowledgment of the article's original publication in the Elsevier journal
- Post, as described on page 3, the article to certain websites or servers

Commercial purposes

Authors of Elsevier-published articles may not make copies of them or distribute them for commercial purposes. Such purposes include:

- The use or posting of Elsevier-published articles for commercial gain, including companies posting for use by their customers Elsevier-published articles written by the companies' employees. (Examples of such companies include pharmaceutical companies and physician-prescribers.)
- Commercial exploitation such as directly associating advertising with online postings of Elsevier-published articles
- Charging fees for document delivery or access to Elsevier-published articles
- Systematic distribution of Elsevier-published articles to parties other than known research colleagues via e-mail lists or listservers, whether for a fee or for free

Offprints of articles

For most Elsevier journals, the corresponding author (the person designated to receive all correspondence concerning an article) receives either free paper offprints or a free electronic offprint of the published article. The e-offprint is a watermarked PDF of the published article and includes a cover sheet with the journal cover image and a disclaimer outlining the terms and conditions of use. Please note that these PDFs may not be posted to public websites.

More information about offprints appears in the Journal Authors' section of the Elsevier website at www.elsevier.com/authors/offprints.

Any author with a specific question about offprints can e-mail authorsupport@elsevier.com.

Source: http://libraryconnect.elsevier.com/sites/default/files/lcp0404.pdf (accessed: March 2016)

B.2 Permission for Manuscripts Used in Chapters 3

The manuscript used in Chapter 4 is published in ASME Journal of Thermal Science and Engineering Application. The following is a written permission to include the published manuscript in this Ph.D. thesis.

"Dear Mr. Fathieh:

It is our pleasure to grant you permission to use ***all or any part of the*** *ASME paper "Effects of Heat Loss/Gain on the Transient Testing of Heat Wheels," by Farhad Fathieh; Robert/W Besant; Richard W. Evitts; Carey J. Simonson*

J. Thermal Sci. Eng. Appl., Accepted Manuscript, 2016, cited in your letter for inclusion in a Ph. D. thesis to be published by University of Saskatchewan.

Permission is granted for the specific use as stated herein and does not permit further use of the materials without proper authorization. Proper attribution must be made to the author(s) of the materials. ***Please note****: if any or all of the figures and/or Tables are of another source, permission should be granted from that outside source or include the reference of the original source. ASME does not grant permission for outside source material that may be referenced in the ASME works. As is customary, we request that you ensure full acknowledgment of this material, the author(s), source and ASME as original publisher. Acknowledgment must be retained on all pages printed and distributed.*

Sincerely,

Beth Darchi
Publishing Administrator
ASME
2 Park Avenue, 6th Floor
New York, NY 10016-5990
Tel 1.212.591.7700
darchib@asme.org"

B.3 Permission for Manuscripts Used in Chapters 4

According to the College of Graduate Studies and Research at the University of Saskatchewan, a written permission is required from each of the co-authors for unpublished manuscripts. The manuscript used in Chapter 4 is unpublished, therefore, copyright permissions are obtained from the co-authors as follows.

Copyright Permission Request Form

I am preparing the publication of a manuscript titled "*Determination of Air-to-Air Energy Wheel Latent Effectiveness in Using Humidity Step Test Data"* to be published as the fourth chapter of my Ph.D. thesis, and to be submitted to the Department of Mechanical Engineering at the University of Saskatchewan. The authors contributing in the completion of this manuscript are

Farhad Fathieh, Mohamad Rafati Nasr, Saied Sadeh, Robert W. Besant, Richard W. Evitts, Jens Müller, Carey J. Simonson

I am requesting permission to use the materials described in the aforementioned manuscript in my Ph.D. thesis and all subsequent editions that may be prepared at the University of Saskatchewan. Please indicate agreeemnt by signing below:

Permission granted by: Carey Simonson

Signature:

Date:

Copyright Permission Request Form

I am preparing the publication of a manuscript titled "*Determination of Air-to-Air Energy Wheel Latent Effectiveness in Using Humidity Step Test Data"* to be published as the fourth chapter of my Ph.D. thesis, and to be submitted to the Department of Mechanical Engineering at the University of Saskatchewan. The authors contributing in the completion of this manuscript are

Farhad Fathieh, Mohamad Rafati Nasr, Saied Sadeh, Robert W. Besant, Richard W. Evitts, Jens Müller, Carey J. Simonson

I am requesting permission to use the materials described in the aforementioned manuscript in my Ph.D. thesis and all subsequent editions that may be prepared at the University of Saskatchewan. Please indicate agreeemnt by signing below:

Permission granted by: Richard Evitts

Signature:

Date:

Copyright Permission Request Form

I am preparing the publication of a manuscript titled "*Determination of Air-to-Air Energy Wheel Latent Effectiveness in Using Humidity Step Test Data"* to be published as the fourth chapter of my Ph.D. thesis, and to be submitted to the Department of Mechanical Engineering at the University of Saskatchewan. The authors contributing in the completion of this manuscript are

Farhad Fathieh, Mohamad Rafati Nasr, Saied Sadeh, Robert W. Besant, Richard W. Evitts, Jens Müller, Carey J. Simonson

I am requesting permission to use the materials described in the aforementioned manuscript in my Ph.D. thesis and all subsequent editions that may be prepared at the University of Saskatchewan. Please indicate agreeemnt by signing below:

Permission granted by: Robert Besant

Signature:

Date:

Copyright Permission Request Form

I am preparing the publication of a manuscript titled "*Determination of Air-to-Air Energy Wheel Latent Effectiveness in Using Humidity Step Test Data"* to be published as the fourth chapter of my Ph.D. thesis, and to be submitted to the Department of Mechanical Engineering at the University of Saskatchewan. The authors contributing in the completion of this manuscript are

Farhad Fathieh, Mohamad Rafati Nasr, Saied Sadeh, Robert W. Besant, Richard W. Evitts, Jens Müller, Carey J. Simonson

I am requesting permission to use the materials described in the aforementioned manuscript in my Ph.D. thesis and all subsequent editions that may be prepared at the University of Saskatchewan. Please indicate agreeemnt by signing below:

Permission granted by: Jens Müller

Signature:

Date:

Copyright Permission Request Form

I am preparing the publication of a manuscript titled "*Determination of Air-to-Air Energy Wheel Latent Effectiveness in Using Humidity Step Test Data"* to be published as the fourth chapter of my Ph.D. thesis, and to be submitted to the Department of Mechanical Engineering at the University of Saskatchewan. The authors contributing in the completion of this manuscript are

Farhad Fathieh, Mohamad Rafati Nasr, Saied Sadeh, Robert W. Besant, Richard W. Evitts, Jens Müller, Carey J. Simonson

I am requesting permission to use the materials described in the aforementioned manuscript in my Ph.D. thesis and all subsequent editions that may be prepared at the University of Saskatchewan. Please indicate agreeemnt by signing below:

Permission granted by: Mohamad Rafati Nasr

Signature:

Date:

Copyright Permission Request Form

I am preparing the publication of a manuscript titled "*Determination of Air-to-Air Energy Wheel Latent Effectiveness in Using Humidity Step Test Data"* to be published as the fourth chapter of my Ph.D. thesis, and to be submitted to the Department of Mechanical Engineering at the University of Saskatchewan. The authors contributing in the completion of this manuscript are

Farhad Fathieh, Mohamad Rafati Nasr, Saied Sadeh, Robert W. Besant, Richard W. Evitts, Jens Müller, Carey J. Simonson

I am requesting permission to use the materials described in the aforementioned manuscript in my Ph.D. thesis and all subsequent editions that may be prepared at the University of Saskatchewan. Please indicate agreeemnt by signing below:

Permission granted by: Saied Sadeh

Signature:

Date:

Copyright Permission Request Form

I am preparing the publication of a manuscript titled "*Determination of Air-to-Air Energy Wheel Latent Effectiveness in Using Humidity Step Test Data"* to be published as the fourth chapter of my Ph.D. thesis, and to be submitted to the Department of Mechanical Engineering at the University of Saskatchewan. The authors contributing in the completion of this manuscript are

Farhad Fathieh, Mohamad Rafati Nasr, Saied Sadeh, Robert W. Besant, Richard W. Evitts, Jens Müller, Carey J. Simonson

I am requesting permission to use the materials described in the aforementioned manuscript in my Ph.D. thesis and all subsequent editions that may be prepared at the University of Saskatchewan. Please indicate agreeemnt by signing below:

Permission granted by: Jens Müller

Signature:

Date:

B.4 Permission for Manuscripts Used in Chapters 5

According to the College of Graduate Studies and Research at the University of Saskatchewan, a written permission is required from each of the co-authors for unpublished manuscripts. The manuscript used in Chapter 5 is unpublished, therefore, copyright permissions are obtained from the co-authors as follows.

Copyright Permission Request Form

I am preparing the publication of a manuscript titled "*Effects of Physical and Sorption Properties of Mesoporous Silica Gel on Dehumidification Performance of Energy Wheels"* to be published as the fourth chapter of my Ph.D. thesis, and to be submitted to the Department of Mechanical Engineering at the University of Saskatchewan. The authors contributing in the completion of this manuscript are

Farhad Fathieh, Majid Nezakat, Robert W. Besant, Richard W. Evitts, Carey J. Simonson

I am requesting permission to use the materials described in the aforementioned manuscript in my Ph.D. thesis and all subsequent editions that may be prepared at the University of Saskatchewan. Please indicate agreeemnt by signing below:

Permission granted by: Carey Simonson

Signature:

Date:

Copyright Permission Request Form

I am preparing the publication of a manuscript titled "*Effects of Physical and Sorption Properties of Mesoporous Silica Gel on Dehumidification Performance of Energy Wheels"* to be published as the fourth chapter of my Ph.D. thesis, and to be submitted to the Department of Mechanical Engineering at the University of Saskatchewan. The authors contributing in the completion of this manuscript are

Farhad Fathieh, Majid Nezakat, Robert W. Besant, Richard W. Evitts, Carey J. Simonson

I am requesting permission to use the materials described in the aforementioned manuscript in my Ph.D. thesis and all subsequent editions that may be prepared at the University of Saskatchewan. Please indicate agreeemnt by signing below:

Permission granted by: Richard Evitts

Signature:

Date:

Copyright Permission Request Form

I am preparing the publication of a manuscript titled "*Effects of Physical and Sorption Properties of Mesoporous Silica Gel on Dehumidification Performance of Energy Wheels"* to be published as the fourth chapter of my Ph.D. thesis, and to be submitted to the Department of Mechanical Engineering at the University of Saskatchewan. The authors contributing in the completion of this manuscript are

Farhad Fathieh, Majid Nezakat, Robert W. Besant, Richard W. Evitts, Carey J. Simonson

I am requesting permission to use the materials described in the aforementioned manuscript in my Ph.D. thesis and all subsequent editions that may be prepared at the University of Saskatchewan. Please indicate agreeemnt by signing below:

Permission granted by: Robert Besant

Signature:

Date:

Copyright Permission Request Form

I am preparing the publication of a manuscript titled "*Effects of Physical and Sorption Properties of Mesoporous Silica Gel on Dehumidification Performance of Energy Wheels"* to be published as the fourth chapter of my Ph.D. thesis, and to be submitted to the Department of Mechanical Engineering at the University of Saskatchewan. The authors contributing in the completion of this manuscript are

Farhad Fathieh, Majid Nezakat, Robert W. Besant, Richard W. Evitts, Carey J. Simonson

I am requesting permission to use the materials described in the aforementioned manuscript in my Ph.D. thesis and all subsequent editions that may be prepared at the University of Saskatchewan. Please indicate agreeemnt by signing below:

Permission granted by: Majid Nezakat

Signature:

Date:

B.5 Permission for Manuscripts Used in Chapters 6

The Manuscript in chapter6 is published by ACS. According to the ACS copyright policies, authors can use their publication for their thesis without a written permission from Elsevier. Following statement has been directly copied from Elsevier website:

"*If your paper has already been published by ACS and you want to include the text or portions of the text in your thesis/dissertation, please print the ACS copyright credit line on the first page of your article:*

Authors may reuse all or part of the Submitted, Accepted or Published Work in a thesis or dissertation that the author writes and is required to submit to satisfy the criteria of degree-granting institutions. Such reuse is permitted subject to the ACS' "Ethical Guidelines to Publication of Chemical Research" (http://pubs.acs.org/page/policy/ethics/index.html); the author should secure written confirmation (via letter or email) from the respective ACS journal editor(s) to avoid potential conflicts with journal prior publication/embargo policies.*"